

**CoPt<sub>3</sub> Nanoparticles:  
Ligand Exchange and Film Preparation**

A dissertation  
submitted to the University of Hamburg for the degree of  
Doctor of Natural Sciences

**Vesna T. Aleksandrović**

from Belgrade (Serbia)

August 2006

The work described in this thesis was carried out in the Institute of Physical Chemistry, University of Hamburg in Prof. Dr. H. Weller group.

1. Referee: Prof. Dr. H. Weller
2. Referee: Prof. Dr. S. Förster

*Dedicated to my family*

*Посвећено мојој породици*

## Acknowledgements

My words of gratitude go first to *Prof. Dr. Horst Weller* for inviting me to join his group, to research a very interesting scientific topic, for providing excellent experimental facilities and for many useful discussions, which eventually led to this manuscript.

I am very thankful to *Prof. Dr. S. Förster* for giving me opportunity to do investigations with polymers synthesised in his group and for useful advices concerning polymer-related issues.

My special thanks go to *Dr. Andreas Frömsdorf* who introduced me to the small secrets of film preparation techniques and their characterisation, who performed SAXS and GISAXS measurements on my samples and acquainted me to both techniques. His highly appreciated advices were always valuable.

I would like to express my gratitude to *Dipl.-Ing. Andreas Kornowski* for many fruitful discussions, for hundreds of SEM and TEM images, but most of all for useful advices and encouragement in the moments when nothing seemed to be working. Thank you for that!

Excellent TEM and HRTEM are the result of highly professional work of *Silvia Bartholdi-Nawrath* my sincere gratitude. *Almut Barck* and *Sandra Hirzberger* are acknowledged for the powder XRD measurements. *Frank Bürli* and glass blowers: *Werner Gehring* and *Hilmar Zacharek* are thanked for their technical support.

I am also very thankful to *Ms Rosemarie Pakula* for her willingness to help in all the bureaucratic affairs, which immersed during these three years.

I would like to thank *Dr. Florence Benoit Marquié* (University Paul Sabatier, Toulouse, France) for the help and cooperation during my investigation of dip coating technique. Florence made everything easier and quicker by applying statistic analyses, and I am very grateful for the effort she invested in the data analysis of measurements I performed.

Also thanks go to *Prof. Dr. J. Falta* and *Dr. J. I. Flege* (University Bremen) as well as to *Prof. Dr. M. Bäumer* and *B. Gehl* (University Bremen) for a very successful cooperation and for a lot of GISAXS measurements done in Trieste - Italy, and much more evaluations of the data.

*Dr. Igor Randjelović* is one of the persons who greatly influenced my decision to start with my doctoral research in Hamburg. I would like to thank him not only for his friendship and constant support during my stay here but also for the very nice and successful collaboration during the work on Langmuir Blodgett films.

Also thanks go to all students that helped me during my work: *Vera, Johan, Eddy, Julia, Meike, Sebastian* and *Olli*.

I am indebted to *Dr. Claudia Pacholski, Dr. Kathrin Hoppe, Dr. Nevena Šušnjar* and *Danijela Jovanović* for thorough reading of this thesis, multiple corrections and valuable comments. Many thanks go to *Mona Nagel* for translating the Summary of this thesis to German, and offering all her unselfish help.

I am very grateful to all my colleges from *AK Weller* for the nice working atmosphere, for fruitful discussions and for the nice moments spend outside the University.

I would also like to mention *Prof. Dr Ivanka Popović*, who recommended me for this PhD position and also gave useful comments concerning thermoanalysis of the investigated materials, and *Prof. Dr. Katarina Jeremić* for being there always when I needed advice and help.

Finally, and most importantly, I thank *my family* and *Saša* for their support, love and patience. They gave me the strength to finalize this thesis.

*The work described in this thesis was carried out within the Institute of Physical Chemistry, University of Hamburg, from January 2003 to Jun 2006, and was supported by the Graduiertenkolleg 611.*

# Content

Title	i
Acknowledgements	iv
Content	vi
Notations	x
<b>1. Introduction</b>	<b>1</b>
1.1. Magnetic nanoparticles	1
1.2. Synthesis of magnetic nanoparticles	2
1.3. Assembly of magnetic nanoparticles	2
1.4. Contents of this thesis	4
1.5. Literature	4
<b>Ligand exchange</b>	
<b>2. Ligand exchange – carboxylic acids</b>	<b>7</b>
2.1. Introduction	7
2.2. Removal of ligands from as-prepared particles	7
2.3. IR analysis of samples before and after ligand exchange	9
2.3.1. <i>IR analysis of particles before ligand exchange</i>	9
2.3.2. <i>IR analyses of particles after ligand exchange</i>	11
Unsaturated acids	11
Saturated acids	14
2.4. TG and DSC analyses of particles before and after ligand exchange	15
2.4.1. <i>TG and DSC analyses of particles before ligand exchange</i>	15
2.4.2. <i>TG and DSC analyses of CoPt<sub>3</sub> nanoparticles after ligand exchange</i>	21
2.5. Influence of the ligands on particle self-assembly	26
2.5.1. <i>2-D structures of CoPt<sub>3</sub> nanoparticles</i>	26
2.5.2. <i>3-D structures of CoPt<sub>3</sub> nanoparticles</i>	30
2.6. Conclusion	34
2.7. Literature	35
<b>3. Ligand exchange – amines</b>	<b>37</b>
3.1. Introduction	37
3.2. Ligand exchange with amines	38
3.3. Ligand exchange with polymers containing -NH <sub>2</sub> groups	40
3.4. Conclusion	42
3.5. Literature	42
<b>4. Ligand exchange – thiols</b>	<b>44</b>
4.1. Introduction	44

4.2. IR analyses of CoPt <sub>3</sub> nanoparticles before and after ligand exchange with DDT	45
4.3. Indications for the formation of complexes during the ligand exchange procedure	46
4.4. Influence of particle size and shape on ligand exchange between CoPt <sub>3</sub> nanoparticles and dodecanthiol	47
4.5. Conclusion	58
4.6. Literature	58

## **Film preparation**

<b>5. Spin coating technique</b>	<b>61</b>
5.1. Introduction	61
5.2. Spin coating: procedure and theory	62
5.3 Influence of concentration and speed on covering	66
5.4 Influence of wafer preparation on film quality	69
5.5 Deposition of CoPt <sub>3</sub> nanoparticles on different polymer substrates	70
5.5.1. <i>Preparation of polymer substrates</i>	71
5.5.2. <i>Particle deposition on polymer substrates</i>	73
5.6 Conclusion	79
5.7. Literature	80
<b>6. Dip-coating technique</b>	<b>82</b>
6.1. Dip coating	82
6.2. Statistical experimental design applied in nanoparticle film preparation by dip coating technique	85
6.2.1. <i>Statistical experimental design</i>	86
6.2.2. <i>Design I</i>	87
6.2.3. <i>Experimental design applied on CoPt<sub>3</sub> deposition on silicon by dip coating technique</i>	88
6.3. Design II	92
6.4. GISAXS investigations	96
6.5. Conclusion	100
6.6. Literature	100
<b>7. Langmuir-Blodgett technique</b>	<b>102</b>
7.1. Principle of the Langmuir-Blodgett technique (LB technique)	102
7.2. Materials suited to the LB technique	103
7.3. Subphase	103
7.4. Isotherms	103
7.5. Application of LB technique	105
7.6. Langmuir – Blodgett films of nanoparticles	106
7.7. Langmuir – Blodgett films of CoPt <sub>3</sub> nanoparticles prepared on water as a subphase	107

7.7.1. Particles stabilised with sorbic acid	111
7.7.2. Particles with different polymer ligands	116
7.8. Langmuir – Blodgett films of CoPt <sub>3</sub> nanoparticles prepared on different glycols as a subphase	117
7.8.1. The LB film preparation	120
7.8.2. Influence of the substrate angle on the particle deposition	121
7.8.3. Influence of the washing procedure on the nanoparticle film quality	126
7.8.4. Influence of buffer layers on particle deposition	128
7.9. Conclusion	129
7.10. Literature	130
<b>8. Ligand removal by thermal and plasma treatment of films</b>	<b>133</b>
8.1. Introduction	133
8.2. Heating of CoPt <sub>3</sub> monolayers deposited on the silicon wafers	134
8.3. Conclusion	137
8.4 Literature	137
<b>9. Experimental part</b>	<b>139</b>
<i>Synthesis of CoPt<sub>3</sub> nanoparticles</i>	
9.1. Synthesis of CoPt <sub>3</sub> nanocrystals	139
Chemicals	139
Syntheses of nanoparticles	139
9.2. Post-preparative procedures	140
9.3. Size selective precipitation	141
9.4. Scaling up the reaction	141
9.5. Synthesis of CoPt <sub>3</sub> nanoparticles stabilised only with ACA	142
9.6. Ligand exchange with acids	142
Chemicals	142
Ligand exchange	142
9.7. Ligand exchange – thiols	143
9.8. Ligand exchange – amines	144
9.9. Methods for particle characterization	144
X-ray diffraction measurements (XRD)	144
Transmission Electron Microscopy (TEM) and high-resolution transmission electron microscopy (HRTEM)	144
Scanning Electron Microscope (SEM)	145
Attenuated Total Reflectance Fourier Transform Infrared Spectroscopy (ATR/FT-IR)	145
Thermo gravimetric analysis (TGA)	145
Differential scanning Calorimetry (DSC)	145
Small angle x-ray scattering (SAXS)	146

<b><i>Film preparation</i></b>	
9.10 Used chemicals:	148
9.11. Procedures for wafer cleaning	149
9.12. Silanisation of silicon wafers	149
9.13. Film preparation	149
Spin coating	149
Dip coating	150
Langmuir Blodgett	150
9.14. Film characterisation	152
9.14.1. <i>Scanning Electron Microscope (SEM)</i>	152
9.14.2. <i>Atomic force microscopy (AFM)</i>	152
9.14.3. <i>Grazing Incidence Small Angle X-Ray Scattering (GISAXS)</i>	154
9.15. Literature	158
<b>10. Summary</b>	<b>160</b>
Zusammenfassung	<b>163</b>
Appendix	<b>166</b>
Appendix 1. IR spectra of different ligands	166
Appendix 2. Safety precaution information on the used chemicals	169
Curriculum Vitae	
Lebenslauf	
Declaration	

## Notations

ACA	1-Adamantane Carboxylic Acid
AFM	Atomic Force Microscopy
ARA	Arachidic Acid
ATR/FT-IR	Attenuated Total Reflectance Fourier Transform Infrared (ATR/FT-IR) S Spectroscopy
DDA	Dodecylamine
DDT	Dodecanthiol
DSC	Differential Scanning Calorimetry
EDX	Energy Dispersive X-ray analysis
GISAXS	Greasing Incident Small Angle X-ray Scattering
HDA	Hexadecylamine
HRSEM	High Resolution Scanning Electron Microscopy
HRTEM	High Resolution Transmission Microscopy
LA	Linoleic Acid
LB	Langmuir Blodgett Technique
P2VP	Poly(2-vinyl pyridine)
P4VP	Poly(4-vinyl pyridine)
PEO	Poly(ethylene oxide)
PEOA	poly(ethylene oxide) with one amino end-group
PEODA	poly(ethylene oxide)-diamine
RT	Room Temperature
SA	Sorbic Acid
SAXS	Small Angle X-ray Scattering
SEM	Scanning Electron Microscopy
TGA	Thermo gravimetric analysis
TEM	Transmission Electron Microscopy
UDA	Undecanoic Acid
XRD	X-Ray Diffraction

# Chapter 1

## Introduction

---

### 1.1. Magnetic nanoparticles

A **nanoparticle** is a microscopic particle, which size is measured in nanometres (nm). It is defined, as a particle with at least one dimension is  $< 200$  nm. Nanoparticles are of great scientific interest as they can be considered to be an effective link between bulk materials and atomic or molecular structures. A bulk material should have constant physical properties regardless of its size, but at the nano-scale this is often not the case. Size-dependent properties, such as quantum confinement in semiconductor particles, surface plasmon resonance in some metal particles and superparamagnetism in magnetic materials are observed.

The first nano-sized magnetic particles were developed in the 1960s. The particles were made by ball milling in the presence of a surface-active agent (surfactant) and liquid carrier. Such obtained dispersions are called magnetic fluids or ferrofluids<sup>[1]</sup>. Nowadays, magnetic nanoparticles are receiving increased attention due to their extensive application in the field of electronics, catalysis, high-density magnetic recording media and biotechnology<sup>[2]-[8]</sup>.

At the nanometer scale, many chemical and physical properties of solids become dramatically dependent on size. Therefore, the challenge has been and remains the control of size, size distribution, and shape of nanoparticles<sup>[9]-[13]</sup>. Control of size and shape of nanoparticles gives opportunity to manipulate their chemical and physical properties<sup>[14]</sup>. If ferromagnetic materials are below some critical size, each particle can contain only a single magnetic domain. Changes in the magnetization can no longer occur through the motion of domain walls and instead require the coherent rotation of spins, resulting in larger coercivity. For a particle size smaller than the single domain size, the spins are increasingly affected by the thermal fluctuations and originally ferromagnetic material becomes super paramagnetic.

## 1.2. Synthesis of magnetic nanoparticles

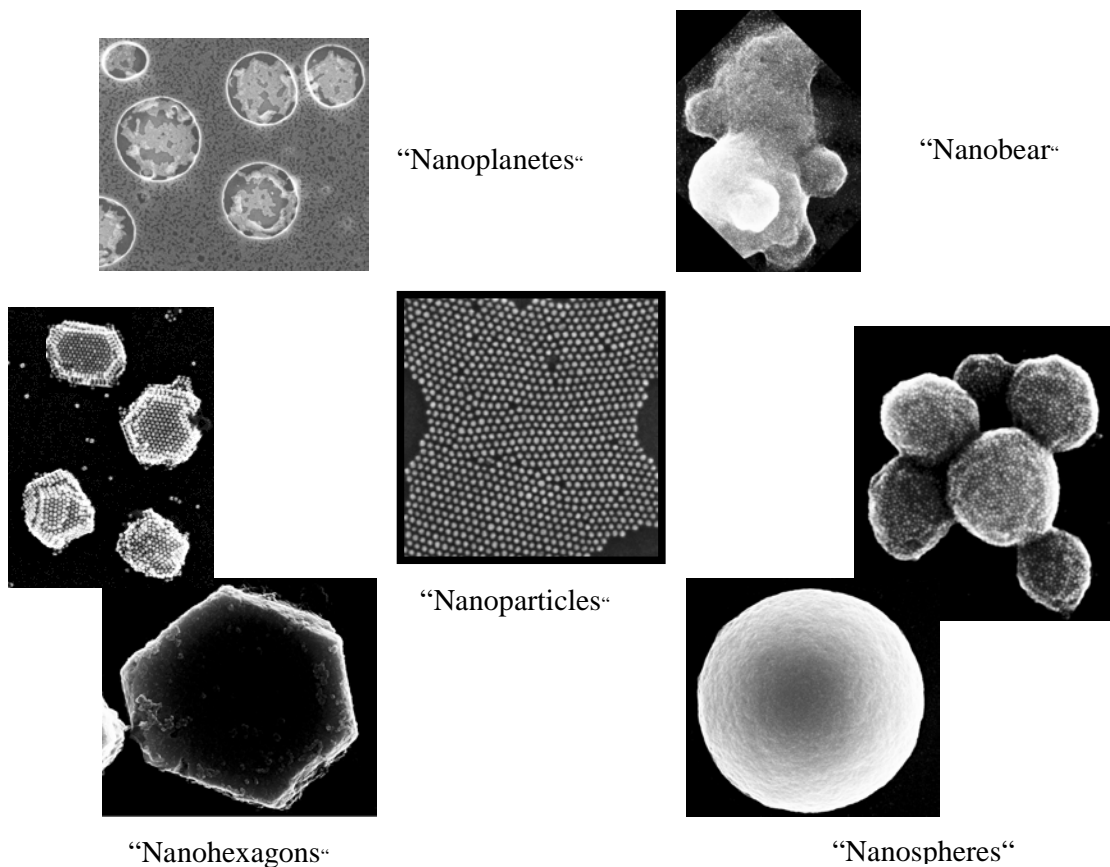
The most investigated magnetic nanoparticles are Co nanoparticles. Several successful approaches for their synthesis were developed, providing particles of controllable shapes and narrow size distributions<sup>[15]-[19]</sup>. These nanoparticles display a wealth of size dependent structural, magnetic, electronic, and catalytic properties. Significant progress in the preparation of magnetic nanoparticles was achieved during the last years by introducing “hot” organometallic synthetic routes where nanocrystals nucleate and grow at 150-300 °C in high-boiling solvents. Such recipes were developed for iron<sup>[17]</sup>, cobalt<sup>[19],[17]</sup> nickel<sup>[17]</sup> and alloys FePt<sup>[20]</sup>, CoPt<sup>[21]</sup> and CoPt<sub>3</sub><sup>[21],[22]</sup> nanocrystals. Monodisperse nanocrystals of magnetic materials (Fe, Co, Ni, FePt, CoPt<sub>3</sub>, etc.) attract special attention because of their potential in ultra-high-density magnetic data storage devices. The monodisperse nanocrystals of CoPt and FePt magnetic alloys are the best candidate for applications in ultra-high-density storage devices because of their large uniaxial anisotropy and high chemical stability<sup>[4]</sup>. Different synthetic approaches were developed for synthesis of Co-Pt particles with different Co to Pt ratio<sup>[21],[23]-[25]</sup>, as well as the core shell (Co-Pt or Pt-Co) particles<sup>[26]-[29]</sup>. Recently combinations of magnetic and semi-conducting (Co/CdSe<sup>[30]</sup>, FePt/CdS<sup>[31]</sup>) or magnetic and metal nanoparticles (CoPt<sub>3</sub>/Au<sup>[32]</sup> and CoPt<sub>3</sub>/Cu<sup>[33]</sup>) are in the scope of interest due to their combined physical properties.

The synthesized magnetic nanoparticles consist of a magnetic core capped with a shell of surface ligands, which prevents their agglomeration in a colloidal solution. The ligand shell composition also allows one to tailor chemical properties such as solubility, chemical reactivity, surface chemistry, and binding affinity. Ligand shells could be formed by covalent attachment of small-molecule ligands, by adsorption of polymers<sup>[34]-[36]</sup> or by encapsulation in block copolymer micelles<sup>[37]-[39]</sup>. Additionally, ligand shells determine the inter-particle spacing in nanoparticles ordered two and three-dimensional superstructures. Therefore, these nanoparticles can be used as the building blocks for assembling and patterning future nano-devices.

## 1.3. Assembly of magnetic nanoparticles

An important step for further commercial exploitation of nanoparticles is assembly of nano-materials into topologically predefined superstructures and their packing. While the properties of individual nanoparticles are no doubt exciting, the collective properties of

assembles of nanoparticles interacting with each other can be radically different from their individual counterparts, with interesting application potential<sup>[40]</sup>.



*Magical world of structures made by self-assembly of CoPt<sub>3</sub> nanoparticles*

For the design of novel nanostructured devices, a technique for preparing industrial-scale highly symmetric periodic particle array within the range of several microns is needed. Large periodic particle arrays can be prepared with ferro-fluids (standard particle size distribution of < 10 %) by simply drying a drop of solution on a suitable substrate. Self-assembly of nanoparticles on appropriate substrates is, without a doubt, the simplest way to make monolayers<sup>[3],[41]-[43]</sup>. However, there are several disadvantages associated with this method. One of the most important is that the formation of self-assembled monolayers depends on experimental conditions, making reproducibility difficult. Nevertheless, many quite impressive structures of metal nanoparticles have been reported in the last years<sup>[44],[45]</sup>.

This self-assembly technique has been improved by employment of different coating techniques (e.g. spin coating, dip coating, or spraying) in combination with applied external forces. The origin of these external forces is mechanical, used for the preparation of Langmuir

Blodgett films or electrostatic, used for layer-by-layer assembly-applying polyelectrolytes. The use of external electric and magnetic fields to improve the self-assembly of charged and magnetic nanoparticles, respectively, has also been reported<sup>[46]-[51]</sup>.

#### 1.4. Contents of this Thesis

In order to facilitate the preparation of nanocrystals particles appropriate for technological applications, relatively simple methods should be developed for the preparation of non-aggregated, monodisperse colloids as well as highly ordered layers on different substrates. Highly crystalline CoPt<sub>3</sub> nanoparticles can be prepared in a predictable and reproducible manner via high temperature synthetic route<sup>[22]</sup>. The development of effective and predictable method of precise size and shape (spherical<sup>[52]</sup>, cubic<sup>[52]</sup>, nanowires<sup>[51]</sup>) control of CoPt<sub>3</sub> nanoparticles, allowed their organisation in one-<sup>[53]</sup>, two-<sup>[22],[50]</sup> and three-dimensional structures<sup>[51]</sup>.

Investigations described in this thesis were performed in order to develop the ligand exchange procedure applicable on different organic molecules that can be used as ligands of nanoparticles. Additionally, the influence of these new ligands on particle properties and particle self-assembly was investigated. (Chapters 2., 3. and 4.). In order to produce highly symmetric periodic particle arrays, different techniques were applied and CoPt<sub>3</sub> nanoparticles were deposited on different surfaces by spin-coating, dip-coating and Langmuir Blodgett technique (Chapters 5., 6. and 7.).

#### 1.5. Literature

1. Jr., C.P.P. and F.J. Owens, *Introduction to Nanotechnology*. 2003: Wiley.
2. Wolf, E.L., *Nanophysics and Nanotechnology an Introduction to Modern Concepts in Nanoscience*. 2004: Wiley -VCH Verlag GmbH & Co. KGaA.
3. Schmid, G., D.V. Talapin, and E.V. Shevchenko, *Nanoparticles: From Theory to Application*, ed. G. Schmid. 2004: Wiley- VCH Verlag, Weinheim.
4. Kotov, N.A., *Nanoparticle Assemblies and Superstructures*. 2006: CRC Press, Taylor & Francis Group.
5. Klabunde, K.J., *Nanoscale Materials in Chemistry*. 2001: John Wiley & Sons, Inc.
6. Berry, C.C., *Possible exploitation of magnetic nanoparticle-cell interaction for biomedical applications*. *J. Mater. Chem.*, 2005. **15**: p. 543-547.
7. Tartaj, P., et al., *Advances in magnetic nanoparticles for biotechnology applications*. *J. Magn. Magn. Mater.*, 2005. **290-291**: p. 28-34.
8. Megens, M. and M. Prins, *Magnetic biochips: a new option for sensitive diagnostic*. *J. Magn. Magn. Mater.*, 2005. **293**: p. 702-708.

9. Burda, C., et al., *Chemistry and Properties of Nanocrystals of Different Shapes*. Chem. Rev., 2005. **105**: p. 1025-1102.
10. Jun, Y.-W., J.-S. Choi, and J. Cheon, *Shape Control of Semiconductor and Metal Oxide Nanocrystals through Nonhydrolytic Colloidal Routs*. Angew. Chem. Int. Ed., 2006. **45**: p. 3414-3439.
11. Lisiecki, I., *Size, Shape, and Structural Control of Metallic Nanocrystals*. J. Phys. Chem. B, 2005. **109**(25): p. 12231-12244.
12. Hyeon, T., *Chemical synthesis of magnetic nanoparticles*. Chem. Commun., 2003. **2003**(8): p. 927-934.
13. Wang, X., et al., *A general strategy for nanocrystal synthesis*. Nature, 2005. **437**(1 September 2005): p. 121-124.
14. Murray, C.B., C.R. Kagan, and M.G. Bawendi, *Synthesis and Characterisation of Monodisperse Nanocrystals and Closed Packed Nanocrystals Assemblies*. Annu. Rev. Mater. Sci., 2000. **30**: p. 545-610.
15. Puntès, V.F., K.M. Krishnan, and A.P. Alivisatos, *Colloidal Nanocrystal Shape and Size Control: The Case of Cobalt*. Science, 2001. **291**: p. 2115-2117.
16. Liu, G., et al., *One-Pot Synthesis of Block Copolymer Coated Cobalt Nanocrystals*. Chem. Mater., 2005. **17**: p. 4985-4991.
17. Murray, C.B., et al., *Monodisperse 3d Transition-Metal (Co, Ni, Fe) Nanoparticles and Their Assembly into Nanoparticle Superlattices*. MRS Bulletin, 2001. **December**: p. 985-991.
18. Lisiecki, I. and M.P. Pileni, *Synthesis of Well-Defined and Low Size Distribution Cobalt Nanocrystals: The Limited Influence of Reverse Micelles*. Langmuir, 2003. **19**: p. 9486-9489.
19. Murray, C.B., et al., *Colloidal synthesis of nanocrystals and nanocrystal superlattices*. J. Res. & Dev., 2001. **45**(1): p. 47-56.
20. Sun, S., et al., *Monodisperse FePt Nanoparticles and Ferromagnetic FePt Nanocrystal Superlattices*. Science, 2000. **287**: p. 1989-1992.
21. Frommen, C., H. Rösner, and D. Fenske, *Wet- Chemical Synthesis and Properties of CoPt and CoPt<sub>3</sub> Alloy Nanoparticles*. J. Nanosci. Nanotech., 2002. **2**(5): p. 509-515.
22. Shevchenko, E.V., et al., J. Am. Chem. Soc., 2002. **124** (38): p. 11480-11485.
23. Wang, Y. and H. Yang, *Synthesis of CoPt Nanorods in Ionic Liquids*. J. Am. Chem. Soc., 2005. **127**: p. 5316-5317.
24. Ely, T.O., et al., *Nanoscale Bimetallic Co<sub>x</sub>Pt<sub>1-x</sub> Particles Dispersed in Poly(vinylpyrrolidone): Synthesis from Organometallic Precursors and Characterisation*. J. Phys. Chem. B, 2002. **104**: p. 695-702.
25. Klem, M.T., et al., *Bio-inspired Synthesis of Protein- Encapsulated CoPt Nanoparticles*. Adv. Funct. Mater., 2005. **15**: p. 1489-1494.
26. Park, J.-I. and J. Cheon, *Synthesis of "Solid Solution" and "Core-Shell" Type Cobalt-Platinum Magnetic Nanoparticles via Transmetalation Reactions*. J. Am. Chem. Soc., 2001. **123**: p. 5743-5746.
27. Zhang, J., et al., *Platinum Monolayer on Nonnoble Metal-Noble Metal Core-Shell Nanoparticle Electrocatalysts for O<sub>2</sub> Reduction*. J. Phys. Chem. B, 2005. **109**: p. 22701-22704.
28. Lee, W.R., et al., *Redox-Transmetalation Process as a Generalized Synthetic Strategy for Core-Shell Magnetic Nanoparticles*. J. Am. Chem. Soc., 2005. **127**: p. 16090-16097.
29. Sobal, N.S., et al., *Synthesis of Core-Shell PtCo Nanocrystals*. J. Phys. Chem. B., 2003. **107**: p. 7351-7354.

30. Kim, H., et al., *Synthesis and Characterization of Co/CdSe Core/Shell Nanocomposites: Bifunctional Magnetic-Optical Nanocrystals*. J. Am. Chem. Soc., 2005. **127**: p. 544-546.
31. Gu, H., et al., *Facile One-Pot Synthesis of Bifunctional Heterodimers of Nanoparticles: A Conjugate of Quantum Dot and Magnetic Nanoparticles*. J. Am. Chem. Soc., 2004. **126**: p. 5664-5665.
32. Pellegrino, T., et al., *Heterodimers Based on CoPt<sub>3</sub>-Au Nanocrystals with Tunable Domain Size*. J. Am. Chem. Soc., 2006. **128**(20): p. 6690-6698.
33. Frommen, C., et al., *Synthesis and magnetic properties of CoPt<sub>3</sub> nanoparticles assemblies containing copper*. Materials Letters, 2004. **58**: p. 953-958.
34. Pellegrino, T., et al., *Hydrophobic nanocrystals coated with an amphiphilic polymer shell: a general route to water-soluble nanocrystals*. Nano Letters, 2004. **4**(4): p. 703-707.
35. Bronstein, L.M., ed. *Encyclopaedia of Nanoscience and Nanotechnology: Nanoparticles in Nanostructured Polymers*. Vol. 7. 2004. 193-206.
36. Hong, R., et al., *Surface PEGylation and Ligand Exchange Chemistry of FePt Nanoparticles for Biological Applications*. Chem. Mater., 2005. **17**: p. 4617-4621.
37. Kim, B.S., et al., *Magnetomicelles: Composite Nanostructures from Magnetic Nanoparticles and Cross-Linked Amphiphilic Block Copolymers*. Nano Letters, 2005. **5**(10): p. 1987-1991.
38. Lazzari, M. and M.A. Lopez-Quintela, *Block Copolymers as a Tool for Nanomaterial Fabrication*. Adv. Mater., 2003. **15**(19): p. 1583-1594.
39. Kang, Y. and T.A. Taton, *Core/Shell Gold Nanoparticles by Self-Assembly and Cross linking of Micellar, Block-Copolymer Shells*. Angew. Chem. Int. Ed., 2005. **44**: p. 409-412.
40. Sastry, M., *Colloids and Colloid Assemblies*, ed. F. Caruso: Wiley, 369-397.
41. Wang, Z.L., *Structural Analysis of Self-Assembling Nanocrystal Superlattices*. Adv. Mater., 1998. **10**(1): p. 13-30.
42. Pileni, M.P., *Nanocrystals Self-Assemblies: Fabrication and Collective Properties*. J. Phys. Chem. B, 2001. **105**: p. 3358-3371.
43. Sun, S., C.B. Murray, and H. Doyle, *Controlled Assembly of Monodisperse e-Cobalt-based nanocrystals*. Mat. Res. Soc. Symp. Proc., 1999. **577**: p. 385-398.
44. Lin, X.M., et al., *Formation of Long-Range-Ordered Nanocrystal Superlattices on Silicon Nitride Substrates*. J. Phys. Chem. B, 2001. **105**(17): p. 3353-3357.
45. Shevchenko, E.V., et al., *Structural diversity in binary nanoparticle superlattices*. Nature, 2006. **439** (5 January 2006): p. 55-59.
46. Cheng, G., et al., *Magnetic-Field-Induced Assemblies of Cobalt Nanoparticles*. Langmuir, 2005. **21**(26): p. 12055-12059.
47. Germain, V., et al., *Mesostructures of Cobalt Nanocrystals. 1. Experiment and Theory*. J. Phys. Chem. B, 2005. **109**: p. 5541-5547.
48. Germain, V. and M.P. Pileni, *Mesostructures of Cobalt Nanocrystals. 2. Mechanism*. J. Phys. Chem. B, 2005. **109**: p. 5548-5553.
49. Hilgendorff, M., B. Tesche, and M. Giersig, *Creation of 3-D Crystals from Single Co Nanoparticles in External Magnetic Fields*. Aust. J. Chem., 2001. **54**:p.497-501.
50. Rogach, A.L., et al., *Organization of Matter on Different Size Scales: Monodisperse Nanocrystals and Their Superstructures*. Adv. Funct. Mater., 2002. **12**(10):p. 653-664.
51. Beecher, P., et al., *Magnetic-Field -Directed Growth of CoPt<sub>3</sub> Nanocrystal Microwires*. Adv. Mater., 2005. **17**(8): p. 1080-1083.
52. Shevchenko, E.V., et al., J. Am. Chem. Soc., 2003. **125**: p. 9090-9101.
53. Govor, L.V., et al., *Self-Assembly of CoPt<sub>3</sub> Nanoparticle Rings Based on Phase-Separated Hexadecylamine Droplet Structure*. Langmuir, 2003. **19**(23): p. 9573-9576.

# **Ligand Exchange**

## Chapter 2

### Ligand exchange – carboxylic acids

---

#### 2.1. Introduction

Two main parameters influence the particle behaviour and determine their further application: the particle size and the chemical properties of the particles. CoPt<sub>3</sub> nanoparticles are a very attractive material for ligand exchange experiments due to their good stability, controllable size and narrow size distribution. In the first step the particle properties are investigated, which are influenced by the ligand composition. Surface coatings on particles play a great role concerning particle solubility, stability, polarity, compatibility with other materials and, of course, particle assembly in two or three-dimensional structures.

The type of ligands on the particle surface is in most cases determined by the reaction procedure and cannot be changed during the synthesis. Since the particle properties are strongly determined by the ligands that stabilise them, there is very often a need for their replacement. Depending on the required characteristic of the nanoparticle shell one wants to add different molecules to the particles that can be used as replacing ligands i.e. short molecules<sup>[1]-[7]</sup>, or polymer chains<sup>[8]-[11]</sup>.

The preparation procedure of CoPt<sub>3</sub> nanoparticles with narrow size distribution and good stability requires the use of adamantane carboxylic acid (ACA) and hexadecyl amine (HDA). Therefore the only way for ligand exchange is to exchange the existing ligands with some other organic molecules. These molecules have to provide good stability and solubility of the particles. In addition, they can influence the particle-particle distance and the particle packing. Three different types of ligands that are already known as good stabilizers for metal particles, were chosen: organic acids<sup>[4],[12]-[15]</sup>, thiols<sup>[3],[5]</sup>, poly(2-vinylpyridine) and poly(4-vinylpyridine)<sup>[16]-[18]</sup>. The variation of the alkyl chain length of the ligand should induce changes in the particle-particle distances. Additionally different ligands should provide different solubility and polarity of the particles. The attachment of acids with double bonds on the particle surface allows further reactions and modifications on the particles. In this way new applications can be developed.

## 2.2. Removal of ligands from as-prepared particles

The first step in the ligand exchange procedure is the removal of “old” ligands prior to the attachment of new ligands. As already mentioned, after the synthesis HDA and ACA are present on the particle surface. After the synthesis (experimental part - Chapter 9.) the excess of ligands is removed by the usual washing procedure. Especially the large excess of HDA that is not only the ligand during the synthesis but also the solvent has to be removed. The amount of ligands present in the particle solution after the washing procedure is usually high, and additional washing is necessary in order to replace the old ligands with the new ones. It is already known that ligands connected to the particle surface and free ligands in solution are in dynamic equilibrium. The amount of free ligands in solution decreases with each washing step. The equilibrium is influenced by this procedure and some of the ligands detach from the surface. In that way it is possible to remove almost all ligands from the surface. However, the washing procedure has to be used carefully. Removal of all ligands present on the particle surface leads to particle agglomeration and further use of the particles is not possible anymore. Based on that it is clear that two very important facts should be taken into account using the washing procedure:

- - a small amount of old ligands is necessary in order to stabilise the particles;
- - for successful ligand exchange it is necessary to remove the excess of old ligands to clear a space on the particle surface for the attachment of new ligands.

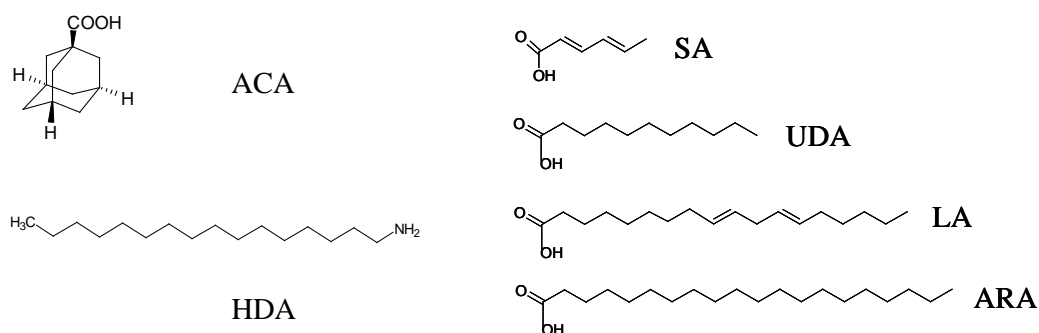


**Fig. 2.1.** The ligand molecules after synthesis (ACA and HDA - left hand side) and molecules used for ligand exchange (sorbic - SA, linoleic - LA, undecanoic - UDA and arachidic - ARA acid - right hand side)

In order to receive good results the adequate number of washing steps before the ligand exchange was determined. A certain amount of particle solution was washed as many times as it was necessary to remove the ligands and to obtain particle agglomeration. It was found that usually three additional washing steps lead to particle agglomeration. Due to that fact the particles were only washed two times. The removal of the ligands was monitored by IR, TG and DSC analyses.

After cleaning, the particles were mixed with the new ligands (experimental part-Chapter 9). Four different acids were used as new ligands: two unsaturated: sorbic and linoleic and two saturated: undecanoic and arachidic acid (Figure 2.1.). Different alkyl chain lengths of these acids can lead to different particle/particle distances.

### 2.3. IR analysis of samples before and after ligand exchange

#### 2.3.1. IR analysis of particles before ligand exchange

IR is the most commonly used technique for the investigation of particle/ligand bonds. For instance, absorption of short chain n-alkanoic acids ( $\text{CH}_3(\text{CH}_2)_n\text{COOH}$ ,  $n = 0 - 9$ ) from the gas phase onto Ag were studied using this technique<sup>[14]</sup>. Many experiments were done on alkanethiolates attached on gold or silver surfaces since using FTIR investigations<sup>[19]-[22]</sup>. It is also very important for the analysis of magnetic nanoparticles, since they cannot be examined by NMR technique<sup>[15],[23]</sup>. For this reason FTIR was chosen to investigate the type of particle/ligand interactions before and after ligand exchange on  $\text{CoPt}_3$  nanoparticles.

Representative set of FTIR spectra of as prepared particles and washed particles in both the high- and the low-frequency region are shown in Fig. 2.2. In the high-frequency region (Fig. 2.2.A) the series of stretching bands corresponding to ligand's methyl and methylene groups can be seen in-between  $2800 - 3000 \text{ cm}^{-1}$ . The two intense bands in the spectrum of non washed sample at  $2849$  and  $2917 \text{ cm}^{-1}$  are assigned to the symmetric ( $\nu_s(\text{CH}_2)$ ,  $d^+$ ) and antisymmetric ( $\nu_{as}(\text{CH}_2)$ ,  $d^-$ ) stretching vibrations of the methylene groups. The  $d^+$  and  $d^-$  modes are usually found in the narrow ranges of  $2846-2850 \text{ cm}^{-1}$  and  $2915 - 2918 \text{ cm}^{-1}$ , respectively for all-trans extended chains. Distinctly different ranges i.e.  $2854 - 2856 \text{ cm}^{-1}$  and  $2924-2928 \text{ cm}^{-1}$  are characteristic for the disordered chains which possess a significant amount of gauche conformers<sup>[14],[21]</sup>. Therefore, the observed bands at frequencies

of 2849 and 2917  $\text{cm}^{-1}$  for the as-prepared sample containing a ligand excess suggest that the alkyl chains of HDA are in an all-trans conformational state. The washing procedure does not remove only ligands immobilized at the particles surface. These ligands cannot form ordered structures and due to this the IR bands shifts to higher values of 2853 and 2922  $\text{cm}^{-1}$ .

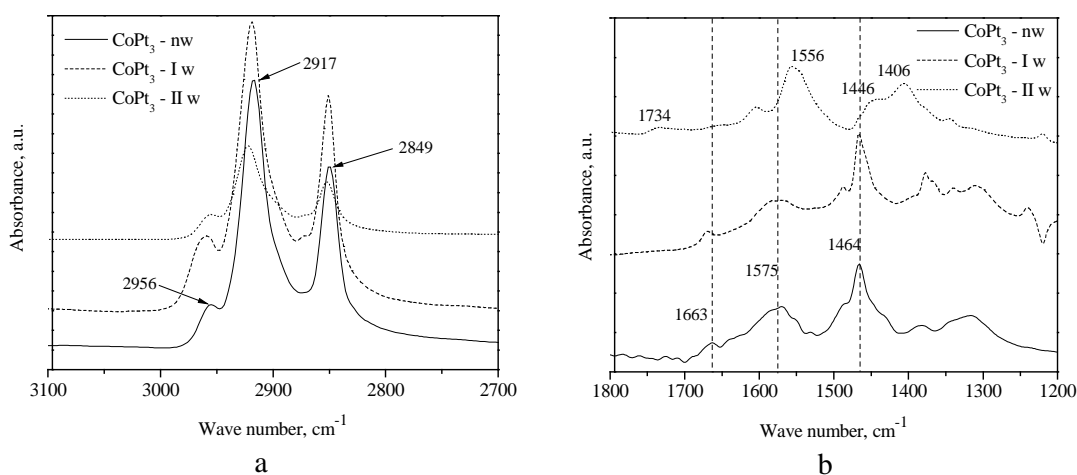


**Fig. 2.2.** IR spectra of  $\text{CoPt}_3$  nanoparticles: as synthesised (solid line), after first (dash line) and after second (dot line) washing step. a) IR spectra in high frequency region, b) IR spectra in low frequency region are displayed.

The methylene scissoring  $\delta(\text{CH})$  band appears in the low frequency region (Fig. 2.2.b) at 1464 and 1380  $\text{cm}^{-1}$ . Two bands at 1556 and 1406  $\text{cm}^{-1}$  that became visible after the second washing step are originating from  $\nu_s(\text{COO}^-)$  of the carboxylate group. The absence of the band around 1700 - 1725  $\text{cm}^{-1}$  related to the  $\text{C}=\text{O}$  stretch indicates the absence of free adamantane carboxylic acid. This leads to the conclusion that ACA is attached as carboxylate onto the nanoparticles, and the two oxygen atoms in the carboxylate groups are coordinated symmetrically to the Co atoms<sup>[23],[24]</sup>.

The bands in the region between 1550 and 1700  $\text{cm}^{-1}$  in the spectra of as prepared and once washed particles are the typical bands of HDA (see Appendix 1.) and they originate from NH and  $\text{NH}_2$  groups. Removal of the HDA from the starting solution by the washing procedure leads to a drastic decrease of these bands. The presence of amines in the particle solution after two washing steps is not detectable anymore.

### 2.3.2. IR analyses of particles after ligand exchange

#### Unsaturated acids

The samples were also investigated by ATR-FTIR after ligand exchange by the procedure described in the experimental part (Chapter 9.). The obtained results are presented in two sections because unsaturated and saturated acids showed different ways of interaction with the particles.

The high frequency region in the IR spectra of the samples obtained after ligand exchange with LA (Fig. 2.3.) shows both bands from the symmetric (d+) and antisymmetric (d-) stretching of methylene groups in the ranges of 2850–2854  $\text{cm}^{-1}$  and 2917–2924  $\text{cm}^{-1}$  that are typical for disordered chains<sup>[14],[21]</sup>. The band around 3010  $\text{cm}^{-1}$  detected in the spectra of particles capped with LA is attributed to =C-H stretching and keeps its position after one washing step. The band disappears after the second washing step.

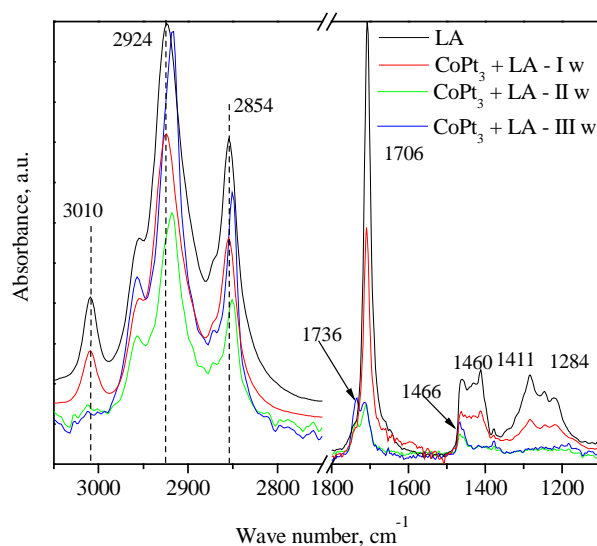


**Fig. 2.3.** IR spectra of pure LA (black line) and particles stabilised with LA after the first (red line), second (green line) and third (blue line) washing step

In the low frequency region of the IR spectra the band at 1706  $\text{cm}^{-1}$  represents C=O asymmetric vibration. This band shifts to higher wave numbers during the washing procedure, with simultaneous appearing of a new band at 1736  $\text{cm}^{-1}$ . Two additional bands characteristic for LA (see Appendix) were observed at 1411 and 1460  $\text{cm}^{-1}$  and they represent the C-O-H in-plane and  $\text{CH}_2$  deformations, respectively. The band around 1280  $\text{cm}^{-1}$  can be assigned to C-OH stretching vibrations.

Bands between 1400 and 1460  $\text{cm}^{-1}$  cannot be distinguished after the first washing step but one new band becomes visible at 1466  $\text{cm}^{-1}$ . The absence of the bands characteristic for  $\text{COO}^-$  groups and the presence of a band at 1710  $\text{cm}^{-1}$  suggest that LA is adsorbed on the nanoparticles surface as  $\text{COOH}$  rather than as dissociated carboxylate ion. Similar behaviour was observed for silver nanoparticles stabilised with various fatty acids<sup>[25],[26]</sup>.

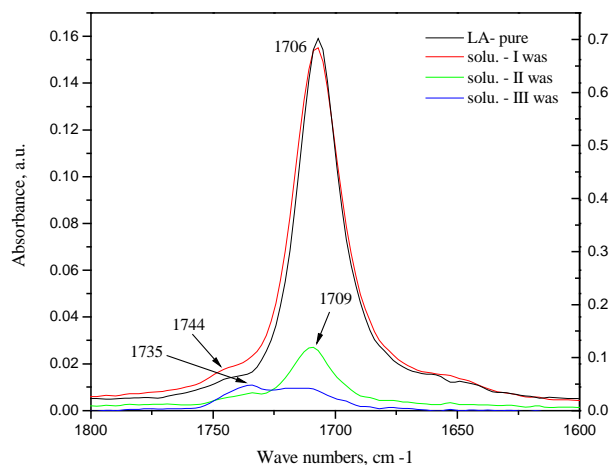


**Fig. 2.4.** Characteristic bands around 1700  $\text{cm}^{-1}$  in the spectra of pure LA (black line) and spectra of supernatants after the first (red line), second (green line) and third (blue line) washing step

Another interesting effect was noticed during the ligand exchange procedure. Namely, in the IR spectra (Fig. 2.4.) of the nanoparticles and of the supernatants (taken after ligand exchange) a band at 1736  $\text{cm}^{-1}$  was observed. Only  $\text{COOH}$  groups of saturated carboxylic acids can give rise to an IR band at this position. Simultaneously the band characteristic for double bonds at 3010  $\text{cm}^{-1}$  disappeared (Fig. 2.3.). As only unsaturated LA was used these results strongly suggest that a chemical modification - hydrogenation of the LA occurred. This might be possible due to the well-known catalytic effect of Pt nanoparticles already described for cyclohexene<sup>[27]</sup>, allyl alcohol and maleic acid<sup>[28]</sup>. This catalytic process occurs at room temperature and needs only a few hours for complete hydrogenation. The  $\text{CoPt}_3$  nanoparticles have enough time to react with the acids during the washing procedure. Most probably hydrogenated acids are present in all samples to some extent, but due to their very small concentration they become only visible in the IR spectra after removing the excess of non-attached molecules.

Similar behaviour was obtained with the samples stabilised with SA (Fig. 2.5.). Due to conjugated double bonds and the vicinity of the carboxylic group to the conjugated double bond the IR spectrum is rather complicated in comparison to the spectra of nanoparticles modified with LA. Bands of asymmetric and symmetric stretches of  $\text{CH}_2$  appear at higher wave numbers between  $2750$  and  $3000\text{ cm}^{-1}$ . After two washing steps the band attributed to stretching vibrations of  $=\text{C-H}$  at  $3020\text{ cm}^{-1}$  disappears. Additionally the band position changes drastically and suggests the transformation of unsaturated to saturated acids.

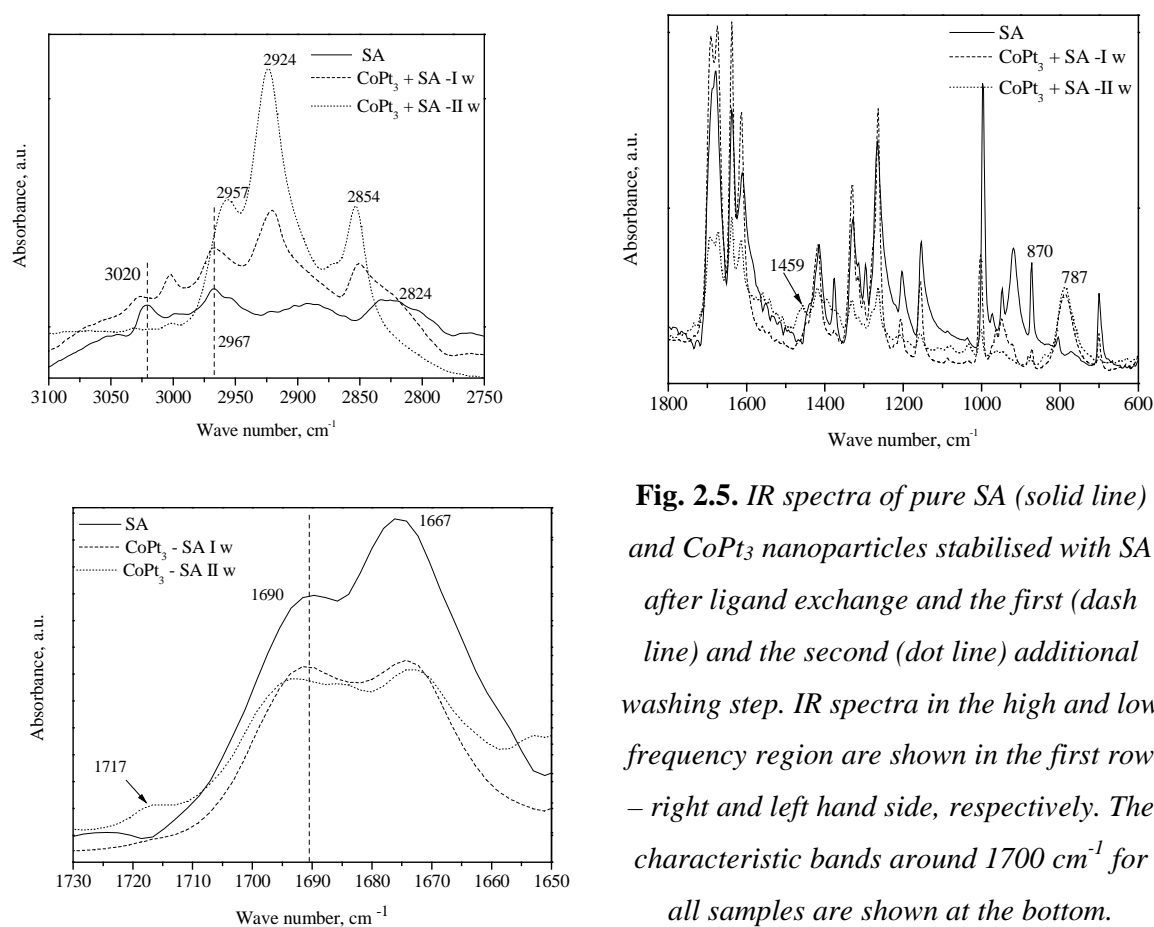


**Fig. 2.5.** IR spectra of pure SA (solid line) and  $\text{CoPt}_3$  nanoparticles stabilised with SA after ligand exchange and the first (dash line) and the second (dot line) additional washing step. IR spectra in the high and low frequency region are shown in the first row – right and left hand side, respectively. The characteristic bands around  $1700\text{ cm}^{-1}$  for all samples are shown at the bottom.

In the low frequency region of the IR spectra the bands of  $=\text{CH-}$  groups and carboxylic groups overlap in two regions: from  $1550 - 1700\text{ cm}^{-1}$  and from  $1450 - 1300\text{ cm}^{-1}$ . As in the case of the LA the two characteristic peaks for  $\text{COO}^-$  groups are also absent suggesting also the adsorption of SA at the nanoparticles surface through  $\text{COOH}$  groups. In the same frequency region a new peak appears at  $1717\text{ cm}^{-1}$  after the second washing step, as well as bands at  $780\text{ cm}^{-1}$  and  $1460\text{ cm}^{-1}$  characteristic for  $\text{CH}_2$  groups (rocking mode and

deformation  $\delta(\text{CH}_2)$ , respectively). At the same time the band at  $870\text{ cm}^{-1}$  characteristic for double bonds ( $=\text{C-H}$  wag mode) disappears. These results support the hypothesis that hydrogenation occurs at the surface of nanoparticles.

### Saturated acids

IR-spectra of pure undecanoic acid (UDA), particles with the same acid after ligand exchange, and after additional washing steps are shown in Fig. 2.6.. The excess of acids is removed from the solution during the washing procedure. This makes more visible by FTIR the acid molecules that are attached to the particles. In the high frequency region of the IR spectra this is observable as a shift of the peaks to higher wave numbers.

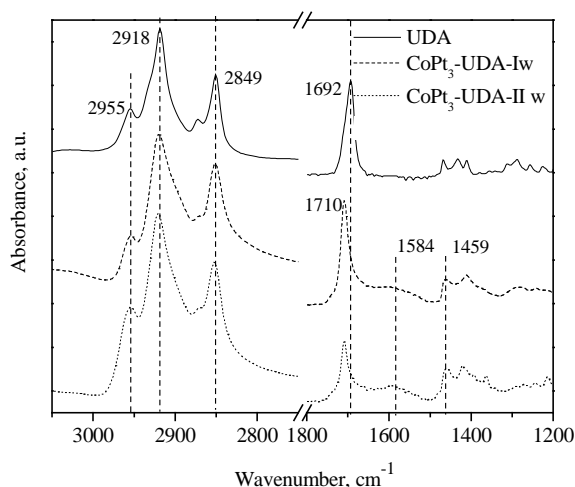


**Fig. 2.6.** IR spectra of pure UDA (solid line) and  $\text{CoPt}_3$  nanoparticles stabilised with UDA after the first (dash line) and second (dot line) washing step

In the low frequency region of the IR spectra the most characteristic band is at  $1700\text{ cm}^{-1}$  that originates from COOH groups. In general COOH groups can form dimmers via H-bonding that shifts the band position towards lower frequencies. This is very evident for pure UDA that shows the carboxylate band at  $1693\text{ cm}^{-1}$  [29]. By using UDA as ligand the H-bonds among dimmers are broken due to the interaction with the particles. This shifts the carboxylate band back to  $1710\text{ cm}^{-1}$ . Additionally a broad peak appears around  $1584\text{ cm}^{-1}$  that can be attributed to  $\text{COO}^-$  groups close to the particle surface. The constant presence of the  $1710\text{ cm}^{-1}$  band suggests that the main part of the ligands in the solution is in a non-dissociated state and attached to the particle via COOH groups.

The same procedure was applied to samples stabilised with ARA (Fig. 2.7.). The bands at higher wave numbers appear almost at the same position and behave in the same way as in the case of the samples stabilised with UDA.

In the low frequency region the most characteristic band is at  $1700\text{ cm}^{-1}$  that originates from C=O groups. This band significantly decreases already after the first washing step and disappears after the second washing step. The new band at  $1529\text{ cm}^{-1}$  together with a band at  $1460\text{ cm}^{-1}$  indicates the presence of  $\text{COO}^-$  groups in the solution. This suggests that ARA is connected to the particle via  $\text{COO}^-$  carboxylate anions. The frequency separation ( $\Delta\nu_{\text{a-s}}$ ) between the  $\text{COO}^-$  asymmetric and symmetric stretches suggests a bidentate bond between the acid and the particles.

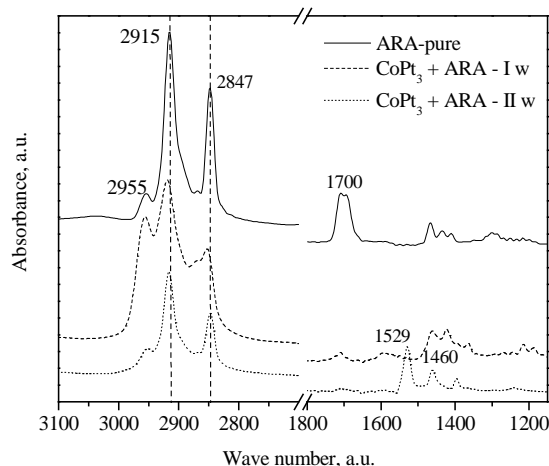


**Fig. 2.7.** IR spectra of pure ARA (solid line) and  $\text{CoPt}_3$  nanoparticles stabilised with ARA after the first (dash line) and second (dot line) washing step.

The IR spectra of all samples indicate that after the ligand exchange the new ligands are attached at the particles. These bonds are strong enough to stabilise the particle solution for several washing procedures. It should also be pointed out that solutions stabilised with the new ligands are stable for months. The absence of the "old" ligand bands in the IR spectra suggests that they do not play a significant role in the particle stabilisation compared to the new ligands.

## 2.4. TG and DSC analyses of particles before and after ligand exchange

### 2.4.1. TG and DSC analyses of particles before ligand exchange

Thermal decomposition studies can provide an insight into chemical processes during thermal treatment of the particles and can give information about the ligand decomposition temperatures. The main information that can be extracted from TG measurements is the

particle to ligand ratio and the average number of ligands per particle. For this reason the method can detect the presence of a ligand excess in the samples and can be used as a good indicator for the removal of a ligand excess during the washing procedure before and after ligand exchange. Additionally the characteristic temperatures and mechanisms of ligand decomposition caused by heating can be observed and compared for different ligands. The information about ligand degradation can be used for further thermal removal of the ligands from the particle surface leading to the formation of ligand free particles that are necessary for certain applications<sup>[30],[31]</sup>.

TG curves and their first derivatives of the pure ligand mixture and particles prior and after washing are presented in Fig. 2.8. The ratio of the ACA/HDA mixture resembles the ratio used for the particle syntheses.

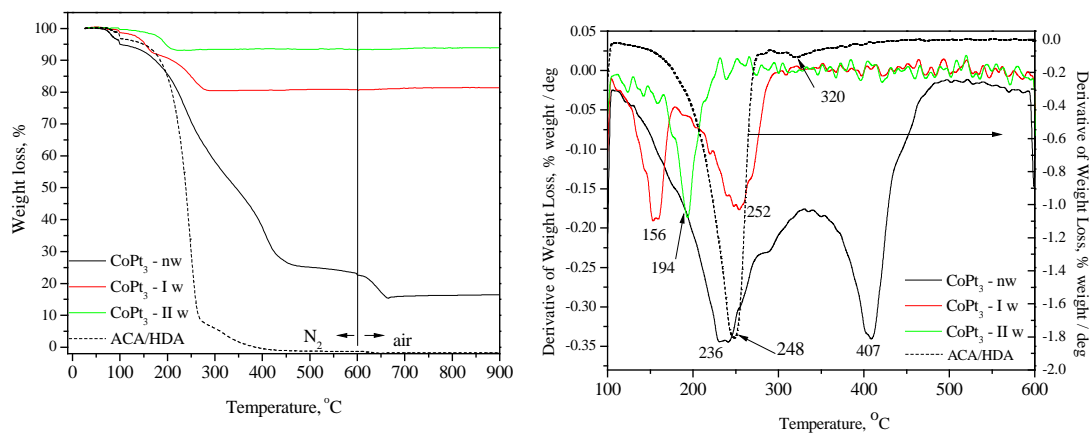


**Fig. 2.8.** TG curves of the pure ligands mixture ACA/HDA (dash line) and of CoPt<sub>3</sub> nanoparticles (stabilised with the same ligands) before (black line) and after first (red line) and second (green line) washing step (left hand side). DTG curves for all samples (right hand side). Heating speed was 10 K/min for all samples.

Apart from the two times washed sample all others show two steps in the TG curves recorded in the temperature region from 25-600 °C in nitrogen atmosphere (Fig. 2.8.). All samples give a small mass loss between 50 and 100 °C (not larger than 5 mass %) due to solvent traces left in the samples. This small mass loss can be ignored in the analysis of the ligand decomposition. The ligands, ACA and HDA, in the sample of non-washed CoPt<sub>3</sub> particles start to decompose at almost the same temperature as a mixture of the pure ligands

(Table 2.1.). At the same time the presence of the particles leads to complete ligand degradation at higher temperatures (439 °C) in comparison to pure ligands (379 °C). Removal of the ligand excess from the samples leads to a shift of the decomposition onset and decomposition end to lower temperatures in comparison to the non-washed sample. After the second washing step the ligands completely decompose in a narrow temperature interval of only 30 °C. That is significantly lower in comparison to the non-washed sample in which the decomposition occurs in an interval of almost 250 °C.

The mass loss after changing the gas atmosphere (Fig. 2.8. - left hand side) from nitrogen to air (above 600 °C) indicates a significant amount of organic residue or carbon, which cannot be degraded in nitrogen. This residue is removed by oxidation in air. This effect appears only if a big excess of ligands is present in the sample. Such behaviour indicates the formation of more stable products during the heating procedure, which is influenced by two factors: presence of the particles and large ligand excess.

Samples of one and two times washed particles do not show a significant weight loss after atmosphere exchange. In contrast it is noticed that the mass of the samples slightly increase. This is due to oxidation of the particles caused by a reaction between oxygen (in the air) and Co in the particles. The oxidation of the Co atoms occurs simultaneously with the ligand decomposition. The oxidation should lead to an increase of the sample mass while ligand decomposition has an inverse effect. Therefore the mass loss is the result of a superposition of these two reactions. The degree of the oxidation is difficult to calculate.

Table 2.1. Temperatures of decomposition onset and end extracted from TG curves and temperatures of first and second weight loss extracted from the peaks in DTG curves. Temperatures are given for a mixture of pure ligands (ACA/HDA) and for particles stabilised with the same ligands before (CoPt<sub>3</sub> - nw) and after the first (CoPt<sub>3</sub> - I w) and second (CoPt<sub>3</sub> - II w) washing step.

Sample	Onset [°C]	1st weight loss derivative peak [°C]	2nd weight loss derivative peak [°C]	End [°C]
ACA/HDA	70*/187	248	320	379
CoPt <sub>3</sub> – n w	70*/186	236	407	439
CoPt <sub>3</sub> - I w	138	156	252	278
CoPt <sub>3</sub> - II w	176	194	-	208

\* Solvent evaporation

The confirmation of a two-step decomposition mechanism was also obtained from the derivatives of the TG curves (Fig. 2.7. - right hand side). They show two well-pronounced peaks for the pure ligands and the particles before and after the first washing step. This indicates that two different degradation mechanisms occur during sample heating. A comparison of the DTG curves of the pure ligands and the non-washed sample also shows that the particles influence the ligand decomposition at higher temperatures. The first peak that corresponds to the first degradation step appears in the same temperature interval in which the pure ligands completely degrade. The second peak appears at higher temperatures indicating the decomposition of some thermally more stable products. These products are formed during decomposition reactions in the first decomposition step.

After the first washing step the degradation of the ligands still occurs in two steps but the derivative peaks shift to lower temperatures, and both degradation steps happen in narrower temperature regions than in the case of the non-washed particles. The DTG curve shows only one peak after one more additional washing step. This peak indicates a one-step degradation mechanism.

There are different theories proposed in order to explain the described behaviour of the particles during the heating procedure and especially the two-step mechanism. The most applicable one is the theory of Y. Sahoo and co-workers<sup>[15]</sup>. They investigated the adsorption of phosphate surfactants on magnetic  $\text{Fe}_3\text{O}_4$  particles and proposed a quasi-two layer mechanism. According to this theory one part of the ligands is strongly bound at the  $\text{CoPt}_3$  particle surface, while another part forms a second layer of weakly bound ligand molecules that are further away from the magnetic core. Therefore these samples show a two-step decomposition mechanism. In the first step the weakly bound layer decompose. The second degradation step is a result of the decomposition of the by-products formed during the first degradation step and the decomposition of ligands that are strongly bound to the particle surface.

In the case of  $\text{CoPt}_3$  nanoparticles stabilised with a mixture of HDA and ACA the similar theory could be applied. TG analyses suggest that one part of the ligands is strongly bound to the surface and degraded at higher temperatures. Another part is weakly or not at all bound in the case of non-washed and once washed samples (ligand excess) and degrades at lower temperatures. Washing of the particles leads to a lower amount of ligand excess and probably complete removal of these molecules after the second washing step. This is the

reason for a one-step degradation mechanism after two washing steps. The influence of the particles on the decomposition reactions is increasing with the removal of the ligand excess. A catalytic effect of the particles influences the shift of the degradation temperatures to lower values.

The IR spectra show the removal of the HDA excess during the washing procedure and the domination of the ACA molecules on the particle surface after the second washing step. A combination of these results with the previously explained degradation mechanism leads to the conclusion that HDA is the most dominant ligand in the ligand excess. Therefore the influence of HDA is more dominant in the samples before and after one washing step. After the second washing procedure the excess of HDA is removed and the degradation mechanism is mainly influenced by ACA. In order to check these predictions DSC measurements were additionally done. The main scope of the investigations is on combination of the DSC measurements with the results from the TG and IR analyses in order to confirm the previously described theory.

The DSC curves of pure ligands show an endothermic peak at 49 °C for the mixture of ACA/HDA and for pure HDA arising from the melting of the compounds. The DSC curve for ACA shows the first endothermic peak at 180 °C as an effect of the acid evaporation ( $T_b = 176$  °C). In the case of HDA the endothermic peaks at higher temperatures are due to evaporation ( $T_b = 330$  °C) and degradation. The peaks at DSC curve of ACA result from degradation; while in the case of the ligand mixture (ACA/HDA) the observed peaks are an effect of both degradation mechanisms (for HDA and ACA).

The DSC curves of non-washed particles and particles after the first and second washing step show exothermic peaks whose minima shift to lower temperatures with removal of the ligand excess from the sample. The peaks for as-prepared and for once washed particles are superimposed and they suggest more than one successive reaction. The existence of more than one peak in the DSC curves is in good agreement with the two-step degradation mechanism observed by TG. Furthermore the differences between the DSC curves of pure ligands and have the particles stabilised with the same ligands should be pointed out. The absence of endothermic peaks in the DCS curves of  $\text{CoPt}_3$  particles samples indicates different decomposition mechanisms of the ligands. The ligands are not removed from the sample by evaporation and their decomposition is rather different. It appears as a combination of several reactions that all together give the exothermic peaks in the DSC curves.

Additionally, the removal of excess ligands leads to a shift of the peaks to lower temperatures. This result agrees with the TG results and confirms once more the strong influence of the particles on the ligand decomposition.

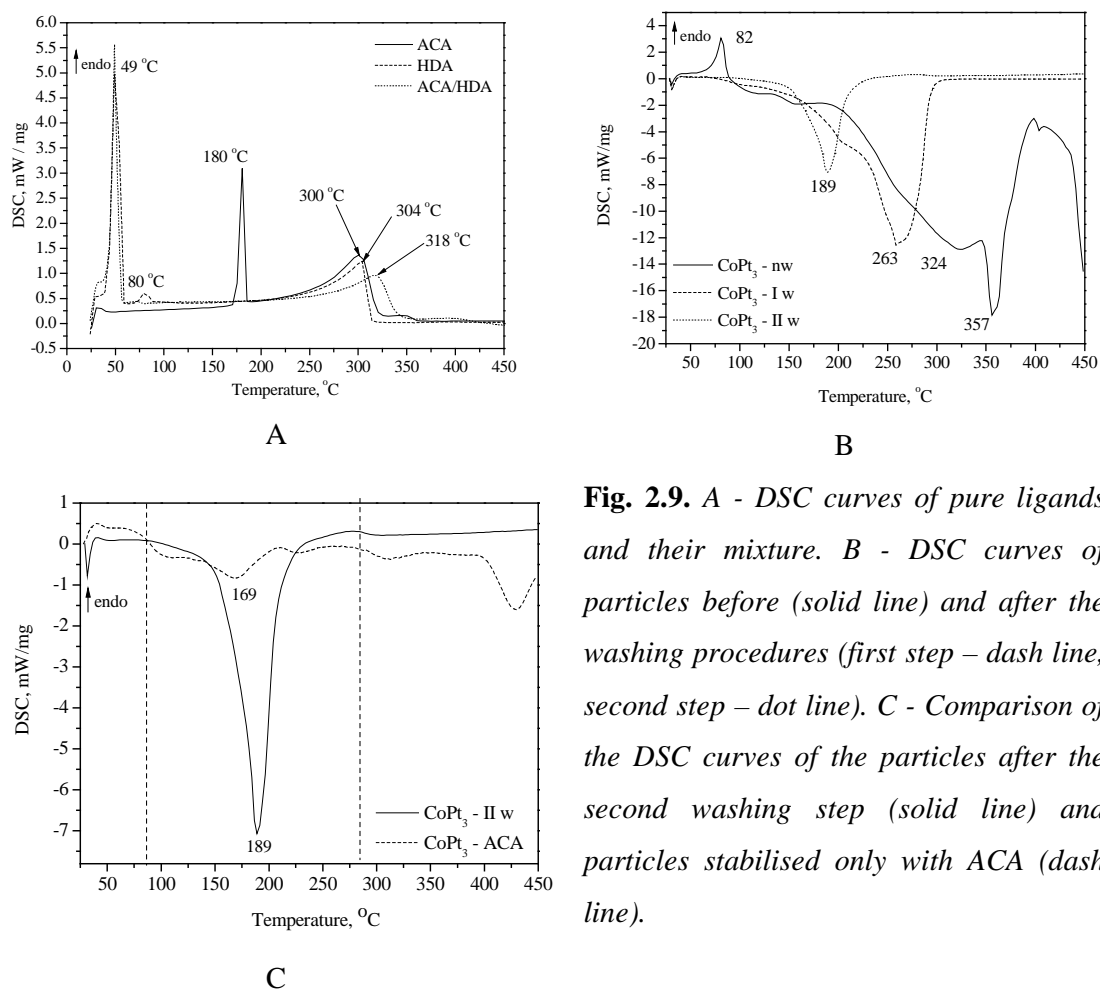


**Fig. 2.9.** A - DSC curves of pure ligands and their mixture. B - DSC curves of particles before (solid line) and after the washing procedures (first step – dash line, second step – dot line). C - Comparison of the DSC curves of the particles after the second washing step (solid line) and particles stabilised only with ACA (dash line).

The DSC curves of the sample stabilised with ACA/HDA and cleaned twice as well as the sample stabilised only with ACA are shown in Figure 2.9. (C). It is interesting to notice that the peaks in both measurements appear at almost the same temperature. This indicates that the degradation after the second washing step is actually determined by the degradation of ACA. This confirms the previous assumptions.

The analyses of TG and DSC measurements lead to the following conclusions:

a) In general a ligand excess and especially a HDA excess leads to a complex degradation mechanism, which occurs in two steps. The ligand excess of HDA is responsible

for the appearance of the second degradation step at higher temperatures. In the presence of a ligand excess a lot of successive and complex reactions lead to the formation of by-products in the first degradation step. These products together with strongly bound ligands degraded in the second step.

b) The DSC and IR curves suggest that after the second washing step ACA is the dominant ligand in the samples. Both TG and DSC analyses confirmed that after two washing steps the ligand degradation is an one-step mechanism. By combination of the results it can be concluded that the decomposition mechanism is mostly influenced by decomposition of ACA after two washing steps.

c) The degradation of bound ligands occurs at lower temperatures in comparison to pure ligands due to a catalytic effect of  $\text{CoPt}_3$  nanoparticles.

#### 2.4.2. TG and DSC analyses of $\text{CoPt}_3$ nanoparticles after ligand exchange

The thermal decomposition of the ligands after ligand exchange was investigated using the same methods. The pure ligands and the samples after ligand exchange were investigated by TG and typical curves are presented in Figure 2.10..

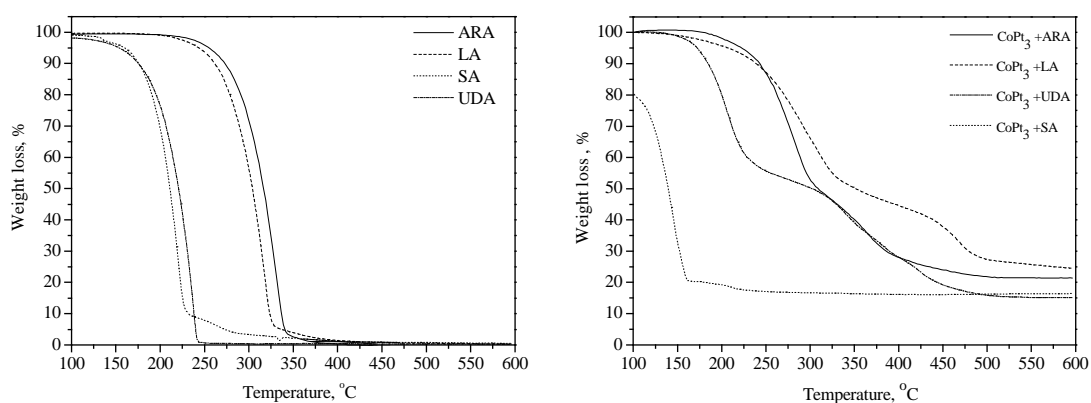


**Fig. 2.10.** TG curves: pure ligands (left hand side);  $\text{CoPt}_3$  nanoparticles after ligand exchange with different ligands and without additional washing procedure (right hand side).

*Heat speed was for all samples 20 K/min*

The TG measurements show that the pure acids decompose at different temperatures. The characteristic temperatures extracted from the TG curves are given in Table 2.2. The

decomposition mechanism of pure SA occurs in two steps in contrast to the decomposition of the other acids. The temperatures at which the acids show a mass loss of 5 mass % are taken as the starting point for the degradation and the temperatures at which the samples have lost 95 mass % of their initial mass were taken as the end point of the degradation process. The results show that all acids completely degrade till 350 °C (Table 2.2.). The saturated acids (UDA and ARA) start to degrade at lower temperatures than the boiling temperature of the acids. This is probably a result of acid evaporation. The unsaturated acids (SA and LA) begin to degrade at higher temperatures than their boiling points. Additionally, the first derivative peak appears at temperatures higher than the boiling points of the pure acids, except for UDA. This shows that probably the first degradation step is a combination of an evaporation process and decomposition reactions, which occur at these temperatures.

Table 2.2. Boiling points and decomposition temperature onsets ( $T_{5\%}$ ) and ends ( $T_{95\%}$ ) extracted from the TG curves of pure ligands. Temperatures of the first and second derivative peak are extracted from DTG curves (curve is not shown)

Sample	Boiling point °C	1st deriv. peak °C	2nd deriv. peak °C	$T_{5\%}$ °C	$T_{95\%}$ °C
SA	133	220	260	160	273
UDA	248	236	/	154	239
LA	230	317	/	244	336
ARA	328	332	/	256	340

The thermal stability of the particles stabilised with different ligands was investigated under the same conditions as in the case of pure ligands. Temperatures of the first and second weight loss were extracted from the DTG curves in the same way. The weight loss of the samples is given in weight percentage for both degradation steps. All data are shown in Table 2.3. All samples were measured after ligand exchange (experimental part) without an additional washing step. The TG measurements were performed in order to investigate the influence of the particles on the ligand degradation when an excess of ligands is present.

The TG curves of all samples show a different and more complex degradation mechanism when the acids are attached to the  $\text{CoPt}_3$  particles in comparison to the pure acids. A similar behaviour was already described in the case of particles stabilised with a mixture of ACA/HDA. The shape of the TG curves shows that the decomposition occurs in two steps (SA; LA; ARA) or in three steps (UDA), depending on the acid. The weight loss shows an

excess of ligands (first weight loss), from 30 mass % for CoPt<sub>3</sub> - LA till 60 mass % for CoPt<sub>3</sub> – SA (Table 2.3.).

Table 2.3. Characteristic temperatures and weight losses of particles for the first and the second degradation step, extracted from the TG curves.

Sample	Onset °C	1st weight loss		2nd weight loss		End °C
		deriv. peak °C	w.loss %	deriv. peak °C	w. loss %	
CoPt <sub>3</sub> - SA	113*	145	60.4	182 / 211	3.0	234
CoPt <sub>3</sub> - UDA	173	206	45.8	343 / 383 / 425	39.8	464
CoPt <sub>3</sub> - LA	217	290	30.2	311 / 470	46.0	492
CoPt <sub>3</sub> - ARA	228	284	51.3	344 / 363	27.8	474

\*This value is not completely reliable because one part of the acid sublimates at lower temperatures than 100 °C.

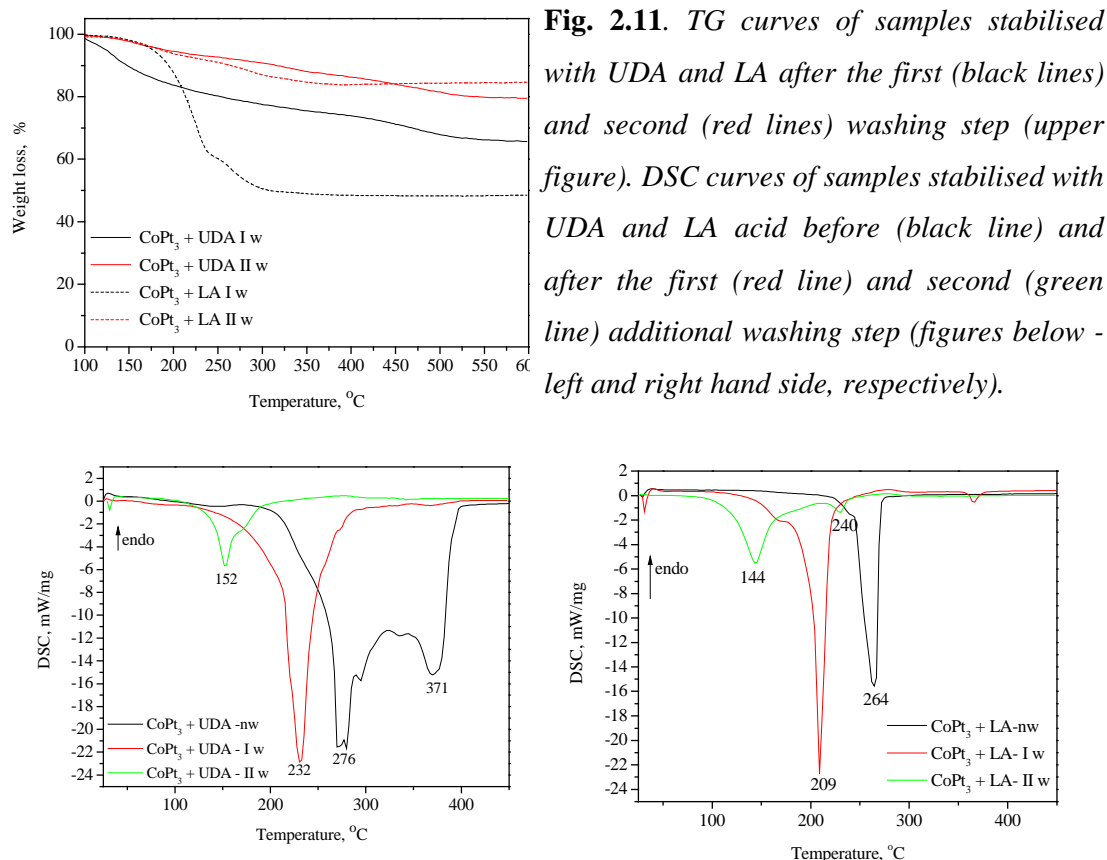
All samples start to lose mass at lower temperatures than the boiling temperatures of the pure ligands. This indicates that in the first degradation step the ligand excess starts to evaporate and then later on degrade through a more complex mechanism. The onset temperatures are higher if the nanoparticles are stabilised with ligands that have long alkyl chains (LA and ARA). This trend can also be measured for the pure ligands. The temperatures of the first derivative peak of the CoPt<sub>3</sub> particle samples are at lower temperatures than the first derivative of the pure ligands. These results are another hint for the catalytic behaviour of CoPt<sub>3</sub> particles, which initiate ligand decomposition at lower temperatures.

CoPt<sub>3</sub> nanoparticles stabilised with SA show a significant weight loss during the drying step at 100 °C. This weight loss is probably due to the evaporation of sorbic acid. Nevertheless the same heating procedure was used for all samples in order to provide comparable results. For the calculations the weight loss of SA at 100 °C was added to the acid weight loss in the first phase.

Additional experiments were performed in order to investigate the influence of the ligand excess on the degradation mechanism. The TG and DSC analyses of the two samples stabilised with UDA and LA show two degradation steps if a ligand excess is present in the solution (Fig. 2.11.) (Not all data are shown for clarity.). After removal of the ligand excess, (after one washing step in the case of UDA, and after two washing steps in the case of LA) the decomposition appears only in one step. Both TG and DSC techniques confirmed these

results. In the case of LA a small peak at higher temperatures in the DSC curve is due to double bonds present in the acid leading to complex exothermic cross-linking reactions.

The DSC curves show a shift of the decomposition temperature region to lower temperatures. This is similar to the behaviour of cleaned particles before the ligand exchange and indicates the strong influence of the particles on the ligand decomposition.



A comparison of the DSC curves of the samples before ligand exchange and stabilised with UDA and LA (all samples are washed two times before the measurement) leads to the conclusion that the peak position is affected by interactions between the particles and the ligands. It was assumed from the data obtained by IR analyses that LA acid is adsorbed at the particle surface through COOH groups, ACA through COO<sup>-</sup> groups and UDA by both groups. The DSC shows the decomposition of LA (144 °C) at the lowest and of ACA at the highest temperature (189 °C). These results indicate a weaker bond between the particles and the COOH groups and a stronger bond of the COO<sup>-</sup> groups, respectively (Figure 2.12.).

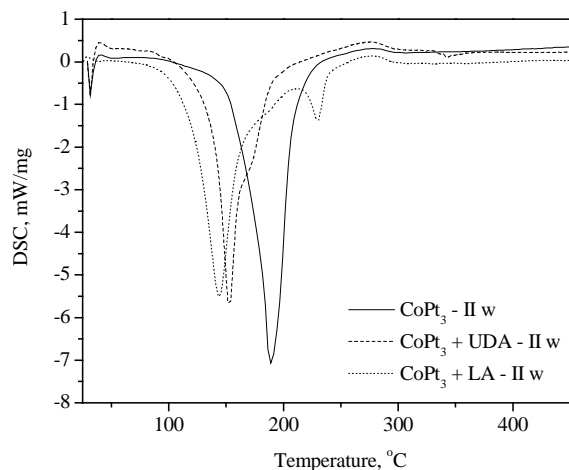


**Fig. 2.12.** DSC curves of particles before ligand exchange and after ligand exchange with UDA and LA (all samples are twice washed)

After the second washing step the ligands left in the sample should be attached at the particles surface or at least strongly interact with the particles and stabilise them. Therefore, it is possible to calculate the amount of ligands attached to the particles (Table 2.4.) by using the data from the TG curves obtained after the second washing step. The amount of ligands was calculated from the weight loss. The number of the particles in the solution was calculated from the particle diameter and the mass of the particles in the sample. The diameter of the particles was calculated from the XRD data. The calculated number of ligand molecules per nanoparticle was divided by the particle surface area in order to provide comparability as different particles were used during the ligand exchange reaction. In this way the influence of the particle size is diminished.

Table 2.4. Ligand loss extracted from TG curves, particle diameter calculated from the XRD data and the calculated number of ligands per particle.

Sample	Ligand loss, mass %	Particle diameter [nm]	Number of ligand molecules / nm <sup>2</sup>
CoPt <sub>3</sub> - II w	12.0	6.2	9
CoPt <sub>3</sub> - SA II w	30.8	6.2	46
CoPt <sub>3</sub> - UDA II w	20.5	6.2	16
CoPt <sub>3</sub> - LA II w	15.2	5.8	7

The data calculated from the TG curves show that the number of ligands per particle depends on the size of the ligand molecule. The biggest molecule will occupy more space of the particle surface and therefore the number of molecules connected to the particles will be

lower. The same behaviour was reported in literature for different thiol ligands connected to gold nanoparticles<sup>[3]</sup>.

TG and DSC analyses of CoPt<sub>3</sub> nanoparticles stabilised with different acids lead to the following conclusions:

a) Ligand excess removal can be monitored by TG. Additionally this technique is very suitable for the calculation of the ligand concentration in the samples as well as the number of ligands per particles.

b) Both techniques, TG and DSC, confirmed the exchange of ACA on the particle surface by new acids.

c) The catalytic effect of the particles and their influence on the degradation mechanism was confirmed by both techniques. This influence was observed through a change of the number of degradation steps and a shift of the characteristic decomposition temperatures to lower values.

All results lead to the conclusion that the used ligand exchange procedure is successful. It is possible to exchange ligands on the particle surface with four new acids by using this procedure. These new ligands should have an influence not only on the thermal properties of the samples but also on the particle assembly. For this reason TEM and SAXS investigations were done in order to investigate the influence of the new ligands on CoPt<sub>3</sub> nanoparticles 2-D and 3-D self-assembly.

## 2.5. Influence of the ligands on particle self-assembly

### 2.5.1. 2-D structures of CoPt<sub>3</sub> nanoparticles

The organisation of CoPt<sub>3</sub> particles in 2-D structures has been investigated by TEM. Two different samples with different particle sizes and narrow size distributions were studied in order to investigate whether the particle size influences the particle packing after ligand exchange. Representative TEM images and the corresponding histograms for both samples are shown in Fig. 2.13. The statistical analyses based on the TEM images for the samples CoPt<sub>3</sub>-5 and CoPt<sub>3</sub>-8 (stabilised with ACA/HDA) gave mean diameters of  $5.6 \pm 0.7$  nm and  $8.0 \pm 0.5$  nm, respectively.

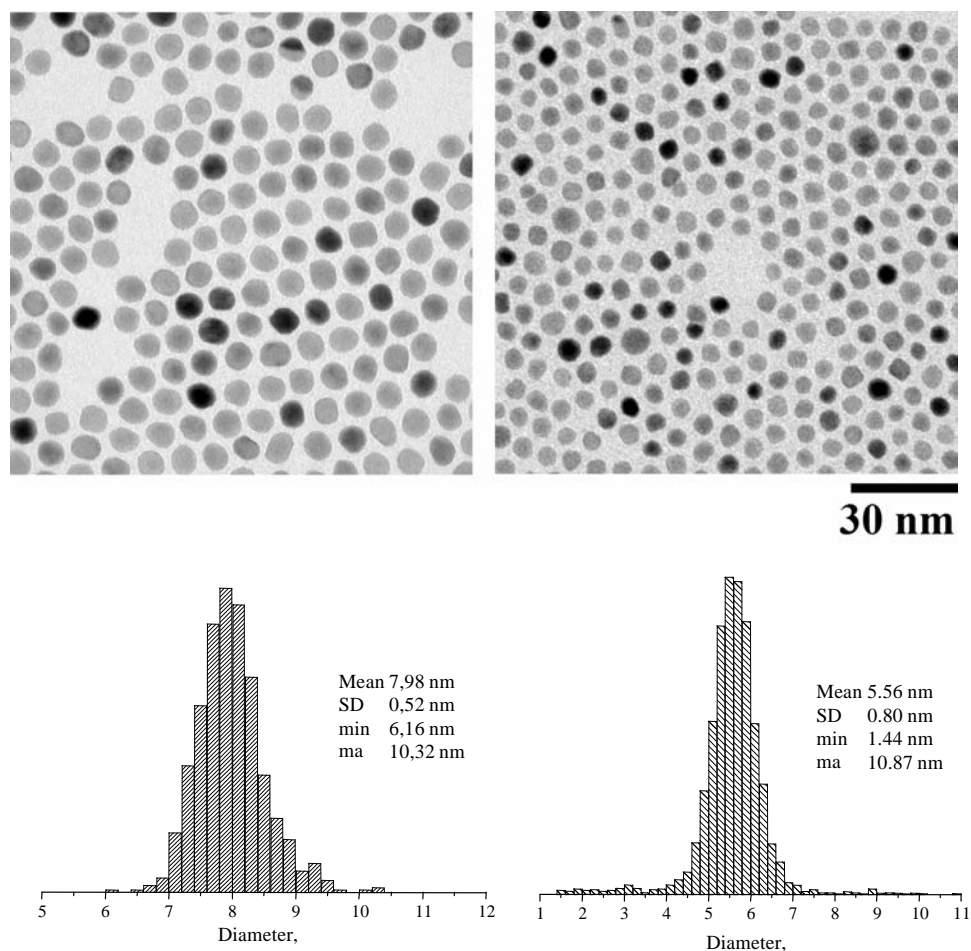


**Fig. 2.13.** TEM images and corresponding histograms (inserts) of the samples CoPt<sub>3</sub> – 8 (left hand side) and CoPt<sub>3</sub> - 5 (right hand side) stabilised with ACA/HDA

The ligand exchange procedure was applied to these two samples. After successful ligand exchange the samples were deposited on carbon grids and investigated by TEM. Images of the larger particles (CoPt<sub>3</sub>-8) before and after ligand exchange with LA and UDA are shown in Fig. 2.14.. All samples were two times washed prior to the TEM investigation. These two acids were chosen in order to compare the influence of the alkyl chain length on the particle packing. TEM images show that the particles (CoPt<sub>3</sub>-8) stabilised with LA and UDA are packed in less ordered structures in comparison to as-prepared particles. This is especially pronounced in the case of LA. This behaviour is probably a result of the longer alkyl chains and two double bonds (two *cis*- bonds) that reduced the possibility of the ligand packing and closer particle packing. Nevertheless, the TEM images confirmed that the

distance between the particles changes after attachment of LA and UDA to the particle surface.

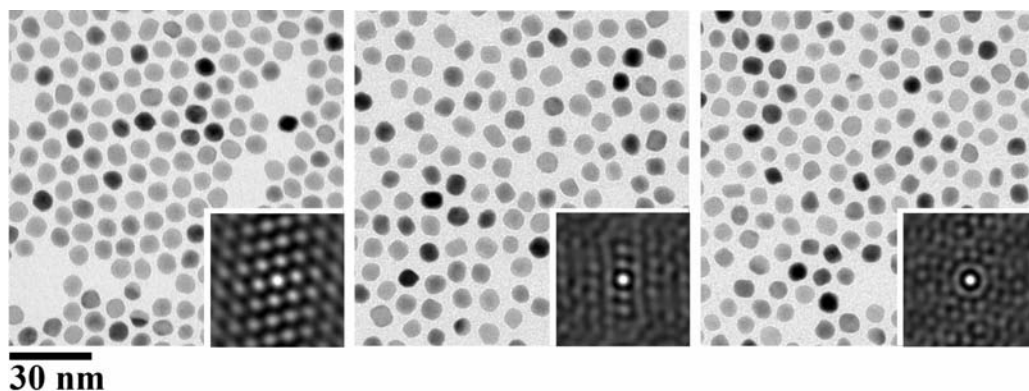


**Fig. 2.14.** TEM images of the  $\text{CoPt}_3\text{-8}$  nanoparticles before (left) and after ligand exchange with LA (middle) and UDA (right) are displayed. Insert images are the corresponding autocorrelation functions of displayed TEM images (selection 512x512 pixels).

TEM images of  $\text{CoPt}_3\text{-5}$  nanoparticles prepared in the same way and treated with the same ligands are shown in Figure 2.15. In contrast to the larger particles the small particles self assemble nicely after ligand exchange. They still form a hexagonal lattice as the as-prepared particles. Autocorrelation function also confirmed the good order of the particles (Fig. 2.15. - insert figures).

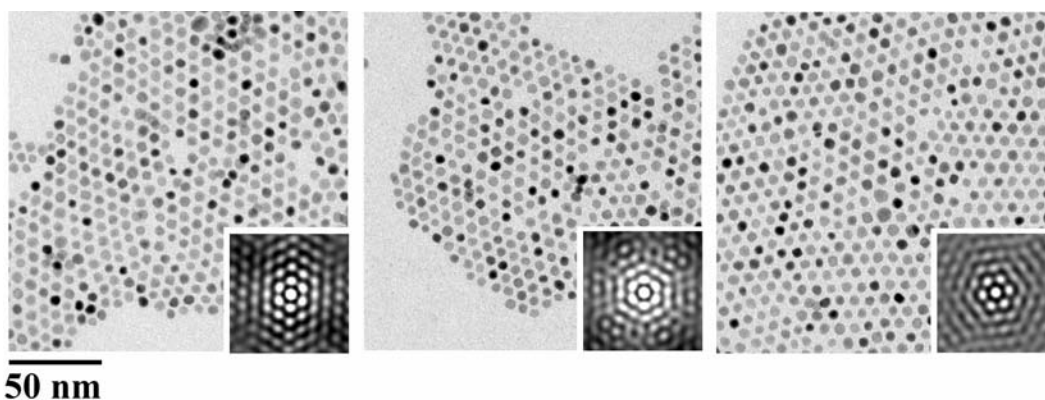


**Fig. 2.15.** TEM images of: as-prepared  $\text{CoPt}_3\text{-5}$  sample (left); the same particles after ligand exchange with LA (middle) and with UDA (right). Insert images are the corresponding autocorrelation functions of displayed TEM images.

Due to the small size difference among the new ligands the change in particle-particle distances is not straightforward observable by the naked eye. Therefore an autocorrelation function of the TEM images was used in order to investigate the influence of the ligands on the particles order. An autocorrelation function gives information about the particle packing in the real space. The slice made through the centre of the image obtained by using the autocorrelation function gives curves from which the particle-particle distance can be calculated. The adequate images obtained after usage of the autocorrelation function and the curves obtained from the function are presented in Fig. 2.16. The distance between the centre peak and the first neighbour peak gives the particle-particle distance (centre-centre). The shift of the peak maxima to higher values (from 7.5 to 8.4 nm) is in good agreement with the increase of the ligand length and indicates the change of the particle-particle distance with ligand exchange.

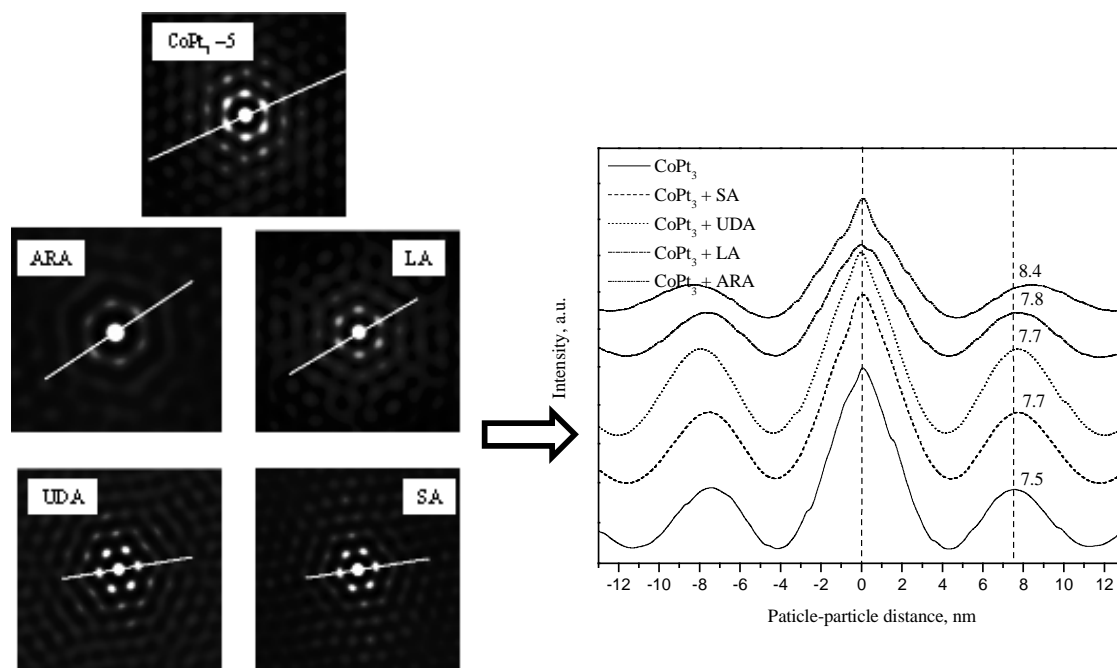


**Fig. 2.16.** Images obtained by applying an autocorrelation function to the TEM images of CoPt<sub>3</sub>-5 particles before and after ligand exchange with different acids (left hand side). The curves obtained by slicing the images of the autocorrelation function through the centre, showing the particle-particle distance (right hand side). (The slices are made in the positions of the white lines in the images.) All samples were two times washed before TEM investigation.

The autocorrelation function and TEM images gives an overview of small particle areas and can not be used for getting information about the particle packing in larger areas, and in 3-D structures. Additionally the influence of the washing procedure on the particle packing is difficult to investigate by TEM due to the fact that a ligand excess causes problems during the measurements. Therefore SAXS was chosen as a better technique for the investigation of particle assembly in 3-D structures.

### 2.5.2. 3-D structures of $\text{CoPt}_3$ nanoparticles

After analysis of the particle packing on carbon grids and the demonstration that it is possible to order the particles in a hexagonal lattice after ligand exchange it was interesting to investigate the self-assembly of  $\text{CoPt}_3$  nanoparticles into 3-D structures. Therefore, samples were dried on carbon foil and SAXS measurements were performed.

SAXS investigations give information about particle-particle distances, the type of lattice (interference function) as well as the shape and size of the particles (form factor). Due to the much higher electron density of the  $\text{CoPt}_3$  core in comparison to the organic ligands, only the form factor scattering of the core can be observed.

Table 2.5. Values of the unit cell, the nearest neighbourhood distance (NND) and the particle radius for samples before and after ligand exchange with UDA calculated using the software

Scatter Version 1.0

Sample	Particle radius* (nm)	Lattice type	Lattice constant (nm)	NND (nm)
$\text{CoPt}_3$ -5 - nw	2.90	FCC	12.90	9.12
$\text{CoPt}_3$ -5 - II w	2.90	FCC	12.30	8.79
$\text{CoPt}_3$ +UDA-nw	3.05	FCC	13.10	9.26
$\text{CoPt}_3$ +UDA-I w	2.95	FCC (60%)	12.80	9.05
	4.00	BCC (40%)	11.10	9.61
$\text{CoPt}_3$ +UDA-II w	2.95	FCC (65%)	12.80	9.05
	2.95	BCC (35%)	10.90	9.44
$\text{CoPt}_3$ +UDA-III w	3.05	FCC (70%)	12.60	8.91
	2.90	BCC (30%)	11.00	9.53

\* All particles have a size distribution of 7 – 10%

The SAXS analysis was done for two different samples: one before ligand exchange and another after ligand exchange with UDA. Additionally these samples were analysed by SAXS before and after applying the washing procedure. The measured curves were analysed using the software Scatter Version 1.0<sup>[32],[33]</sup>. The results obtained by this analysis are shown in Table 2.5. The measured and fitted curves for the sample before ligand exchange (not washed and two times washed) are shown in Figure 2.17.

The cleaned particles before ligand exchange show curves that can be fitted to a model for ideal spheres packed in a FCC lattice (Fig. 2.17.). Nevertheless the coexistence of a small amount of particles packed in a BCC lattice is possible and that can lead to small errors in the fit curves.

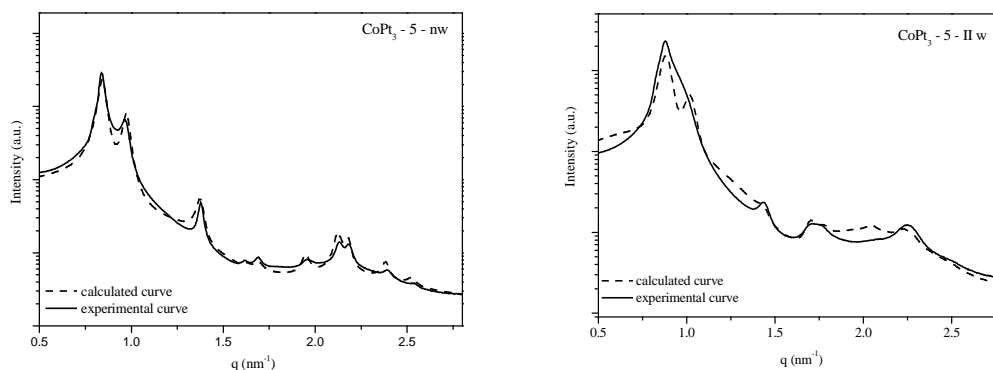


**Fig. 2.17.** SAXS patterns of  $\text{CoPt}_3\text{-5}$  particles before (left hand side) and after the second washing step (right hand side) are shown. The corresponding theoretical curves are shown as dash lines.

The nearest neighbourhood distance (NND) and the lattice constant give information about the particle packing. If their values are small the particles are packed closer to each other i.e. they give a smaller unit cell. The particles before ligand exchange show a decrease in the NND after the second washing step (Table 2.5.). The smaller NND indicates closer packing of the particles after removal of the ligand excess. Simultaneously the SAXS curve for the sample after the second washing step shows that the particles are packed in a less ordered lattice. The smaller numbers and the broadening of the peaks and the reduced possibility for good fitting by theoretical curves are indicators for a decreasing quality of order.

After ligand exchange with UDA the particles are packed in a FCC lattice as revealed by SAXS (Fig. 2.18.). The theoretical curve obtained using a model for FCC lattices and the measured curve fit very well. After additional washing the particles stabilised with UDA start to pack in two different lattices, face centred cubic (FCC) and body centred cubic (BCC). Already after the first washing step the characteristic peak for a BCC lattice is clearly observed in the SAXS curve (Fig. 2.18. sample CoPt<sub>3</sub>+UDA-I w). Further removal of the ligands leads to a broadening of the peaks and a disappearance of some of them indicating a less ordered structure. The NND values and lattice constant increase in comparison to the values of particles before ligand exchange. This is a result of the attachment of slightly larger ligand molecules to the particle surface. Larger ligands lead to particle packing in bigger distances. This has an influence on the NND values.

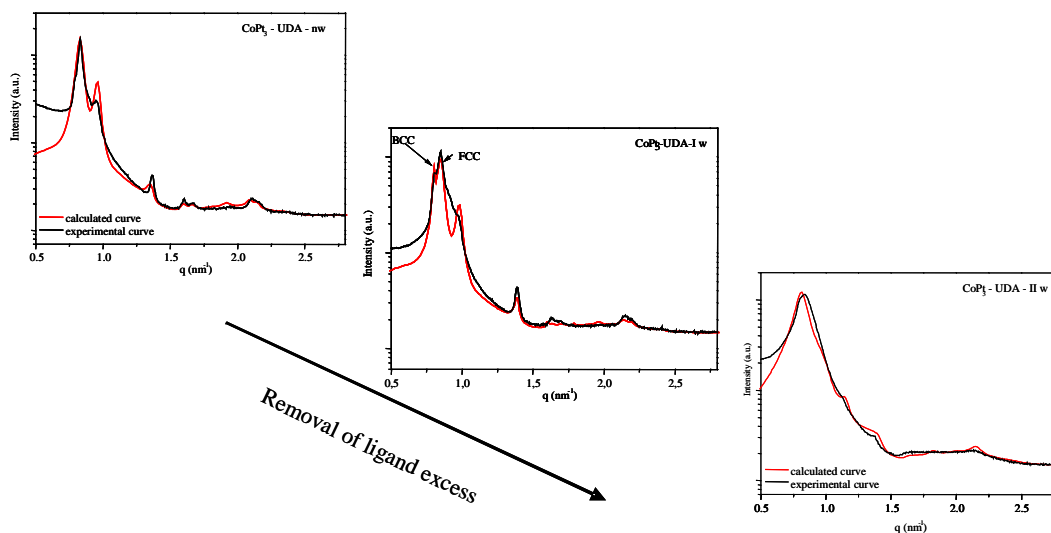


**Fig. 2.18.** SAXS patterns of CoPt<sub>3</sub>-5 particles stabilised with UDA before (CoPt<sub>3</sub>-UDA-nw) and after the first (CoPt<sub>3</sub>-UDA-I w) and second (CoPt<sub>3</sub>-UDA-II w) washing step. The corresponding theoretical curves are shown in red.

In the series of samples stabilised with UDA the NND values decrease with removal of the ligand excess. This indicates the closer packing of the particles. The closer particle packing (observed from NND values) and less ordered structures (observed from SAXS curve) are a result of ligand removal from the particle surface. By removing the ligands the particles have less and less ligands on the surface. Additionally it is possible that not all particles are stabilised with the same amount of ligands. A different ligand amount probably

leads to different packing. Depending on the ligand amount the particles can be packed in different distances. Due to that they formed small differently oriented domains of closely packed particles. Moreover it is possible that some of the particles agglomerate due to ligand removal. Obviously the particles are losing the possibility of good self-assembly by washing. For this reason the domains are getting smaller leading to peak broadening.

The ligand exchange with larger particles (CoPt<sub>3</sub>-8) was investigated in the same way. A representative curve is shown as an example in Figure 2.19. The experimental data (black line) fits very well to the calculated line (red line). The calculation was done using the assumption that the particles form a face centred cubic (FCC) lattice.

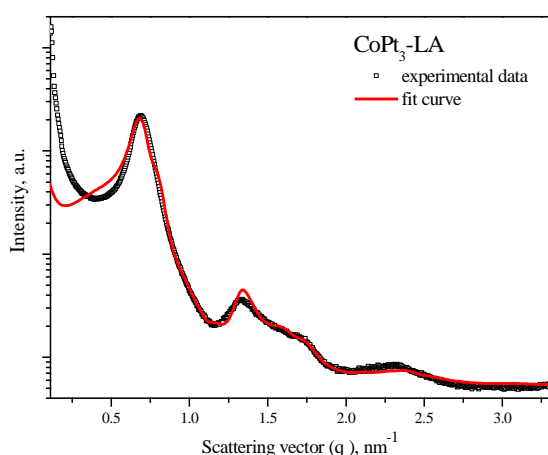


**Fig. 2.19.** Comparison of the SAXS pattern of CoPt<sub>3</sub>-8 particles stabilised with LA (black line) to a theoretical curve (red line).

The position of the reflections at different  $q$  values indicates the different particle-particle distances for different organic ligands. By using the software Scatter Version 1.0 it was possible to calculate the unit cell, nearest neighbourhood distance, as well as the relative displacement and diameter of the particles with the organic shell (Table 2.6.) for all samples.

Table 2.6. Values of the unit cell (FCC), the NND, the relative displacement (RD), particle diameter, the theoretical length of the stretched ligands ( $l$ ) and shell thickness (extracted from the SAXS data).

Ligand	Unit cell [nm]	NND [nm]	RD.	$d_{\text{core+shell}}$ [nm]	$d_{\text{core}}$ [nm]	$l$ [nm]	Shell thickness* [nm]
CoPt <sub>3</sub> -ARA	19.2	13.6	21%	10.4	8.4	2.9	2.8
CoPt <sub>3</sub> -8	16.5	11.7	14%	10.0	8.4	2.0 <sup>+</sup>	1.9
CoPt <sub>3</sub> -LA	15.6	11.0	9%	10.0	8.0	2.7	1.5
CoPt <sub>3</sub> -UDA	15.2	10.0	13%	9.0	8.2	1.7	1.0
CoPt <sub>3</sub> -SA	14.1	9.98	17%	9.2	8.2	0.8	1.0

\* Calculations were done using the values for the NND and the statistic value of diameters calculated from the TEM images ( $d = 7.98$  nm).

<sup>+</sup> Estimated value for the length of the ACA molecule

The SAXS measurements gave additional evidence for the influence of the ligand type on the particle-particle distance (Table 2.6.). By using ligands with different lengths it is possible to vary the nearest neighbourhood (particle-particle) distance from 9.98 nm for CoPt<sub>3</sub>-SA to 13.6 nm for CoPt<sub>3</sub>-ARA. Additionally, at the same time the unit cell size decreases from 19.2 nm (CoPt<sub>3</sub>-ARA) to 14.1 nm (CoPt<sub>3</sub>-SA). The calculated data for the relative displacement (Table 2.6.) demonstrates that a less perfect ordering exist in sample CoPt<sub>3</sub>-ARA (RD = 21%). The SAXS revealed the best packing for the CoPt<sub>3</sub>-LA (RD = 9 %) sample.

The shell thickness for the different ligands is calculated from the values of the NND and from the particle diameter obtained from TEM images. Due to the variation ( $d_{\text{core}}$ ) of the core diameter the TEM data are more reliable than the values from the SAXS calculation. The calculated shell thickness increases in the same way as the ligand length. The calculated value for ARA is close to the theoretical length of the stretched molecule, while for other samples these values are lower. In all cases the distance between the particles is smaller than the double length of the stretched ligand molecules, indicating penetration and folding of the ligands. The differences between the values obtained from autocorrelation function and obtained by SAXS measurements are due to the different particle packing (2-D and 3-D, respectively) as well as due to the differences between the used methods for analyses.

## 2.6. Conclusion

The ligands (ACA and HDA) present on the particle surface after synthesis are successfully exchanged with a series of different carboxylic acids such as: sorbic, undecanoic, linoleic and arachidic acid. The applied procedure is reproducible and efficient for particles of different sizes. The new ligands lead to particle solutions, which are stable for a long period of time. The acids are adsorbed at the particle surface trough COOH or COO<sup>-</sup> groups. The number of ligand molecules connected to the particle surface depends on the molecule length and decreases with increasing ligand length.

It was shown that the ligand excess is completely removed after two washing steps. The ligand decomposition occurs at lower temperatures after removal of the ligand excess and the degradation mechanism changes.

Particles stabilized with the new ligands are still able to self-assemble in well ordered 2-D and 3-D structures. The presence of a ligand excess is necessary for good ordering in 3-D structures. By using short acids as ligands with different numbers of C-atoms, i.e. different lengths, it is possible to vary the particle-particle distance from 13.6 nm (for ARA) to 9.9 nm (for SA). The control of the particle distance in films will open new opportunities for the application of nanoparticle films. Controlling the distance between the particles is for example, very important for the catalytic, magnetic or electric properties of the particle assemblies.

## 2.7. Literature

1. Sun, X., et al., *Self-assembly of magnetic biofunctional nanoparticles*. J. Appl. Phys., 2005. **97**: p. 10Q901-1 - 10Q901-3.
2. Lee, S.Y. and M.T. Harris, *Surface modification of magnetic nanoparticles capped by oleic acids: Characterization and colloidal stability in polar solvents*. Journal of Colloid and Interface Science, 2006. **293**: p. 401-408.
3. Woehrle, G.H., L.O. Brown, and J.E. Hutchison, *Thiol-Functionalized, 1.5-nm Gold Nanoparticles through Ligand Exchange Reactions: Scope and Mechanism of Ligand Exchange*. J. Am. Chem. Soc., 2005. **127**: p. 2172-2183.
4. Yee, C., et al., *Self-Assembled Monolayers of Alkanesulfonic and -phosphonic Acids on Amorphous Iron Oxide Nanoparticles*. Langmuir, 1999. **15**: p. 7111-7115.
5. Woehrle, G.H., M.G. Warner, and J.E. Hutchison, *Ligand Exchange Reactions Yield Subnanometer, Thiol-Stabilized Gold Particles with Defined Optical Transitions*. J. Phys. Chem. B, 2002. **106**: p. 9979-9981.
6. Warner, M.G., S.M. Reed, and J.E. Hutchison, *Small, Water-Soluble, Ligand-Stabilized Gold Nanoparticles Synthesized by Interfacial Ligand Exchange Reactions*. Chem. Mater., 2000. **12**: p. 3316-3320.
7. Kumar, A., et al., *Investigation into the Interaction between Surface-Bound Alkylamines and Gold Nanoparticles*. Langmuir, 2003. **19**: p. 6277-6282.
8. Diana, F.S., et al., *Nano Letters*, 2003. **3**(7): p. 891-895.
9. Liu, X., et al., *Surface Modification and Characterization of Magnetic Polymer Nanospheres Prepared by Miniemulsion Polymerization*. Langmuir, 2004. **20**: p. 10278-10282.
10. Vadala, M.L., et al., *J. Magn. Magn. Mater.*, 2005. **293**: p. 162-170.
11. Kim, B.S., et al., *Magnetomicelles: Composite Nanostructures from Magnetic Nanoparticles and Cross-Linked Amphiphilic Block Copolymers*. Nano Letters, 2005. **5**(10): p. 1987-1991.
12. Sang-Yup Lee, M.T.H., *Journal of Colloid and Interface Science*, 2006. **293**: p. 401-408.
13. Frederic Dumestre, S.M., David Zitoun, Marie-Claire Fromen, P.L. Marie-Jose Casanove, Marc Respaud, Arnaud Serres, and C.A.a.B.C. Robert E. Benfield, *Faraday Discuss.*, 2004. **125**: p. 265-278.

14. Smith, E.L. and M.D. Porter, *Structure of Monolayers of Short Chain n- Alkanoic Acids (CH<sub>3</sub>(CH<sub>2</sub>)<sub>n</sub>COOH, n= 0-9) Spontaneously Adsorbed from the Gas Phase at Silver As Probed by Infrared Reflection Spectroscopy*. J. Phys. Chem., 1993. **97**: p. 8032-8038.
15. Sahoo, Y., et al., *Alkyl Phosphonate/Phosphate Coating on Magnetite Nanoparticles: A Comparison with Fatty Acids*. Langmuir, 2001. **17**: p. 7907-7911.
16. Malynych, S., I. Luzinov, and G. Chumanov, *Poly(Vinyl Pyridine) as a Universal Surface Modifier for Immobilization of Nanoparticles*. J. Phys. Chem. B, 2002. **106**: p. 1280-1285.
17. Yin, B., et al., *Electrochemical Synthesis of Silver Nanoparticles under Protection of Poly(N-vinylpyrrolidone)*. J. Phys. Chem. B, 2003. **107**: p. 8898-8904.
18. Hao, E. and T. Lian, *Buildup of Polymer/Au Nanoparticle Multilayer Thin Films Based on Hydrogen Bonding*. Chem. Mater., 2000. **12**: p. 3392-3396.
19. Sandhyarani, N., et al., J. Chem. Phys., 2000. **114**(21): p. 9794-9803.
20. Porter, M., et al., J. Am. Chem. Soc., 1987. **109**: p. 3559-3568.
21. Hostetler, M.J., J.J. Stokes, and R.W. Murray, Langmuir, 1996. **12**: p. 3604-3612.
22. Hostetler, M.J., R.W. Murray, and A.C. Templeton, Langmuir, 1999. **15**: p. 3782-3789.
23. Wu, N., et al., *Interaction of Fatty Acid Monolayers with Cobalt Nanoparticles*. Nano Letters, 2004. **4**(2): p. 383-386.
24. Nara, M., H. Torii, and M. Tasumi, *Correlation between the Vibrational Frequencies of the Carboxylate Group and the Types of Its Coordination to a Metal Ion: An ab Initio Molecular Orbital Study*. J. Phys. Chem., 1996. **100**: p. 19812-19817.
25. Wang, W., X. Chen, and S. Efrima, *Silver Nanoparticles Capped by Long-Chain Unsaturated Carboxylates*. J. Phys. Chem. B, 1999. **103**: p. 7238-7246.
26. Wang, W., S. Efrima, and O. Regev, *Directing Oleate Stabilized Nanosized Silver Colloids into Organic Phases*. Langmuir, 1998. **14**: p. 602-610.
27. Molnar, E., et al., *Infrared spectroscopy studies of cyclohexene hydrogenation and dehydrogenation catalyzed by platinum nanoparticles supported on mesoporous silicate (SBA-15). Part 1: The role of particle size of Pt nanocrystals supported on SBA-15 silicate*. Catalysis Letters, 2005. **101**(3-4): p. 159-167.
28. Eklund, S.E. and D.E. Cliffl, *Synthesis and Catalytic Properties of Soluble Platinum Nanoparticles Protected by Thiol Monolayer*. Langmuir, 2004. **20**: p. 6012-6018.
29. Milosavljevic, S.M., *Strukturne instrumentalne metode*. 1997, Beograd: Hemijski fakultet.
30. Beecher, P., et al., *Insulator-to-Metal Transition in Nanocrystal Assemblies Driven by in Situ Mild Thermal Annealing*. Nano Letters, 2004. **4**(7): p. 1289-1293.
31. Boyen, H.G., et al., *Electronic and Magnetic Properties of Ligand-Free FePt Nanoparticles*. Adv. Mater., 2005. **17**(5): p. 574-578.
32. S. Förster, A.T., M. Konrad, C. Schellbach, A. Meyer, S.S. Funari, P. Mulvaney, R. Knott, J. Phys. Chem. B, 2005. **109**: p. 1347.
33. Förster, S. and C. Burger, *Macromolecules*, 1998. **31**: p. 879.

## Chapter 3

### Ligand exchange – amines

---

#### 3.1. Introduction

Amines are known as good ligands for metallic nanoparticles. They have been used as stabilisers during the synthesis of Ag<sup>[1]</sup>, Au<sup>[2]</sup>, FePt<sup>[3]</sup>, Co<sup>[4]</sup> and Co<sub>x</sub>Pt<sub>y</sub> (x/y is 1/3 or 1/1)<sup>[5],[6]</sup> nanoparticles. By using the amines it is possible to synthesize gold nanoparticles with a narrow particle size distribution and also to tune their size<sup>[7],[8]</sup>. It was found that amino-capped gold nanocrystals are nearly as stable as their thiol capped counterparts<sup>[2]</sup>. Gold nanocrystals stabilised with amines can arrange in highly ordered structures. These structures are excellent candidates for the preparation of nanoscale devices<sup>[9]</sup>. The formation of strong bands between amines and metal nanoparticles is also used for the phase transfer of Ag<sup>[10]</sup> and Pt<sup>[11]</sup> nanoparticles from aqueous to organic solutions. These amino-metal interactions are also used for encapsulation of metal nanoparticles with poly(amidoamine) and poly(propylene imine) dendrimers<sup>[12]</sup>. Additionally poly(amidoamine) dendrimers can be used for the manipulation of the interparticle spacing between magnetic nanoparticles. Different distances between magnetic particles lead to different magnetic properties<sup>[13]</sup>.

In the CoPt<sub>3</sub> nanoparticle syntheses described in this thesis hexadecylamine (HDA) was not only used as a ligand but also as a solvent. Investigations have shown that the presence of HDA is necessary for long-term stability of the particle solution.

The main goal of the investigation described in this chapter was to study the applicability of the same ligand exchange procedure applied for carboxylic acids to amines. Two different amines with shorter alkyl chains than HDA were used: trihexylamine and diaminobutan. Additionally, the same procedure was applied to amines with longer polymer chains based on poly(ethylene oxide). Poly(ethylene oxide) has already been used as a reducing reagent during the synthesis of CoPt nanoparticles<sup>[5]</sup>. Furthermore, it can be used for the synthesis of FeO nanoparticles<sup>[14]</sup> or for the coating of other magnetic nanoparticles<sup>[15],[16],[18]</sup>. The modification of PEO and the attachment of SH groups at the end of the polymer chain allowed the application as a ligand for different types of particles<sup>[19],[20],[21]</sup>. Particles protected with a PEO shell can be used for biological applications since it is a non-toxic, non-immunogenic, non-antigenic, and protein-resistant polymer<sup>[14]</sup>.

### 3.2. Ligand exchange with amines

CoPt<sub>3</sub> nanoparticles were cleaned (experimental part – Chapter 9.) and mixed with different amounts of amines. Five to ten times larger amounts of amines in comparison to the amount of particles in the solution were used for the investigation. Smaller amounts of amines are not sufficient to stabilise the particles. The same procedure as for the carboxylic acids was used (experimental part – Chapter 9). The particles previously dissolved in chloroform were mixed with a solution of amines in chloroform. Our investigations show that such small amounts of 1,4-diaminobutan (5 times larger amount in comparison to the particles) lead to particle agglomeration. It was not possible to obtain stabile particle solution with this ligand. In contrast trihexylamine gives a stabile particle solution in both cases (5 and 10 times larger amount of ligands). The particles were washed with 2-propanol after the ligand exchange in order to remove the ligand excess and IR spectra were measured (Fig. 3.1.).

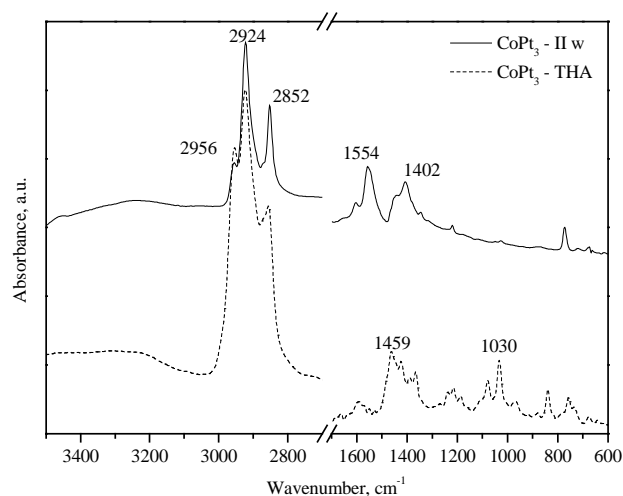


**Fig. 3.1.** The FTIR spectra of particles before ligand exchange (solid line) and after ligand exchange with trihexylamine and washing (dash line)

Representative sets of FTIR spectra, comparing the spectral characteristics of particles before and after the ligand exchange, are shown in Fig. 3.1. Series of stretching bands corresponding to methyl and methylene groups can be seen in-between 2800 - 3000 cm<sup>-1</sup>. The band at 2956 cm<sup>-1</sup> is assigned to antisymmetric CH<sub>3</sub> stretching modes and bands at 2924 and 2852 cm<sup>-1</sup> are assigned to the  $\nu_a$  and  $\nu_s$  CH<sub>2</sub> modes, respectively<sup>[22]-[24]</sup>. Two bands at 1554 and 1402 cm<sup>-1</sup> in the spectra of the particles before ligand exchange are originating from

symmetric stretching mode  $\nu_s$  (COO<sup>-</sup>) of the carboxylate group. After the ligand exchange these two bands disappeared. This result indicates the presence of trihexylamine at the particle surface that is schematically shown in Figure 3.2.. The FTIR spectrum of the particles after ligand exchange shows methylene scissoring and methyl antisymmetric bending in the frequency region from 1460 - 1380  $\text{cm}^{-1}$ . The C-C stretching modes are between 950 and 1150  $\text{cm}^{-1}$ . The presence of bands characteristic for CH<sub>2</sub> and CH<sub>3</sub> groups after the ligand exchange indicates the presence of trihexylamine at the particle surface. A scheme of the ligand exchange is shown in Figure 3.2. Stable particle solutions are obtained after ligand exchange with trihexylamine, while 1,4-diamine leads probably to the formation of a network. The network is formed due to the presence of two amino groups at both alkyl chain ends, which lead to connections between the particles.

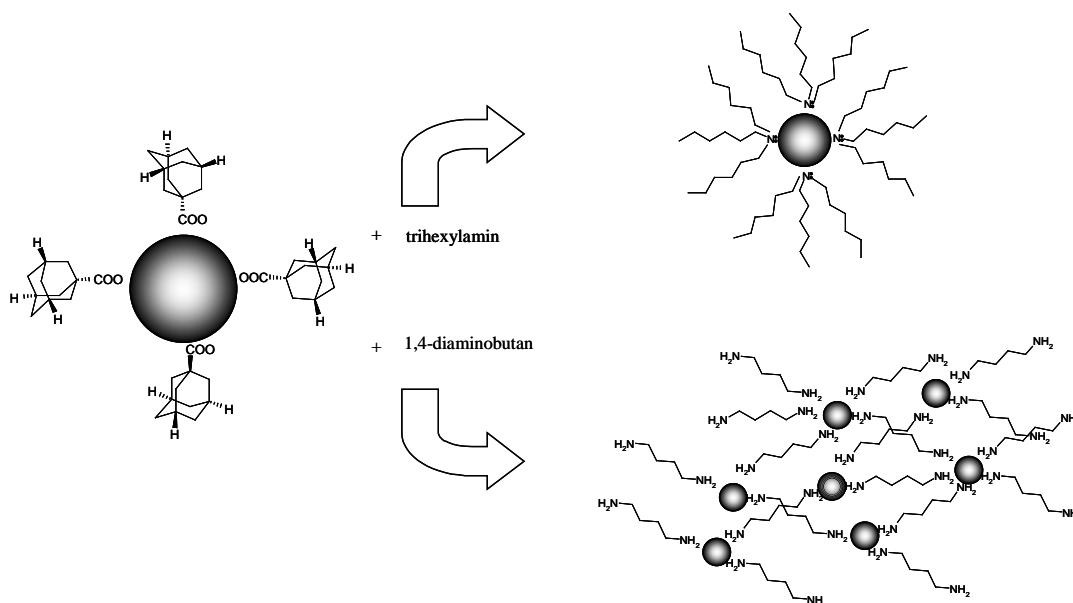


**Fig. 3.2.** The scheme of the ligand exchange at CoPt<sub>3</sub> nanoparticles with trihexylamine and 1,4-diaminobutan

Ligand exchange experiments with tertiary amines such as trihexylamine show that the presence of a free electron couple at the nitrogen atom is probably the most important parameter for the attachment of amines at the CoPt<sub>3</sub> nanoparticles surface. This result implies that other molecules that contain nitrogen with a free electron couple can be used as new ligands which stabilize the particles. This observation was used later for the examination of CoPt<sub>3</sub> nanoparticle film formation on different polymer surfaces containing pyridine or amino groups in the polymer chain (Chapter 5.).

### 3.3. Ligand exchange with polymers containing -NH<sub>2</sub> groups

It has been shown in the previous chapter that amines interact strongly with CoPt<sub>3</sub> nanoparticles. For this reason polymers with amine head groups were chosen as potentially good candidates for the attachment of polyethylene oxide to CoPt<sub>3</sub> nanoparticles. In order to enlarge the particle-particle distance two polymers with amino head groups were chosen for the investigation: PEOA-1 ( $\overline{M}_p = 3200$  g/mol) and PEOA-2 ( $\overline{M}_p = 1750$  g/mol) (see experimental part).

The CoPt<sub>3</sub> nanoparticles were cleaned and then mixed with polymer solutions in chloroform and stirred for approximately 24 h. Different amounts of polymers were used for the investigation. The particles were cleaned once with 2-propanol and a fresh new polymer solution (the same like in the first step of the procedure) was added. The procedure was repeated once more. The obtained particle solutions were cleaned two times with 2-propanol. Afterwards the particles were redissolved in chloroform. The as-prepared solutions were filtered through a PTFE 0.2 µm filter.

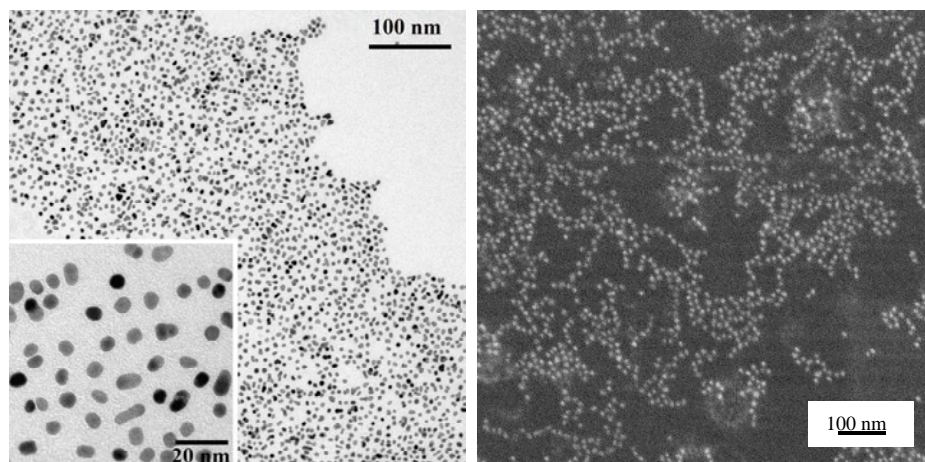
The solubility of the particles was tested in order to check which amount of polymers is necessary for a successful ligand exchange. Therefore 100 µl each solution was dried under nitrogen, and then 200 µl of water was added to the dried particles under vigorous stirring. The water solutions of particles were stirred for several days and stability of the solutions was studied. The obtained results are presented in Table 3.1.

Table 3.1. Ratio between the used amounts of particles and polymers during the ligand exchange and stability of polymer stabilised particles after their transfer to water

Polymer	n(CoPt <sub>3</sub> ) : n(polymer)	Stability
PEOA-1	1:0.16	Precipitated immediately
	1:0.33	One day
	1:0.66	Stabile for months
PEOA-2	1:0.33	Precipitated immediately
	1:0.66	Five days
	1:1.20	Stabile for months
	1:2.40	Stabile for months

CoPt<sub>3</sub> nanoparticle transfer from non-polar solvents into water confirmed the successful ligand exchange with polymers based on poly(ethylene oxide). Stable water solutions were obtained for particles to polymer ratio of 1 : 0.66. Lower polymer concentrations are not sufficient for particle stabilisation. Larger amounts of polymers in comparison to the particle amount (1 : 0.66) lead to more stable solutions.

The stabilisation of the particles and their transfer into water did not show the formation of agglomerations or small clusters stabilised with polymers (Figure 3.3.). They are packed in a non-ordered structure what is expected from aqueous solutions. (The particles deposited from aqueous solution on carbon grids (for TEM measurements) show only seldom 2D lattices.) The distances between the particles increased in comparison to particles before ligand exchange (usually ~ 2.5 nm). This indicates that the polymer chains around the particles make a shell, which does not allow closer particle packing. An influence of different polymer length on the particle-particle distance was not observed. One explanation for this behaviour is that the polymer chains are long and they are not stretched but bended around the particles<sup>[25],[26]</sup>. Therefore the interparticle distance is not proportional to the polymer length. The polymer bending around the particles probably leads to different interparticle distances.



**Fig. 3.3.** TEM image of CoPt<sub>3</sub> nanoparticles stabilised with PEOA-2 and transferred to water (left hand side). SEM image of the same particles deposited from a chloroform solution on silicon by spin coating (right hand side)

The particles deposited on silicon from a chloroform solution show self-assembly in rope shape structures (Figure 3.3.). SEM shows that the polymer ligands do not allow particle self-assembly in 2-D super lattice. The distances between the particles are larger but not

controllable. A possible solution for this problem can be the use of shorter and/or more rigid polymer chains. Recent investigations show that PEO with more than one amino group at the end of the alkyl chain and with shorter PEO chains can lead to the assembly of CoPt<sub>3</sub> nanoparticles at different distances and in a hexagonal lattice<sup>[27]</sup>.

### 3.4. Conclusion

The ligand exchange procedure used for different carboxylic acids is also applicable to molecules with amino groups. It is possible to use not only primary but also tertiary amines in this procedure. This result indicates that the most important parameters for amine attachment to CoPt<sub>3</sub> nanoparticles are the presence of the lone electron pair at the nitrogen atom. Interactions between ligands and CoPt<sub>3</sub> nanoparticles are realised owing to this electron couple. The same procedure can also be used for the ligand exchange with poly (ethylene oxide) that was functionalised with an amino group. By using these polymers it is possible to transfer the nanoparticles from organic solutions to an aqueous phase. This can be interesting for further biological application. TEM images showed that the particles are separated from each other in water. The solution is stable for months. These polymer ligands lead to larger particle-particle distances, but they do not allow a self-assembly of the particles into 2-D super lattice. Due to the strong interactions between the used polymers and CoPt<sub>3</sub> nanoparticles these polymers are used as sublayers in spin coating and Langmuir – Blodgett techniques.

### 3.5. Literature

1. Manna, A., et al., *Formation of Silver Nanoparticles from a N-Hexadecylethylenediamine Silver Nitrate Complex*. Langmuir, 2001. **17**: p. 6000-6004.
2. Leff, D.V., L. Brandt, and J.R. Heath, *Synthesis and Characterisation of Hydrophobic, Organically - Soluble Gold Nanocrystals Functionalized with Primary Amines*. Langmuir, 1996. **12**: p. 4723-4730.
3. Gu, H., et al., *Facile One-Pot Synthesis of Bifunctional Heterodimers of Nanoparticles: A Conjugate of Quantum Dot and Magnetic Nanoparticles*. J. Am. Chem. Soc., 2004. **126**: p. 5664-5665.
4. Bao, Y., et al., *Controlled Crystalline Structure and Surface Stability of Cobalt Nanocrystals*. J. Phys. Chem. B, 2005. **109**(15): p. 7220-7222.
5. Tzitzios, V., et al., *Synthesis of CoPt nanoparticles by a modified polyol method: characterization and magnetic properties*. Nanotechnology, 2005. **16**: p. 287-291.
6. Frommen, C., H. Rösner, and D. Fenske, *Wet- Chemical Synthesis and Properties of CoPt and CoPt<sub>3</sub> Alloy Nanoparticles*. J. Nanosci. Nanotech., 2002. **2**(5): p. 509-515.

7. Brown, L.O. and J.E. Hutchison, *Controlled Growth of Gold Nanoparticles during Ligand Exchange*. J. Am. Chem. Soc., 1999. **121**: p. 882-883.
8. Kumar, A., et al., *Investigation into the Interaction between Surface-Bound Alkylamines and Gold Nanoparticles*. Langmuir, 2003. **19**: p. 6277-6282.
9. Brown, L.O. and J.E. Hutchison, *Formation and Electron Diffraction Studies of Ordered 2-D and 3-D Superlattices of Amine-Stabilized Gold Nanocrystals*. J. Phys. Chem. B, 2001. **105**: p. 8911-8916.
10. Kumar, A., et al., *Phase transfer of silver nanoparticles from aqueous to organic solutions using fatty amine molecules*. J. Coll. Int. Sci., 2003. **264**: p. 396-401.
11. Yang, J., et al., *An Alternative Phase-Transfer Method of Preparing Alkylamine-Stabilized Platinum Nanoparticles*. J. Phys. Chem. B, 2004. **108**: p. 2181-2185.
12. Crooks, R.M., et al., *Dendrimer-Encapsulated Metal Nanoparticles: Synthesis, Characterisation and Applications to Catalysis*. Acc. Chem. Res., 2001. **34**(3): p. 181-190.
13. Frankamp, B.L., et al., *Direct Control of the Magnetic Interaction between Iron Oxide Nanoparticles through Dendrimer-Mediated Self-Assembly*. J. Am. Chem. Soc., 2005. **127**: p. 9731-9735.
14. Li, Z., et al., *One-Pot Reaction to Synthesize Biocompatible Magnetite Nanoparticles*. Adv. Mater., 2005. **17**(8): p. 1001-1005.
15. Flesch, C., et al., *Poly(ethylene glycol) Surface Coated Magnetic Particles*. Macromol. Rapid Commun., 2005. **26**: p. 1494-1498.
16. Liu, X., et al., *Surface Modification and Characterization of Magnetic Polymer Nanospheres Prepared by Miniemulsion Polymerization*. Langmuir, 2004. **20**: p. 10278-10282.
17. Yoon, T.J., et al., *Multifunctional Nanoparticles Possessing A "Magnetic Motor Effect" for Drug or Gene Delivery*. Angew. Chem. Int. Ed., 2005. **44**: p. 1068-1071.
18. Kohler, N., et al., *Methotrexate-Immobilized Poly(ethylene glycol) Magnetic Nanoparticles for MR Imaging and Drug Delivery*. Small, 2006. **2**(6): p. 785-792.
19. Wuelfing, W.P., et al., *Nanometer Gold Clusters Protected by Surface-Bound Monolayers of Thiolated Poly(ethylene glycol) Polymer Electrolyte*. J. Am. Chem. Soc., 1998. **120**: p. 12696-12697.
20. Latham, A.H. and M.E. Williams, *Versatile Routes toward Functional, Water-Soluble Nanoparticles via Trifluoroethylester-PEG-Thiol Ligands*. Langmuir, 2006. **22**: p. 4319-4326.
21. Zheng, M., Z. Li, and X. Huang, *Ethylene Glycol Monolayer Protected Nanoparticles: Synthesis, Characterization, and Interactions with Biological Molecules†*. Langmuir, 2004. **20**: p. 4226-4235.
22. Porter, M., et al., J. Am. Chem. Soc., 1987. **109**: p. 3559-3568.
23. Hostetler, M.J., J.J. Stokes, and R.W. Murray, Langmuir, 1996. **12**: p. 3604-3612.
24. Sandhyarani, N., et al., J. Chem. Phys., 2000. **114**(21): p. 9794-9803.
25. Tadd, E., et al., *Adsorption and Polymer Film Formation on Metal Nanoclusters*. Macromolecules, 2003. **36**: p. 6497-6502.
26. Tannenbaum, R., et al., *FTIR Characterization of the Rective Interface of Cobalt Oxide Nanoparticles Embedded in Polymer Matrices*. J. Phys. Chem. B, 2006. **110**: p. 2227-2232.
27. Nikolic, M.S., et al., *Taylor-made ligands for biocompatible nanoparticles*. Angew.Chem, 2006. **accepted**.

## Chapter 4

### Ligand exchange - thiols

---

#### 4.1. Introduction

It was shown in the previous chapter that ligands present on the particle surface after the synthesis (ACA and HDA) could be successfully exchanged with carboxylic acids and amines. The used ligand exchange procedure should also be applicable to other ligands. In order to test these hypothesis ligands with -SH groups (thiols, mercapto alcohols or acids etc.) are chosen. These ligands are already known as good ligands for metal nanoparticles, such as Au<sup>[1]-[6]</sup>, Pd<sup>[7]</sup> and Pt<sup>[8],[9]</sup> nanoparticles. Thiols are not only used as ligands during the nanoparticles syntheses<sup>[8],[9],[10]</sup>, but also in the post-preparative exchange of the capping ligands on different nanoparticles. The ligand exchange leads to the formation of a more polar shell around CdSe<sup>[11]</sup> and Au<sup>[12]</sup> nanoparticles and increase their ability to form films on different surfaces. Additionally thiols can be used as ligands for the transfer of nanoparticles from the water to the organic phase<sup>[7]</sup>, for the stabilisation of CdSe nanoparticles during the formation of Langmuir Blodgett films at the air/water interface<sup>[13]</sup> or for the deposition of Au particles on polymer surfaces<sup>[14]</sup>.

Mercapto alcohols, mercapto acids or anionic and cationic thiol-containing ligands are usually used for the transfer of nanoparticles from non-polar solvents into the water phase<sup>[2],[4],[15]</sup>. Previous investigations have shown that the initial stabilisers (ACA and HDA) of CoPt<sub>3</sub> nanoparticles can be exchanged with 11-mercaptoundecanoic acid. By using this procedure CoPt<sub>3</sub> nanoparticles can be successfully transferred from non-polar solvents into water<sup>[15]</sup>.

Other ligand exchange reaction between thiols and CoPt<sub>3</sub> nanoparticles have not been described till now. As thiols have been used as ligands during the syntheses of Pt nanoparticles<sup>[8],[9]</sup> one can assume that they will also attach to outer Pt atoms in CoPt<sub>3</sub> nanoparticles. The Pt content in CoPt<sub>3</sub> nanoparticles is high and should provide a lot of places for thiol attachment. Therefore the possibility to exchange the present ligands on CoPt<sub>3</sub> nanoparticles with dodecanthiol (DDT) by using the already described ligand exchange procedure was investigated in this study.

4.2. IR analyses of CoPt<sub>3</sub> nanoparticles before and after ligand exchange with DDT

The ligand exchange is performed by the procedure described in the experimental part (Chapter 9.). Briefly, previously cleaned particles are mixed with DDT. The IR analysis of the particles before and after ligand exchange with DDT shows significant differences in the spectra (Fig. 4.1.). The two bands at 1563 and 1415 cm<sup>-1</sup> in the spectra of the particles before ligand exchange arise from COO<sup>-</sup> groups attached to the particle surface. (The IR-spectrum of the particles before ligand exchange is explained in detail in the previous chapter.) The band at 2957 cm<sup>-1</sup> in the spectra of the sample after ligand exchange arise from the antisymmetric -CH- stretching, while the bands at 2917 and 2848 cm<sup>-1</sup> are results of the antisymmetric and symmetric stretching vibrations of CH<sub>2</sub> [16],[17].

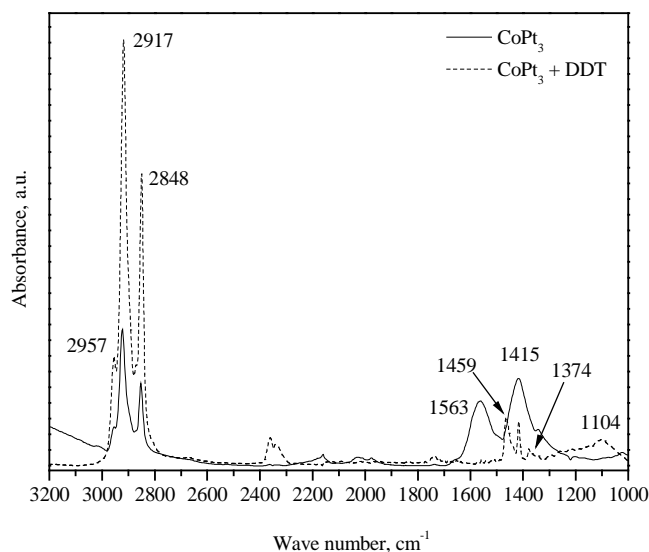


**Fig. 4.1.** Typical IR spectra of the sample before (solid line) and after ligand exchange with DDT (dash line)

After the ligands exchange with DDT and the washing procedure (two times washed) the bands of the COO<sup>-</sup> groups disappear suggesting the complete removal of ACA from the particle surface. A new band appears at 1459 cm<sup>-1</sup> that can be assigned to antisymmetric bending vibrations of the methyl groups. The narrow band at 1415 cm<sup>-1</sup> is assigned to the methylene scissoring CH<sub>2</sub>-S<sup>[9],[18]</sup>. The CH<sub>3</sub> symmetric bending vibration, also known as the umbrella mode, appears at 1374 cm<sup>-1</sup>. In the literature two relevant sets of bands are described in the region between 1000 and 1200 cm<sup>-1</sup>. The first set is assigned to C-C stretching modes,

commonly found between 950 and 1150  $\text{cm}^{-1}$ . The other important spectral features are two weak chain end-gauche defect bands, which involve the combination of either a methylene and methyl rock ( $\sim 1165 \text{ cm}^{-1}$ ) or a methylene wag and C-C stretch ( $\sim 1078 \text{ cm}^{-1}$ )<sup>[18]</sup>.

The IR spectra indicate the absence of free thiol molecules in the solution and suggest their attachment to the  $\text{CoPt}_3$  surface. Also they indicate the complete removal of the previous ligands (ACA and HDA).

#### 4.3. Indications for the formation of complexes during the ligand exchange procedure

$\text{CoPt}_3$  nanoparticle solutions change their colour from black to dark red during the ligand exchange. After this procedure the particles are precipitated and redissolved in chloroform using the washing procedure described in the Experimental part (Chapter 9.). The particle solution appears black after the washing procedure. Simultaneously the supernatant obtained after particle washing is red coloured. The red colour of the supernatant indicates the presence of complexes or clusters that are formed during the ligand exchange reaction. This colour does not originate from a rest of  $\text{Co}_2(\text{CO})_8$  after the synthesis. The colour of the supernatant obtained after particle synthesis contains a rest of  $\text{Co}_2(\text{CO})_8$  which is usually violet or in some cases blue, depending on the amount of oxygen. UV spectra were measured (Fig. 4.2.) in order to compare these two supernatant solutions (after synthesis and after ligand exchange).

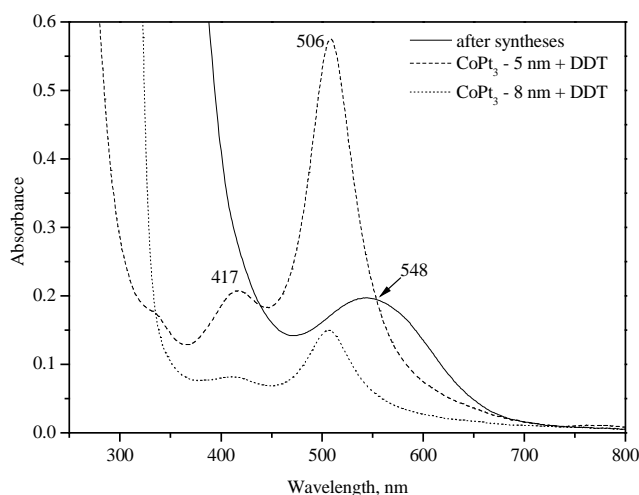


**Fig. 4.2.** Typical UV-vis spectra of the supernatants obtained after particle synthesis and after ligand exchange with DDT (for two different samples of particles)

The UV-vis spectrum of the supernatant obtained after particle synthesis shows only one peak. This spectrum is in agreement with the spectra measured in the case of Co clusters formation (probably  $\text{Co}_2$  and  $\text{Co}_3$ )<sup>[19]</sup>. The UV spectrum of the supernatant obtained after ligand exchange with DDT (Fig 4.2.) is different. It shows two peaks at lower wavelengths in comparison to the spectrum after synthesis. The peak positions do not change if the particle size changes. This indicates the formation of the same compound independent of the particle size. The UV spectra of the supernatants after ligand exchange are comparable to the UV spectra measured for a mixture of Co clusters and  $\text{Co}^{2+}$  - thiol complexes, both formed with DDT<sup>[20]</sup>. Therefore, it can be assumed that the formed complex is probably a complex between Co atoms and DDT.

Cobalt atoms have a tendency to form stable complexes with different ligands such as O-donor, N-donor and S-donor ligands, halides, etc.<sup>[21]-[24]</sup>. In order to check the tendency of Co to form complexes with DDT the following experiment was performed: a cobalt foil was placed in a glass vial with DDT and stored at room temperature. The reaction between the Co foil and DDT at room temperature starts after one day, and after a few days a dark red solution was obtained. The UV-vis spectrum of this solution was identical to the UV-vis spectrum of a supernatant after ligand exchange. All these results lead to the conclusion that Co clusters/complexes with DDT are formed during the ligand exchange. Nevertheless the reaction of Pt atoms and DDT during ligand exchange cannot be excluded, especially due to the fact that thiols are used as ligands for the synthesis of Pt nanoparticles<sup>[8],[9]</sup>.

In order to get a better understanding of the reaction between  $\text{CoPt}_3$  nanoparticles and DDT a detailed investigation was performed using samples with different particles sizes and different shapes. Three different sets of conditions were tested: a) reaction in nitrogen and at 90 °C, b) in air and 90 °C and c) in air and at room temperature. The samples were characterised by XRD, EDX and TEM.

#### 4.4. Influence of particle size and shape on ligand exchange between $\text{CoPt}_3$ nanoparticles and dodecanthiol

Three different, freshly prepared samples were used for the investigation. Two of them are composed of spherical particles with different sizes ( $\text{CoPt}_3$ -4,  $\text{CoPt}_3$ -8) and one of cubic shaped particles ( $\text{CoPt}_3$ -8-c). (The numbers in the sample names are the approximate values of the particle diameter. The letter c indicates cubic particles.)

The ligand exchange reaction was performed in the way described in the experimental part (Chapter 9.). All samples show a tendency to react with DDT independent of size and shape. The required time for a colour change from black to red is very short. In the case of the heated samples the colour changes usually before the final temperature of 90 °C has been reached.

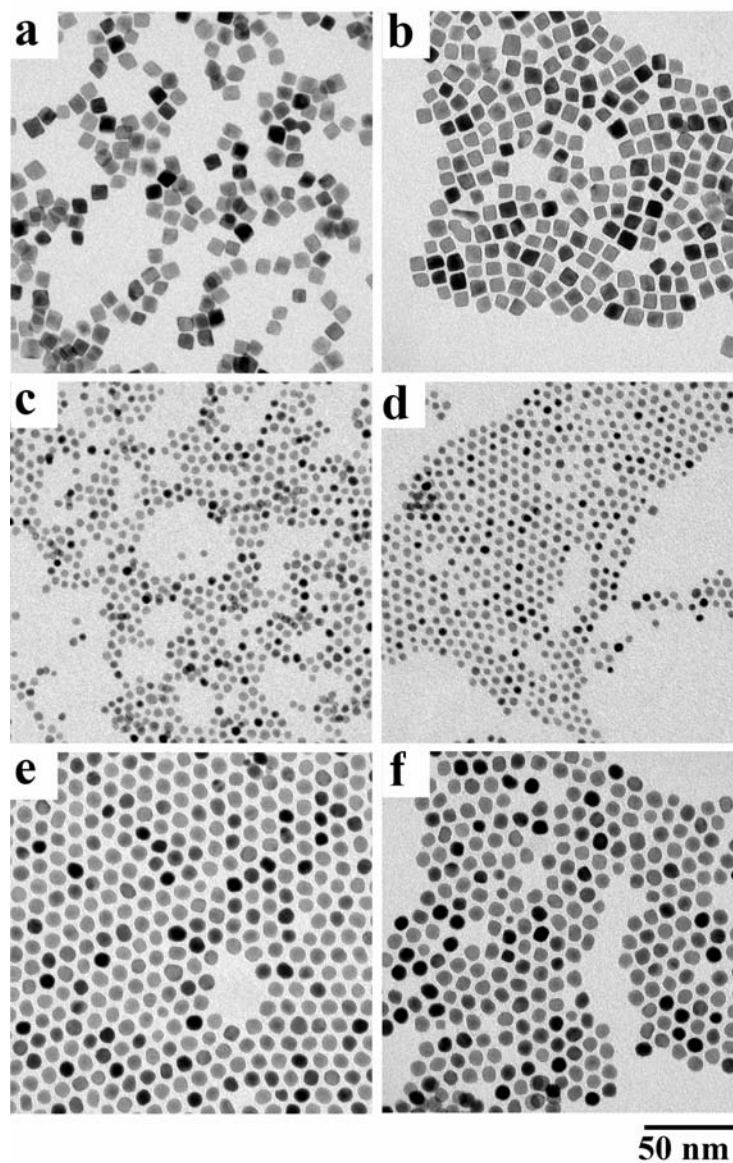


**Fig. 4.3.** TEM images of particles before (a - CoPt<sub>3</sub>-8c; c - CoPt<sub>3</sub>-4 and e - CoPt<sub>3</sub>-8) and after ligand exchange with DDT (b - CoPt<sub>3</sub>-8c, d - CoPt<sub>3</sub>-4 and f - CoPt<sub>3</sub>-8) performed in air at 90 °C, for 72 h.

The TEM images of the samples after ligand exchange (in air and with heating at 90 °C for 72 h) show good particle packing in hexagonal 2-D structures. The particles were

highly monodisperse before the ligand exchange and it is possible to notice changes after the ligand exchange (especially in the case of the bigger particles ( $\text{CoPt}_3\text{-8}$  and  $\text{CoPt}_3\text{-8-c}$ )). The investigation of the smaller particles ( $\text{CoPt}_3\text{-4}$ ) by TEM is not simple. The particles are already small and differences in particle size and shape before and after the ligand exchange cannot be easily distinguished.

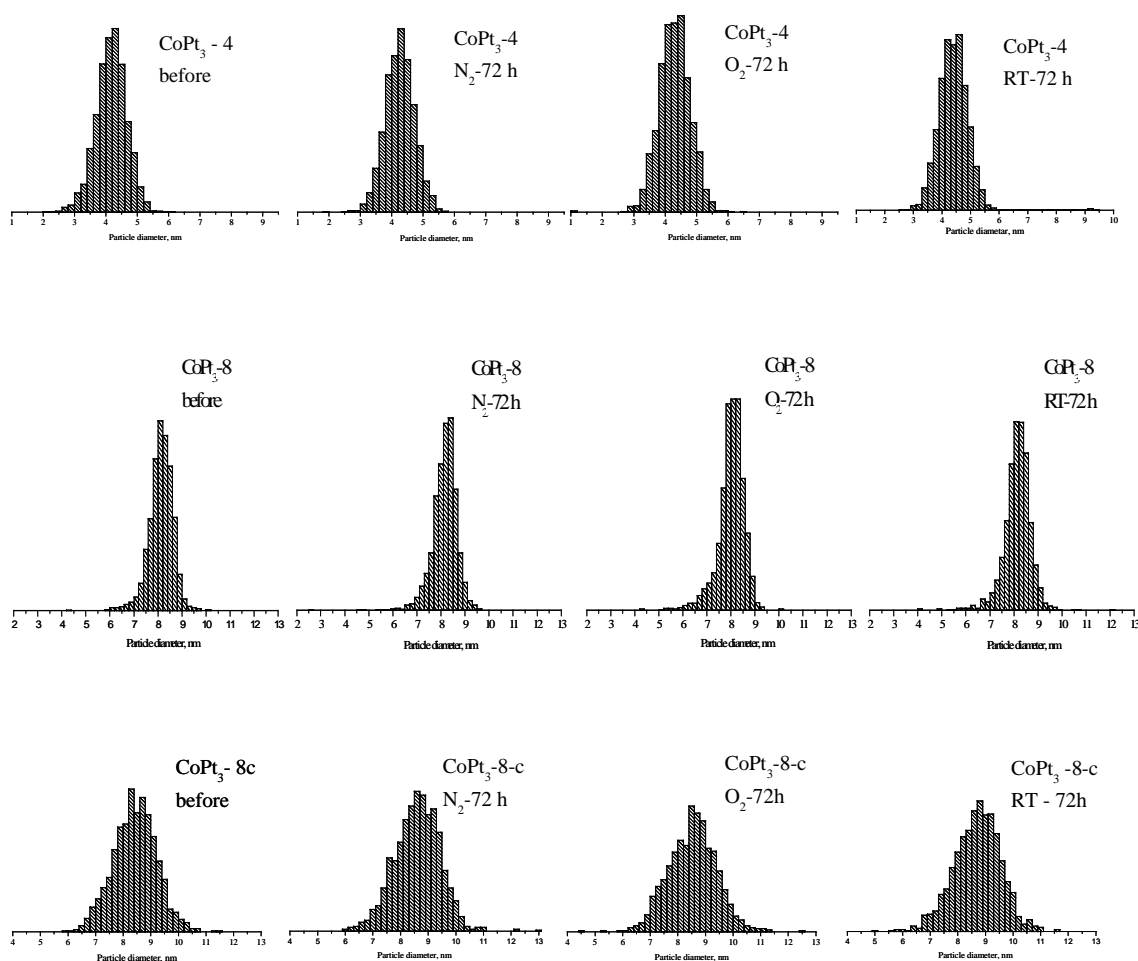


**Fig. 4.4.** Histograms for all three samples ( $\text{CoPt}_3\text{-4}$ ,  $\text{CoPt}_3\text{-8}$ ,  $\text{CoPt}_3\text{-8-c}$ ) before and after ligand exchange under different conditions. The samples were heated with DDT in nitrogen ( $\text{N}_2\text{-72h}$ ) and air ( $\text{O}_2\text{-7h}$ ) or kept at room temperature for 72 h ( $\text{RT-72h}$ ).

In order to have more reliable data of the particle sizes, histograms of the particle diameters were obtained. TEM images and the program *Image J* have been used for the histograms calculation. The histograms of all samples are shown in Figure 4.4. The particle diameter has been calculated from the project areas of the particles (A) on the images as  $d =$

$2(A/\pi)^{1/2}$ . The particle diameter has been defined as the diameter of a sphere equivalent to the cross-sectional area on the image (Table 4.1.). This should be taken into account especially in the interpretation of the histograms of the cubic particles. The described approximation leads in that case to higher deviations from the real value. The same procedure was applied to all samples before mixing with DDT and after 72 h.

Table 4.1. Summary of the results obtained for the average, minimal ( $d_{\min}$ ), and maximal particle diameter ( $d_{\max}$ ) and the standard deviation calculated using statistical analyses of the data shown in the histograms

Sample	Number of particles	Average diameter [nm]	Standard deviation [nm/%]	$d_{\min}$ [nm]	$d_{\max}$ [nm]
<b>CoPt<sub>3</sub>-4</b>					
before	2411	4.17	0.481/11.5	2.19	6.13
N <sub>2</sub> -72h	2945	4.25	0.462/10.9	1.85	5.71
RT-72h	1713	4.40	0.518/11.8	2.75	9.18
O <sub>2</sub> -72h	2152	4.30	0.494/11.5	1.18	6.42
<b>CoPt<sub>3</sub>-8</b>					
before	2221	8.12	0.497/6.1	4.30	10.19
N <sub>2</sub> -72h	1550	8.15	0.517/6.3	2.57	9.68
RT-72h	1550	8.13	0.581/7.1	4.12	12.20
O <sub>2</sub> -72h	1732	8.00	0.562/7.0	4.28	10.13
<b>CoPt<sub>3</sub>-8-c</b>					
before	1243	8.43	0.777/9.2	5.95	11.41
N <sub>2</sub> -72h	1400	8.61	0.822/9.5	5.93	12.90
RT-72h	1176	8.70	0.858/9.9	5.00	11.60
O <sub>2</sub> -72h	1213	8.53	0.865/10	4.56	12.58

The histograms of the small particles (CoPt<sub>3</sub>-4) show changes in the size distribution after all three applied procedures (Table 4.1.). The average particle diameter shifts slightly to higher values under all reaction conditions. In the case of samples prepared in air the standard deviation values increase in comparison to the values of the samples before the ligand exchange with DDT (Table 4.1.). The increase of the standard deviation indicates a broadening of the particle size distribution. This is also recognizable in the histograms. The broadest particle size distribution is observed for samples treated at room temperature for 72 h (RT-72h). The values for the minimum particle diameter indicate that the smaller particles are more dominant if the reaction mixture is heated at 90 °C (N<sub>2</sub>-72h and O<sub>2</sub>-72h).

The same analysis was applied to the bigger spherical particles (CoPt<sub>3</sub>-8). In all cases the standard deviation increases in comparison to the sample before the reaction. This result indicates broadening of the particle size distribution after ligand exchange. The broadest size distribution is again achieved for the sample prepared at room temperature. The shape of the histogram of the particles heated in air indicates a larger number of smaller particles in comparison to the other samples. Additionally the average particle diameter shifts to lower values in comparison to the sample before the reaction.

The cubic particles show a similar behaviour (Table 4.1.) as the spherical particles. The standard deviation is almost two times larger than in the case of the spherical particles with the same size. This observation can be caused not only by the particle size but also by the approximations taken for the particle diameter calculations. The broadening of particle size distribution is more pronounced than in the case of the spherical particles.

The results obtained by analysis of the histograms show an influence of the atmosphere and temperature on the particle diameter. Due to the reaction between the particle surface and DDT the shape and size of the particles change. The particle size distribution broadens. The experiments in different atmospheres show a more pronounced influence of air (oxygen) on the reaction in comparison to nitrogen. Sample heating in air leads to the formation of a larger amount of smaller particles. The formation of smaller particles observed after the reaction is probably a result of Co (and Pt) detaching from the nanoparticles surface. In this way the particles are “digested” by DDT during the reaction<sup>[25],[26],[27]</sup>. Some particles are not attacked by DDT while other are more or less dissolved. That leads to the formation of fractions with smaller particles in comparison to the samples before the reaction. Nevertheless more conclusions about the reaction mechanism are difficult to obtain only by analysis of the particle size and the TEM images. For this reason UV-vis measurements of all supernatants obtained after cleaning of the particles were done.

The supernatants of all samples were obtained by washing the samples (experimental part) after the ligand exchange reaction. Typical spectra of supernatants are shown in Fig. 4.5. Three aliquots were taken from the sample CoP<sub>3</sub>-8-c that was heated in air at 90 °C, at different reaction times (24h, 48h and 72 h). The shown spectra are obtained from the same amount of sample that was washed with a mixture of 2-propanol/acetone (experimental part – Chapter 9.).

The intensity of the absorption changes with time, suggesting an increase of the complex/cluster concentration in solution. This result suggests a continuous reaction. The reaction is stopped after 72 h. The continuous reaction indicates a continuous accessibility of

Co (and Pt) atoms for the reaction with thiol. One possible explanation is that thiols dissolve the Co and Pt atoms, leading to particles dissolution and disappearance. Simultaneously new clusters are formed and therefore complex concentration in the solution increased (detected by UV-vis).

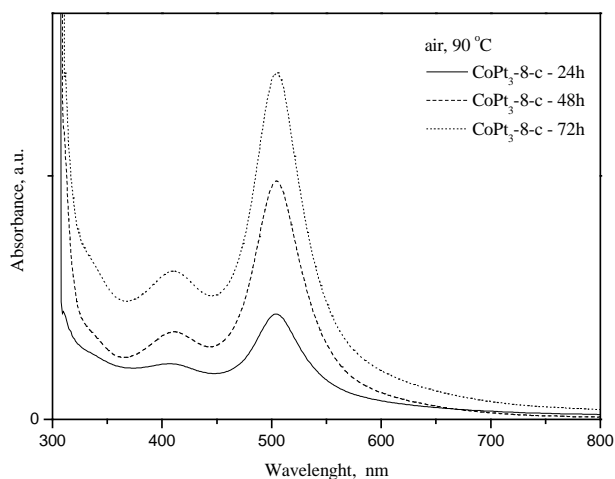


**Fig. 4.5.** UV-vis spectra of supernatants after ligand exchange with  $\text{CoPt}_3\text{-8-c}$  particles in air at  $90^\circ\text{C}$ , for 24 (solid line), 48 (dash line) and 72 h (dot line).

If the reaction takes only place between the Co atoms and the thiols the change of the Co concentration in the particles should influence the Co to Pt ratio in the samples. Therefore the Co to Pt ratio was determined by EDX (energy dispersive x-ray spectroscopy). The values for all samples are given in Table 4.2. Larger spherical particles show slightly different Co : Pt ratios before and after the reaction. Cubic particles show almost the same Co : Pt ratio before and after the ligand exchange. The difference between the Co : Pt ratio is only higher in the case of smaller spherical particles ( $\text{CoPt}_3\text{-4}$ ) and indicates a decrease of the cobalt concentration in the samples after the ligand exchange reaction (Table 4.2.). In this case the ratio of Co : Pt changes from 1:2 for the sample before the reaction, to 1 : ~3.7 for the samples after the reaction. This large difference in the Co : Pt ratio should be also detectable in the XRD diffractograms of the samples before and after the ligand exchange reaction. The different positions should change from the position for  $\text{CoPt}_3$  with a cubic lattice to the diffraction pattern characteristic for CoPt with a tetragonal lattice. Therefore, XRD measurements of all samples were performed and analysed in order to check and confirm the EDX data. Additionally XRD gives information about the whole sample concerning

changes in particle diameter after ligand exchange and also crystal lattice transformations. All XRD measurements were done in the range of  $2\Theta = 30-100^\circ$  (experimental part - Chapter 9).

Table 4.2. Percentage of Co and Pt (weight and atomic) and calculated ratio of Co:Pt for all samples (CoPt<sub>3</sub>-4, CoPt<sub>3</sub>-8, CoPt<sub>3</sub>-8-c) before and after ligand exchange for 72 h in different atmospheres and at different temperatures. Data were obtained by EDX.

Sample	Co(K), weight %	Pt(L), weight %	Co(K), atomic %	Pt(L), atomic %	Ratio Co:Pt
CoPt <sub>3</sub> -4					
before	11.9	88.1	30.8	69.2	1: 2.2
N <sub>2</sub> -72h	7.6	92.4	21.4	78.6	1: 3.7
RT-72h	7.1	92.9	20.2	79.8	1: 3.9
O <sub>2</sub> -72h	7.8	92.2	21.8	78.2	1: 3.6
CoPt <sub>3</sub> -8					
before	9.0	91.0	24.8	75.2	1: 3.0
N <sub>2</sub> -72h	8.4	91.6	23.4	76.6	1: 3.3
RT-72h	8.2	91.8	22.9	77.1	1: 3.4
O <sub>2</sub> -72h	9.8	90.2	26.4	73.6	1: 2.8
CoPt <sub>3</sub> -8-c					
N <sub>2</sub> -72h	12.0	88.0	31.2	68.8	1: 2.2
RT-72h	13.6	86.4	34.3	65.7	1: 1.9
O <sub>2</sub> -72h	12.1	87.9	31.2	68.8	1: 2.2

The XRD diffractograms of spherical particles (CoPt<sub>3</sub>-8 and CoPt<sub>3</sub>-4) show almost the same peak positions before and after the reaction (Fig. 4.6.a). The reflex positions are compared to the reflex positions of CoPt<sub>3</sub> (cubic lattice) and CoPt (tetragonal lattice). In the case of smaller spherical particles the reflex positions are almost the same as the reflex positions of CoPt<sub>3</sub> bulk<sup>[28]</sup>. This results does not agree with the values obtained by EDX measurements of the CoPt<sub>3</sub>-4 particles before ligand exchange (Co : Pt = 1 : 2.2, Table 4.2.). One possible explanation is that during the reaction all particles do not react in the same way. This can lead to different Co : Pt ratios in different parts of the sample. Especially the EDX measurements can be influenced because this technique can only take into account small sample areas. In contrast XRD measurements give an average value for the whole sample.

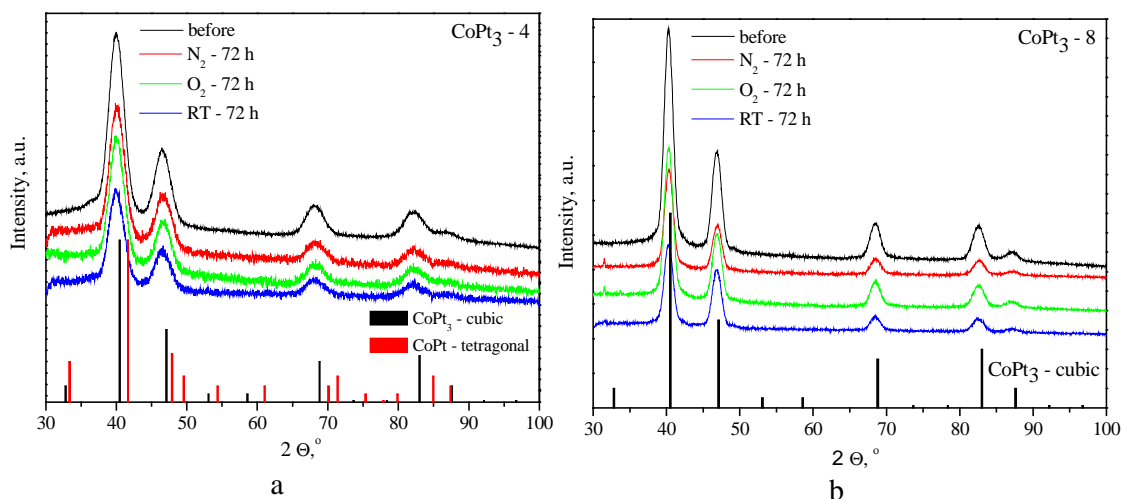


**Fig. 4.6.** XRD diffractograms of samples before (black line) and after ligand exchange for 72h (in  $N_2$  at  $90^\circ C$  - red line, in air at  $90^\circ C$  - green line, in air at room temperature - blue line). a) Sample  $CoPt_3-4$ . b) Sample  $CoPt_3-8$ . The peak positions of the cubic lattice of  $CoPt_3$  and the tetragonal lattice of  $CoPt$  are given as thin vertical lines (black and red, respectively).

Larger spherical particles also do not show a significant change in the reflex positions before and after the reaction (Fig 4.6. b).

In general XRD measurements give also information about the average particle diameter. The particle diameters are calculated from two reflections ((111) and (200) ( $2\Theta \approx 40$  and  $47^\circ$ , respectively)). They are fitted to a combined profile consisting of Gaussian and Lorentzian functions using a linear background function. Diameters are calculated from the width of the Bragg reflections according to the Scherrer formula. (Detailed information are given in the Appendix). The Scherrer formula is used with a form factor of  $K = 1$  to give a rough estimation of the particle size. For more precise calculations the equation should be adapted to the geometrical properties of the sample. In this study we used an equation that already provided good results for  $CoPt_3$  spherical particles<sup>[29]</sup>:

$$d = \frac{4}{3} \frac{0.9\lambda}{\omega \cos \Theta}$$

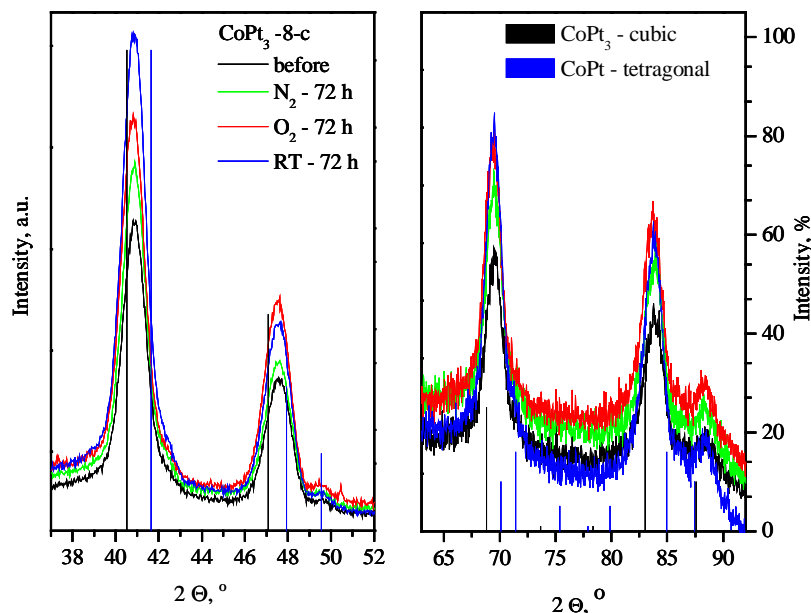
where  $d$  is the particle diameter,  $\lambda$  is the wavelength of the X-radiation,  $\omega$  is the peak width at half maximum and  $\Theta$  is the Bragg angle. The diameters of the particles for both samples ( $CoPt_3-8$  and  $CoPt_3-4$ ) are calculated using this equation and they are given in Table 4.3.

Table 4.3. Average particle diameters for all samples before and after ligand exchange for 24, 48 and 72 h in different conditions. All diameters are calculated by using two reflections (111) (angle ~ 40.0°) and (200) (angle ~ 46.5°).

Sample	2 $\theta$	Particle diameter [nm], after			
		0 h*	24 h	48 h	72 h
CoPt <sub>3</sub> -4 – N <sub>2</sub>					
(111)	40.02	4.33	4.82	4.22	4.22
(200)	46.57	4.21	4.80	4.32	4.32
Average			4.81	4.27	4.27
CoPt <sub>3</sub> -4 – O <sub>2</sub>					
(111)	40.02	4.33	4.56	4.44	4.44
(200)	46.54	4.31	4.80	4.54	4.80
Average			4.68	4.49	4.62
CoPt <sub>3</sub> -4 – RT					
(111)	40.02	4.33	4.33	4.22	4.44
(200)	46.54	4.31	4.31	4.31	4.66
Average		4.30	4.32	4.27	4.55
CoPt <sub>3</sub> -8 – N <sub>2</sub>					
(111)	40.29	8.05	8.05	8.46	8.03
(200)	46.87	7.55	7.81	7.51	7.81
Average			7.93	7.99	7.92
CoPt <sub>3</sub> -8 – O <sub>2</sub>					
(111)	40.29	7.69	8.04	7.69	8.04
(200)	46.87	7.85	7.65	7.85	7.90
Average			7.85	7.77	7.97
CoPt <sub>3</sub> -8 – RT					
(111)	40.29	8.05	7.34	7.69	7.67
(200)	46.87	7.48	7.85	8.27	7.85
Average		7.78	7.60	7.98	7.76

\* Average values for samples before the reaction are calculated from all measured samples

The average particle diameter of sample CoPt<sub>3</sub>-4 calculated from the XRD measurements is in good agreement with the average diameter obtained from the histograms. For larger particles the XRD measurements lead to slightly lower values. A reason for this result can be a lower crystallinity of the particles or a texture effect. Both of them can cause differences in the width of the reflex at half maximum. In addition the standard deviation is higher for larger particles than for smaller once. However, a trend cannot be noticed and more information cannot be extracted from this data.



**Fig. 4.7.** XRD diffractograms of sample  $\text{CoPt}_3\text{-8-c}$  before (black line) and after ligand exchange for 72h (in  $\text{N}_2$  at  $90^\circ\text{C}$  - red line, in air at  $90^\circ\text{C}$  - green line, in air at room temperature - blue line). Reflexes at lower angles (left hand side) and higher angles (right hand side) are shown. Reflex positions for the  $\text{CoPt}_3$  cubic lattice and for the  $\text{CoPt}$  tetragonal lattice are given as thin vertical lines (black and blue, respectively)

Cubic  $\text{CoPt}_3$  particles ( $\text{CoPt}_3\text{-8-c}$ ) were investigated in the same way as spherical particles. The different Co to Pt ratio of cubic particles in comparison to spherical once is confirmed by EDX and by XRD measurements. The XRD reflexes show a slight shift to Co-rich alloys. Additionally small peaks appear at positions that are characteristic for a  $\text{CoPt}$  tetragonal lattice at  $49.5^\circ$  (Fig. 4.7.). The EDX also shows that the ratio is close to 1:2.

XRD and EDX show almost no change after the reaction of the cubic particles with DDT. This is in opposition to the results of the TEM images analysis that show significant changes in the particle shape and size. In order to check the reproducibility of the results achieved for cubic particles one more sample was prepared. The particle size was almost the same (around 8 nm) as for the previous sample. The sample was heated at  $90^\circ\text{C}$  for 96 h in nitrogen. An intensive red-coloured supernatant is formed during the reaction. Samples are taken after 24, 48 and 96 h. They were analysed by EDX, XRD and TEM measurements. The EDX shows a Co to Pt ratio of 1:2 as for the previous sample and very small changes after the reaction. The XRD analysis shows that the peak positions are closer to a tetragonal  $\text{CoPt}$

structure, but the particle diameter does not change. The only obvious difference between the sample before and after the reaction was again noticed in the TEM images (Figure 4.8.).

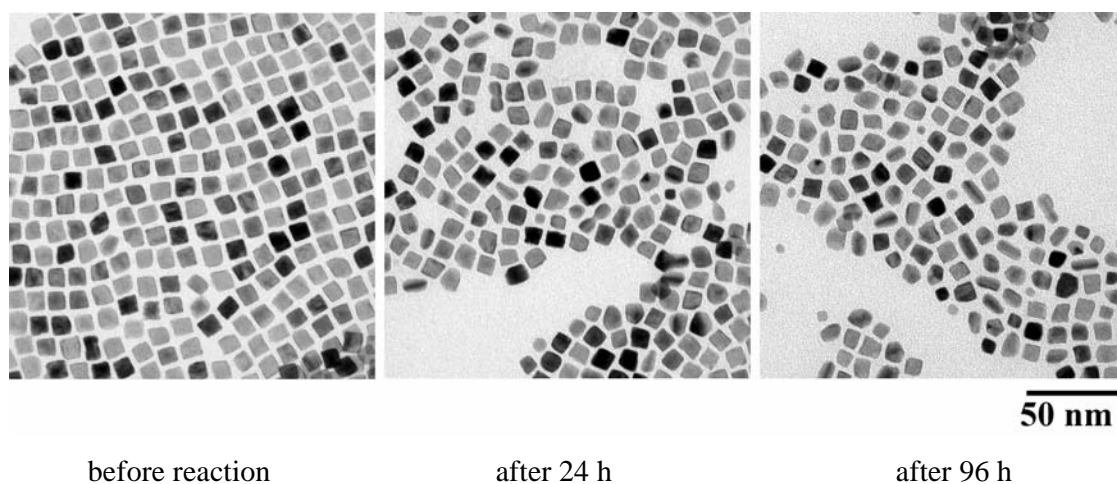


**Fig. 4.8.** TEM images of cubic particles before and after heating with DDT in  $N_2$  for 24 and 96 h

The TEM images show that the particles drastically change during the reaction with DDT. Some of them are almost completely dissolved. The influence of DDT on the particles and the formation of a red coloured complex are noticed once more, but it was not possible to detect changes in the Co to Pt ratio using EDX or in diameter size using XRD.

The small changes in the Co : Pt ratio and in the peak positions in the XRD diffractograms lead to the conclusion that probably DDT reacts with both elements Co and Pt at the same time and leads to particle dissolving. The difference between the particle size and shape recognised in the TEM images suggests that not all particles react in the same way. Some of them are more stable and do not change the shape during the reaction, while others are getting drastically smaller. An explanation could be differences in the particle stability. Probably particles with lattice defects are less stable and more amenable to a reaction with DDT. Particles without defects do not react so easily with DDT, and they keep the shape and the size during the reaction.

If this theory is correct cubic particles are less stable than spherical once and they react more intensively. This leads to drastic changes in the particle shape and to the dissolution of the particles.

#### 4.5. Conclusion

The presented results show that the interactions between CoPt<sub>3</sub> nanoparticles and DDT are very strong and lead to the formation of complexes and/or clusters. The reaction occurs at higher temperatures (90 °C) as well as at room temperature, and in air or nitrogen. The particles self-assemble in 2-D structures even after the ligand exchange. After the reaction the difference in the Co : Pt ratio is not pronounced (despite obvious reaction between CoPt<sub>3</sub> nanoparticles and thiols). Different Co to Pt ratios, lattice structures and different numbers of lattice defects in the particles before the reaction can cause the different behaviour of the particles. Probably particles with more lattice defects and with a higher content of Co start to react faster and dissolve faster. Therefore cubic particles with Co : Pt ratio of 1:2 are less stable than spherical ones with a different crystal lattice and a different Co : Pt ratio (1:3).

These investigations open a lot of questions concerning the reaction between thiols and CoPt<sub>3</sub> nanoparticles. A more detailed analysis and application of additional techniques for the investigation are necessary in order to explain the reaction mechanism.

#### 4.6. Literature:

1. Terrill, R.H., et al., *Monolayers in Three Dimensions: NMR, SAXS, Thermal, and Electron Hopping Studies of Alkanethiol Stabilized Gold Clusters*. J. Am. Chem. Soc., 1995. **117**: p. 12537-12548.
2. Woehrle, G.H., M.G. Warner, and J.E. Hutchison, *Ligand Exchange Reactions Yield Subnanometer, Thiol-Stabilized Gold Particles with Defined Optical Transitions*. J. Phys. Chem. B, 2002. **106**: p. 9979-9981.
3. Woehrle, G.H., L.O. Brown, and J.E. Hutchison, *Thiol-Functionalized, 1.5-nm Gold Nanoparticles through Ligand Exchange Reactions: Scope and Mechanism of Ligand Exchange*. J. Am. Chem. Soc., 2005. **127**: p. 2172-2183.
4. Warner, M.G., S.M. Reed, and J.E. Hutchison, *Small, Water-Soluble, Ligand-Stabilized Gold Nanoparticles Synthesized by Interfacial Ligand Exchange Reactions*. Chem. Mater., 2000. **12**: p. 3316-3320.
5. Chechik, V., J. Am. Chem. Soc., 2005.
6. Hostetler, M.J., R.W. Murray, and A.C. Templeton, Langmuir, 1999. **15**: p. 3782-3789.
7. Murayama, H., et al., *Structures and Stabilities of Alkanethiolate Monolayers on Palladium Clusters As Studied by Gel Permeation Chromatography*. J. Phys. Chem. B, 2004. **108**: p. 3496-3503.
8. Eklund, S.E. and D.E. Cliffler, *Synthesis and Catalytic Properties of Soluble Platinum Nanoparticles Protected by Thiol Monolayer*. Langmuir, 2004. **20**: p. 6012-6018.
9. Yee, C., et al., *Self-Assembled Monolayers of Alkanesulfonic and -phosphonic Acids on Amorphous Iron Oxide Nanoparticles*. Langmuir, 1999. **15**: p. 7111-7115.

10. Kataby, G., et al., *Self-Assembled Monolayer Coatings on Amorphous Iron and Iron Oxide Nanoparticles: Thermal Stability and Chemical Reactivity Studies*. Langmuir, 1997. **13**: p. 6151-6158.
11. Tsuruoka, T., K. Akamatsu, and H. Nawafune, *Synthesis, Surface Modification, and Multilayer Construction of Mixed-Monolayer-Protected CdS Nanoparticles*. Langmuir, 2004. **20**: p. 11169-11174.
12. Choo, H., E. Cutler, and Y.S. Shon, *Synthesis of Mixed Monolayer-Protected Gold Clusters from Thiol Mixtures: Variation in the Tail Group, Chain Length, and Solvent*. Langmuir, 2003. **19**: p. 8555-8559.
13. Shen, Y.J., Y.L. Lee, and Y.M. Yang, *Monolayer Behaviour and Langmuir-Blodgett Manipulation of CdS Quantum Dots*. J. Phys. Chem. B, 2006. **110**(19): p. 9556-9564.
14. Supriya, L. and R.O. Claus, *Colloidal Au/Linker Molecule Multilayer Films: Low - Temperature Thermal Coalescence and Resistance Changes*. Chem. Mater., 2005. **17**: p. 4325-4334.
15. Shevchenko, E.V., *Monodisperse magnetic alloy nanocrystals and their superstructures*, in *Institute for Physical chemistry*. 2003, University Hamburg: Hamburg.
16. Porter, M., et al., J. Am. Chem. Soc., 1987. **109**: p. 3559-3568.
17. Sandhyarani, N., et al., J. Chem. Phys., 2000. **114**(21): p. 9794-9803.
18. Hostetler, M.J., J.J. Stokes, and R.W. Murray, Langmuir, 1996. **12**: p. 3604-3612.
19. Samia, A.C.S., et al., *Ligand Effect on the Growth and the Digestion of Co Nanocrystals*. J. Am. Chem. Soc., 2005. **127**: p. 4126-4127.
20. Marin-Almazo, M., et al., *Cobalt-Based Superparamagnetic Nanorings*. Nano Letters, 2004. **4**(8): p. 1365-1371.
21. Greenwood, N.N. and A. Earnshaw, *Chemistry of the Elements*, ed. Elsevier. 1998, Oxford: Butterworth-Heinemann.
22. Wang, W., et al., *New Thiolate-Cobalt(II) Complexes for Catalytic Chain Transfer Polymerization of Methyl Methacrylate*. Macromolecules, 2004. **37**: p. 6667-6669.
23. Sisley, M.J., M.J. Ferguson, and R.B. Jordan, *Reaction of Thiols with N-Bonded Sulfenamide Complexes of Cobalt(III): Steric Effect and Reaction Pathway*. Inorganic Chemistry, 2005. **44**: p. 293-299.
24. Anand, V.D., G.S. Deshmukh, and C.M. Pandey, *Spectrophotometric Determination of Cobalt with Thioglycolic Acid*. Analytical Chemistry, 1961. **33**(13): p. 1933-1937.
25. Lin, X.M., C.M. Sorensen, and K.J. Klabunde, *Digestive ripening, nanophase segregation and superlattice formation in gold nanocrystal colloids*. Journal of Nanoparticle Research, 2000. **2**: p. 157-164.
26. Prasad, B.L.V., et al., *Digestive Ripening of Thiolated Gold Nanoparticles: The effect of Alkyl Chain Length*. Langmuir, 2002. **18**: p. 7515-7520.
27. Prasad, B.L.V., et al., *Digestive-Ripening Agents for Gold Nanoparticles: Alternatives to Thiols*. Chem. Mater., 2003. **15**: p. 935-942.
28. Shevchenko, E.V., et al., J. Am. Chem. Soc., 2002. **124**: p. 11480-.
29. Borchert, H., et al., *Determination of Nanocrystal Sizes: A Comparison of TEM, SAXS, and XRD Studies of Highly Monodisperse CoPt<sub>3</sub> Particles*. Langmuir, 2005. **21**(5): p. 1931-1936.
30. Akamatsu, K., T. Tsuruoka, and H. Nawafune, *Band Gap Engineering of CdTe Nanocrystals through Chemical Surface Modification*. J. Am. Chem. Soc., 2005.

# **Film preparation**

## Chapter 5

### Spin coating

---

#### 5.1. Introduction

The preparation and investigation of ordered arrays of nanoparticles has attracted an increasing interest during the last years due to their wide range of potential applications e.g. in opto-electronics, magnetic storage devices and catalysis<sup>[1]</sup>. Therefore, the concept of well-ordered, multi-dimensional structures that cover large areas prepared from colloidal dispersions of nanoparticles is very promising. Naturally, one of the key issues is the reliable synthesis of nanoparticles of tunable dimensions. This is already achieved in the case of CoPt<sub>3</sub> nanoparticles<sup>[2]</sup>. A second major aspect of the film preparation comprises the controlled deposition and arrangement of the nanoparticles on the substrate. Very often ligands around nanoparticles influence the surface chemistry of the particles and determinate the particles packing. Therefore stabilization of particles with different ligands can change chemical properties of the particle surface and influence on their packing<sup>[3],[4]</sup>. Additionally, the use of polymeric buffer layers, “surface modifiers”, can modify the particle-substrate interaction<sup>[5]-[9]</sup>. Usually the used polymers have specific functional groups that provide interaction to nanoparticles, e.g. thiol, pyridyl, amino and carboxy group. High numbers of specific groups in polymer layers make the polymers efficient adhesives. Interactions between particles and polymers can be electrostatic, hydrogen bonding, charge-transfer, and other. Beside the interactions one also very important factor is to produce smooth polymer surfaces as a good underground for particle deposition.

In this chapter, the focus will be on the application of the spin-coating technique in order to prepare ultra-thin films of CoPt<sub>3</sub> nanoparticles. Special emphasis will be put on the study of the influence of polymeric surface modifiers on both, the nanoscopic particle arrangement as well as the large-scale film morphology. In particular, the effect of the functional amino and pyridyl groups on the mesoscopic over layer structure was investigated as a function of the polymer type, the buffer layer thickness, and the rotation speed. Techniques that were used for investigations are: Grazing-Incidence Small Angle X-ray

Scattering (GISAXS), Scanning Electron Microscopy (SEM) and Atomic Force Microscopy (AFM).

The influence of pyridyl groups was investigated by using poly (2-vinyl pyridine), P2VP, and poly (4-vinyl pyridine), P4VP, as buffer layers. Poly (vinyl pyridine)s (P2VP and P4VP) are already known as attractive polymers for the immobilization of nanoparticles due to the strong affinity of pyridyl groups to metals and their ability to undergo hydrogen bonding with polar species<sup>[5],[10]</sup>. From literature it is known that after deposition and adsorption on wafers, PVP molecules still have numerous unbound pyridine groups that do not participate in the interaction with the surface and that are capable of binding of nanoparticles<sup>[5]</sup>. Therefore PVP-s were successfully used as a buffer layers for deposition of silver<sup>[5],[6]</sup>, and gold<sup>[7],[8],[9]</sup> nanoparticles. Additionally, the UV cross-linked P4VP films acted as reversibly responsive coatings that controlled the surface wettability and the swelling toward external stimuli, solvent and pH<sup>[11]</sup>, which can broaden the application field. The interactions between the nanoparticles and PVP polymers also enable the use of the block-copolymers, which can be used as a matrix for guided self-assembly of nanoparticles. Previously such polymers were used in a combination with gold nanoparticles<sup>[9],[12]</sup>, cobalt nanoparticles<sup>[13]</sup>, and very recently for CdSe quantum dots<sup>[14]</sup>.

A second group of polymers based on poly (ethylene oxide), PEO, terminated with one or two amino groups were chosen in order to investigate the influence of amino groups on the attachment of nanoparticles. It was found that this polymer readily attaches to the surface of CoPt<sub>3</sub> nanoparticles due to the amino groups (see Chapter 3.). Therefore, the ability of these polymers as substrate modifiers was investigated, in other words the presence of amino groups at the end of polymer chains is sufficient to improve the packing and covering of the silicon wafers with CoPt<sub>3</sub> nanoparticles.

## 5.2. Spin coating: procedure and theory

Spin coating is used for many applications where relatively flat substrates or objects are coated with thin layers of material. This is a simple technique that can lead to very uniform films of well-controlled thickness over a large area ( $\varnothing \geq 30\text{cm}$ ). The typical spin coating procedure involves deposition of material onto the centre of a substrate and spinning the substrate at high speed. Material must be previously dissolved or dispersed in a proper solvent. During the spinning centripetal acceleration will cause the solution to spread to and eventually off the edge of the substrate leaving a uniform layer.

Some technologies that depend heavily on high quality spin coated layers are:

- Photoresist for defining patterns in microcircuit fabrication.
- Magnetic disk coatings - magnetic particle suspensions, head lubricants, etc.
- Flat screen display coatings - antireflection coatings, conductive oxide, etc.
- Compact Disks – DVD, CD ROM, etc.
- Television tube phosphor and antireflection coatings.

The spin coating technique is fast, simple and industrial applicable. As already mentioned, this technique is by now used for the production of magnetic disk coatings and compact disks. Hence, it is really important to investigate the possibilities for applying this technique on CoPt<sub>3</sub> nanoparticle deposition on different substrates.

From literature it is known that parameters that influence on the final film thickness and other film properties are contingent on the used material (viscosity, drying rate, percent solids, surface tension, etc.) and the parameters chosen for the spin process (rotational speed, acceleration and drying procedure).

The selection of solvents was narrowed by the solubility of CoPt<sub>3</sub> nanoparticles. The particles are soluble in only few types of solvents (chloroform, toluene, and hexane). Toluene as a solvent with higher boiling point, surface tension and viscosity than the other two solvents, and as a very good solvent for the particles (the particle solutions in a very broad scope of concentrations stay stable over months) was chosen for preparing the particle solutions. Concentrations used for the film preparation during the investigations were small (less than 2 mass % of the particles) and one can say that viscosity, drying rate and surface tension of the particle solution were approximately the same as for toluene. The only parameter, which was possible to be changed, concerning the used material, was the concentration i.e. percentage of the nanoparticles. Therefore the only possibility to influence the film quality is by changing the parameters for the spin process in order to find the best for the CoPt<sub>3</sub> film preparation. As good parameters for the spin process one can consider the parameters that lead to production of large substrate areas covered with a well-organised particle monolayer.

One should always have in mind that one of the most important factors in spin coating is reproducibility. It is already known that slight variations in the parameters during the spin process can result in drastic variations of the obtained film. The experiments were done in the way to keep as much parameters constant as possible.

For better understanding of the spin coating procedure the main process phases and theory behind them will be described and considered. During the spin coating process, four different stages can be distinguished:

- 1) Deposition;
- 2) Acceleration;
- 3) Spinning at a constant rate where the fluid viscosity dominates the fluid thinning behaviour;
- 4) Spinning at a constant rate where the solvent evaporation dominates the film thinning behaviour.

### 1) Deposition

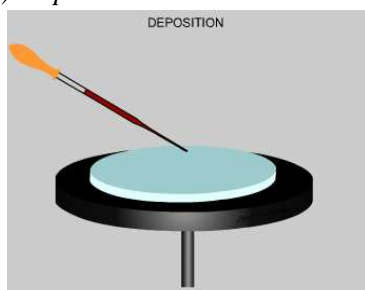


**Fig. 5.1.** Scheme of the deposition phase during spin coating

The first phase is the deposition of a material solution onto the wafer or substrate (Figure 5.1.). It can be done by using a nozzle, or it can be sprayed onto the surface etc. Two things are very important in this phase: a) to provide the necessary amount of solution onto the wafer; b) the surface wettability with the used solvent. Both of these will result in a complete coverage of the wafer.

To prevent from incomplete coverage all experiments described in this chapter were done by deposition of an excess of solution on the wafers. Typically the used volume was 50  $\mu\text{l}$  if the wafers were 8 x 8 mm large, increasing the volume for bigger wafer surfaces. In all cases, the deposited volume was enough to cover the full wafer. Wafers used in the experiments had a good wettability by toluene. Also all solutions were filtrated before deposition to eliminate aggregates that could lead to flaws.

### 2) Acceleration

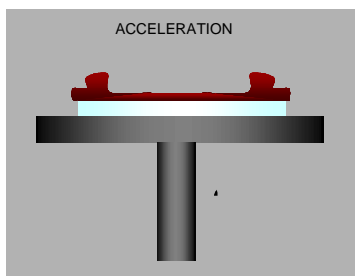


**Fig. 5.2.** Scheme of acceleration phase during spin coating

After the deposition phase, the next step is to accelerate the substrate up to its final, desired, rotational speed. During this phase a large amount of the solution will be removed from the substrate by the centripetal force. Moreover in some processes up to 50% of the solvent can be evaporated in the first few seconds.

The possible fluid profile during this process is shown schematically in Figure 5.2. Because of the initial depth of

fluid on the wafer surface, spiral vortices may briefly be present during this stage. This form is a result of the twisting motion caused by the inertia that the top of the fluid layer exerts while the wafer below rotates faster and faster<sup>[15]</sup>. Finally, the fluid is thin enough to be completely co-rotating with the wafer.

Investigations showed that better results were obtained with a very short acceleration phase (1 s), using the maximal possible speed in this phase. Longer acceleration periods and lower speed lead to the production of non-uniform and multilayered particle films on the silicon surface.

### 3) *Spinning at a constant rate where the fluid viscosity dominates the fluid thinning behaviour*

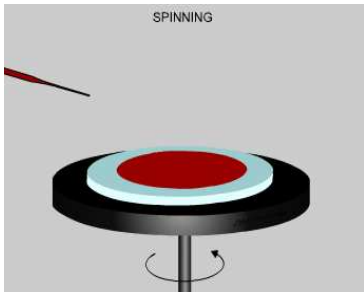


**Fig. 5.3.** *Scheme of spinning during spin coating*

Relatively high speeds (from 1000 – 6000 rpm) can be used in this phase to thin the fluid to the final thickness. This step can take from few seconds to several minutes. The combination of the rotation speed and time will define the final film thickness (Fig. 5.3.). In general, higher rotation speeds and longer spinning time lead to the formation of a thinner film. This stage is characterised by gradual fluid thinning. If the liquid exhibits Newtonian viscosity and if

the fluid thickness is initially uniform across the wafer, the fluid thickness profile will also be uniform at any time, leading to a uniform final coating<sup>[15],[16]</sup>.

### 4) *Spinning at a constant rate where the solvent evaporation dominates the film thinning behaviour*

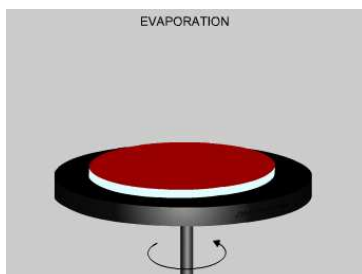


**Fig. 5.4.** *Scheme of evaporation phase during spin coating*

In this phase the film thickness is not changing, or it is changing negligible due to the substrate spinning (Fig. 5.4.). The main influence in this phase has the solvent evaporation. Due to the solvent evaporation the viscosity of the fluid increases. Therefore, the rotation speed is not strong enough to remove the fluid from the surface and to thinner the film in this way. All further changes of the film thickness are only the effect of the evaporation process. The slower

rate of drying offers the advantage of increased film thickness uniformity across the substrates.

The two phases (3 and 4) must be occurring simultaneously during all spin coating procedures.

From the previous explanations it is obvious that the rotation speed is one of the most important factors in spin coating. Therefore the rotation speed has been investigated in the range from 1000-5000 rpm. The spinning time in all experiments was 30 s. During that period of time, the final film thickness was reached and the films had enough time to dry, because the low concentrated solutions, in volatile solvents, were used.

Modelling of the spin coating process is complex due to the many involved mechanisms. The first authors who described the spin coating procedure, were Emslie, Bonner and Peck<sup>[17]</sup>. They assumed a Newtonian behaviour of the fluid and they also made a model with a lot of approximations. Later more complicated models appeared, which described the experimental data better. The new models assume non-Newtonian behaviour taking into account the influence of an evaporation process during the spin coating procedure<sup>[18]</sup>. Other authors described in detail the spin coating of colloidal suspensions<sup>[19]</sup>.

### 5.3. Influence of the concentration and speed on wafer covering

Four different concentrations were used in order to investigate how the nanoparticle concentration influences on the substrate covering. The particles from one synthesis (same quality and size distribution of the particles) were dissolved in toluene and spin coated on the previously cleaned silicon wafers. The cleaning procedure of the silicon wafers and the preparation of the particle solution, as well as the used program for the spin coating, are described in more details in the Experimental part – Chapter 9.

The first issue was optimisation of the particle concentration. To investigate the influence of the particle concentration several solutions were prepared and used for the spin coating. The quality of the films was investigated by SEM technique. From the SEM images of the prepared samples it is obvious that the nanoparticle concentration has a huge influence on the film quality and degree of covering. Lower concentrations lead to formation of a smaller number of bigger islands or a bigger number of smaller particle islands on the silicon surface depending on the concentration, 0.45 mass % or 0.9 mass %, respectively (Fig. 5.5). The more concentrated solutions lead to particle packing in some kind of network (1.2 mass %) or with enough particles it is possible to cover larger areas of the wafer (1.8 mass %) as can be seen in Figure 5.5. The most important fact is that in all samples the particles are packing in a dense hexagonal lattice and only as a monolayer.

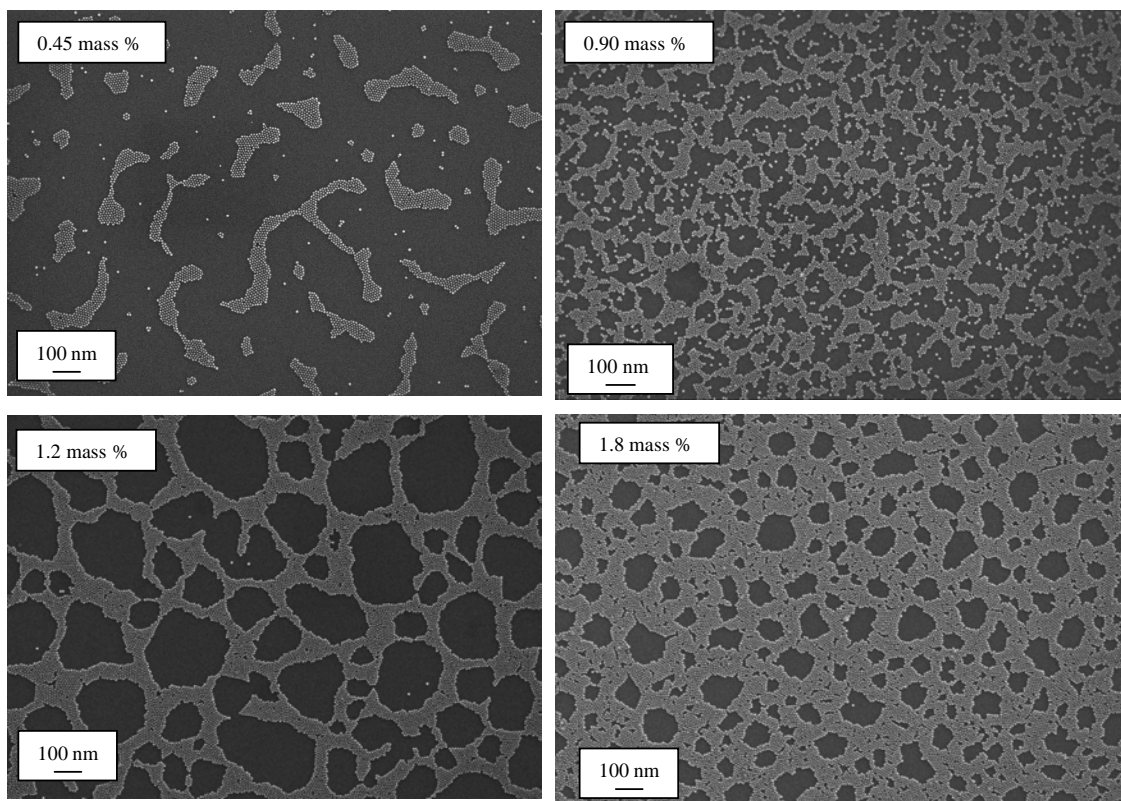


**Fig. 5.5.** SEM micrographs of the samples prepared on silicon oxide by deposition of  $\text{CoPt}_3$  nanoparticles from toluene solutions with different concentration 0.45, 0.90, 1.2 and 1.8 mass % by rotation speed of 3000 rpm

Further investigations show that different solutions with particle concentrations higher than 1.5 mass % provide close packed monolayer films with a high percentage of covering. The more concentrated solutions give nearly 100 % covering of the wafer but in the same time it is not possible to avoid multilayer structures. Areas covered with the particles packed in multilayers are different from sample to sample and it is difficult to control their size.

The same particle solution, concentration 1.8 mass %, was used to investigate the influence of the speed during the spinning on the film quality. Three different speeds were used: 1000, 2000 and 3000 rpm. A three-step program was used for all three different speeds (more details in the experimental part - Chapter 9). The first phase in the program is when the substrate is accelerated up to its final, desired, rotation speed. In all cases the required time to achieve the desired speed was 1s. In the case of 1000 rpm the same speed was set in this phase, and in the two other experiments the required corresponding speeds. The sample prepared with the speed 1000 rpm was non-uniform and the particles were packed in

multilayers that were recognizable by naked eye (by different colours on the wafer). Therefore this sample was not further investigated. The samples prepared with the speed 2000 and 3000 rpm were investigated by SEM (Figure 5.6.) and in both cases the particles are packed in a dense hexagonal lattice and only as monolayers. The main difference between these two samples was in the percentage of covering. Using the speed of 2000 rpm leads to less covered wafers than using the speed of 3000 rpm. More than one sample was made using these two speeds and the reproducibility of the film quality was rather satisfying.

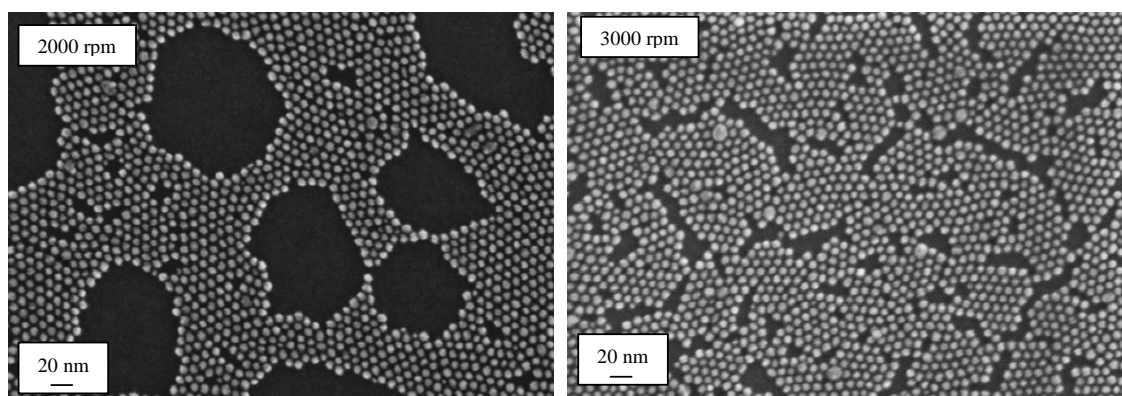


**Fig. 5.6.** SEM micrographs of the samples prepared on silicon oxide from 1.8 mass % solution of  $\text{CoPt}_3$  nanoparticles in toluene using different rotation speeds, 2000 and 3000 rpm

Further increase of the rotation speed does not give better covering or ordering of the particles on the wafer. The speeds of 4000 and 5000 rpm lead to almost the same quality of the films. Some more investigations were done in order to understand better the spin coating process at 1000 rpm.

As already mentioned the solution with high concentrations of  $\text{CoPt}_3$  nanoparticles, (1.8 mass %) gives multilayered non-homogenous films if deposited with the speed of 1000 rpm. Therefore the solutions with smaller particle concentrations were used for investigations. Few samples were made from the solutions with concentration 0.4 mass % and 0.3 mass % (Fig. 5.7.). Both solutions after spreading on the wafer gave a mono and multi layered structure. The area covered with multilayers of particles is larger in the case of the smaller particle concentration. The spin coating of such solution leads to a cascade particle packing in monolayer, double, triple and multilayers (Figure 5.7. (c)). This layer-by-layer packing is better shown on the high resolution SEM (Figure 5.7. (d)). The higher concentrated solution spreads on the wafer mostly as a monolayer and only some small areas of the wafer are

covered with a multilayer structure. The high resolution SEM-s, for both samples (Figure 5.7.), show the dense packed particles in a hexagonal lattice.

Nevertheless, reproducibility at such lower speed is not satisfying and this speed is not recommendable for the film preparation from  $\text{CoPt}_3$  particle solution in toluene on silicon wafers.

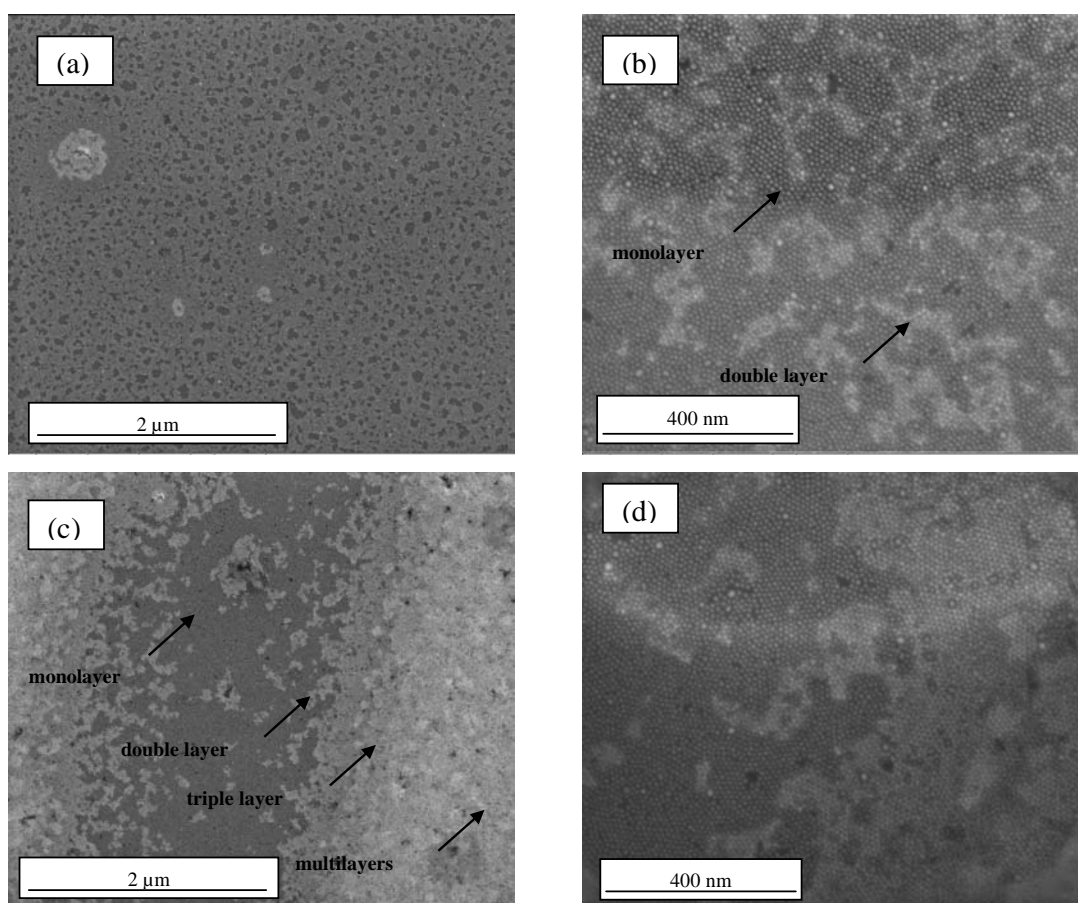


**Fig. 5.7.** SEM micrographs of samples prepared on silicon oxide from two different  $\text{CoPt}_3$  solutions (a and b – 0.4 mass %; c and d – 0.3 mass %) using the rotation speed of 1000 rpm

#### 5.4. Influence of wafer preparation on the film quality

The cleaning procedure of silicon wafers can also have a significant influence on the film quality. Silicon wafers can be cleaned in different ways. The wafers, which have been investigated in the described experiments, were cleaned with *piranha* mixture or in a plasma oven (see Experimental part). The results obtained using the wafers cleaned with two different procedures and the same solution of  $\text{CoPt}_3$  nanoparticles in toluene show that the wafers

cleaned by oxygen plasma are not really suitable substrates for the film preparation. The covering and the packing of the oxygen plasma cleaned wafers are not as good as on the chemically cleaned wafers. Explanation for such behaviour can be searched in the surface chemistry of the wafers after these two procedures.

From literature, it is known that the chemical cleaning with piranha mixture will remove all organic residues from the wafer surface, but it does not strip inorganic residues effectively. Besides piranha mixture will grow an oxide on bare silicon but will not grow oxide on oxidized surfaces. Additionally after this procedure it is possible that a high amount of sulphur was left on the surface<sup>[20],[21]</sup>. Using the oxygen plasma will remove all organics from the surface and it will grow an oxide on all surfaces. The thickness of the oxide layer will increase with exposition time of the sample. This leads to the conclusion that these two procedures will give a different surface after cleaning. Probably the surface after the chemical cleaning is richer with hydrogen groups than the surface after the plasma cleaning, what can guide to different hydrophilicity of the surface. Therefore it is concluded that these differences influence the attachment of the particles.

#### 5.5. Deposition of CoPt<sub>3</sub> nanoparticles on different polymer substrates

The spin coating of polymer films is used in various applications such as coating of photoresist on silicon wafers, sensors, protective coatings, paint coatings, optical coatings and membranes<sup>[22]</sup>. The spin coating procedure and some theoretical explanations are already described in general. Here only some characteristics pointed out of the polymer films spinning. Investigations of the polymer film preparation by spin coating show the following:

- a) During deposition of the solution the disc should either be static or rotating at a low angular velocity, followed by rapid acceleration of the angular velocity.
- b) Higher polymer concentrations or viscosities result in thicker films, and higher angular velocities result in thinner films.
- c) Higher solvent volatilities result in thicker films at a given initial concentration and initial viscosity. If the solvent is highly volatile then chilling effects become dominant which results in non-uniformities. Moreover, greater solvent/polymer compatibility results in more uniform films, i.e. less topographical variation in the resulting polymer film surface.
- d) The spin coating process can be very sensitive to: temperature, airflow velocity, relative humidity and thermal surroundings for the evaporating solvent (heat transfer).

Taking all these parameters in account it is evident that first the preparation of polymer film substrates onto silicon wafers and optimal conditions for that step should be investigated and afterwards processed with particle deposition.

### 5.5.1. Preparation of polymer substrates

Three different rotation speeds (1000, 2000 and 3000 rpm) and three different concentrations (0.1, 0.5 and 1.0 mass %) were investigated for the polymer film deposition. All polymer solutions were spin coated onto the silicon wafers previously cleaned by chemical procedure (see Experimental part). The polymer concentration was varied in order to produce polymer films with different thickness in order to investigate the influence of the polymer layer thickness on the particle deposition. The speed was changed in order to find the optimal conditions for the production of a smooth polymer film on the silicon surface. As investigation technique of the film quality AFM technique was used.

Figure 5.8. shows AFM images of three samples prepared under the same conditions from P4VP solution in chloroform ( $c = 0.1$  mass %), using different rotation speeds.

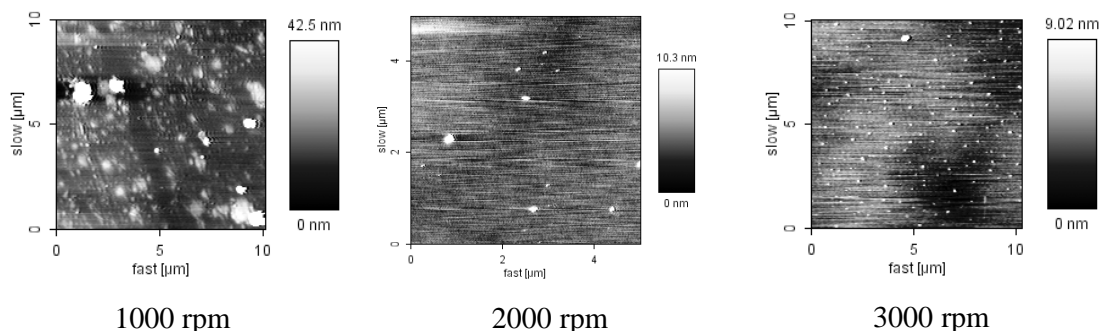


**Fig. 5.8.** AFM micrographs of the films prepared from P4VP 0.1 mass % solution in chloroform using different rotation speeds

The displayed micrographs demonstrate the influence of rotation speed on the polymer layer thickness and roughness. At low rate speed (1000 rpm) it can be expected that the thickness of the polymer layer is high, and decreasing with increase of the rate speed. For these investigations the more important factor is roughness. For the rate speed of 1000 rpm roughness is much higher than for the other two speeds. The AFM micrograph shows that the film prepared with the speed of 2000 rpm is very smooth, with only few aggregates. Similar

roughness is obtained also at 3000 rpm, but the number of small aggregates, with a height of around 10-15 nm, is higher than in the case when 2000 rpm was used. Few different parameters can influence on thin-film morphology as polymer-substrate interactions, glass transition temperature, solvent, molecular weight, dispersity etc.<sup>[22]</sup>. Very smooth films at higher rate speeds exclude solvent as possible reason for such behaviour. It is known from literature, that only *good solvents* produce uniform polymer films. *Good solvents* mean solvents in which interactions between the polymer and the solvent are energetically favourable, more than the interactions polymer-polymer or solvent-solvent, causing the polymer chain to expand. Short-range interchain attraction forces cause aggregation. These forces are minor in low concentrated solutions, but with increase of concentration they become significant and the polymer coils start to tangle to form so-called “loose aggregates” which turn to “strong aggregates” at higher concentrations. If the concentration of the polymer solution leads to the formation of “loose aggregates” then the morphology is influenced by angular velocity. This can be one of possible explanations for the morphology of the prepared P4VP films.

The same investigations were done with the PEODA solution in chloroform ( $c = 0.1$  mass %).

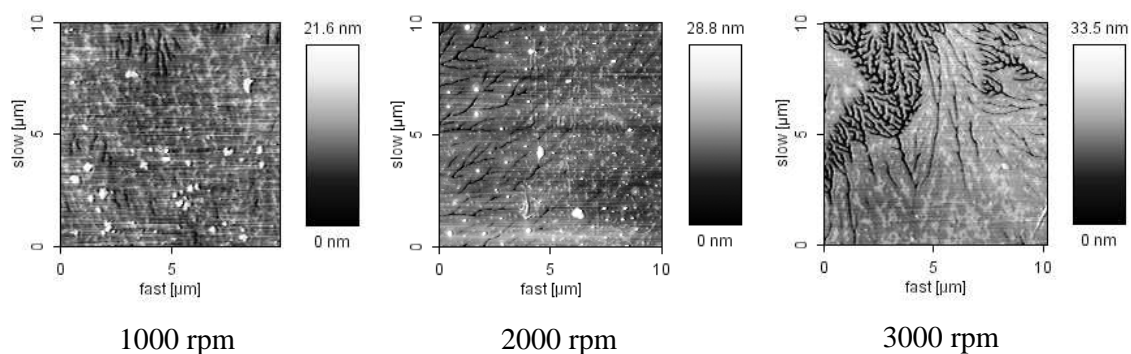


**Fig. 5.9.** AFM micrographs of the films prepared from PEODA 0.1 mass % solution in chloroform using different rotation speeds

Topography of the produced films is much more complicated, what can be seen from the AFM images shown in Figure 5.9. It can be expected that the polymer layers are thinner in comparison with P4VP layers prepared with the same rotational speed. Such behaviour is predictable as a result of the much lower molar mass of PEODA than the molar mass of the used P4VP, and that means that the viscosity of the solution is smaller what leads to the

thinner film production. Specific branch shaped structures on the surface are an effect of polymer crystallisation. Higher speed leads to more intensive PEOA crystallisation. Such crystal structures disappear when higher polymer concentrations have been used, and only lamellas can be seen on the surface<sup>[23],[24]</sup>. Aggregates with height from 20-30 nm are also present in all samples. Their formation is probably a combination resulting from already mentioned parameters.

The film formation of the other two polymers, P2VP and PEOA, was done in the same way (data are not shown). Since the higher rotation speeds did not give considerably better films compared to 2000 rpm, this speed was chosen for further polymer film preparation.

#### 5.5.2. Particle deposition on polymer substrates

*The following work concerning GISAXS measurements and evaluations of data was done in collaboration with Prof. Dr. J. Falta and Dr. J. I. Flege (University Bremen) as well as with Prof. Dr. M. Bäumer and B. Gehl (University Bremen).*

The nanoparticles were deposited on polymer substrates prepared on silicon dioxide wafers in the way already described above. Despite its volatility hexane was used as a solvent for nanoparticles due to the fact that it is a non-solvent for the used polymers. Using the non-solvent for the polymers their dissolving at the surface layer was diminished. Accordingly it will suppress diffusion and deposition of the particles within the polymer film as a result of polymer solution formation.

The particles were deposited using two different rotation speeds 1000 and 2000 rpm. The particle-polymer interactions were investigated by investigation of:

- a) Influence of polymer type, i.e. functional groups in the polymer (pyridyl and amino);
- b) Influence of polymer layer thickness and
- c) Influence of rotation speed during particle deposition.

After the film preparation GISAXS technique was used for the sample investigation and quantitative characterisation of ordering characteristics and the film morphology. This technique gives the opportunity to investigate the full sample surface (size 8 x 8 mm) and calculate the average particle-particle distance, and also allows quantifying the degree of ordering of the nanoparticles in the film. In more details GISAXS technique is described in the experimental part. Additional information about the overlayer structure is received using

SEM, which provides local structural information, and AFM, which is used to determine the roughness of the film on the mesoscopic scale.

For a general and quantitative GISAXS analysis of separate islands, a theoretical treatment within the framework of the distorted-wave Born approximation (DWBA) is demanded<sup>[25],[26]</sup>. Information about the film morphology is extracted from the features visible in the 2D GISAXS pattern as well as quantitative data within a defective hexagonal lattice approach in reciprocal space<sup>[27]</sup>. By fitting Lorentzian shape functions including a suitable background, which was found to yield satisfactory results in this case, the mean particle-particle distance  $\langle d \rangle$  can be calculated from the in-plane distance between the two first-order satellite peak positions  $\Delta q_{\parallel}$  by virtue of the relation<sup>[27]</sup>:

$$\langle d \rangle = \frac{2}{\sqrt{3}} \frac{4\pi}{\Delta q_{\parallel}}$$

The peak width  $\delta q$  provides a measure for the degree of ordering in the film. Accordingly, the correlation length  $\Gamma$  of the particle arrangement may be defined as  $\Gamma = 2\pi/\delta q$ . However, this definition is by no means unique and generally depends on the model of correlation assumed for the analysis. Finally, the convolution of the “ideal” scattering pattern with the incident beam profile in principle has to be taken into account for an accurate determination of  $\Gamma$ . A deconvolution assuming a Gaussian profile yielded only corrections in the order of less than 10% even for the best ordered films, and thus within the overall error bar, and will for this

reason will be neglected.

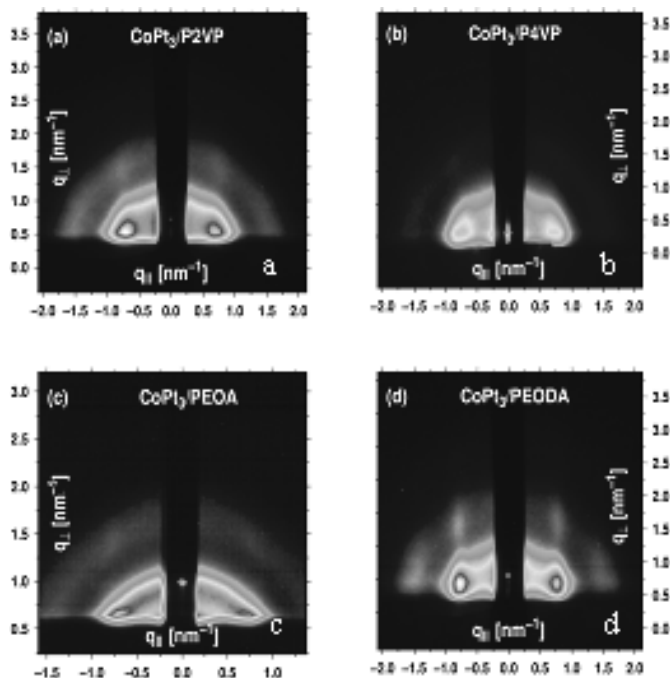


**Fig. 5.10.** GISAXS CCD images of  $\text{CoPt}_3$  nanoparticles spin coated on silicon oxide using different polymer substrates. The vertical dark blue strip indicates the position of the semi-transparent Al absorber

GISAXS patterns of spin coated CoPt<sub>3</sub> nanoparticle films using rotation speed of 1000 rpm and deposited on four different surface modifiers (P2VP, P4VP, PEOA, PEODA) are shown in Fig. 5.10. Observing features obtained for different samples it can be assumed that the heavy CoPt<sub>3</sub> nanoparticles dominate the small angle scattering while the contribution of the polymer films is negligible in this case. The validity of this expectation has been verified by taking GISAXS data of polymer films without nanoparticles. The films were deposited under exactly the same conditions in which especially the strong scattering features at  $q_{\parallel} \approx 0.75 \text{ nm}^{-1}$  are completely absent (image not shown). Hence, these satellite peaks are a direct proof of a correlation of the nanoparticles in the overlayer.

From a qualitative comparison, it is evident that the GISAXS image for PEODA (Fig. 5.10. (d)) show the closest similarity to the rod-like reciprocal space map corresponding to an ideal two-dimensional arrangement of scattering objects. Also, weak second-order peaks are visible in the lateral direction. The diffuse scattering between the first order satellites, which is particularly pronounced for the P2VP sample (Fig. 5.10. (a)), originates from the spherical shape of the nanoparticles. These broad and ring-like structures make up the complete scattering pattern for an uncorrelated assembly of spherical objects of similar size. In case (a) and (d), the superposition of the fringes due to the particle shape and the rods arising from the lateral arrangement leads to an better appearance of features in the vertical direction at  $q_{\parallel} \approx 0.75 \text{ nm}^{-1}$  and at higher values of  $q_{\perp}$ .

Using a quantitative evaluation of Figs. 5.10. (a) and 5.10. (b) it is calculated that the particles on both polymer surfaces have a mean nearest-neighbour distance of about  $\langle d \rangle \approx 9.7 \pm 0.2 \text{ nm}$  (from centre to centre). Interestingly, the correlation length  $\Gamma$  is slightly increased from 27 nm to 35 nm in case of P2VP (Table 5.1.) as surface modifier (relative errors lie in the order of 10%). This trend has been verified for several nanoparticle films prepared on P2VP and P4VP layers.

Comparing the PEOA and the PEODA sample (Fig. 5.10. (c) and (d), respectively) it can be concluded that amino groups do play an active role in the formation of the polymer buffer layer. The strongly “tilted” satellite peaks for PEOA may be interpreted in terms of tilted nanoparticle domains or faceted nanoparticle arrays. This hypothesis is confirmed by inspection of the AFM and SEM micrographs presented in Fig. 5.11. and Fig. 5.12., respectively. As can clearly be seen from AFM, the surface appears very rough in the case of PEOA (Fig. 5.11. (a)) while for PEODA (Fig. 5.11. (b)) a smooth and flat surface with only a

few areas of nanoparticle multilayers is observed. Hence, the microscopy findings are in very good agreement with the scattering data.

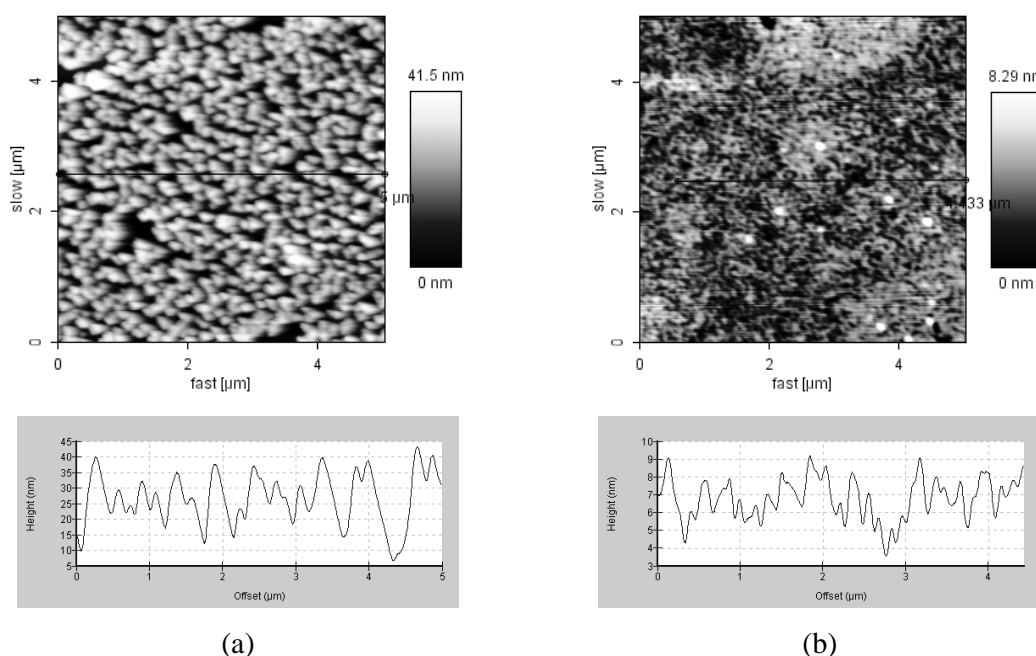


**Fig. 5.11.** AFM micrographs and cross sections of CoPt<sub>3</sub> nanoparticle films spin coated on (a) PEOA and (b) PEODA as a buffer layer, respectively.

Comparison of AFM and SEM images also can lead to conclusion that the particles are strongly attached to the polymer layer. The SEM image of the particles deposited on PEOA (Fig. 5.12 (a)) shows islands of particles, what is the result of particle attaching for rough polymer layer with similar topography. In the case of PEODA the polymer gives flat surface and the particles are packed as flat large areas.

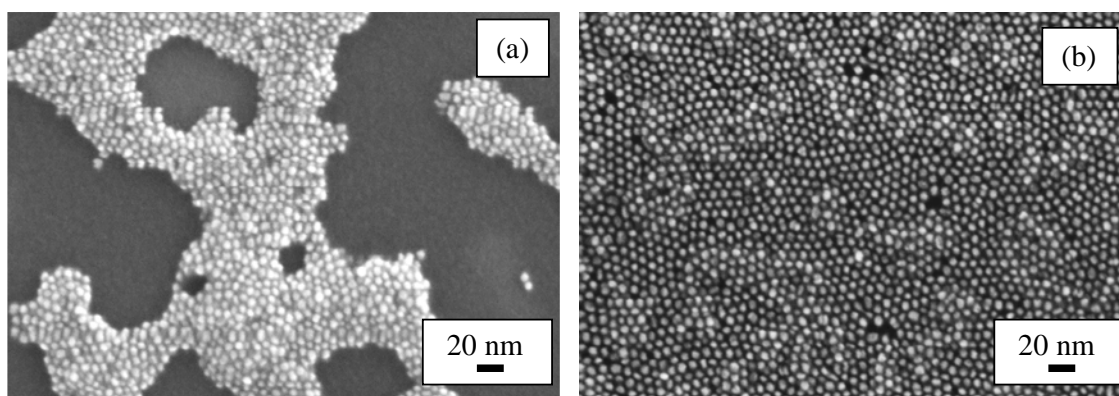


**Fig. 5.12.** SEM images of CoPt<sub>3</sub> nanoparticle films spin coated on (a) PEOA and (b) PEODA as a buffer layer, respectively.

Since the only difference in preparation between the samples has been the exchange of the surface modifier, i.e. doubling the number of amino groups available for film preparation and nanoparticle immobilization in case of PEODA instead of PEOA, it is evident that amino groups strongly favour the formation of a relatively smooth buffer layer and a flat nanoparticle film.

Table 5.1. Mean CoPt<sub>3</sub> particle-particle distance, correlation length and layer thickness after spin coating on different polymer buffer layers

Substrate	Rotation speed <sup>a)</sup> rpm	Part.-Part. Distance nm	Correlation length nm
P4VP-0.1 %	1000	9.9	27
P4VP-0.5 %	1000	9.9	33
P4VP-1.0 %	1000	9.7	35
P2VP-0.1 %	1000	9.6	35
P2VP-0.5 %	1000	10.3	38
P2VP-1.0 %	1000	9.7	36
P4VP-0.1 %	2000	10.8	42
P4VP-0.5 %	2000	11.0	47
P4VP-1.0 %	2000	11.2	42
P2VP-0.1 %	2000	10.3	50
P2VP-0.5 %	2000	10.3	43
P2VP-1.0 %	2000	9.9	60
PEODA-0.1 %	1000	9.3	54
PEODA-0.5 %	1000	9.4	52
PEODA-1.0 %	1000	9.5	53
PEODA-0.1 %	2000	10.2	102
PEODA-0.5 %	2000	10.6	70
PEODA-1.0 %	2000	10.8	59
PEOA – 0.1 %	1000	10.2	48
PEOA – 0.5 %	1000	10.3	48
PEOA – 1.0 %	1000	9.7	71

<sup>a)</sup> rotation speed used for deposition of particle solution;

In view of the fact that the use of PEODA provides the best conditions for smooth nanoparticle film growth, more attention will be dedicate on this surface modifier in the following. Now, it is possible to turn to the optimisation of the buffer layer thickness and the

spin-coating conditions, i.e. the rotation speed for nanoparticle deposition. In order to study the dependence of the ordering characteristics on the thickness of the buffer layer, three different concentrations for PEODA and two different speeds were chosen.

A comprehensive overview of the resulting particle-particle distances and the respective correlation lengths for the corresponding preparation conditions are given in Table 5.1. The most dramatic change is observed with respect to the increase of the correlation length with the rotation frequency. For samples prepared on PEODA from 0.1 mass % solution the correlation length is increasing almost two times, from 54 to 102. Obviously, the nanoparticles are homogeneously distributed on the PEODA buffer layer, leading to the formation of a smooth film. The mean particle-particle distance is slightly stretched for an enhanced rotation frequency and it slightly increases with increasing buffer layer thickness in case of  $\nu = 2000$  rpm,  $9.4 \pm 0.1$  nm to approximately  $10.5 \pm 0.3$  nm.

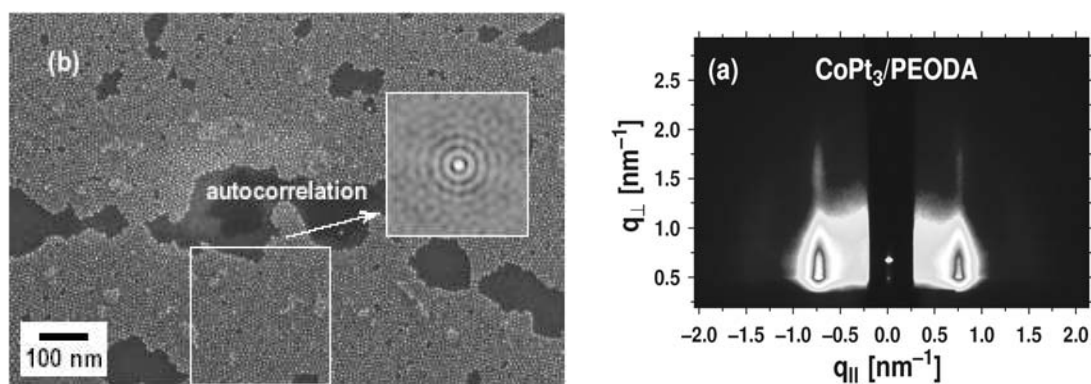


**Fig. 5.13.** GISAXS data (a) and high-resolution SEM micrograph (b) of a  $\text{CoPt}_3$  nanoparticle film spin-coated on a PEODA buffer layer, respectively. The inset in (b) shows a magnified view of the autocorrelation function near the central maximum.

The GISAXS pattern and the SEM micrograph for  $\nu = 2000$  rpm and  $c = 0.1$  mass %, i.e. the best-ordered nanoparticle array, are shown in Fig. 5.13. (a) and (b), respectively. The SEM image and the autocorrelation function (given as inset) computed from an arbitrarily chosen surface region illustrate the local hexagonal ordering of the nanoparticles and the high degree of lateral order which has been achieved, in qualitative agreement with the correlation length of about 100 nm determined by GISAXS for this type of preparation. A quantitative evaluation using the autocorrelation function yields an average nearest-neighbour distance of  $\langle d \rangle_{\text{SEM}} = 9.9 \pm 0.5$  nm which matches the corresponding GISAXS result of

$\langle d \rangle_{\text{GISAXS}} = 10.2 \pm 0.1$  nm. Furthermore, the formation of an almost uniform film of monolayer height is confirmed.

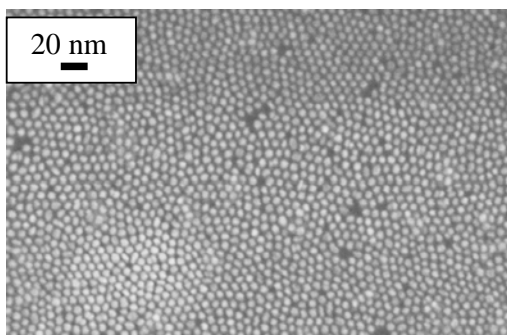


**Fig. 5.14.** HRSEM micrograph of the sample prepared on PEOA layer deposited from 1.0 mass % solution with speed of 1000 rpm

GISAXS analyses of samples deposited on PEOA shown some very interesting results concerning the correlation length. The correlation length for samples prepared on layers from low concentrated solutions (0.1 and 0.5 mass %) is almost the same and then drastically increases for the sample deposited on layer formed from 1.0 mass % solution (from 48 to 71 nm respectively, Table 5.1.). AFM and SEM measurement confirm once more the reliability of GISAXS measurements. As it is possible to see from the micrographs made by this two technique the

layers formed from less concentrated solutions are not uniform and some kind of the small polymer islands covered with the particles can be distinguished on the surface (Figs. 5.11 (a) and 5.12. (a)). This islands might be the result of crystallisation of PEOA, when the polymer is deposited as a very thin film<sup>[23],[24]</sup>. More concentrated polymer solution, 1.0 mass %, leads to the formation of smoother polymer layer and complete covering of the surface. On such layer particles are packing much better what can be seen from the SEM image (Figure 5.14.).

## 5.6. Conclusion

In this chapter, it was shown that smooth and ultra-thin CoPt<sub>3</sub> nanoparticle films might be prepared by the spin coating technique on silicon wafer as well as using different polymer substrates. The optimal rotation speed for the particle deposition on all types of substrates is 2000 rpm or in the case of silicon 3000 rpm. Using this rotation speed, it is possible to form high covered areas of well-ordered particles. The particles form a defective lattice of local hexagonal symmetry that is confirmed by high resolution SEM. The high substrate covering is possible only with solutions which hold more than 1.5 mass % of the CoPt<sub>3</sub> nanoparticles.

The GISAXS data prove that the particle correlation in the film deposited on PEODA is superior to films otherwise identically prepared on PEOA, P2VP and P4VP buffer layers. Diluted solutions of P2VP and P4VP (0.1 mass %) are good buffer layers in the sense of producing the large covered areas (around 100%), but the particle correlation is not

satisfactory and particles are packed as multilayers. The comparison of samples prepared on PEOA and PEOA substrates leads to the conclusion that the concentration of amino groups strongly influences the particle deposition. Despite the fact that these polymers are not good for preparation of a smooth polymer surfaces and in that way not recommended, surprisingly good particle films were obtained, what is probably due to the strong interactions between the amino groups and particles. Furthermore, the GISAXS analysis demonstrates that the particle correlation is very sensitive to the buffer layer thickness and the rotation speed used during the spin-coating process.

#### 6.7. Literature:

1. Schmid, G., D.V. Talapin, and E.V. Shevchenko, *Nanoparticles: From Theory to Application*, ed. G. Schmid. 2004: Wiley- VCH Verlag, Weinheim.
2. Shevchenko, E.V., et al., *J. Am. Chem. Soc.*, 2003. **125**: p. 9090-9101.
3. Lalatonne, Y., J. Richardi, and M.P. Pileni, *Van der Waals versus dipolar forces controlling mesoscopic organisations of magnetic nanocrystals*. *Nature Materials*, 2004. **3**: p. 121-125.
4. Thomas, P.J., G.U. Kulkarni, and C.N.R. Rao, *An Investigation of Two-Dimensional Arrays of Thiolized Pd Nanocrystals*. *J. Phys. Chem. B*, 2000. **104**: p. 8138-8144.
5. Malynych, S., I. Luzinov, and G. Chumanov, *Poly(Vinyl Pyridine) as a Universal Surface Modifier for Immobilization of Nanoparticles*. *J. Phys. Chem. B*, 2002. **106**: p. 1280-1285.
6. Rao, K.M., et al., *Preparation and characterization of silver particulate structure deposited on softened poly(4-vinylpyridine) substrates*. *J. Phys. D: Appl. Phys.*, 1999. **32**: p. 2327-2336.
7. Martin S. Kunz, K.R.S., and Andrew J. Kellock, *Morphologies of discontinuous gold films on amorphous polymer substrates*. *J. Appl. Phys.*, 1992. **72**(9): p. 4458-4460.
8. Dement'eva, O.V., et al., *Metal Nanoparticles on Polymer Surfaces: 4. Preparation and Structure of Colloidal Gold Films*. *Colloid Journal*, 2005. **67**(2): p. 123-133.
9. Liu, Z., et al., *Organization of Nanoparticles on Soft Polymer Surfaces*. *Nano Letters*, 2002. **2**(3): p. 219-224.
10. Schmitz, K.S., *Macromolecules*, 2002. **33**: p. 2284-2285.
11. Harnish, B., et al., *UV-Cross-Linked Poly(vinylpyridine) Thin Films as Reversibly Responsive Surfaces*. *Chem. Mater.*, 2005. **17**: p. 4092-4096.
12. Djalali, R., S.Y. Li, and M. Schmidt, *Amphipolar Core-Shell Cylindrical Brushes as Templates for the Formation of Gold Clusters and Nanowires*. *Macromolecules*, 2002. **35**: p. 4282-4288.
13. Abes, J.I., R.E. Cohen, and C.A. Ross, *Selective Growth of Cobalt Nanoclusters in Domains of Block Copolymer Films*. *Chem. Mater.*, 2003. **15**: p. 1125-1131.
14. Lin, Y., et al., *Nature*, 2005. **434**: p. 55-59.
15. <http://www.mse.arizona.edu/faculty/birnie/Coatings/index.htm>, *Application of Spin Coating*.
16. <http://www.cise.columbia.edu/clean/process/spintheory.pdf>, *Spin Coat Theory*.
17. Emslie, A.G., F.T. Bonner, and L.G. Peck, *J. Appl. Phys.*, 1958. **29**: p. 858-862.

18. Meyerhofer, D., *Characteristics of resist films produced by spinning*. J. Appl. Phys., 1978. **49**(7): p. 3993-3997.
19. Britten, J.A. and I.M. Thomas, *Non-Newtonian flow effects during spin coating large-area optical coatings with colloidal suspensions*. J. Appl. Phys., 1992. **71**(2): p. 972-979.
20. Roche, T.S., *Surface Preparation and Wet Processing*.
21. Gu, S.Q., et al., *Replacing piranha cleans with an O<sub>2</sub> RIE/fluorine process to remove post-ion-implant residues*, in *Micromagazine*.
22. Norrman, K., A. Ghanbari-Siahkali, and N.B. Larsen, *Studies of spin-coated polymer films*. Annu. Rep. Prog. Chem., Sect. C, 2005. **101**: p. 174-201.
23. Zhai, X.M., et al., *Spontaneous and Inductive Thickenings of Lamellar Crystal Monolayers of Low Molecular Weight PEO Fractions on Surface of Solid Substrates*. Macromolecules, 2005. **38**: p. 1717-1722.
24. Meyer, A., *Untersuchung der molekularen Orientierung in dünnen Polymerfilmen mit Hilfe der Röntgenstreuung bei streifendem Einfall*, in *Fachbereiches Chemie*. 1998, University Hamburg: Hamburg. p. 130.
25. Sinha, S.K., et al., Phys. Rev. B, 1988. **38**: p. 2297-2311.
26. Rauscher, M., et al., 1999. J. Appl. Phys. **86**: p. 6763-6769.
27. Lazzari, R., *IsGISAXS: a program for grazing-incidence small-angle X-ray scattering analysis of supported islands*. J. Appl. Cryst, 2002. **35**: p. 406-421.

## Chapter 6

### Dip coating technique

#### 6.1. Dip coating

Dip coating is widely used in industrial applications because of its simplicity and high throughput. Flat or curved substrates, which are normally smooth and wettable by the sample solution, is withdrawn at constant velocity from a liquid reservoir.

The preparation by dip coating may be divided in four stages: 1) choice of substrate; 2) thin layer deposition; 3) film formation and 4) drying or drainage (Fig. 6.1.). In industry this procedure is used for high production painting of relatively simple shapes. The transfer efficiency is very high, equipment requirements are low and the process can be automated. However, dip coating has some negative aspects. The dipping is extremely dependent on the viscosity of the solution (paint) and used chemicals may be highly hazardous especially if the solution (paint) is flammable.

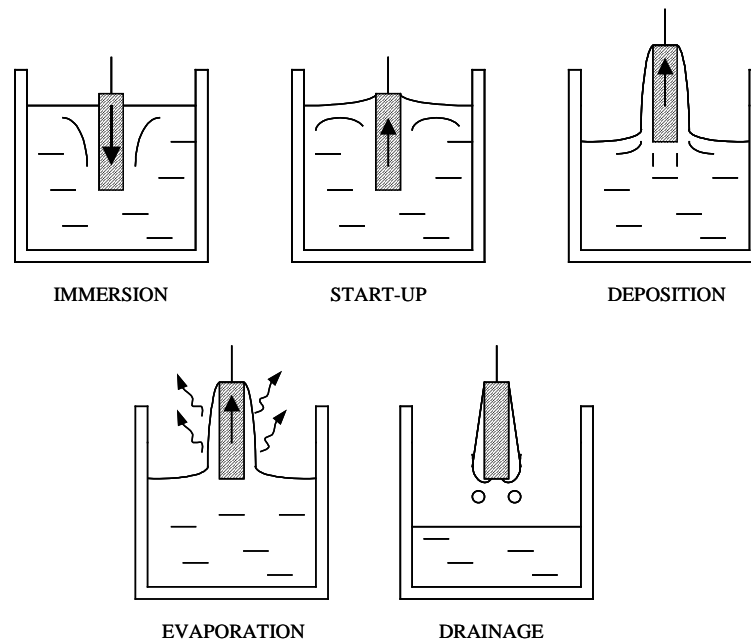


**Fig. 6.1:** Steps of the dip-coating process: immersion, start-up, deposition, evaporation and drainage.

As already mentioned the film preparation with dip coating is very simple and fast. Additionally, the sample loss is smaller for this technique in comparison to spin coating. Dip coating has already been used for the deposition of magnetic nanoparticles on different surfaces<sup>[1],[2]</sup>, for gold or TiO<sub>2</sub> nanoparticles which are used as catalysts<sup>[3],[4],[5]</sup> or for polymer nanoparticles deposition used for preparation of larger order areas with specific optical properties<sup>[6]</sup>. During the last years, dip coating found also application in selective coating or “inking” chemically patterned surfaces. It was found that this technique allows precise deposition of the liquid coatings with thickness in the micron range<sup>[7]</sup>.

To achieve deposition of large areas of well-order particles on the substrates using dip coating, it was necessary to investigate different process conditions and find the optimal one. Therefore the influence of the solvent, substrate, particle concentration and the dipping speed was studied. These parameters strongly influence the deposition process and they will be investigated first.

During the dip coating a thin film of particle solution stays on the surface. The solvent then evaporates and leaves the particles on the surface. Good covering of the surface is only obtained if the solution evaporates without de-wetting. De-wetting will result in the formation of islands of particles on the surface. To avoid de-wetting it is necessary to choose the appropriate combination of substrate and solution. Self-assembly of the particles requires additionally that they can diffuse across the surface and form self-assembled structures. It was found that the amount of surfactants is very important for the particle self-assembly. The influences of the parameters were reported in the literature<sup>[1],[2]</sup>. For example in the case of FePt nanoparticles an increase of the surfactant concentration (oleic acid and oleyl amine) can retard the solvent evaporation, allowing more time for self-assembly. This leads to a higher covering of the substrate<sup>[1]</sup>. A completely different behaviour was shown with Fe<sub>2</sub>O<sub>3</sub> nanoparticles stabilised with oleic acid and deposited on three different types of wafers such as: Si, Si<sub>3</sub>N<sub>4</sub> and SiO<sub>2</sub>. In this case competitive adsorption between the Fe<sub>2</sub>O<sub>3</sub> nanoparticles and their surfactants led to low covering of the substrates and repeated dipping was performed in order to produce a higher coverage<sup>[2]</sup>.

Dimitrov and Nagayama<sup>[6]</sup> developed a model, which explains the particle film formation during dip coating of polystyrene nanoparticles from water on glass (Fig. 6.2.). This model can also be applied to any other system of particles and solvents. They found that the particle film can be formed by dipping the clean wettabale surface into the particle solution and then withdraw it by a rate that equals the array formation rate in a well controlled environmental humidity. In Figure 6.2. the withdrawal process is schematically displayed.

The formation of the particle layer occurs in two phases: a) convective transfer of particles from the suspension to the thin wetting film due to water evaporation from the film surface and b) interactions between the particles that lead to specific textures. The balance between the viscosity and capillary forces determines the coating thickness.

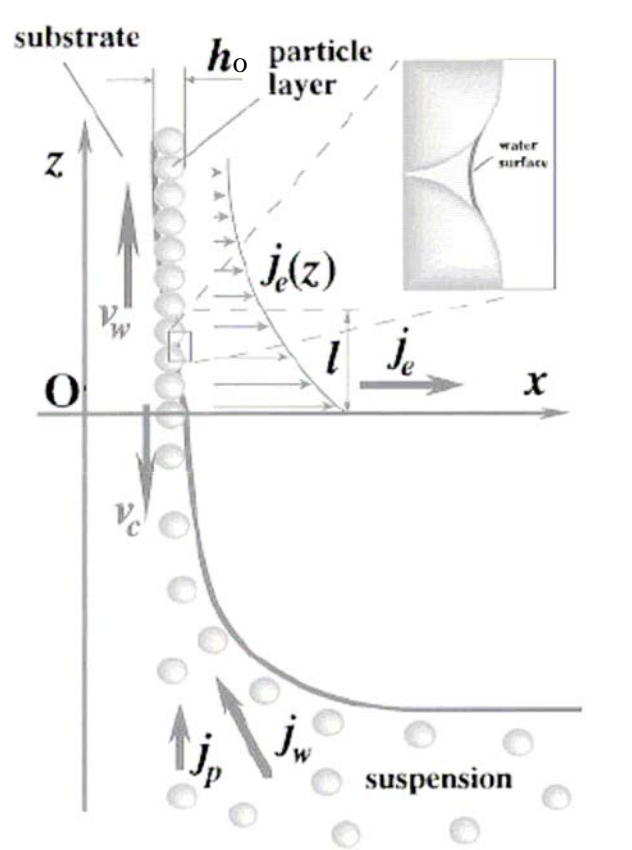


**Fig. 6.2.** The scheme of particle and water fluxes at the beginning of 2D array growth. Here,  $v_w$  is the substrate withdrawal rate,  $v_c$  is the array growth rate,  $j_w$  is the water influx,  $j_p$  is the respective particle influx,  $j_e$  is the water evaporation flux, and  $h$  is the thickness of the array<sup>[6]</sup>

Due to the hydrostatic pressure in vertical wetting films, the film thickness decreases as the relative height increases. Thus, the water-air interface may actually have a relatively high attraction to the substrate (water-plate interface) and may cause a capillary force, which pushes the particles out of the film regions thinner than the diameter of the particles. Therefore, the lateral capillary forces are not able to initiate the array growth process. The particles with diameters,  $d$ , less than  $h_0$  will be packed in irregularly placed islands after drying, and when  $d$  is much bigger than  $h_0$  no particles stay after the film drying (Fig. 6.3.).

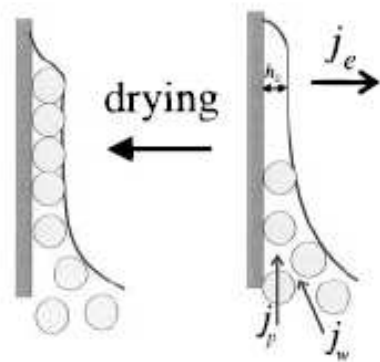


**Fig. 6.3.** *The particle diameter is slightly larger than the thickness  $h_0$ . The water evaporation from the film causes suspension influx from the bulk toward the film<sup>[6]</sup>.*

Investigations with polystyrene spheres show that not only the particle diameter but also the polydispersity of the particles strongly influence the quality of particle packing. Large uniformly oriented domains of highly aligned particles can only be obtained with low polydispersity. Large particles (size from 400-800 nm) usually form monolayers of differently oriented domains, and much larger particles with broader particle size distribution form multilayers<sup>[6]</sup>.

## 6.2. Statistical experimental design applied on nanoparticle film preparation by dip coating

*The following work concerning statistical experimental design was done in collaboration with Dr. Florence Benoit - Marquie from the Laboratory I.M.R.C.P. of University Paul Sabatier from Toulouse (France).*

Due to the fact that all mentioned parameters are connected to each other, the preparation of the good quality films requires the right combination of them. In order to reduce the number of experiments and to make an investigation faster and more reliable we used a method so-called “*statistical experimental design*”. By using this method it was possible to find the optimal conditions for preparation of highly covered silicon substrates with  $\text{CoPt}_3$  nanoparticles<sup>[8]</sup>.

### 6.2.1. Statistical experimental design

Firstly, the principle of statistical experimental design will be explained. A statistical experimental design or design of experiments is defined as a methodology of how to conduct and plane experiments in order to extract the maximum amount of information in the fewest number of runs<sup>[9],[10]</sup>.

Most experimentation involves several factors with mutual relationship and the influence of the characteristics on the process (responses) should be understood in order to optimise a process.

All parameters, which have influence on the process and which can be dictated changeable, are called factors (temperature, concentration, pH, catalyst type...), and all parameters of the process which result in a change of the factors are cold responses (yield, purity, biological activity...).

The usual investigation method is to change one separate factor (variable) at a time (COST) and investigate its influence on the response. This procedure is usually followed with many experiments and in most of the cases does not lead to real optimum conditions. Especially it is not possible to find the position of the optimum in the case of interactions between the factors. The main problems associated with COST are:

- a) Does not lead to the real optimum.
- b) Inefficient, too many runs.
- c) Provides no information about what happens when factors are varied simultaneously.
- d) Provides less information about the variability of the response.
- e) Isolated, unconnected experiments, etc.

To investigate the influence of several factors a better strategy than COST is needed. For this purposes it is recommended to use the *experimental design approach*, DoE. The basic idea of this approach is to plan a small set of experiments (between 10 and 20) in which all important factors are varied systematically. By using mathematics for the analysis it is possible to find the optimal conditions, the factors that influence the results most and those that do not. In addition, it is possible to find the presence of interactions and synergisms, and so on. The main advantages of the DoE are:

- a) A small number of experiments.
- b) All factors are varied together.
- c) Noise is decreased by means of averaging.
- d) Interactions and synergisms are noticed.

### 6.2.2. Design I

The first step in the DoE process is the problem formulation. For the system, which has been investigated and described here, the problem can be formulated as a searching for the optimal conditions in order to produce high areas of particle monolayers on the substrate by improving the knowledge of the role of the factors.

The second step is the definition of factors: important factors and dominating ones, as well as definition of the range of investigation and further steps. Here, four factors were chosen: particle concentration ( $X_1$ ), solvent ( $X_2$ ), dipping speed ( $X_3$ ) and substrate ( $X_4$ ). It is known that these factors can have an influence on the percentage of covering. It is not known if all of them have an influence or not, and which are the most important.

The third step consists of choosing the strategy (design), which will enable to answer the objectives defined in the first step. In this particulate case **factorial design** was performed as a preliminary screen to evaluate the significance of the factors. In the case when the full factorial design is used the number of required experiments can be calculated as  $N = 2^k$ , where “k” is the number of factors. A full  $2^k$  factorial design allows estimating all interactions between the factors. If k increases ( $k > 3$ ) more and more then interactions between three (or more) factors generally become less important. In that case is better to use **fractional factorial design**. This fractional factorial design uses the “main effect” principle: main effects tend to dominate two-factor interactions; two-factor interactions tend to dominate three-factor interactions, and so on. In other words: in a fractional factorial design, it is assumed that interaction effects between three ( $b_{ijk}$ ) or more factors are negligible. Useful information on the main effects and low order interactions may be obtained, thus, by running only a fraction of the complete factorial design. Therefore, it can be said that the fractional factorial designs “sacrifice” the ability to estimate higher-order interactions in order to reduce the number of experiments.

For the system that has been described here  $k = 4$  (four factors were chosen for investigation). Therefore, fractional factorial design ( $2^{4-1}$ ) was used to study the main effects ( $b_i$ ), and two-factor interaction effects ( $b_{ij}$ ). Indeed, fractional factorial design reduces the total number of experiments (from 16 to 8) while saving the basic factorial structure of the strategy.

### 6.2.3. Experimental design applied to $\text{CoPt}_3$ deposition on silicon by dip coating

Experimental conditions of concentration, such as type of solvent, dipping speed and type of surface were fixed by considering results of the previous experiments. Two different concentrations of the  $\text{CoPt}_3$  nanoparticles ( $d = 4.4$  nm, from XRD data) were chosen and hexane and toluene were used as solvents. These solutions were deposited on two different types of silicon wafers: one only cleaned by a chemical procedure and another chemically treated to facilitate hydrophobic surface (experimental part). The deposition speeds were 1 and 10 mm/min. The factorial design was evaluated by using the percentage of coverage as response (noted Y). Firstly, the samples were investigated by SEM, and then the images were treated using the program *Image J* in order to calculate the percentage of coverage. In the  $2^{4-1}$  fractional factorial design, four variables (factors) are studied each at two levels (level -1 noted as – and level +1 noted as +). For calculations, coded variables ( $X_i$ ) are used instead of actual variables ( $U_i$ ). The range of variation of each  $U_i$  is transformed into variation of  $X_i$  between -1 and +1. The factors and levels used in the factorial design are shown in Table 6.1.

Table 6.1.: Factors and levels used in factorial design

Actual variable ( $U_i$ )	Coded variable ( $X_i$ )	(-)	(+)
Concentration (mmol/l)	$X_1$	4.0	2.4
Solvent	$X_2$	hexane	toluene
Dipping speed (mm/min)	$X_3$	1	10
Surface	$X_4$	hydrophilic	hydrophobic

The design in coded ( $X_i$ ) and actual ( $U_i$ ) independent variables is described in Table 6.2. The coded variables are always +1 or -1 and they are used for writing the basic matrix. The actual variables are the real parameters which were used for investigations. In this work the  $2^{4-1}$  fractional factorial design is obtained by writing down the complete  $2^3$  factorial as the basic design (with 3 variables  $X_1, X_2, X_3$ ) and then equating factor  $X_4$  with the  $X_1X_2X_3$  interactions. This last condition allows us to identify the defining relation ( $I = X_1X_2X_3X_4$ ). For further analyses only experiments corresponding to the positive defining relation ( $I = +$ ) were chosen.

Table 6.2.:  $2^{4-1}$  Fractional Factorial Design with coded and actual independent variables and results of the surface coverage (Y, the coverage is given in % of area used for calculation SEM image taken with a magnification of 50 000 and with scale bar 200 nm).

N°	Coded: $X_i$				Actual: $U_i$				Response: (Covering)
	$X_1$	$X_2$	$X_3$	$X_4$	$U_1$	$U_2$	$U_3$	$U_4$	Y
1	-1	-1	-1	-1	4,0	hexane	1	hydrophilic	100*
2	+1	-1	-1	+1	2,4	hexane	1	hydrophobic	99*
3	-1	+1	-1	+1	4,0	toluene	1	hydrophobic	23
4	+1	+1	-1	-1	2,4	toluene	1	hydrophilic	16
5a	-1	-1	+1	+1	4,0	hexane	10	hydrophobic	70
5b	-1	-1	+1	+1	4,0	hexane	10	hydrophobic	72
5c	-1	-1	+1	+1	4,0	hexane	10	hydrophobic	75
5d	-1	-1	+1	+1	4,0	hexane	10	hydrophobic	74
6	+1	-1	+1	-1	2,4	hexane	10	hydrophilic	56
7	-1	+1	+1	-1	4,0	toluene	10	hydrophilic	26
8	+1	+1	+1	+1	2,4	toluene	10	hydrophobic	12

\*The values of 100 and 99 % correspond to multilayer structures

From this defined relation ( $I = X_1X_2X_3X_4$ ) it is possible to develop the complete structure of mutual effects for this design and to obtain the 8 *contrasts* (Table 6.3. noted  $L_i$ ) that may be estimated from the experimental data. Each main effect ( $b_i$ ) is related to other three-factor interactions ( $b_{ijk}$ ), and each two-factor interaction ( $b_{ij}$ ) is related to the other two-factor interaction. It can be reasonably assumed that three-factor interactions ( $b_{ijk}$ ) are negligible and would expect that this design would provide excellent information concerning the main effects. After neglecting three- and four-factor interactions the first four contrasts are related only to the main effects and other three are combination of two different two-factor interactions (Table 6.4. – the first column). The  $b_0$  is average value of all values obtained as a response after analyses of performed experiments Table 6.4.).

Table 6.3: Contrasts expressions in  $2^{4-1}$  Fractional Factorial Design: alias structure of different factors. ( $b_1$  – influence of concentration;  $b_2$  – influence of solvent;  $b_3$  – influence of dipping speed;  $b_4$  – influence of surface)

Expression
$L_0 = b_0 + b_{1234}$
$L_1 = b_1 + b_{234}$
$L_2 = b_2 + b_{134}$
$L_3 = b_3 + b_{124}$
$L_4 = b_4 + b_{123}$
$L_5 = b_{12} + b_{34}$
$L_6 = b_{13} + b_{24}$
$L_7 = b_{23} + b_{14}$

For the investigation of a mutual effect of these four parameters it was necessary to prepare only 11 samples. Three of them were prepared in the same way in order to assure the reproducibility of the sample preparation (5b to 5d in the Table 6.2.) The experiments were carried out in random order. The obtained experimental results were treated with the computer program NEMROD<sup>®[11]</sup>. From the obtained results, estimates of the main effects and (interactions) related to confounded two-variable interactions effects can be computed. These values are shown in Table 6.4., where  $b_0$  is the average.

Table 6.4. Contrasts expressions in  $2^{4-1}$  Fractional Factorial Design after simplification and estimated effects obtained by the computer program NEMROD<sup>®</sup>

$L_0 = b_0$	50,6
$L_1 = b_1$	-4,8
$L_2 = b_2$	-31,3
$L_3 = b_3$	-8,9
$L_4 = b_4$	1,1
$L_5 = b_{12} + b_{34}$	-0,4
$L_6 = b_{13} + b_{24}$	-2,8
$L_7 = b_{23} + b_{14}$	8,7

The analysis of variation (ANOVA) was used for further study of obtained responses (percentage of coverage). A graphical analysis of contrasts (Fig. 6.4.) was used to find the significant effects.

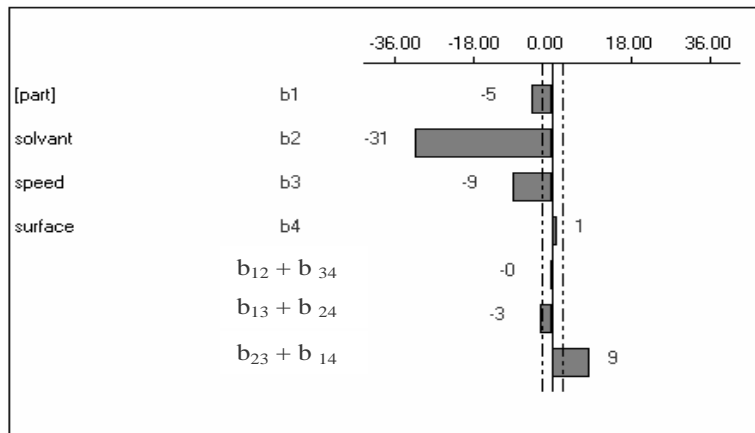


**Fig. 6.4.** The graphical analysis of effects is displayed. The dotted lines represent the confidence interval of the calculated effects.

In this plot, two vertical lines calculated according to the experimental error represent both factor effects and the confidence interval. The effects that exceed the reference lines are those significant for the response. From the analysis of the results it can be concluded that three main effects are significant: the most important is  $b_2$  (related to the solvent), after that  $b_3$  (the dipping speed) and less important is  $b_1$  (concentration), while the surface effect  $b_4$  has negligible influence on the coverage. Also, it is important to notice the significant influence of the confounded interactions effect,  $b_{23} + b_{14}$ . It is not possible to determine which of these confounded effects contribute to the high value of the estimate. In the absence of complementary fraction design, it can be assumed that  $b_{23}$  (interaction between solvent and dipping speed) is the dominating term since  $X_2$  and  $X_3$  have the greatest effect on the response. For the confounded interaction effects  $b_{13} + b_{24}$  it is almost the same, but the value of this effect is very low. For physical reasons (the interactions between the solvent and surface are expected) it was decided to select  $b_{24}$  as probably less significant interactions. There is no interaction between the concentration and the solvent ( $b_{12}$ ), the speed and the surface ( $b_{34}$ ).

To present better the interactions between the solvent and the speed and between the solvent and the surface, two schemes are given in Fig. 6.5. In both cases the percentage of coverage from hexane solution is appreciably higher than from toluene solution. The

hydrophobic surface seems to be better for the production of large areas covered with particles deposited on the substrates from hexane solution. Lower speed gives better results for the covering, but at the same time leads to multilayer formation. This is not desirable in the investigated system. Therefore higher speed will be more acceptable.

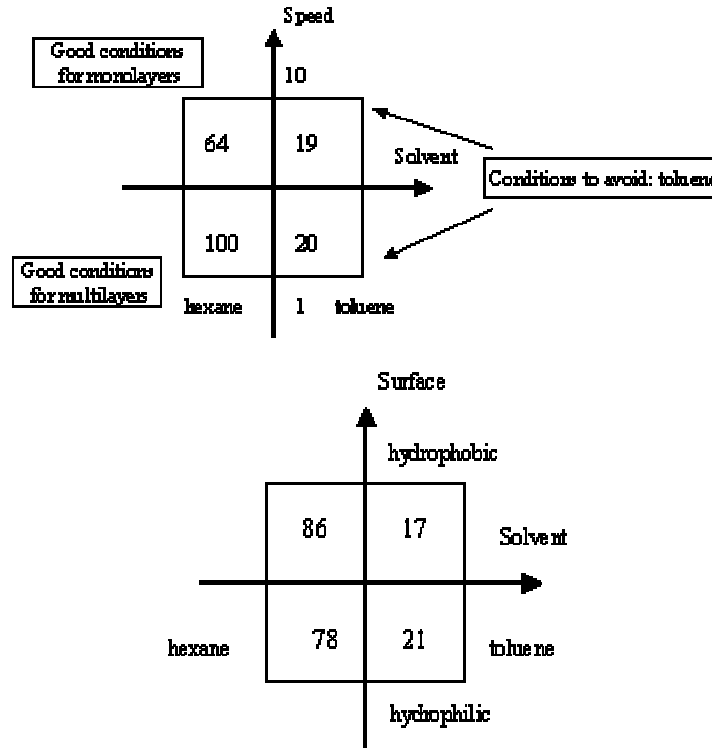


**Fig. 6.5.** The interactions between the dipping speed and the solvent (left diagram) and between the solvent and the surface (right diagram)

### 6.3. Design II

The results from factorial design demonstrated that hexane and hydrophobic surfaces lead to better results. The concentration and the dipping speed required a final optimisation. A second-order mathematical model can be used to represent the relationship between the variation of experimental response  $Y$  (percentage of coverage) and the variation of these factors. It is assumed that the studied phenomenon is non-linear:

$$Y_c = b_0 + b_1X_1 + b_2X_2 + b_{11}X_1^2 + b_{22}X_2^2 + b_{12}X_1X_2,$$

where  $Y_c$  is the response calculated by the model and  $X_1$ ,  $X_2$  are the coded variables corresponding to the factors  $U_1$  (dipping speed),  $U_2$  (particles concentration). Letters  $b_i$ ,  $b_{ii}$

and  $b_{ij}$  are coefficients estimated by the model, and they respectively represent the linear, quadratic and cross-product effects of the  $X_1$ ,  $X_2$  factors on the response

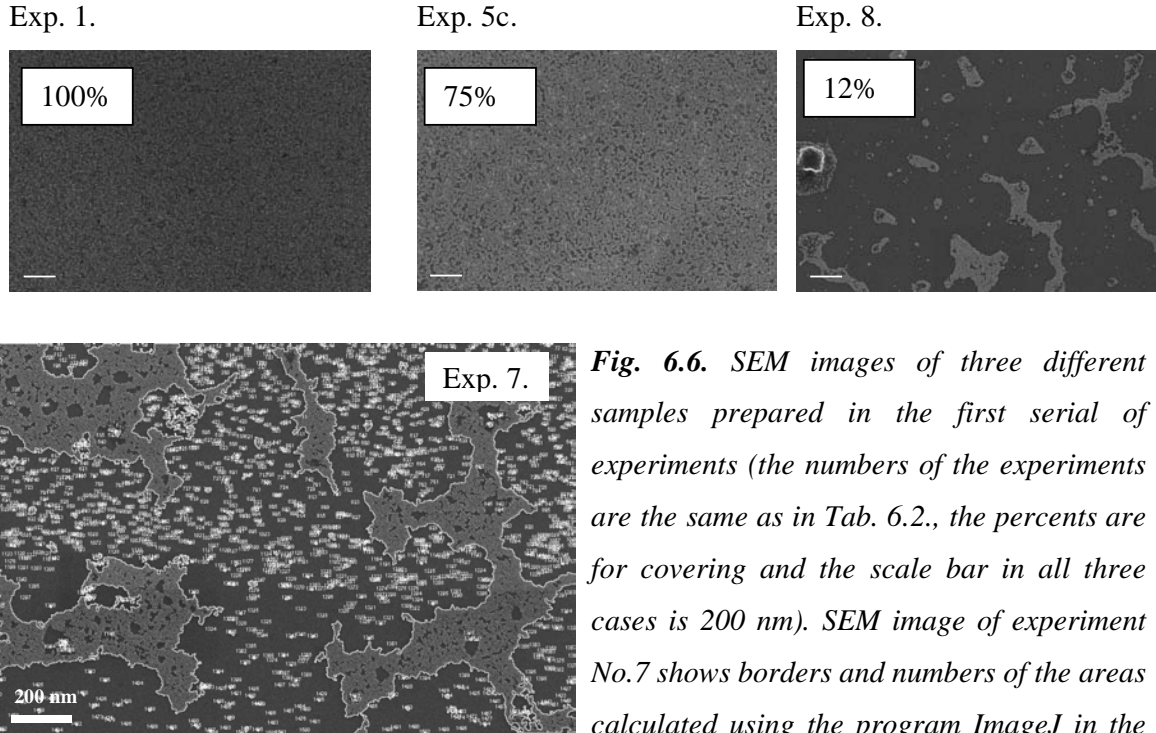


**Fig. 6.6.** SEM images of three different samples prepared in the first serial of experiments (the numbers of the experiments are the same as in Tab. 6.2., the percents are for covering and the scale bar in all three cases is 200 nm). SEM image of experiment No.7 shows borders and numbers of the areas calculated using the program ImageJ in the process of determination the percentage of coverage.

The relation  $U_i = U_i^0 + X_i \Delta U_i$  allows to switch from the coded to the real variables.  $U_i^0$  is the value of the real variable  $i$  at the centre of the experimental domain ( $I = (U_{i,max} + U_{i,min})/2$ ),  $\Delta U_i$  is the step of variation of the real variable  $i = (U_{i,max} - U_{i,min})/2$ . The range of variation of the natural variables determines the experimental region of interest.

It was of interest to investigate the percentage of coverage for a wider range of dipping speeds than for the factorial design (from 1-19 mm/min). In addition, a lower concentrations range (lower than 2.4 mmol/l) should be investigated because it can provide monolayer formation (Table 6.5.).

To calculate the coefficients with the best precision an optimal matrix of experiments for the postulated model was chosen, as proposed by Doehlert<sup>[12]</sup>.

Table 6.5.: The factors and variation domain:

Factor	Unit	Centre	Variation domain
Dip speed $U_1$	mm/min	10	1-19
Particle concentration $U_2$	mmol/l	1.5	0.75 – 2.3

The Doehlert matrix is a second order design, which has been widely used in several situations. Usually it was used for identification of critical points (maximum, minimum, and saddle points) at each step of the optimisation process. This process consists of an experimental design in which a set of points is uniformly distributed in a hexagon for two variables. The number of experiments ( $N$ ) can be calculated using the equation  $N = k^2 + k + C_0$ , where  $k$  is the number of variables and  $C_0$  is the number of centre points. Therefore, the used matrix consists of seven distinct experiments (Table 6.6.). Experiment No. 7 (centre of the experimental domain) was repeated in order to check the reproducibility. The Fig 6.7. gives a graphical representation of this network in the space defined by the factors. This uniform distribution of experimental points (shown as squares) allows interpolating by the mathematical model of response anywhere within the circular experimental domain. Furthermore, the quality of the interpolation remains constant, since the network is uniform. The Doehlert design shows a great flexibility: a point of the network can be reused to build and explore adjacent domains, without quality loss for the model. All the calculations and response surface generation were performed with NEMROD software<sup>[11]</sup>.

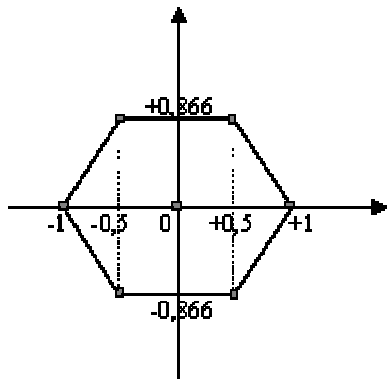


**Fig. 6.7.** The location of seven points of a two-factor Doehlert uniform shell design in coded factor space.

The measured responses  $Y_{\text{exp}}$  for the ten experiments are reported in Table 6.6. together with the response  $Y_{\text{cal}}$  predicted by the model. The difference ( $Y_{\text{exp}} - Y_{\text{cal}}$ ) shows that the prediction by the model and the experimental data accurately fit, thus validating the model.

Table 6.6.: Experimental design, measured ( $Y_{exp}$ ) and calculated response ( $Y_{cal}$ ).

No. Exp.	Real variables		Coded variables		Responses (%)		
	$U_1$ (mm/min)	$U_2$ (mmol/L)	$X_1$	$X_2$	$Y_{exp}$	$Y_{cal}$	$Y_{exp} - Y_{cal}$
1	19	1.49	1	0	41	38.6	2.4
2	1	1.49	-1	0	50	51.9	-1.9
3	15	2.23	0.5	0.866	26	28.1	-2.1
4	6	0.75	-0.5	-0.866	7	4.9	2.1
5	15	0.75	0.5	-0.866	10	12.1	-2.1
6	6	2.23	-0.5	0.866	47	44.9	2.1
7	10	1.49	0	0	30	27.7	2.3
8	10	1.49	0	0	25	27.7	-2.7

Calculated values for coefficients  $b_i$ ,  $b_{ii}$  and  $b_{ij}$  can be inserted in the response function predicting the percentage of the coverage:

$$Y_c = 27.7 - 6.6X_1 + 16.9X_2 + 17.5X_1^2 - 12.4X_2^2 - 13.9X_1X_2.$$

It can be seen from these coefficient values, that the  $X_1^2$  and  $X_2^2$  coefficients indicate a non-linear phenomenon. Therefore, the choice of a second-order equation for the model was appropriate.

Using the NEMROD software and the complete model (the equation is reliable, with a  $R_2$  value of 0.977), a response surface displaying the variation of two factors was drawn. The response surface (Fig. 6.8.) and the corresponding projection (Fig. 6.9.) with iso-response curves (blue lines which present calculated response) are shown below.

Three areas are recognisable in the Fig. 6.9. :

- Area A is called stability area. In this area, where the dipping speed is approximately 13-15 mm/min, the substrate coverage is constant (around 30 %) if the particle concentration is in the range of 1.5 – 2.2 mmol/l. Small changes in the concentration in this range will not influence the coverage.
- Area B is the area that should be avoided. For concentrations lower than 1 mmol/l the coverage is very low and it cannot be improved by speed change. In this area it is not possible to obtain coverage higher than 20 %.
- Area C is the area where it is possible to produce higher coverage (around 50 %). This is the area where the concentration is higher than 1.5 mmol/l and where the speed is in the range of 1 – 10 mm/min.

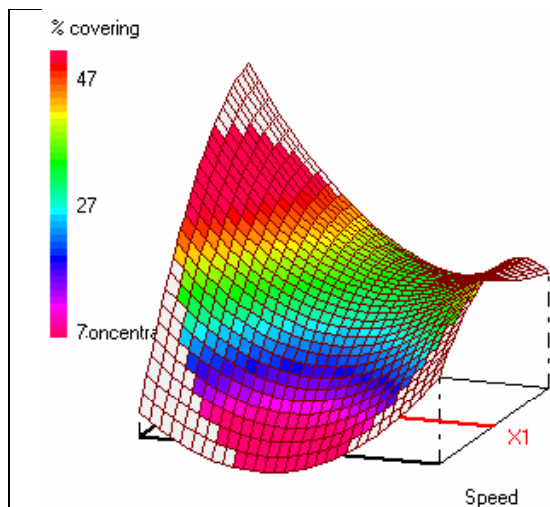


**Fig. 6.8.** *Three-dimensional surface representing response variations (predicted percentage of coverage).*

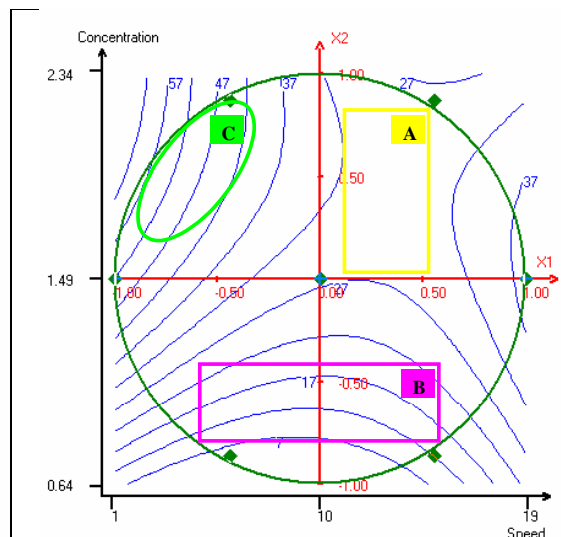


**Fig. 6.9.** *Two-dimensional curves representing response (predicted percentage of coverage) variations (blue lines).*

The use of an experimental design (Doelhart's matrix) allowed us to quickly screen the experimental domain defined by low particle concentrations and a range of speed. The results obtained show that such small concentrations cannot guide to higher coverage of the substrates. Nevertheless, it is possible to produce samples with 50 % of covering. If the concentration of the particle solution is known, this map is very useful for choosing the right speed that allows the production of samples with the best possible coverage. Therefore, one interesting possibility would be to study another experimental domain, using the same method, and moving the concentration range to higher values, from 2 – 4 mmol/l.

#### 6.4. GISAXS investigations

*The GISAXS measurements were done in collaboration with Dr. Andreas Frömsdorf from the Institute for Physical Chemistry of University Hamburg.*

The samples prepared from the particles used in the first set of experiments show good coverage, but the ordering of the particles was less satisfying. According to the literature such behaviour was expectable because of the broad particle size distribution and the shape variation. The particles can be seen in the TEM image shown in the Fig. 6.9. The histogram of

the particles was obtained using the program *ImageJ* (Fig. 6.9. (b)). The statistic shows a main diameter size of  $d = 6.28$  nm and a standard deviation of  $\pm 0.58$  nm.

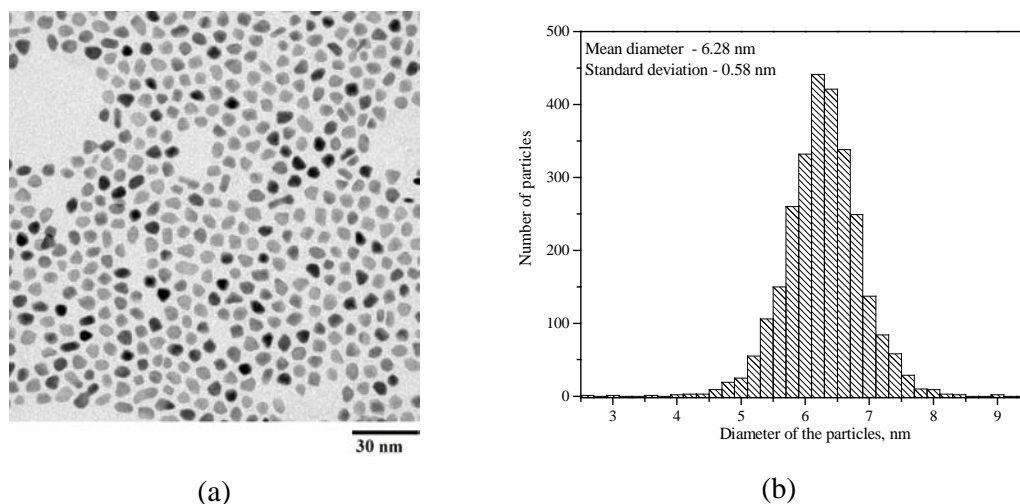


**Fig. 6.9.** *Particles used for the statistical experiment design: (a) TEM image of the particles; (b) histogram of the size distribution of the particles.*

Analysis of the SEM images of prepared nanoparticles films showed that particles give slightly better packing if they are arranged in smaller islands on the surface. Two samples were chosen, one with low percentage of coverage (12 %) and another one with high percentage of coverage (74 %) (Fig. 6.10. (a) and (b), respectively). In both cases particles are packed in monolayer structure. Images of the autocorrelation function show the poor order of the particles. By comparing the curves obtained from the images of the autocorrelation function, it can be confirmed that higher coverage leads to poorer order of the particles. The curve extracted from the autocorrelation image for the first sample shows the first pronounced peak and second almost negligible peak. That indicates lower order. Only the first neighbour distance can be calculated, and the order at longer distances is neglectable. The obtained value of 8.42 nm is a little smaller than in the case of particle packing on a carbon grid. Approximately the same area of the SEM image of the second sample was used for further calculations and the same procedure was applied. In this case already the first peak is minor. This indicates the very small order of the particles. In this case it is not possible to calculate centre - centre distances.

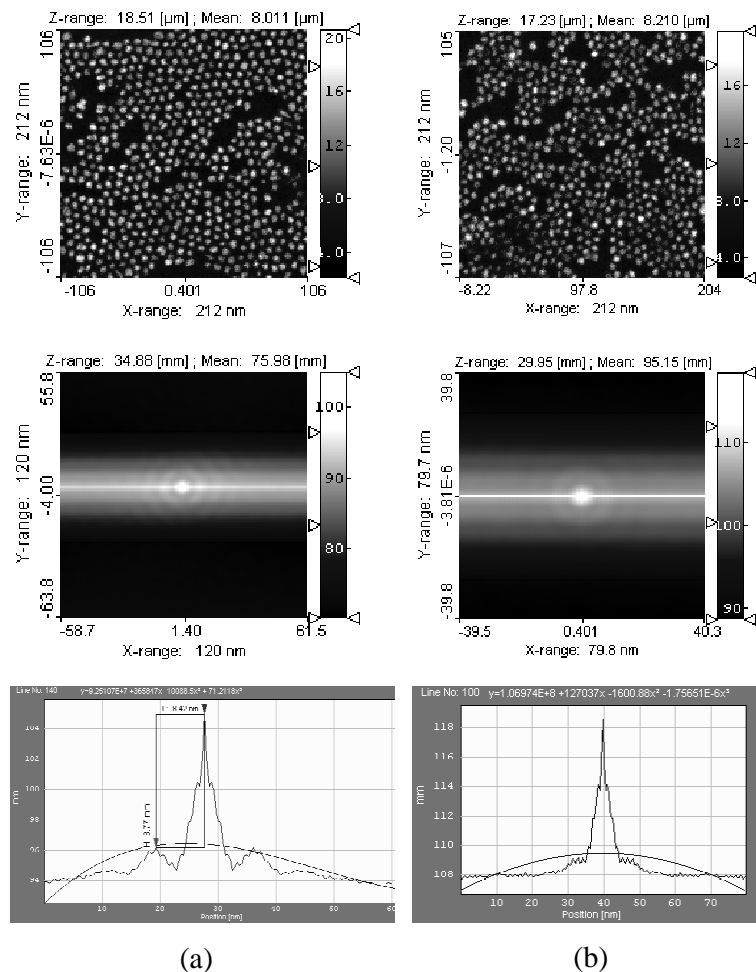


**Fig. 6.10.** Parts of the SEM images at higher magnification (low covered sample (a), and high covered sample (b)) used for analysis by application of the autocorrelation function and by slicing the autocorrelation function in order to obtain curves analogue to the SAXS curves

It was shown that dip coating is useful for the preparation of large areas of  $\text{CoPt}_3$  nanoparticles on silicon. The next step is the preparation of large areas of well-ordered nanoparticles by this technique. Therefore the monodisperse and well defined particles with an average diameter of  $d = 6.4$  nm (calculated from XRD) were used in order to investigate the applicability of dip coating to the preparation of highly ordered 2D structures. The layer was prepared from a hexane solution ( $c \approx 4$  mmol/l) on a hydrophobic substrate with a speed of 10 mm/min. As it was expected the results were significantly different. The SEM image shows highly ordered areas of the particles on the silicon surface. The particles are packed in a hexagonal lattice and form a monolayer. The high order is also recognizable from the auto correlation image and the adequate curve (Fig. 6.11.).

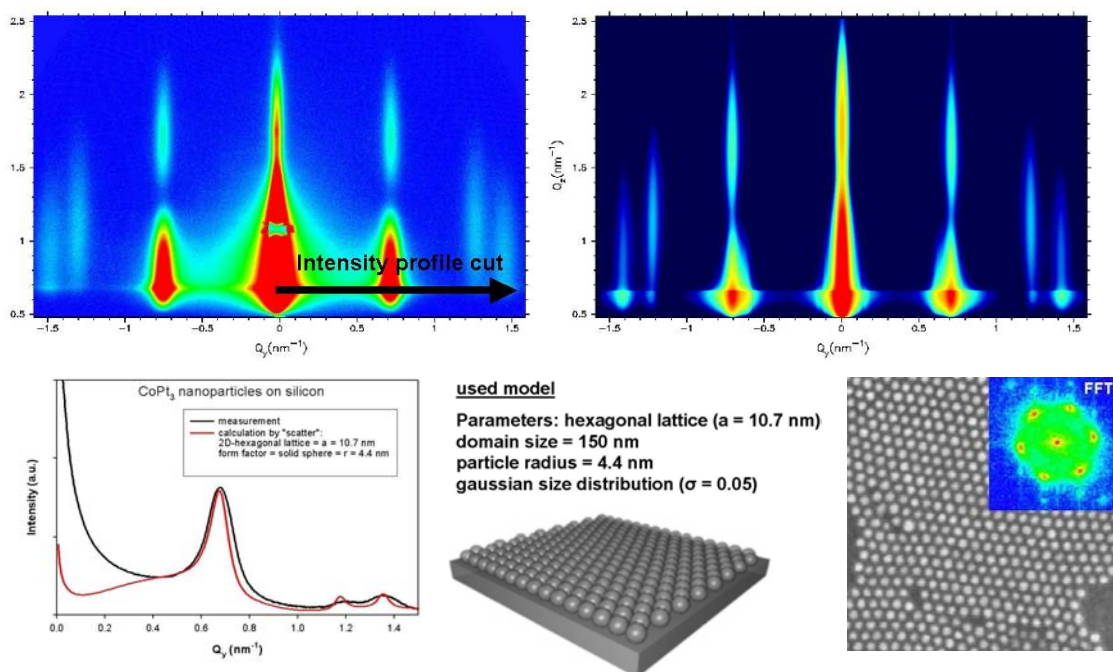


**Fig. 6.11.** Example of a 2D nanoparticles array- upper left: GISAXS, upper right: IsGISAXS simulation; lower left: intensity profile cut along  $q_y$  and “Scatter” simulation; in the middle of the lower part: used model for simulation; lower right: SEM image and FFT of the sample

The investigated sample shows that it is possible to form a lateral hexagonal wide-range ordered nanoparticle array. This can be seen in the SEM image (and by the FFT) and also in the corresponding GISAXS image, which shows strong hexagonal diffraction peaks. By analysing the scattered intensity along a  $q_y$  cut by using the software “Scatter”<sup>[13]</sup>, it was possible to determine the lateral scales of the structure. Furthermore, a simulation of the diffraction pattern with the software “IsGISAXS”<sup>[14]</sup> was successfully generated and a model with precise length scale parameters was calculated (Figure 6.11.).

The diameter distance calculated from GISAXS measurements is 8.8 nm. The autocorrelation function centre - centre distance is 8.4 nm. The difference in the values is a result of different diameter calculations. The GISAXS method gives average values for large areas of the sample, and the autocorrelation is only based on a small part of the image and depends on the colour scale. The colour scale has influence on the calculated particle sizes (they seem to be smaller).

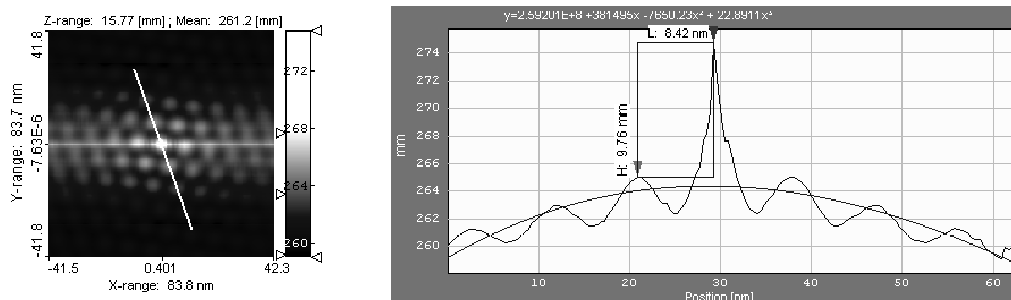


**Fig. 6.12.** *The autocorrelation function and adequate slice (curve) for the sample measured by GISAXS technique*

The SEM image of the sample prepared by deposition of  $\text{CoPt}_3$  nanoparticles from hexane solution onto silicon shows additionally that particles are packed in the smaller domains with different orientation. The same effect was reported also in the literature but for much larger particles (hundreds of nanometers)<sup>[6]</sup>.

### 6.5. Conclusion

Dip coating appears to be a good technique for the production of highly ordered monolayers of  $\text{CoPt}_3$  nanoparticles on silicon substrates. The investigations showed that it is possible to produce highly covered areas of the substrates using this technique with polydisperse particles (with broader particle size distribution). The best results concerning the order of the particles were achieved by using very monodisperse particles. This behaviour was expected. Concerning the coverage it was found that for highly covered areas it is necessary to use particle solutions in hexane with concentrations between 2.5 and 4 mmol/l, and speeds between 1 and 10 mm/min. Lower speed lead to a complete coverage of the surface with several layers, while higher speed lead to monolayers with lower coverage. Also, it was found that the better coverage and order of the particles was received for the particle deposition on the hydrophobic substrates.

### 6.6. Literature:

1. Shukla, N., J. Ahner, and D. Weller, *Dip-coating of FePt nanoparticle films: surfactant effects*. Journal of Magnetism and Magnetic Materials, 2004. **272–276**: p. e1349–e1351.

2. Yoon, T.S., et al., *Single and Multiple-Step Dip-Coating of Colloidal Maghemite ( $\gamma$ - $Fe_2O_3$ ) Nanoparticles onto Si,  $Si_3N_4$  and  $SiO_2$  Substrates*. *Adv. Funct. Mater.*, 2004. **14**(11): p. 1062-1068.
3. Jaramillo, T.F., et al., *Catalytic Activity of Supported Au Nanoparticles Deposited from Block Copolymer Micelles*. *J. Am. Chem. Soc.*, 2003. **125**: p. 7148-7149.
4. Sohn, B.H., T.H. Kim, and K. Char, *Process-Dependent Photocatalytic Properties of Polymer Thin Films Containing  $TiO_2$  Nanoparticles: Dip vs Spin Self-Assembly Methods*. *Langmuir*, 2002. **18**: p. 7770-7772.
5. Hartmann, C.S., *Nanostructuring of Surfaces with Block Copolymer Micelles and Metal Nanoparticles*, in *Fakultät für Naturwissenschaften*. 2003, University Ulm: Ulm.
6. Dimitrov, A.S. and K. Nagayama, *Continuous Convective Assembling of Fine Particles into Two-Dimensional Arrays on Solid Surfaces*. *Langmuir*, 1996. **12**: p. 1303-1311.
7. Darhuber, A.A., et al., *Selective dip-coating of chemically micropatterned surfaces*. *J. Appl. Phys.* **88**(9): p. 5119-5126.
8. Trygg, J. and S. Wold, *Introduction to Statistical Experimental Designe -What is it? Why and Where is it Useful?* 2002.
9. Box, G.E.P., W.G. Hunter, and J.S. Hunter, *Statistics for Experiments: an introduction to Design, Data Analysis and Model Building*. 1978, New York: Wiley.
10. Kheri, A.I., J.A. Cornell, and T. Dekker, *Response Surfaces, Design and Analysis*. 1987, New York: ASQC Quality Press.
11. Mathieu D., P.-T.-L.R., Logiciel, *NEMROD. LPRAI*. 1999: Marseille.
12. Doehlert, D.H., *Appl. Stat.*, 1970. **19**: p. 231.
13. Förster, S., et al., *J. Phys. Chem. B*, 2005. **109**: p. 1347.
14. Lazzari, R., *IsGISAXS: a program for grazing-incidence small-angle X-ray scattering analysis of supported islands*. *J. Appl. Cryst*, 2002. **35**: p. 406–421.

## Chapter 7

### Langmuir-Blodgett technique

#### 7.1. Principle of the Langmuir-Blodgett technique (LB technique)

The LB technique (named after the American scientists Irving Langmuir<sup>[1]</sup> and Katherine Blodgett<sup>[2]</sup>) is a method used to create a molecular film of a surfactant at the air-water interface and to transfer it onto a solid substrate. The surfactant is spread onto the water surface with a highly volatile solvent. After solvent evaporation the amphiphilic molecules start to organize. At this point, the molecules need space and the film is not continuous<sup>[1]</sup>. Then a barrier on the water surface pushes the molecules. A feedback (Wilhelmy plate) controls the position of the barrier and thus the pressure. Before this step, the pressure-area isotherms of the surfactants must be studied, in order to obtain information about the stability of the film, the reorientation of the molecules, the phase transitions and the conformational transformations. After this step, the deposition on a solid substrate can be performed (Fig 7.1).

There are several parameters that influence the type of the produced LB film. These are: the nature of the spread film, the subphase composition and temperature, the surface pressure during the deposition and the deposition speed, the type and nature of the solid substrate and the time the solid substrate is stored in air or in the subphase between the deposition cycles.

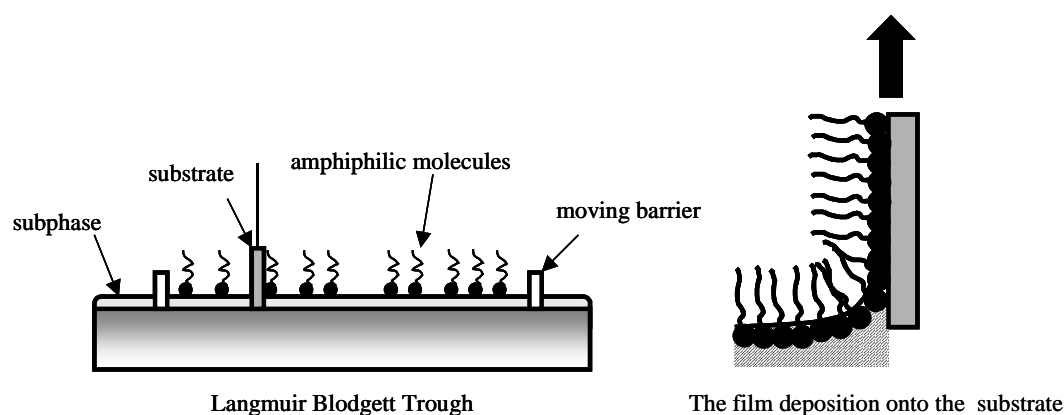


**Fig. 7.1.** Schematic presentation of Langmuir film formation at the Langmuir-Blodgett trough, and Langmuir-Blodgett film deposition onto a substrate

## 7.2. The materials suited for the LB technique

The LB technique, by definition, requires amphiphilic molecules to be trapped at the interface of two phases. The amphiphilic molecules are composed of a hydrophilic part (carboxylic acids, sulphates, amines and alcohols etc.) and a hydrophobic part (usually alkyl chains). The hydrophilic parts are attracted to a polar medium such as water and the forces acting upon them are predominantly coulomb type ( $1/r^2$ ). Hydrophobic groups, such as hydrocarbon chains, fats and lipids are much less (if at all) water soluble and the forces acting upon them are predominantly Van der Waals type ( $1/r^{12}$  and  $1/r^6$ )<sup>[3]</sup>.

A surface monolayer will only be achieved if the amphiphatic balance of the molecule is correct; that is the balance between hydrophobic and hydrophilic parts. If the hydrophobic 'tail' group is too short (not hydrophobic enough) the molecules will be dragged into the water and will dissolve. Whereas if there is no hydrophilic part, the molecules may form thicker multilayers films on the surface or even evaporate. The materials, which have been studied extensively as floating monolayers, are the carboxylic acids and their salts and long chain alcohols.

## 7.3. Subphase

The subphase mostly used for the study of monomolecular films is ultra pure water, which has strong intermolecular interactions and thus a high surface tension (tendency of the liquid to reduce its surface area). Any factor, which decreases the strength of this interaction, will lower the surface tension. Hence, an increase in the temperature of this system will lower the surface tension. Any contamination, especially by surfactants, will also lower the surface tension. Other high surface-tension liquids that have been used as subphase include ethyleneglycol, glycerol and mercury.

## 7.4. Isotherms

As already mentioned a very important step before film deposition onto the substrate is the study of pressure-area isotherms. The isotherms are the plot of surface pressure versus area occupied per molecule. The term isotherm is used because compression takes place at constant temperature. The shape of the isotherm is characteristic of the molecules that form the film and provides a two-dimensional "fingerprint".

A number of distinct regions are immediately obvious examining the isotherms. These regions are called phases. The isotherms usually consist of three distinct phases: gas, liquid and solid. The phase behavior of the monolayer is mainly determined by the physical and chemical properties of the amphiphile, the subphase temperature and the subphase composition. For instance, various monolayer states exist depending on the length of the hydrocarbon chain and the magnitude of other cohesive and repulsive forces existing between the head groups. As an example for a better explanation of the distinct phases the isotherm of stearic acid is chosen (Fig. 7.2.).

After initial spreading onto the subphase, no external pressure is applied to the monolayer and the molecules behave as a two-dimensional gas, which can be described by:

$$\pi A = KT$$

where  $\pi$  is the surface pressure,  $A$  the molecular area,  $K$  the Boltzmann constant and  $T$  is the thermodynamic temperature.

Further compression of the monolayer leads to some ordering of the molecules and the film behaves as expected of a two-dimensional liquid. The first molecules are packed in a so-called “liquid-expanded state”. Incrementally closing the barrier and reducing the area of the monolayer leads to a transition to the “liquid-condensed” state. At even higher densities the monolayer finally reaches the solid state. This solid state is characterised by a steep and usually linear relationship between the surface pressure and the molecular area. If the monolayer is further compressed after reaching the solid state, it will collapse into three-dimensional structures. The collapse is generally seen as a rapid decrease in the surface pressure or as a horizontal break in the isotherm if the monolayer is in a liquid state. The collapse pressure,  $\pi_c$ , can be defined as the maximum to which a monolayer can be compressed without the detectable expulsion of molecules from the Langmuir film.

When the monolayer is in the two-dimensional solid or liquid condensed phase the molecules are relatively well oriented and closely packed and the zero-pressure molecular area ( $A_0$ ) can be obtained by extrapolating the slope of the solid phase to zero pressure. The point of intersection with the x-axis is the hypothetical area occupied by one molecule in the condensed phase at zero pressure<sup>[3]</sup>.

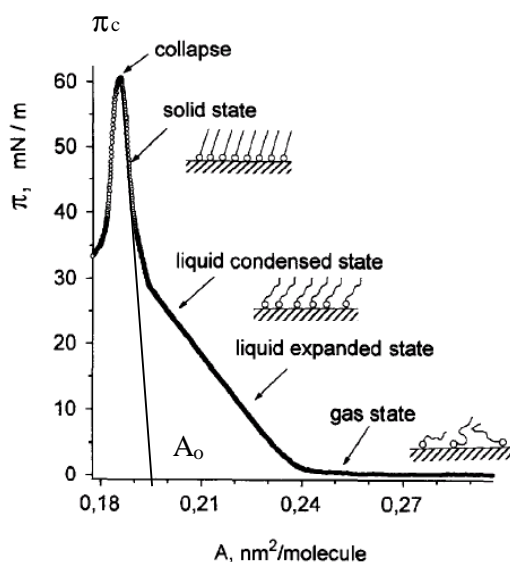


**Fig. 7.2.** Pressure-area isotherm for a stearic acid. Langmuir monolayer with different intralayer physical states and schemes of the molecular packing<sup>[3]</sup>

Once the monolayer has reached a selected  $\pi$  at the air-water interface, which involves a specific molecular orientation, it could be transferred onto solid substrates to fabricate mono- or multilayered LB films. When the substrate moves below the monolayer at the air-water interface, the monolayer is deposited onto the solid substrate. A monolayer at the air-water interface can be transferred by an up-move onto a hydrophilic surface and via a down-move on to a hydrophobic surface.

### 7.5. Application of the LB technique

The LB-technique is one of the most promising techniques to prepare thin molecular monolayer films. This technique enables the precise control of the thickness, homogeneous deposition of the monolayer over large areas and the possibility to make multilayer structures with varying layer composition. An additional advantage of the LB technique is that monolayers can be deposited on almost any kind of solid substrate<sup>[4]</sup>. Due to these characteristics, the LB technique has been widely used to handle and assemble different functional molecules in a predefined manner with the aim of e.g. fabricating molecular devices, or investigating physicochemical processes occurring in the monolayer at the gas-substrate interface<sup>[5],[6-12]</sup>.

Research groups throughout the world are currently investigating many possible applications of Langmuir-Blodgett films in the fields of electronics, optics, molecular

electronics, and biotechnology<sup>[13]</sup>. To emphasize the wide variety of materials that can be employed with these techniques in some cases the reviews address specific issues such as the thin organic film preparation<sup>[14]</sup>, producing of supramolecular structures involving inorganic compounds combined with organic materials, particularly in the case of mixtures of metal complexes with polymer films<sup>[15],[16]</sup>; the applications in electro optics, sensors and nonlinear optical devices<sup>[17],[18]</sup>; as well as some fundamental experiments in which LB films have served as model surfaces to study interactions<sup>[17]</sup>.

### 7.6. Langmuir – Blodgett films of nanoparticles

Inorganic nanoparticles can be assembled at the air-water interface by various routes. Muraly Sastry in his review classified these routes into physical and chemical assembly methods<sup>[19]</sup>. This classification is illustrated schematically in Fig. 7.3. In the physical assembly method, the nanoparticles are synthesised separately (commonly as a colloidal solution) and depending on the type of organization, the nanoparticles' surface is modified by chemisorptions of suitable surfactant molecules. The nanoparticles, which are hydrophobic, and soluble in non-polar organic solvents can be spread on the surface of water like conventional amphiphilic molecules, compressed to a closed-packed configuration and transferred by LB method onto different substrates. On the other hand, if the nanoparticles are water-soluble and capped with hydrophilic groups, they may be taken in the aqueous subphase and their surface functionality is used to complex with Langmuir monolayers at the air-water interface via electrostatic or hydrogen bonding and other interactions.

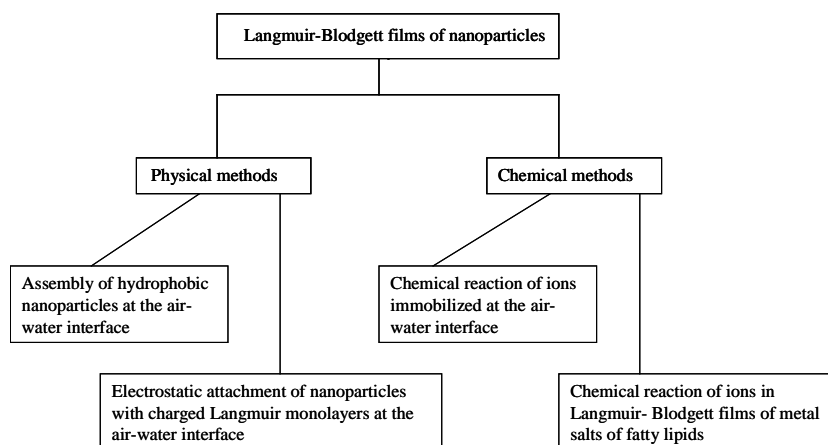


**Fig. 7.3.** The classification of different methods used for LB film preparation from nanoparticles<sup>[19]</sup>

The second (chemical) method requires assembly of ions at the air-water interface followed by chemical reaction with the ions either in situ at the air-water interfaces or after formation of LB films of the ion-amphiphilic complex. A number of reactions can be considered leading to the formation of metal, metal sulphide, and metal oxide nanoparticles in lamellar superstructures<sup>[15],[16]</sup>.

The coating of the nanoparticles is an important factor in the ability of such particles to form monolayers with well-defined surface pressure-area isotherms. When the hydrophobicity is too low, the particles sink. If the coating is too hydrophobic the particles tend to stick to unwanted aggregates.

The transfer of the nanoparticles onto substrates is a very complex process and it is governed by many parameters. It does not mean that Langmuir layers and deposited layers will adopt an identical structure. It can even occur that the corresponding structures are completely different. The probability for structural changes during the deposition is linked to the rigidity of the system. Structural changes are more likely to occur in less rigid structures which are quite sensitive to details of the local environment. Rigid structures lack this sensitivity, and structural changes with deposition are less likely to occur. However, it is still a challenge to establish proper deposition conditions for stiff systems and LB films of such materials commonly exhibit a fairly high number of defects such as domains or grain boundaries<sup>[17]</sup>.

#### 7.7. Langmuir – Blodgett films of CoPt<sub>3</sub> nanoparticles prepared on water as a subphase

The film preparation by spin coating and dip coating technique was used as a first approach for film preparation due to their relative simplicity and possibility for production of films on bigger surfaces within short periods of time. Unlike these two methods, the Langmuir-Blodgett technique requires more time and has much more parameters that influence the quality of the films what makes this technique more complex. Apart from that, LB technique provides more possibilities for optimization of the film preparation. In recent times this technique combined with micro contact printing has been more and frequently used for the formation of 2D-patterned monolayers of Au<sup>[20]</sup>, Pt/Fe<sub>2</sub>O<sub>3</sub><sup>[5]</sup> and Co<sup>[21]</sup> nanoparticles. The aim of the work shown in this chapter was to investigate the conditions for production of large areas of close-packed and well-ordered particles on air-water surface.

The usual LB technique implies the film preparation by deposition of the particles onto the water. Different approaches can be chosen depending on the particle behavior. If the particles are hydrophobic they can be simply deposited onto the water surface<sup>[21],[22]</sup>. Some organic molecules can be used as a Langmuir film which helps to deposit the particles from the solution<sup>[23],[24]</sup>. If the particles are water-soluble they should be first transferred from water to an organic solvent and then be deposited onto the water surface<sup>[25],[26]</sup>.

Due to their solubility in organic solvent, the CoPt<sub>3</sub> nanoparticles could be directly deposited onto the water surface. As already known two ligands are present on the particle surface (ACA and HDA): adamantanecarboxylic acid is water-soluble and it does not behave amphiphilic. Hexadecylamine shows amphiphilic behaviour due to the carboxylic chain of 16 C atoms and the amino group at the one end of the molecule. Therefore, these molecules can form the Langmuir layer.

To obtain the typical isotherm for HDA very dilute chloroform solution was made ( $c = 0.08$  mol/l) and 110  $\mu$ l of the solution was spread at the water-air interface using a micro syringe. Compression of the film was performed after chloroform evaporation (approximately after 10-15 min). The surface pressure versus area ( $\pi$ -A) isotherm for the Langmuir film made from HDA shows three typical phases: gas phase above the 12 cm<sup>2</sup>/particle, liquid phase between 3 and 12 cm<sup>2</sup>/particle and beginning of the solid phase below 3 cm<sup>2</sup>/particle. The collapse pressure is approximately 40 mN/m (Fig. 7.4.).

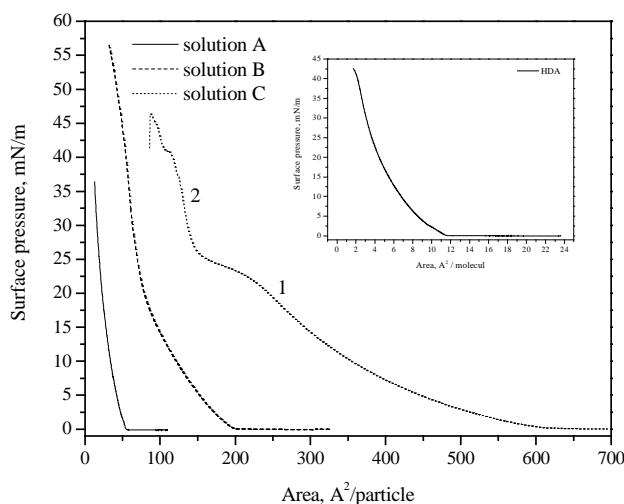


**Fig. 7.4.** The isotherms of Langmuir films for a film formed from HDA solution (inserted graph) and from solutions A, B and C with different particle to ligand ratio. Numbers 1 and 2 locate the pressures at which the films were taken.

To get Langmuir film of particles on the water surface and transfer a monolayer film on a substrate it is necessary to have a very stable particle solution. It is found that high concentrated solutions of the particles lead to precipitation or very quick agglomeration on water.

The particle washing procedure, which precedes the particle deposition, leads to removal of excess of ligands. This lack of ligands can influence the particle agglomeration. It is known that the stability of the magnetic nanoparticles against aggregation, both in solution and in films, depends on the relative magnitudes of the competing interpartical attractive and repulsive forces<sup>[25]</sup>. Therefore, it is necessary to find the balance between the particle concentration and the amount of ligands in the solution to produce stable Langmuir films. Three different solutions are made starting from a particle solution with concentration of  $c \approx 0.01 \text{ mol/dm}^3$ , adding the certain amount of ligand solution ( $c = 0.0016 \text{ mol/dm}^3$ ) and dissolving everything in chloroform. Different amounts of the ligand solution were mixed with the same amount of the particle solution and three different solutions were obtained. The ratio between the amount of HDA and the particles in the solutions is given in Table 7.1. With these ligand concentrations, stable Langmuir films of particles are obtained. It should be mentioned that the particles have a specific amount of ligands on the surface after the washing procedure, but this amount is constant because the same particle solution has always been used.

Table 7.1. The ratio between the amount of HDA and particles in the prepared solutions

Solution	$n_{\text{HDA}} : n_{\text{particles}}$ [mol:mol]
A	1 : 6.0
B	1 : 2.5
C	1 : 1.2

The curves from these three different solutions are shown in Fig 7.4. Comparing the isotherms of the pure HDA and the particles with the lower amount of additional ligands it can be observed that the isotherms are similar and show a slope change around 40 mN/m, which is in agreement with the collapse of the HDA film. The presence of particles changes the slope of the isotherm, suggesting that the obtained film is less rigid. The added amount of the particles is not sufficient to change the curve shape drastically. Nevertheless, in the

presence of higher ligand amounts the isotherm shape changes and two plateaus appear. The first plateau appears at 25 mN/m and the second, but smaller plateau at 40 mN/m, just below the complete collapse of the curve at 48 mN/m. The plateau, which appears at 25 mN/m is probably a consequence of the ligand molecules, and/or particles rearrangement on the surface, or the collapse of one of the phases and their extraction from the surface. Supposing that the film collapses, the reduction of the collapse pressure can be explained by smaller free volume available on the subphase surface to achieve equilibrium of the film. Thus, with a higher initial concentration of ligands and particles on the subphase, molecular freedom is restricted and equilibration of the particle film during compression is retarded<sup>[25],[27]</sup>.

The first samples are taken at the pressure just below the first plateau (noted with number 1 in Fig. 7.4.). This plateau probably appears due to the beginning of the particle agglomeration. The next series of samples is taken out at higher pressure (34 mN/m), below the curve collapse (noted with number 2 in Fig. 7.4.). The films formed at higher surface pressure were simultaneously deposited on three different surfaces in order to investigate the influence of the surface properties on the film formation.

The images of the films deposited on Si wafers at lower pressure show significant influence of ligands since two different areas are observed: one area with only organic phase and another with only particles. The particles are packed in (more or less) ring structures (brighter areas on the image), which are always surrounded by organic regions on the substrate (the darker areas on the image) (Fig. 7.5. (a)). Similar ring structures of close-packed particles in a hexagonal lattice, but with different quality, are obtained by deposition of Langmuir films onto a carbon grid for TEM images (Fig. 7.5. (b)).

The increase of the surface pressure does not lead to better film quality. Again large areas without particles are observed leading to the conclusion that a significant amount of stabilizer prevents from formation of large particle areas (Fig. 7.5. c, d and e). The domains consisting of pure surfactant molecules are observed at all stages of compression. Such behavior could be typical for a nanoparticles–ligand system and it has also been observed for some other particles spread onto water surfaces as for example Pt, Pd and Pt/Pd particles<sup>[28]</sup> or Ag particles<sup>[27]</sup>.

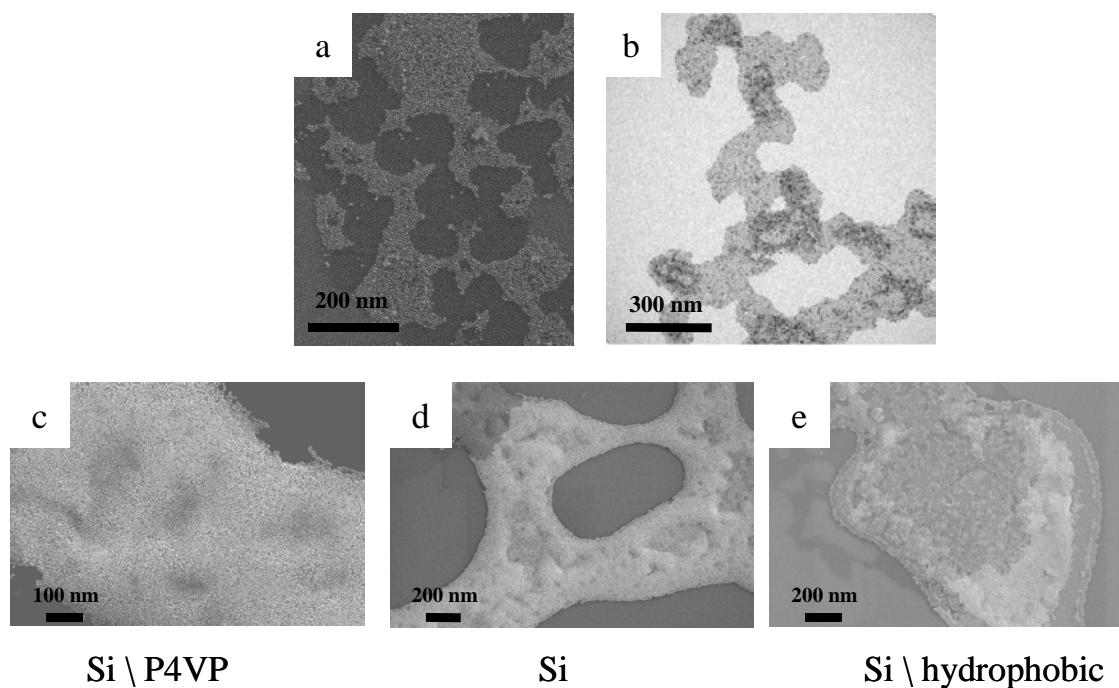


**Fig. 7.5.** SEM images of the films deposited on silicon at lower pressure (a), and on three different surfaces at higher pressure (c, d and e; all scales are 100 nm), as well as TEM image of the film deposited on a carbon grid at lower pressure (b).

The SEM images of the films deposited onto different surfaces show almost the same particle behavior. The particles are usually packed in multilayered structures. This behavior is less pronounced for the samples prepared at lower pressure. The covering of the samples is not satisfactory for any of the surfaces. It appears that the substrate surface does not influence much the packing of nanoparticles, since in all three investigated cases the similar quality is observed.

#### 7.7.1. Particles stabilised with sorbic acid

*The following work concerning GISAXS measurements and evaluations of data was done in collaboration with Prof. Dr. J. Falta and Dr. J. I. Flege (University Bremen).*

Even though HDA is a good ligand and can be used as an amphiphil in LB technique it does not give good quality films. In order to obtain large areas of close-packed particles, the particles with different ligands are probed and sorbic acid is employed to produce LB films. (The procedure for ligand exchange of HDA/ACA with SA is given in the experimental part).

This acid is short and it does not behave as an amphiphile, and therefore it will not give films on the air-water surface. Preventing a ligand film formation onto the air-water surface, it might be possible to increase the area of well-packed particles.

The  $\pi$  - A isotherms of the films, which were prepared from stock solutions of  $\text{CoPt}_3$  ( $d = 5.2$  nm) nanoparticles stabilized with sorbic acid are shown in the Fig. 7.6. Different amounts of the particle solution were spread on the LB trough. All isotherms show small plateaus between 6-8 mN/m. The surface pressure of the plateau does not change with increasing the particle concentration. The plateau region can be interpreted in terms of a transition from monolayer to multilayer particle packing. Further, the film compression leads to the particle agglomeration in large scale, which is visible even with the eye. This behavior is different from the particles stabilised with HDA/ACA

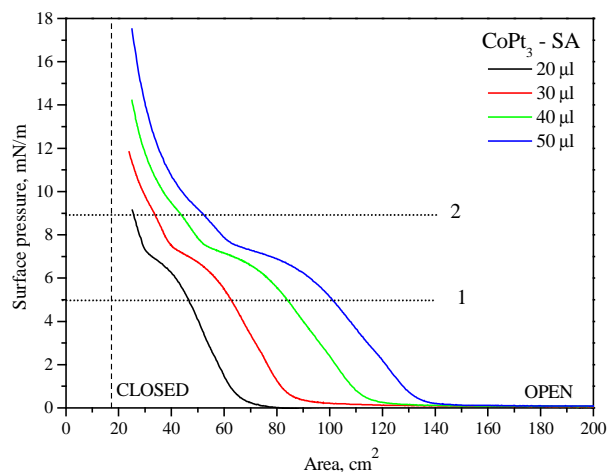


**Fig. 7.6.** The pressure area isotherms for films obtained by spreading different volumes of  $\text{CoPt}_3$  - SA solution in chloroform. “Closed” and “open” denote the positions of the barrier at the beginning and at the end of the compression. The lines marked 1 and 2 are the surface pressures at which the samples were taken.

The samples were taken at two different pressures to obtain additional knowledge about the particles behaviour. Three samples were taken at 5 mN/m (Fig. 7.6. line 1) with different dipper speeds and one sample at the higher pressure 9 mN/m (Fig. 7.6. line 2) where agglomeration is already expected, due to the isotherm shape. All samples were subsequently investigated by SEM technique. The SEM images of the samples taken at 5 and 9 mN/m with the same dipper speed of 1 mm/min are shown in Fig. 7.7. The images (a) and (b) show a larger overview of the samples and (c) and (d) a closer view on the particle packing. In both

cases the coverage of the surface is small and different types of structures are obtained. At lower pressure the structures are ring-like, while compressing the particles to higher surface pressure leads to more chain-like structures, which is similar to the behavior of the particles stabilized with HDA/ACA.

Having a closer look on the particle packing, it is difficult to say which pressure leads to multilayer packing. In both cases some amount of multilayers is present. It is expected that higher pressure lead to larger areas with double-layered particles. In the obtained experimental data such behavior is not observed and it can be concluded that these structures are present from the very beginning. They are not influenced by surface pressure but rather they are a consequence of a delicate balance between the hydrophobic and hydrophilic properties of the particles. The particles should not be too hydrophilic; otherwise, they cannot stay at the water surface. On the other hand, the excessively strong hydrophobic interactions would result in a strong interparticle aggregation, which is probably the case in this particular system<sup>[28]</sup>.

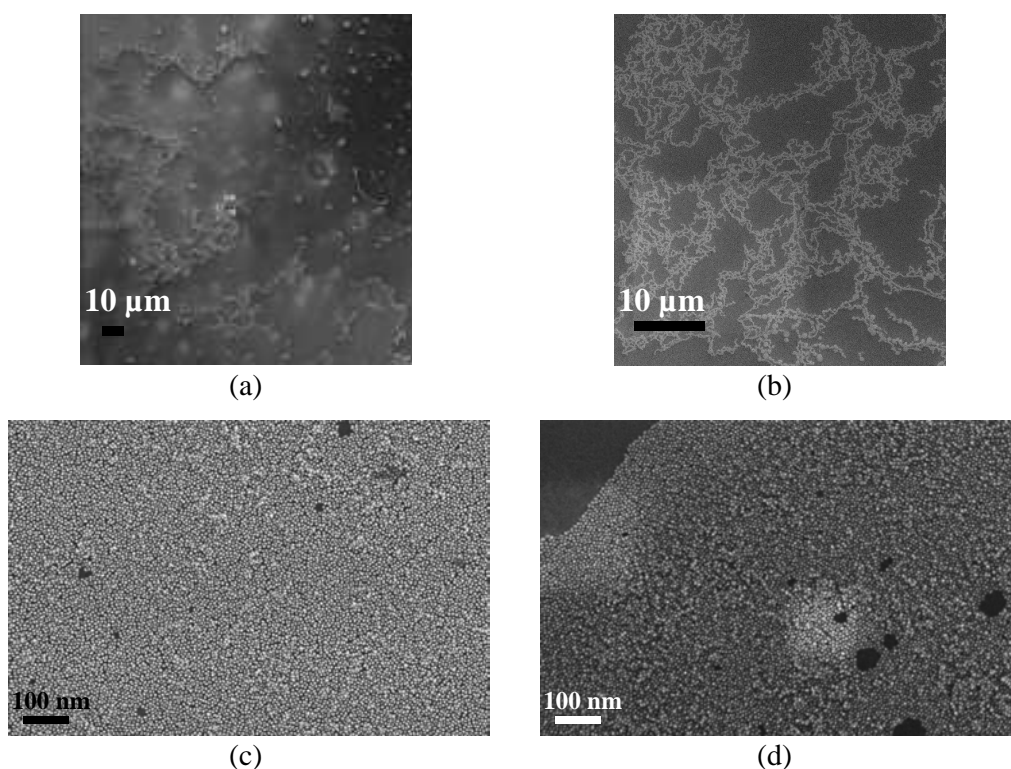


**Fig. 7.7.** SEM images of the Langmuir-Blodgett films of  $\text{CoPt}_3$ -SA nanoparticles deposited onto silicon, under a pressure of 5 mN/m (a and c) and 9 mN/m (b and d), respectively

To gain a better insight into the particle packing and the particle-particle distance over the whole sample area GISAXS measurements are performed. Samples with different dipper speeds were investigated, as well as a sample of particles with HDA/ACA ligands prepared

under the same conditions. This sample was taken at 34 mN/m pressure and with the speed of 1 mm/min.

In Figure 7.8. (a), a 2D GISAXS scattering image is shown for the sample stabilized with HDA/ACA. The Al attenuator thickness was chosen in such way that the intensities of the specular reflected beam and the so-called Yoneda peak<sup>[29]</sup> match the intensities of the features found at  $q_y = \pm 0,76 \text{ nm}^{-1}$ . These features are a direct evidence for a lateral correlation of the CoPt<sub>3</sub> nanoparticles adsorbed on the SiO<sub>2</sub> surface. Moreover, the shape of the scattering features under consideration is rod-like with a decreasing intensity in the  $q_z$  direction, which is comparable with the model of a monolayer of nanoparticles (Chapter 6.).

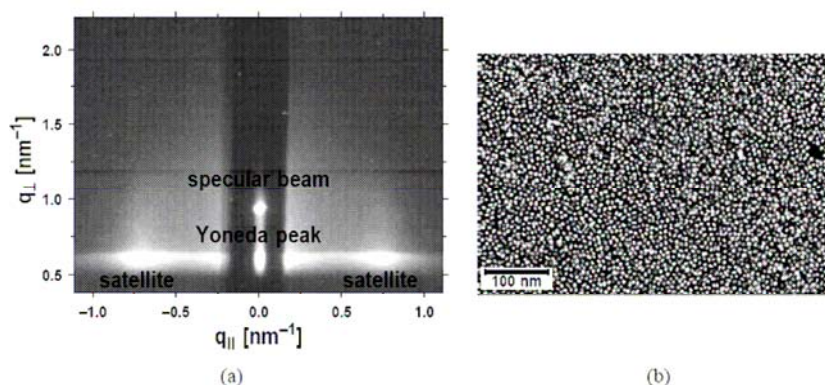


**Fig. 7.8.** (a) GISAXS image of CoPt<sub>3</sub> nanoparticles adsorbed on SiO<sub>2</sub>/Si (001) by LB technique. The images are taken at an incident angle of  $\alpha_i \approx 0,6^\circ$  using 8 keV photons. The vertical black stripe indicates the position of the semi-transparent Al absorber. (b) High-resolution SEM image of the same sample as investigated in (a). Nanoparticles appear bright in contrast.

The analysis of the data presented in Fig. 7.8 (a) according to the simple Born approximation yield an average particle-particle distance of  $\langle d \rangle = (8.23 \pm 0.06) \text{ nm}$  and a correlation length of  $\xi = (22.3 \pm 1.2) \text{ nm}$ , respectively. In Fig. 7.8. (b) a high-resolution SEM image of the same sample is displayed. Qualitatively, the particles form a defective close-packed assembly. In accordance with the determined value for the correlation length, long-range order is absent. By calculating the autocorrelation function of the SEM data an average particle-particle distance of approx.  $7.8 \pm 0.5 \text{ nm}$  could be derived, which is in good agreement with the GISAXS result. A closer view shows a fraction of the sample surface in which the film of nanoparticles covers almost the complete substrate. However, this is not representative for the whole sample surface.

Table 7.2: Structural parameters derived from GISAXS data as functions of the retraction speed  $v$  for CoPt<sub>3</sub> nanoparticles adsorbed on SiO<sub>2</sub> by Langmuir-Blodgett technique.

Sample	$v$ mm/min	$\langle d \rangle$ nm	$\xi$ nm	$I_{\text{norm}}$ a.u.
a	1	$8.23 \pm 0.06$	$22.3 \pm 1.2$	1.00
b	5	$8.21 \pm 0.08$	$22.5 \pm 2.1$	0.33
c	10	$8.23 \pm 0.15$	$23.7 \pm 4.9$	0.13

A series of GISAXS and large-scale SEM images of CoPt<sub>3</sub>-SA adsorbed on silicon using different retraction speeds  $v$  is presented in Fig. 7.9. The analysis of the GISAXS images yields virtually identical particle-particle distances  $\langle d \rangle = (8.23 \pm 0.06)$  nm,  $(8.21 \pm 0.08)$  nm, and  $(8.23 \pm 0.15)$  nm, respectively. Since the corresponding correlation lengths only vary between  $(22.3 \pm 1.2)$  nm and  $(23.7 \pm 4.9)$  nm, which lie within the error bar, the ordering properties of the nanoparticle films may be regarded as independent of the dipper speed. Hence, the particle ordering on the surface in this case cannot be improved by choosing a slow dipper speed.

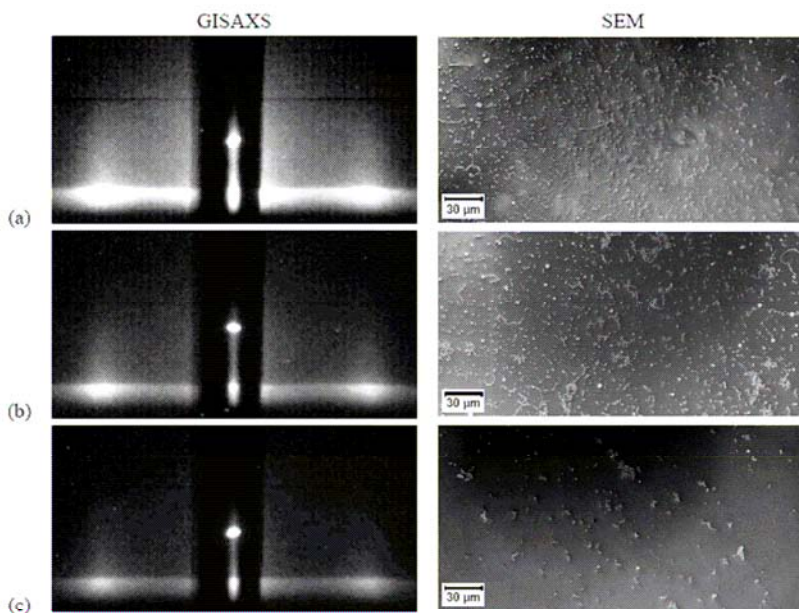


**Fig. 7.9.** GISAXS scattering patterns and large-scale SEM images of CoPt<sub>3</sub> nanoparticles adsorbed on SiO<sub>2</sub>/Si(001) by Langmuir-Blodgett technique using different retraction speeds  $v$ . The GISAXS data were taken at an incident angle of  $\alpha_i \approx 0,6^\circ$  using 8 keV photons with identical exposures. (a):  $v = 1$  mm/min. (b):  $v = 5$  mm/min. (c):  $v = 10$  mm/min. The nanoparticle islands appear bright in the SEM images.

These findings suggest that the particle configuration on the substrate surface is already pre-defined by the self-organization of the nanoparticles in the compressed Langmuir film at the surface of the Langmuir-Blodgett trough. However, the satellite peak intensity  $I_{\text{norm}}$  tremendously decreases as a function of the retraction speed, as can be seen in Table 7.2. Therefore, it is concluded that the change in intensity is directly related to a change in the overall nanoparticle coverage. This interpretation is justified by inspection of the corresponding series of SEM images as given in Fig. 7.9. A steep decrease in surface coverage with increasing dipper speed is observed. Interestingly, even with the slowest dipper speed applied in the sample preparation no fully coherent film could be produced. This result indicates that higher coverage might be obtained by further reducing of the retraction speed below 1 mm/min. Unfortunately, the used LB trough cannot operate with lower dipper speed and the investigations were not performed. Another possibility is to use subphases with different pH values and investigate whether it is possible to obtain better coverage.

#### 7.7.2. Particles with different polymer ligands

In order to obtain different distances between the particles, the organic ligands that surround them were exchanged. After the syntheses, ACA and HDA that were present on the  $\text{CoPt}_3$  surface were exchanged with poly(ethylenoxide)-amine (PEOA,  $M_n = 3200$  g/mol), and poly(ethyleneoxide)-diamine (PEODA;  $M_n = 1500$  g/mol). Langmuir-Blodgett films were prepared by compression of  $\text{CoPt}_3$  particles at the air-water interface into a film. Using a slow dipping rate of 1mm/min the films were transferred onto silicon wafers at constant surface pressures.

Areas covered with particles stabilized with polymers are much smaller in comparison with areas covered by particles stabilized with shorter ligands (SA, HDA/ACA). The particles stabilized with PEOA form dense-packed particle domains. PEODA as ligand improves the particle interconnection and generates network-like structures. Nevertheless, in all cases the coverage of the surface is not satisfactory and the particle-particle distance does not change significantly, which was confirmed by GISAXS measurements (Tab. 7.3.). These results indicate that the particle-particle interactions are much stronger than the interactions between the particles and polymers. Furthermore, during the deposition procedure, the particles seem to be attracting and pushing polymer molecules.

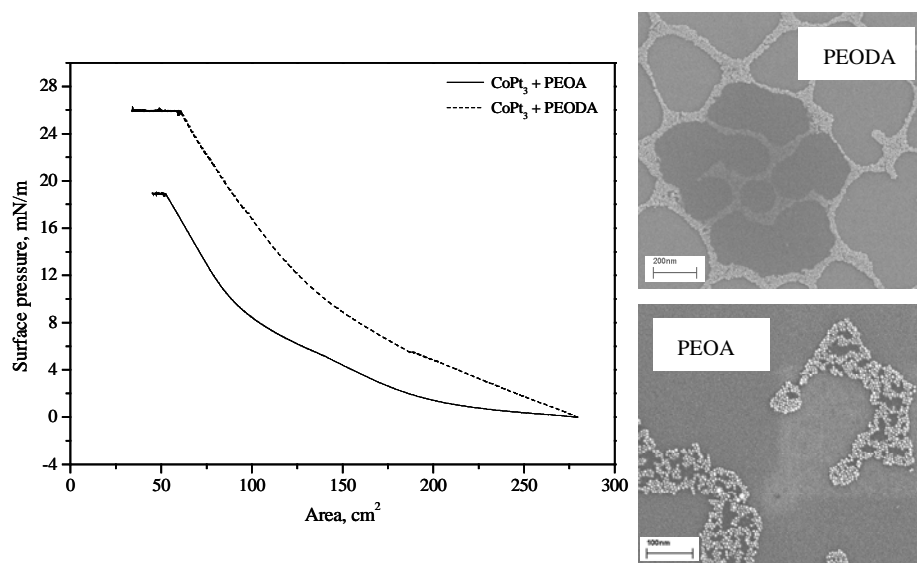


**Fig. 7.10.** The SEM images of the films taken from the Langmuir films of CoPt<sub>3</sub> nanoparticles stabilized with different polymers, and the surface pressure-area isotherms for both samples.

Table 7.3: Structural parameters derived from GISAXS data for CoPt<sub>3</sub> nanoparticles stabilized by different polymers and adsorbed on SiO<sub>2</sub> by Langmuir-Blodgett technique.

Sample	$\langle d \rangle$ nm	$\xi$ nm	Average domain size nm
CoPt <sub>3</sub> - PEODA	6.93	16.5	46.7
CoPt <sub>3</sub> - PEOA	6.42	16.1	45.5

A possible solution to overcome these problems is to use less flexible polymers, which are more firmly attached to the particles (via chemical bonding, for instance). However, the question of poor coverage still remains a problem. In the next part a solution, which gave excellent results will be presented.

#### 7.8. Langmuir – Blodgett films of CoPt<sub>3</sub> nanoparticles prepared on different glycols as a subphase

Although formation of stable LB films onto a water surface is possible, the quality of the obtained films was not satisfactory considering the substrate coverage. It is not possible to produce large areas of well-ordered particles. To overcome this problem, instead of water as a

subphase, different glycols are tried: ethyleneglycol (EG), diethyleneglycol (DEG) and triethyleneglycol (TEG).

For the first investigations the same solutions (noted as B and C) used for film preparation onto water are used for spreading the particles onto glycols (previous chapter). The solution B ( $n_{\text{HDA}} : n_{\text{p}} = 1 : 2.5$ ) with a particle concentration of  $4.2 \cdot 10^{-4} \text{ mol/dm}^3$  and a ligand concentration of  $1.7 \cdot 10^{-4} \text{ mol/dm}^3$ , that gave nice isotherms on the water surface (Fig. 7.4.), behaves totally different on the ethylene glycol surface. It is considerably less sensitive to the area reduction and it abruptly goes from the gas to the solid phase where particles immediately agglomerate (isotherm is not shown). In order to overcome this, the solution C ( $n_{\text{HDA}} : n_{\text{p}} = 1 : 1.2$ ) with a higher ligand concentration is used ( $c_{\text{HDA}} = 3.1 \cdot 10^{-4} \text{ mol/dm}^3$ ). Different amounts of this solution were spread onto ethylene glycol and the surface pressure-area isotherms were measured. Langmuir films were obtained after increasing the amount of solution almost four times in comparison with the amount spread onto the water surface. The obtained isotherms have a different shape than the isotherms for water subphase (Fig. 7.11.).

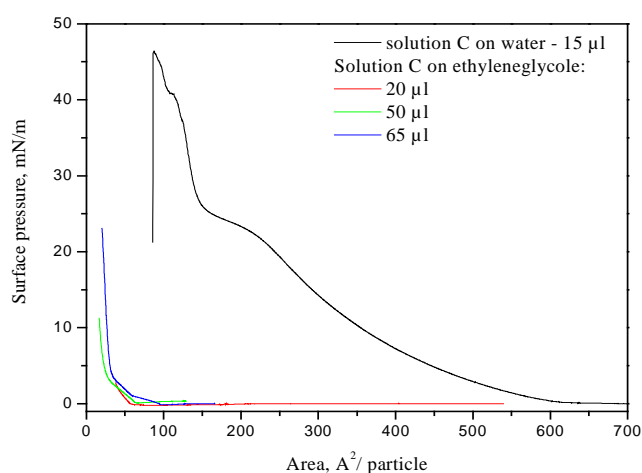


**Fig. 7.11.** *The surface pressure-area isotherms for films formed by spreading different amounts of solution C onto ethylene glycol.*

The increase of surface pressure starts at much lower areas compared to films on the water surface, and it changes suddenly the slope at approximately 4 mN/m and becomes steeper. This rapid change of the slope suggests a transition from one phase into another, i.e. from liquid to solid state. Such behaviour of particles indicates that to reach their solid state a higher amount of spreading solution compared to water is necessary. Another possibility is to

use more concentrated solutions. The isotherms show that larger amounts of nanoparticles occupy smaller areas on the glycol surface in comparison with water. The ligand effect is not as pronounced as in the case of the films spread onto the water surface. Therefore it can be concluded that particles and ligands are less dispersed on the glycol surface and the ligand-ligand and ligand-glycol interactions are considerably different due to the higher ligand solubility in glycol than in water. The larger ligand solubility causes a removal of ligand excess into the glycol, leading to smaller amounts of ligands on the surface. Smaller surface concentration of ligands allows the particles to come closer to each other and pack better.

Similar behaviour of particles is observed using DEG as a subphase. In this case it is necessary to increase the amount of spread solution (solution C) more than 16 times in order to obtain the surface pressure that suggests the formation of a Langmuir film. The formation of Langmuir films on TEG from the same starting particle solution is not possible even if much larger amounts of solution are spread. The particles and ligands seem to be absorbed by the subphase and therefore it is not possible to form films on the TEG surface. The reason for the different behaviors of the nanoparticles on the glycols that almost have the same chemical composition lies in their difference in polarity. Increasing the number of monomer units from 1 for EG to 3 in TEG results in decreasing the influence of OH groups at the end of the molecule chains and therefore decreasing the polarity of the molecule in total. Since nanoparticles are soluble in “non-polar” organic solvents they are also “soluble” in TEG.

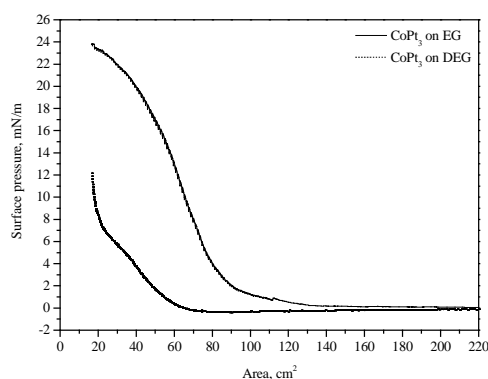


**Fig. 7.12.** The surface-pressure isotherms obtained by spreading the same amount (20  $\mu\text{l}$ ) of the  $\text{CoPt}_3$  nanoparticles solution ( $c = 0.01 \text{ mol/dm}^3$ ) onto different glycols: EG and DEG

All experiments lead to the conclusion that the influence of the ligands on the surface pressure is less dominant on the glycol surface than on the water surface (Fig. 7.11.). Interactions

between the particles and free ligands are less pronounced and both of them start to pack in more ordered structures after compression at low areas in comparison with water. Therefore, glycols are a much better subphase for the production of Langmuir films from CoPt<sub>3</sub> nanoparticles.

In order to investigate which glycol, from the two that can be used for Langmuir film formation, is more suitable, the isotherms of the films formed on both glycols are compared (Fig. 7.12). The surface pressure starts to increase at larger areas in the case of EG when compared to DEG. This indicates that the particles are more spread on the surface. The particles spread onto EG show a transition from the gas to the liquid phase, while in the case of the DEG the same amount of the particles also show the solid state. This indicates a much closer packing of the particles on DEG. Additionally the slope of the isotherm for the diethyleneglycol is less steep curve indicating a less rigid film. According to the literature<sup>[17]</sup> it should be easier to transfer such film onto the substrate and produce a LB film. Therefore DEG is chosen as a subphase for further LB film preparation.

#### *7.8.1. The LB film preparation*

After the particle deposition on the glycol surface and formation of Langmuir films, the next step is to transfer the films from the glycol-air interface onto silicon wafers. For that purpose two different samples concerning the particle size were used (particle diameter approximately 3.5 nm and approximately 6.4 nm, respectively). Both samples were prepared by size selective precipitation of the particles and their redissolving with chloroform, as already described in the experimental part. The films are formed by deposition of the Langmuir films of the particles from DEG to silicon substrate with the dipper speed of 1 mm/min. The surface pressure during sample deposition was in both cases just below the surface pressure at which the particles transfer from liquid to solid state (for smaller particles 5.5 mN/m and for larger 8 mN/m).

The SEM images of the larger areas (a and b) show that almost the complete substrate is covered with particles (Fig. 7.13.). The film consisting of bigger particles ruptured as transferred onto the substrate, while the film formed by smaller particles shows some small islands that were not covered with particles. Besides, 6.4 nm particles showed the tendency to form multilayers, unlike the small particles that are giving mono-layered films (Fig. 7.13. c and d). The small round holes in the layer of the small particles are due to the drying procedure after film deposition. This substrate was dried at 250 °C (just above the boiling

point of DEG) for few hours in order to remove the rest of DEG. Such high temperature leads to DEG boiling and forming of holes in the layer. Additionally at such temperature it seems that the particles start to loose their ordering due to the ligand degradation (more information in the next chapter). The sample prepared from bigger particles was dried at 80 °C under vacuum for approximately 24 h, and the influence of the drying procedure cannot be discerned. There are no holes or other defects in the film caused by the drying procedure. Therefore all further samples were dried in that way.

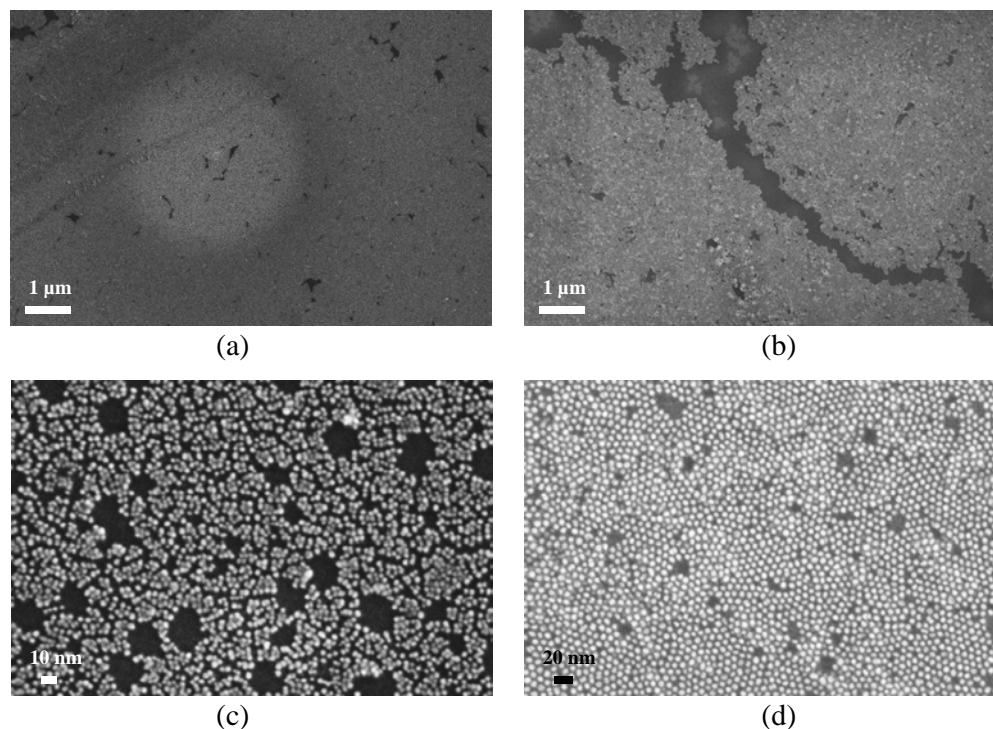


**Fig. 7.13.** SEM images of LB films deposited onto silicon. (a) and (c) - the film made from  $\text{CoPt}_3$  nanoparticles with a diameter of 3.5 nm; (b) and (d) - the film made from  $\text{CoPt}_3$  nanoparticles with a diameter of 6.4 nm;

### 7.8.2. Influence of the substrate angle on the particle deposition

*The GISAXS measurements were done in collaboration with Dr. Andreas Frömsdorf from the Institute for Physical Chemistry of University Hamburg.*

The investigations show that, unlike film preparation on the water surface the film formation on the glycol subphase is strongly dependent on the pressure-time program. Namely, due to higher viscosity of DEG and different interactions between the subphase and

the particles/ligand system, the system needs more time to relax and adapt to the new surface area. In order to obtain a good film quality it is necessary to decrease the surface area step by step and to allow the system to relax and form a better ordering. Therefore different techniques are used for compression of the Langmuir films and their deposition. The particles were first compressed to the desired surface pressure using the program “Isothermal cycle” and then the samples were taken at constant pressure (experimental part). All samples were prepared from the same solution and deposited at the same pressure with the dipper speed of 1 mm/min. The substrates were fixed under different angles, and the angles were varied from  $90^\circ$  (parallel to the subphase surface (Langmuir-Schäffer technique) angle is between the sample and the sample holder) until  $180^\circ$  (normal on the subphase surface). All samples are transferred onto the wafer by dipping it from the subphase at different angles, while the sample under  $90^\circ$  was taken only by touching the surface with the Langmuir layer (compressed to a certain surface pressure) with the substrate being in the position parallel to the film surface.

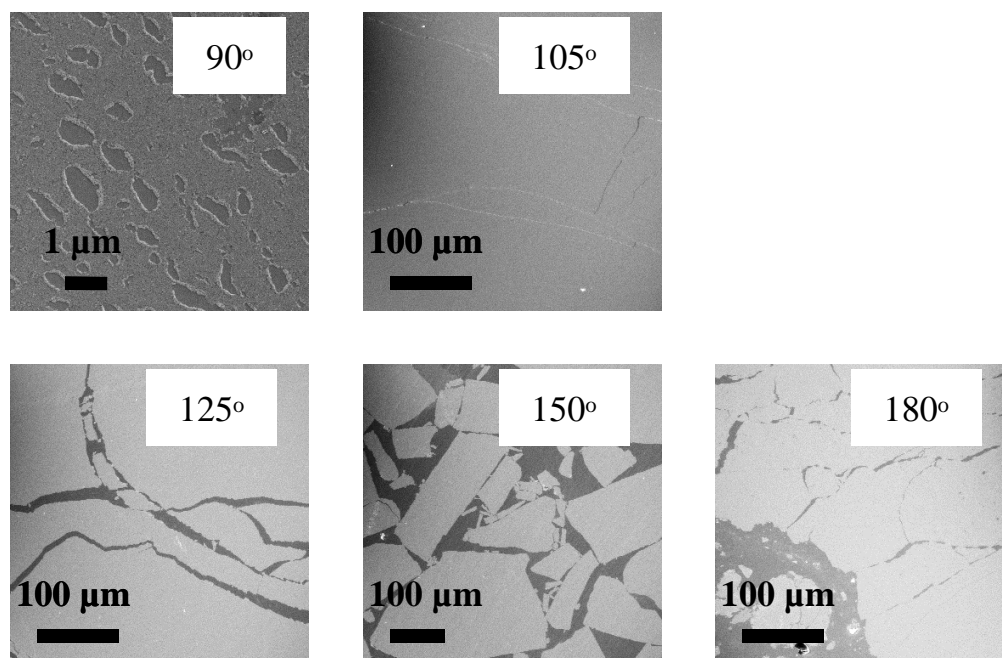


**Fig. 7.14.** SEM images: overview of the LB films deposited under different angles onto silicon wafers. The bright areas correspond to particles and dark areas correspond to the wafer. The dark spherical areas are the places where high-resolution SEM measurements were performed.

The film deposition under  $90^\circ$  results in a film with holes between areas of well-ordered particles. The films taken under bigger angles were broken due to the influence of the substrate angle on the film deposition. The best results, considering substrate coverage, were obtained for the vertical substrate ( $180^\circ$ ) and the substrate fixed under small angle ( $105^\circ$ ), where latter shows better coverage and less ruptures on the surface (Fig. 7.14.).

Since SEM only shows a small area of the films GISAXS analyses are performed in order to investigate better influence of the angle on the particle packing. Two samples (transferred to substrates under  $105^\circ$  and  $150^\circ$ ), which exhibit the best results in SEM concerning the particle packing, were investigated by GISAXS. Additionally, a sample prepared with the bigger particles ( $d = 8.4$  nm) under the same conditions ( $105^\circ$ ) is examined. All GISAXS measurements were done in HASYLAB (Hamburg/Germany). More details about the measurements are given in experimental part.

The GISAXS patterns, the curves obtained by slicing the GISAXS patterns along the  $q_y$  axis, and the high-resolution SEM images of the samples are given in the Fig. 7.15. The curves obtained from GISAXS measurements were analysed by using the software "Scatter"<sup>[30]</sup> and the obtained data are given in the Table 7.3.

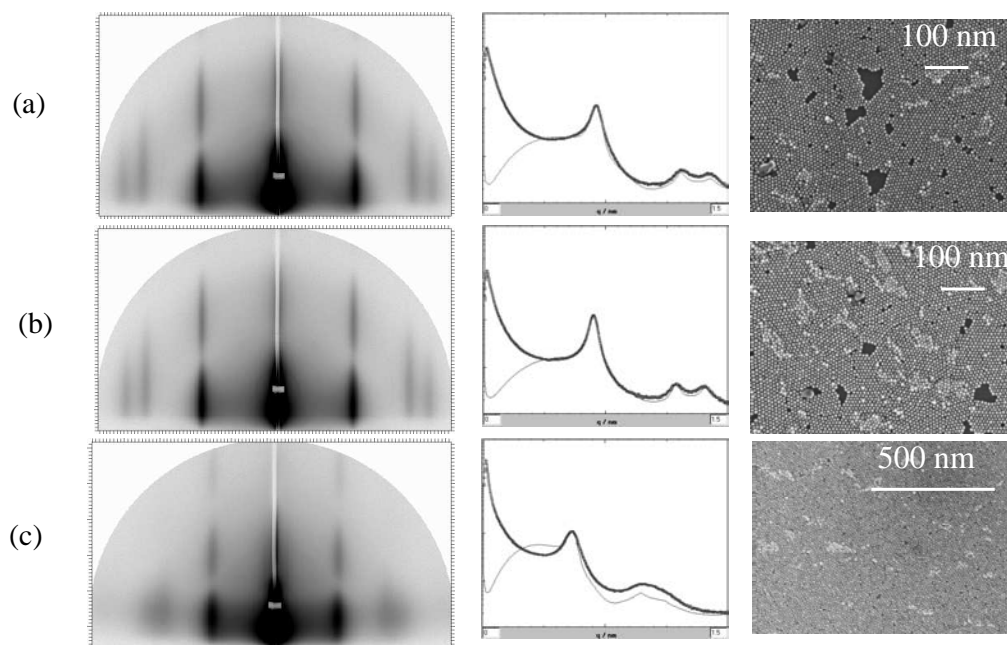


**Fig. 7.15.** The GISAXS patterns, the curves obtained from GISAXS measurements and the fitted curves, and SEM images of the samples:  $\text{CoPt}_3$  nanoparticles ( $d = 6.5$  nm) deposited under  $105^\circ$  (a) and  $150^\circ$  (b) and  $\text{CoPt}_3$  nanoparticles ( $d = 8.4$  nm) deposited under  $105^\circ$  (c).

From a qualitative comparison, it is evident that the GISAXS images for the samples prepared from the smaller particles show a rod-like reciprocal space map corresponding to a very good two-dimensional arrangement of scattering objects. The sample, noted with C, shows less pronounced features at higher values of  $q_y$ , what indicates less ordered structures at longer distances, i.e. a higher relative displacement. The broad and ring-like structures are the result of scattering from an assembly of spherical objects of similar size. In all cases the superposition of the fringes due to the particle shape and the rods arising from the lateral arrangement lead to a better appearance of features in the vertical direction at  $q_y \approx 0.75 \text{ nm}^{-1}$  and at higher values of  $q_y$ .

Tabele 7.3. Data obtained by GISAXS analyses of the samples deposited under different angles on silicon substrate

Sample	Unit cell nm	Radius core/(core + shell) nm	Standard deviation	Correlation length nm	Relative displacement %
A	10.4	4.1/4.6	0.12	60	15.4
B	10.7	4.2/4.6	0.14	100	16.8
C	13.0	5.2/6.0	0.12	80	23.0

Quantitative evaluation of GISAXS patterns (Figs. 7.17.), i.e. fitting the experimentally obtained curves, gives a particle radius of 4.1 nm and a particle-particle distance of 9.2 nm for the first two samples (a and b), and a radius of 5.2 nm and particle-particle distance of 12.0 nm for the last sample (c). The fitted curves were obtained using the model for a hexagonal packing of the spherical particles, and as can be seen from Figure 7.15. the calculated and experimental curves are fitting very well. The calculated values are in a good agreement with the values obtained using the SEM images and the autocorrelation function (Fig. 7.16.). For the samples (a) and (b) the particle-particle distance obtained from SEM images using the autocorrelation function is 8.8 nm and for the sample C it is 12.5 nm.

The correlation length is larger for the sample taken under  $150^\circ$  than for the sample taken under  $105^\circ$  and increases from 60 nm to 100 nm, respectively (Table 7.3.). This suggests that the particles are packed in larger well-ordered domains if the substrate is taken under higher angle during the film deposition procedure.

Besides influencing the ordering of the particles and the size of these well-ordered domains, the angles also have a great influence on the coverage of the substrate. Bigger angles (more vertical substrates) lead to better packing on the micro scale, while on the macro level the films are not compact and they are usually ruptured in more pieces during the deposition. Lower angles (more horizontal substrates) are better for the production of compact films but the ordering is not as good as in the previous case. Consequently, the angle should be chosen depending on the further requests for the film.

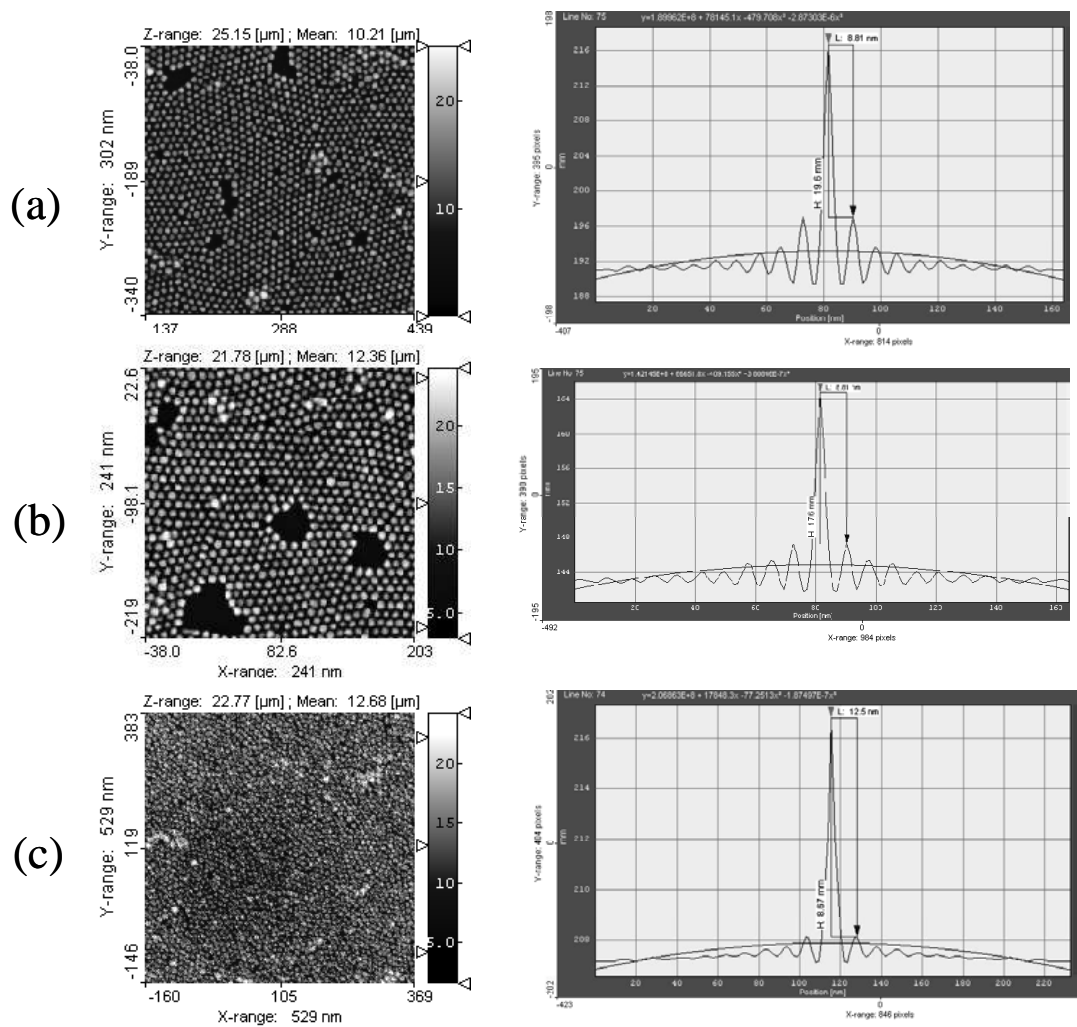


**Fig. 7.16.** Zoomed parts of the SEM images of the samples investigated by GISAXS technique and autocorrelation function calculated from the presented areas.

The angle of  $105^\circ$  was chosen for further depositions of LB films, since it is giving good covering, and a satisfactory ordering of the particles.

### 7.8.3. Influence of the washing procedure on the nanoparticle film quality

The analysis of the isotherms obtained on water and glycol surfaces show an influence of the ligands on the particle packing and film formation. It has been already shown that this influence is very strong if the films are formed on the water subphase, and less dominant if glycols are used. For this reason it was interesting to investigate the influence of the ligands on the film formation onto the DEG subphase. No additional ligands were added to the particles solution used for LB film preparation. In contrary, washing of the particles lead to a smaller amount of ligands around particles. There are two approaches to monitor the effects of the cleaning procedure on the nanoparticles: indirectly, by studying the supernatants after separation of the particles, and directly, by studying the particles themselves<sup>[31]</sup>. Here the second approach was used for the investigation.

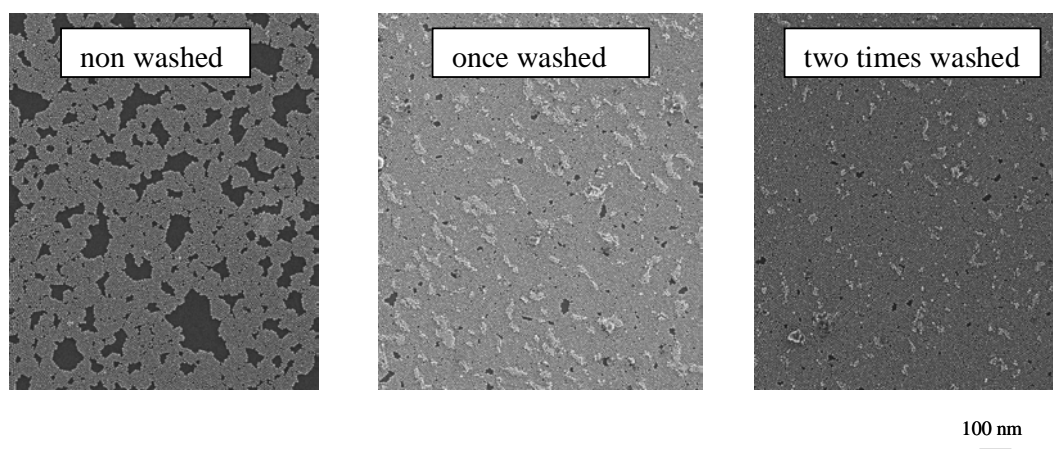


**Fig. 7.17.** SEM images of samples prepared with non washed, once and two times washed particles taken out at angle of  $105^\circ$ .

A solution of monodisperse  $\text{CoPt}_3$  nanoparticles ( $d = 6.4$  nm, calculated from XRD analysis) in toluene was used for the investigation. The first sample was prepared with a solution that was not additionally washed, the second one with a solution washed once (50  $\mu\text{l}$  of particle solution washed with 300  $\mu\text{l}$  of 2-propanol and redissolved again in toluene) and the third one with a solution two times washed (the same procedure as for the previous one). The particle solutions were spread onto the DEG surface and samples were taken on silicon

wafer at a surface pressure that is just below the pressure where the isotherm collapses (non-washed at 5 mN/m, once washed at 11 mN/m, and twice washed at 10 mN/m). The influence of the ligands on the film quality can be observed in the SEM images of the LB films (Fig. 7.17.).

Non-washed particles form films with larger and smaller domains of particles packed in monolayers. On the other hand, films obtained with a solution of washed particles show a good surface coverage, but double layers are observed as well.

A higher amount of ligands does not increase the surface pressure drastically, as that for the solution spread onto water. However, the ligand excess leads to collapsing films at lower surface pressure. This is the main reason why non-washed samples have to be taken out at lower surface pressures in comparison to washed samples. One of the reasons might be the formation of pure ligand domains on the surface. If such domains exist and they are large enough, the resultant monolayers will begin to collapse at lower characteristic collapse pressure<sup>[27]</sup>. Non-washed samples have almost five times more ligands than washed samples (see the Chapter- Ligand exchange-acids). This is the reason for assumption that ligand domains are formed. Difference in the amount of ligands between samples washed one or two times is not drastic, and for this reason the washed particles collapse at almost the same surface pressure.

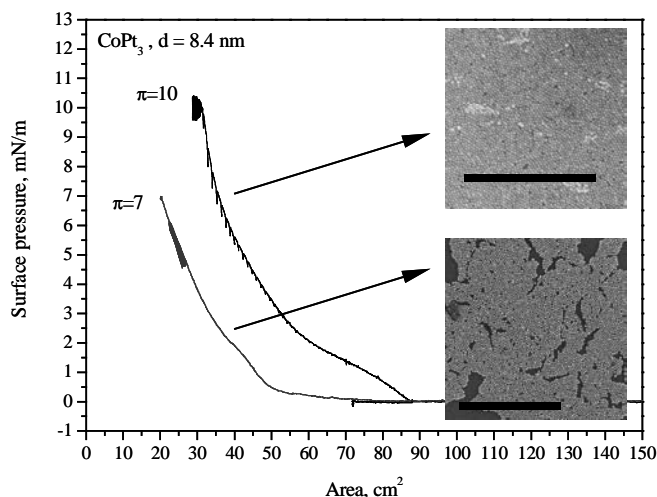


**Fig. 7.18.** The surface pressure-area isotherms and SEM images of the samples taken out at different surface pressures. Both scales are 500 nm.

The films prepared from the washed particles and taken out at different surface pressures show that at lower surface pressures the particles formed monolayers with

uncompleted coverage. The similar behaviour was noticed for different particle sizes. Particles with diameters of 8.4 nm are deposited onto a silicon substrate, with an angle of  $105^\circ$  and from the DEG surface at two different surface pressures: one just below the collapse of the film and another much lower (Fig. 7.18.). At lower surface pressures the particles are packed in large domains as monolayers. These domains are packed closer to each other during the compression and at higher surface pressures compact film can be formed. Some of the domains can overlap on their boundaries leading to the formation of double layers.

The examples demonstrate that non-washed particles give a LB films with poor particle packing and lower coverage of the substrate in comparison to the washed particles. It should be noticed that non-washed particles are packed only as monolayers, in contrast to washed particles. Removing the excess of ligands by the washing procedure gives an opportunity to spread more particles onto the surface and increase the particle concentration. It is already known from literature that higher particle concentration usually lead to overlapping and the formation of double layer in small areas<sup>[32]</sup>.

These investigations can demonstrate that additional washing of the particles is necessary if large areas of well ordered particles are required. Monolayers can be obtained on the whole substrate surface finding the balance between particle concentration and surface pressure at which the sample is taken.

#### *7.8.4. Influence of buffer layers on particle deposition*

Spin coating experiments have shown that the best films concerning the order of the particles have been obtained using polymers with amino groups that serve as anchor points for the particles. The same investigations were done using the LB technique. From literature it is known that gold particles as well as FePt can be successfully deposited using the LB technique onto a layer of block copolymers based on P4VP<sup>[20],[33]</sup>. Therefore, polymer layers were deposited onto silicon by spin coating first under the same preparation conditions as before (Experimental part - Chapter 9). The concentration of all polymer solutions was 0.5 mass %. The same particle solution ( $d = 6.4$  nm) used in previous investigations was used again. The dipper speed was 1 mm/min.

In all cases particles were deposited successfully from the DEG onto substrates coated with different polymers. The substrate coverage was very good and large compact films were produced. Layer deposited on polymer surfaces based on PEOCH<sub>3</sub> show slightly lower coverage. All samples have small aggregates that can be recognised in AFM images as higher

or lower peaks, and in SEM images as small irregular brighter areas. This aggregation can be explained by interactions between the particles. Namely at lower surface pressures the main particle spacing exceeds the distance at which the interparticle potential attracts neighbouring particles, while at high pressures the main particle spacing falls within this distance, and particle aggregate<sup>[31]</sup>. AFM and SEM images of two samples prepared on P4VP and on PEOA as a buffer layers are given in Fig. 7.19., as an example.

According to the AFM images the influence of the characteristic groups in the polymers is not so dominant and they are not as important as for films prepared by spin coating technique. With buffer layer it was not possible to notice considerable differences in particle packing. Polymers do not influence the driving forces, which lead to particle deposition. The quality of the films only depends on the particle concentration and the surface pressure. Such behaviour is very preferable since it enables successful particle deposition on different surfaces. This might be very important for further applications.

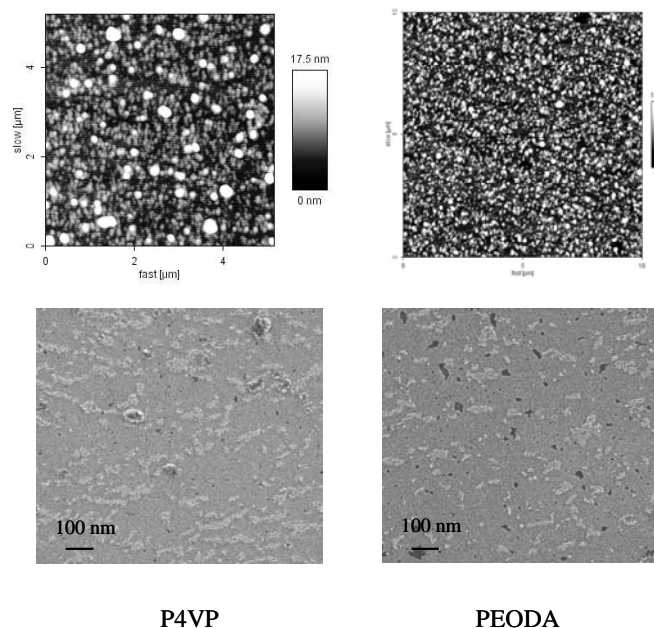


**Fig. 7.19.** AFM and SEM images of samples prepared on different polymer buffer layers (P4VP and PEOA) by LB technique from CoPt<sub>3</sub> nanoparticles under angle of 105°

## 7.9. Conclusion

The presented results have shown that it is possible to deposit CoPt<sub>3</sub> nanoparticles onto water and glycol surfaces and to form Langmuir films on water/air and glycol/air interfaces.

Film deposited on the water/air interface by using the Langmuir – Blodgett technique leads to low substrate coverage. The LB films are highly influenced by free ligands present in the solution. Without ligand excess the particles could not form Langmuir films. At the same time ligand excess prevent the formation of large closed-packed particle films.

LB films of particles deposited onto DEG/air surfaces were successfully transferred onto silicon, as well as onto different polymer buffer layers. High coverage of the substrate and well-ordered packing was obtained with different particle, under different substrate angles and with different amounts of ligands. It was shown that ligands have only a small effect on film formation in comparison to water/air surfaces. Removing of the ligand excess is necessary for the production of highly ordered areas.

The film compactness and particle order are influenced by the substrate angle during the film deposition. Substrates under a bigger angle lead to a better order, while more horizontal substrates lead to a better coverage. Film deposition at lower surface pressures gives monolayers with lower coverage. At higher surface pressures high coverage is observed but with more multilayered areas. This method is very efficient for the deposition as well on silicon as on different polymers based on polyethylene oxide and polyvinyl pyridine. The production of large areas of well-ordered particles on different surfaces can be interesting for a lot of applications.

#### 7.10. Literature

1. Langmuir, I., J. Am. Chem. Soc., 1916. **38**: p. 2221.
2. Blodgett, K.B., J. Am. Chem. Soc., 1934. **56**: p. 495.
3. Martin, P. and M. Szablewski, *Langmuir Blodgett Troughs - operating manual*, ed. N.T. Ltd. 2002, Coventry.
4. LTD, K.I., *Langmuir and Langmuir-Blodgett Films WHAT and HOW?* www. ksvltd.fi
5. Guo, Q., X. Teng, and H. Yang, *Fabrication of Magnetic FePt Patterns from Langmuir-Blodgett Films of Platinum-Iron Oxide Core-Shell Nanoparticles*. Adv. Mater., 2004. **16**(15): p. 1337.
6. Perez, H., et al., *Elaboration and Electrical Characterization of Langmuir-Blodgett Films of 4-Mercaptoaniline Functionalized Platinum Nanoparticles*. Chem. Mater., 2001. **13**: p. 1512-1517.
7. Huo, L., et al., *An organic-inorganic hybrid ultrathin film: preparation and characterization of copper phthalocyanine derivative-ferric oxide nanoparticles*. J. Mater. Chem., 2002. **12**: p. 3268-3274.
8. Hamann, H.F., S.I. Woods, and S. Sun, *Direct Thermal Patterning of Self-Assembled Nanoparticles*. Nano Letters, 2003. **3**(12): p. 1643-1645.
9. Chen, S., *Electrochemical Studies of Langmuir-Blodgett Thin Films of Electroactive Nanoparticles*. Langmuir, 2001. **17**: p. 6664-6668.

10. Achermann, M., et al., *Picosecond Energy Transfer in Quantum Dot Langmuir-Blodgett Nanoassemblies*. J. Phys. Chem. B, 2003. **107**: p. 13782-13787.
11. Greene, I.A., et al., *Electronic Conductivity of Semiconductor Nanoparticle Monolayers at the Air-Water Interface*. 2003. **107**: p. 5733-5739.
12. Zhao, X.K., S. Xu, and J.H. Fendler, *Ultrasmall Magnetic Particles in Langmuir-Blodgett Films*. J. Phys. Chem., 1990. **94**: p. 2573-2581.
13. Kuzmenko, I., et al., *Design and Characterization of Crystalline Thin Film Architectures at the Air-Liquid Interface: Simplicity to Complexity*. Chem. Rev., 2001. **101**: p. 1659-1696.
14. Peterson, I.R., *Langmuir-Blodgett films*. J. Phys. D: Appl. Phys., 1990. **23**: p. 379-395.
15. Ferreira, M., et al., *Encyclopedia of Nanoscience and Nanotechnology*. Vol. 4. 2004. 441-465.
16. Grieve, K., F. Grieser, and D.N. Furlong, *Nanoparticles in Organized Amphiphilic Films*. 639-665.
17. Möhwald, H.M.a.H., *Handbook of Applied Surface and Colloid Chemistry*, ed. K. Holmberg. p: 79-98.
18. Prieto, I., M.T. Martin, and L. Camacho, *New applications and properties of Langmuir-Blodgett films*.
19. Sastry, M., *Colloids and Colloid Assemblies*, ed. F. Caruso: Wiley. p: 369-397.
20. Tanaka, H., M. Mitsuishi, and T. Miyashita, *Tailored-Control of Gold Nanoparticle Adsorption onto Polymer Nanosheets*. 2003. **19**: p. 3103-3105.
21. J. I. Park., W.R.L., S. S. Bae, Y. J Kim, K. H. Yoo, J. Cheon, S. Kim, *Langmuir Monolayers of Co Nanoparticles and Their Patterning by Microcontact Printing*. J. Phys. Chem. B, 2005. **109**: p. 13119-13123.
22. Guo, Q., et al., *Patterned Langmuir-Blodgett Films of Monodisperse Nanoparticles of Iron Oxide Using Soft Lithography*. J. Am. Chem. Soc., 2003. **125**: p. 630-631.
23. Lee, D.K., et al., *Structure and Characterization of Nanocomposite Langmuir-Blodgett Films of Poly(maleic monoester)/Fe<sub>3</sub>O<sub>4</sub> Nanoparticle Complexes*. J. Phys. Chem. B, 2002. **106**: p. 7267-7271.
24. Kang, Y.S., et al., *In Situ Observation of Domain Structure in Monolayers of Arachidic Acid/ $\gamma$ -Fe<sub>2</sub>O<sub>3</sub> Nanoparticle Complexes at the Air/Water Interface*. J. Phys. Chem. B, 2002. **106**: p. 9341-9346.
25. Meldrum, F.C., N.A. Kotov, and J.H. Fendler, *Preparation of Particulate Mono- and Multilayers from Surfactant-Stabilized, Nanosized Magnetite Crystallites*. J. Phys. Chem., 1994. **98**: p. 4506-4510.
26. Lefebure, S., et al., *Langmuir Monolayers of Monodispersed Magnetic Nanoparticles Coated with a Surfactant*. J. Phys. Chem. B, 1998. **102**: p. 2733-2738.
27. Meldrum, F.C., N.A. Kotov, and J.H. Fendler, *Utilization of Surfactant-Stabilized Colloidal Silver Nanocrystallites in the Construction of Mono- and Multiparticulate Langmuir-Blodgett Films*. Langmuir, 1994. **10**(7): p. 2035-2040.
28. Meldrum, F.C., N.A. Kotov, and J.H. Fendler, *Formation of Thin Films of Platinum, Palladium, and Mixed Platinum:Palladium Nanocrystallites by the Langmuir Monolayer Technique*. Chem. Mater., 1995. **7**: p. 1112-1116.
29. Yoneda, Y., Phys. Rev., 1963. **131**: p. 2010.
30. Förster, S., et al., J. Phys. Chem. B, 2005. **109**: p. 1347.
31. Ozturk, B., G.I. Behin-Aein, and B.N. Flanders, *Hard-Disk Behaviour and Beyond in Langmuir Films of CdSe Nanoparticles*. Langmuir, 2005. **21**(10): p. 4452-4457.
32. Huang, S., et al., *Effects of the Surface Pressure on the Formation of Langmuir-Blodgett Monolayer of Nanoparticles*. Langmuir, 2004. **20**: p. 2274-2276.

33. S Sun, S.A., H. F. Hamann, J.-U. Thiele, J. E. E. Baglin, T. Thomson, E. E. Fullerton, C. B. Murray, B. D. Terris, *Polymer Mediated Self-Assembly of Magnetic Nanoparticles*. J. Am. Chem. Soc., 2002. **124**(12): p. 2884.

## Chapter 8

### Ligand removal by thermal treatment of nanoparticle films

---

#### 8.1. Introduction

*(The GISAXS measurements were done in collaboration with Dr. Andreas Frömsdorf from the Institute for Physical Chemistry of University Hamburg.)*

It was shown in previous chapters that it is possible to produce a large area of the closed-packed and well-ordered CoPt<sub>3</sub> nanoparticles on different surfaces. These areas can have electric, magnetic and catalytic properties<sup>[1]-[5]</sup>. The electronic configuration of the nanoparticles core and the magnetic properties of the nanoparticles are influenced by the ligand shell covering the nanoparticles<sup>[1],[3]</sup>. Also for catalytic applications a ligand free particle surface is favourable because it provides better contact between the reactants and the particles<sup>[5],[6],[7]</sup>. Therefore the procedures for the preparation of ligand free particles are of great interest.

Different methods can be used for the ligand removal from the particle surface. The usual methods are: plasma treatment<sup>[3]</sup>, heating<sup>[4],[8],[6],[9],[10]</sup> or various chemical processes which lead to ligand desorption<sup>[9]</sup>.

First investigations on the influence of plasma treatment on CoPt<sub>3</sub> monolayers deposited on silicon surfaces have been described recently<sup>[11]</sup>. Investigations have been carried out using oxygen plasma or a combination of oxygen and hydrogen plasma. Oxygen plasma removes the ligands successfully from the particle surface. Cobalt oxide is formed in this procedure and it can be reduced afterwards to cobalt using hydrogen plasma. Additionally, particles show no agglomeration for powers up to 30 W, and slight agglomeration in the region from 30-100 W (for all investigations the samples were treated with plasma for 5 min). Further studies have to be performed in order to find the optimal conditions for plasma treatment.

## 8.2. Heating of CoPt<sub>3</sub> monolayers deposited on the silicon wafers

The thermal stability and especially the annealing behaviour of CoPt<sub>3</sub> nanoparticles were already investigated. Multilayers of particles were heated in air or under vacuum in order to investigate the particle stability and to find the transition temperature from a disordered to an ordered FCC structure<sup>[12],[13]</sup>. The investigations have shown that particles start to oxidize if they are heated for 2 h at 300 °C in the air. In contrast heating under vacuum prevents oxidation until 500 °C. In this study preliminary results will be described that were obtained by heating of CoPt<sub>3</sub> monolayers on silicon wafers under vacuum for 30 min at different temperatures (300, 400 and 600 °C). The heating time is shorter than in previous investigations because only monolayers are present in this study. In contrast to previous, the main focus of this investigation is the ordering of the particles on the silicon surface.

The previous thermo gravimetric analysis (Chapter 2) has shown that the amount of ligands is very important for the thermal stability of the sample. Ligand excess increases the temperature at which all organics are removed from the surface. For not cleaned samples the temperature used for removal of ligands was around 400 °C, whilst for washed samples the temperature decrease drastically and was around 200 °C. In addition, investigations show that large amount of ligands lead to a larger organic residue (carbon or resins), which can be removed from the particle surface by heating the sample in air. However, this procedure should be avoided due to the easy oxidation of cobalt at higher temperatures.

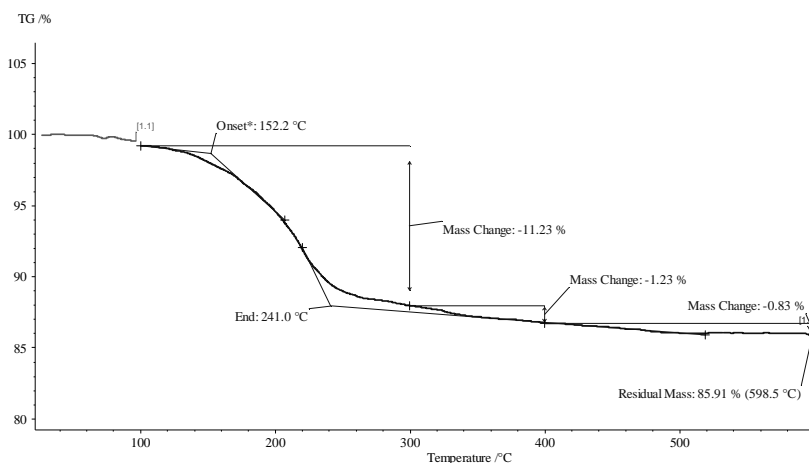


**Fig. 8.1.** TG curve of CoPt<sub>3</sub> nanoparticles used for film preparation. The sample was heated under N<sub>2</sub> with 10 K/min

The sample was washed once before TG measurements using the procedure described in the experimental part (Chapter 9.). The TG curve of the sample is displayed in Figure 8.1. It can be seen that the particles degrade in a one-step process. The amount of ligands is approximately 15 mass %, which indicates that sample is well washed and ligand excess is removed before film preparation.

The TG analysis shows that most of the ligands degrade until 300 °C. A small amount of organic residue can be removed until 400 °C. At 600 °C all organics should be removed. These three temperatures were chosen for further investigation and comparison of particle packing.

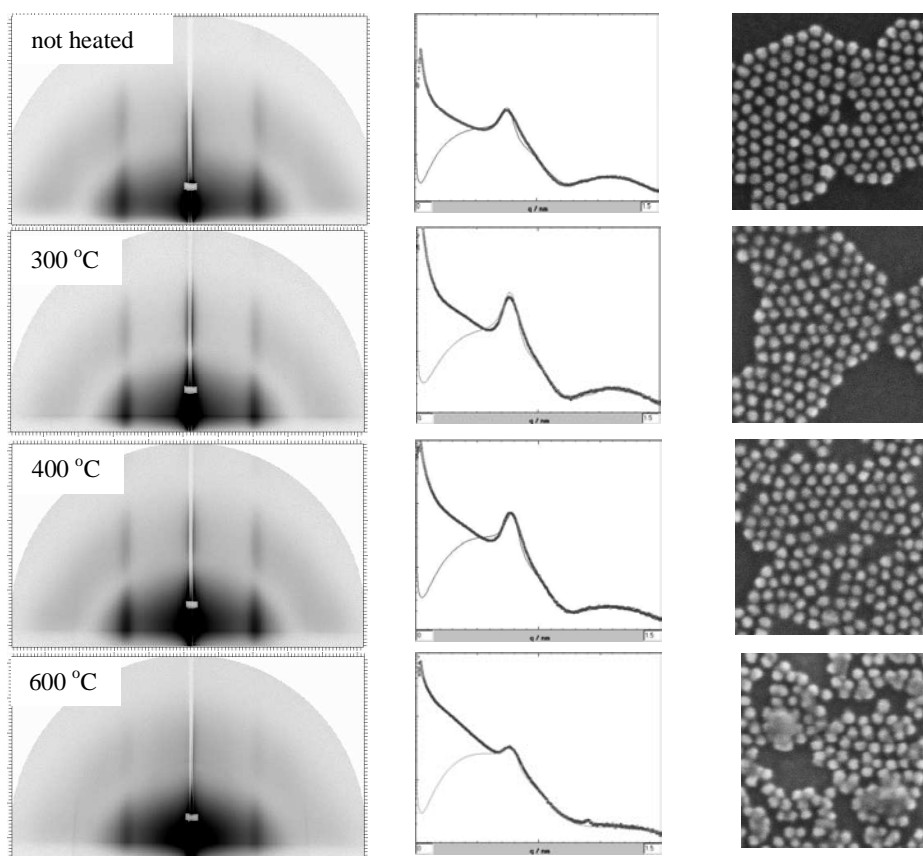


**Fig. 8.2.** GISAXS patterns; experimental and fitted curves and high resolution SEM images of a sample before heating and of samples heated at 300, 400 and 600 °C.

In order to check how particles will behave after ligand removal, the samples prepared by spin coating were first heated to a certain temperature in the oven under vacuum for 30 min. All samples were prepared by spreading 50  $\mu\text{l}$  of the particle solution ( $c \approx 0.02 \text{ mol/dm}^3$ ) in toluene onto silicon wafers using the procedure described in the experimental part. The

coverage of all samples was between 70 and 75 %. After heating the samples were rapidly cooled down using liquid nitrogen in order to freeze the particle position. The samples were afterwards stored in air.

GISAXS technique has been used for the determination of particle ordering on silicon wafers before and after heating. Large areas of the samples (few square millimetres) were investigated by this technique and the GISAXS patterns are shown in Fig 8.2. Additionally, the curves obtained by slicing the GISAXS patterns along the  $q_y$  axis and the high-resolution SEM images of the samples are shown in the same figure. The curves obtained from GISAXS measurements were analysed by using the software "Scatter"<sup>[14]</sup> and the obtained data are given in Table 8.1.

The specific rod-like reciprocal space map indicates a very good, two-dimensional arrangement of particles for the not heated sample, and samples heated until 400 °C. Significant changes can be seen for samples heated at 600 °C. These samples show less pronounced features at higher values of  $q_y$  indicating less ordered structures at longer distances.

Table 8.1. Parameters calculated from GISAXS analysis.

Sample	Unit cell nm	Radius nm	Standard deviation	Domain size	Relative displacement
Not heated	12.6	4.9	0.13	60	19.8
Heated at 300 °C	12.3	4.8	0.11	60	20.3
Heated at 400 °C	12.3	4.9	0.13	60	24.3
Heated at 600 °C	12.3	4.9	0.18	50	26.0

Curves obtained from GISAXS patterns were fitted using the model for ideal spheres packed in a perfect hexagonal lattice. The fitted and experimental curves are in agreement as can be seen in Figure 8.2. The calculations give the same radius (4.9 nm) and the same size of the unit cell for all samples. The domain size does not change until 600 °C and further decreases. This indicates smaller numbers of particles that are packed in ordered domains. By heating the samples at higher temperatures the relative displacement increases from 19.8-26.0 nm. The values for domain size and relative displacement indicate particle movement at the surface and transition from a well ordered to a less ordered structure. All of these results demonstrate that the particles are still good ordered at 300 °C (where the degradation step ended) despite removal of the ligands. Further heating of the samples at 400 °C leads to

ordered structures with a smaller degree of ordering in comparison to the previous one. At 600 °C all ligands are removed and the particles start to melt and to fuse. Consequently, the order of the particles is much lower.

The high-resolution SEM analysis confirms the results obtained by GISAXS. The SEM images show that the particles are well ordered and are packed in a hexagonal lattice before heating. Also it can be noticed that the disturbance of order increases by heating (Fig 8.2.). The particles show significant changes after heating at 600 °C, due to melting and agglomeration of small clusters.

Particle movement at the surface depends on particle-surface interactions. If the amount of interactions decreases, higher mobility and disorder will be achieved. In addition, the length of the ligands is very important. Longer ligands keep the particles on larger distances. In this case it will be more difficult for the particles to agglomerate and fuse after ligand removal<sup>[9],[10]</sup>.

### 8.3. Conclusion

The studies have shown that heating of CoPt<sub>3</sub> nanoparticle films until 400 °C can be used for ligand removal without significant loss of particle order. Higher temperatures (above 400 °C) lead to particles fusion. The heating procedure has several advantages in comparison to the plasma cleaning. It is easier, and it does not lead to particle oxidation if the particles are heated under vacuum.

Further investigations of the film stability in different atmospheres and at broader range of temperatures should be done in order to understand the processes that occur during the heating procedure. Also it will be interesting to investigate the influence of various ligands on the stability of the films as well as the influence of different surfaces.

### 8.4. Literature

1. Beecher, P., et al., *Insulator-to-Metal Transition in Nanocrystal Assemblies Driven by in Situ Mild Thermal Annealing*. Nano Letters, 2004. **4**(7): p. 1289-1293.
2. Zeng, H., et al., *Chemical ordering of FePt nanoparticles self-assemblies by rapid thermal annealing*. Journal of Magnetism and Magnetic Materials, 2003. **266**: p. 227-232.
3. Boyen, H.G., et al., *Electronic and Magnetic Properties of Ligand-Free FePt Nanoparticles*. Adv. Mater., 2005. **17**(5): p. 574-578.
4. Frommen, C., et al., *Synthesis and magnetic properties of CoPt<sub>3</sub> nanoparticles assemblies containing copper*. Materials Letters, 2004. **58**: p. 953-958.

5. Baturina, O., S.R. Aubuchon, and K.J. Wynne, *Thermal Stability in Air of Pt/C Catalysts and PEM Fuel Cell Catalyst Layers*. Chem. Mater., 2006. **18**: p. 1498-504.
6. Luo, J., et al., *AFM Probing of Thermal Activation of Molecularly Linked Nanoparticles Assembly*. J. Phys. Chem. B, 2004. **108**: p. 9669-9677.
7. Raghuvver, V., A. Manthiram, and A.J. Bard, J. Phys. Chem. B, 2005. **109**: p. 22909-22912.
8. Luo, J., et al., *Spectroscopic Characterizations of molecularly Linked Gold Nanoparticles Assemblies upon Thermal Treatment*. Langmuir, 2004. **20**: p. 4254-460.
9. Isaacs, S.R., et al., *Chemical, Thermal, and Ultrasonic Stability of Hybrid Nanoparticles and Nanoparticle Multilayer Films*. Chem. Mater., 2006. **18**: p. 107-114.
10. Supriya, L. and R.O. Claus, *Colloidal Au/Linker Molecule Multilayer Films: Low - Temperature Thermal Coalescence and Resistance Changes*. Chem. Mater., 2005. **17**: p. 4325-4334.
11. Gehl, B., et al., *Design of a UHV-compatible RF plasma source and its application to self-assembled layers of CoPt<sub>3</sub>-nanoparticles*. submitted, 2006.
12. Frommen, C., H. Rösner, and D. Fenske, *Wet- Chemical Synthesis and Properties of CoPt and CoPt<sub>3</sub> Alloy Nanoparticles*. J. Nanosci. Nanotech., 2002. **2**(5): p. 509-515.
13. Shevchenko, E.V., et al., J. Am. Chem. Soc., 2002. **124** (38) p. 11480-11485
14. Förster, S., et al., J. Phys. Chem. B, 2005. **109**: p. 1347.

## Chapter 9

### Experimental part

#### **Synthesis of CoPt<sub>3</sub> nanoparticles**

##### 9.1. Synthesis of CoPt<sub>3</sub> nanocrystals<sup>[1],[2]</sup>

###### **Chemicals**

Toluene, methanol, n-hexane, 2-propanol (all p.a. Merck), diphenyl ether (DPE, 99%, Alfa Aesar), 1,2-hexadecandiol (HDD, 90%, Fluka), 1-adamantanecarboxylic acid (ACA, 99%, Fluka), 1,2-dichlorobenzene (99%, Acros Organics), cobalt carbonyl (Co<sub>2</sub>(CO)<sub>8</sub>), stabilised with 1–5% of hexane, Strem), and platinum(II)-acetylacetonate (Pt(acac)<sub>2</sub>, 98%, Strem), hexadecylamine (HDA, Merck) were of the highest purity available and used as received.

###### **Synthesis of nanoparticles**

High quality CoPt<sub>3</sub> nanocrystals were synthesized via simultaneous reduction of platinum acetylacetonate (Pt(acac)<sub>2</sub>) and thermal decomposition of cobalt carbonyl (Co<sub>2</sub>(CO)<sub>8</sub>) in the presence of 1-adamantanecarboxylic acid (ACA) and hexadecylamine (HDA) as stabilizing agents. The used concentrations were slightly modified in comparison to the preparation method of Shevchenko et al<sup>[1]</sup>.

The synthesis was carried out by using standard Schlenk line technique under nitrogen. 0.033 g of Pt(acac)<sub>2</sub>, 0.13 g of 1,2-hexadecandiol and 0.043 g of 1-adamantanecarboxylic acid were dissolved in a mixture of coordinating solvents (diphenyl ether 2 ml and HDA 4.0 g). The reaction mixture was heated to 65 °C in a three-neck flask until a clear solution was formed (Figure 9.1.). The apparatus was evacuated and flushed with nitrogen three times at 65 °C in order to remove traces of water and oxygen. To produce CoPt<sub>3</sub> nanocrystals, the reaction mixture was heated to the desired temperature, in the range from 140 °C to 220 °C. The cobalt stock solution was injected into the flask under vigorous stirring. The *cobalt stock solution* was freshly

prepared before the synthesis by dissolving 0.043 g of  $\text{Co}_2(\text{CO})_8$  in 0.8 ml of 1,2-dichlorobenzene at room temperature under nitrogen atmosphere. Different temperatures were used in order to control the size and the shape of the  $\text{CoPt}_3$  nanocrystals. After the injection the reaction mixture was heated one hour at the injection temperature, and two hours at 230 °C, in order to improve the crystallinity of the nanoparticles<sup>[1]</sup>. The reaction yield of  $\text{CoPt}_3$  nanocrystals was ~0.030 g after washing.

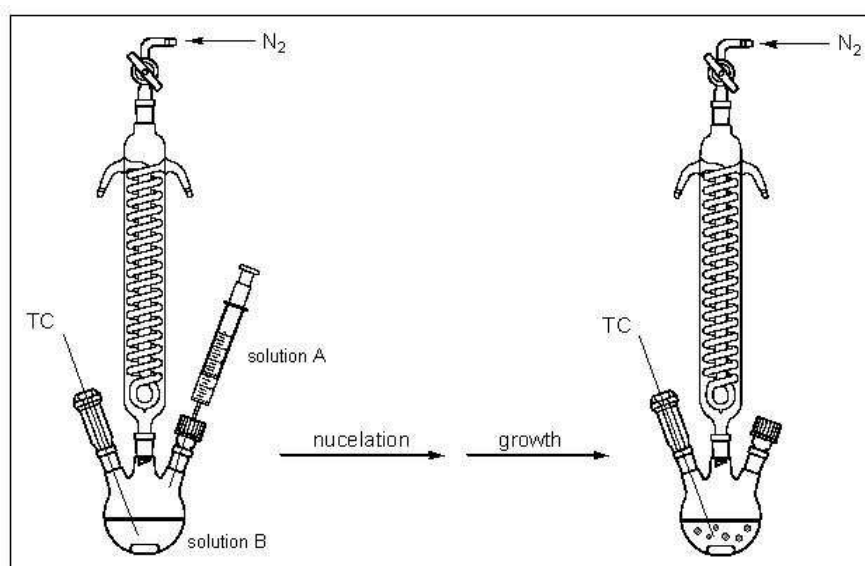


Fig. 9.1. Apparatus for synthesis of  $\text{CoPt}_3$  nanocrystals. Solution B: mixture of HDA, HDD, ACA, DPE and  $\text{Pt}(\text{acac})_2$ ; solution A: solution of  $\text{Co}_2(\text{CO})_8$  in 1,2-dichlorobenzene; TC - thermocouple

## 9.2. Post-preparative procedures

The reaction mixture was cooled down to 60 °C. All subsequent steps were performed in air. The crude solution of  $\text{CoPt}_3$  nanoparticles was mixed with 5 ml of chloroform. Subsequently, 15 ml of 2-propanol were added. The resulting black precipitate was isolated by centrifugation (10 min at 4500 rpm). The purple supernatant was discarded. The precipitate was re-dissolved in chloroform (~2 ml) and the nanoparticles were precipitated again by addition of ~6 ml 2-propanol and centrifugation. The resulting black precipitate containing  $\text{CoPt}_3$  nanocrystals can be re-dissolved in various nonpolar solvents (toluene, hexane, chloroform, etc.). At the end the nanoparticle solution was filtered through a PTFE 0.2  $\mu\text{m}$  filter.

The size distribution strongly depended on the reaction temperature<sup>[1],[2]</sup>. If the synthesis did not yield monodisperse particle size, a selective precipitation was applied by the conventional solvent/nonsolvent precipitation technique<sup>[3],[4]</sup> in order to narrow particle size distribution.

### 9.3. Size selective precipitation

After synthesising and cleaning the CoPt<sub>3</sub> nanoparticles were re-dissolved in chloroform (~ 5 ml) in order to narrow the size distribution by size selective precipitation. The nanoparticle solution was treated with 0.5 ml of 2-propanol and centrifuged. Adding 2-propanol as a non-solvent resulted in gentle destabilisation of the colloidal solution and aggregation of the nanocrystals. Since larger nanocrystals exhibit larger attractive van der Waals forces<sup>[5]</sup> addition of a non-solvent results in aggregation of the largest particles in a given sample, while the particles with smaller sizes are still stable in the solution.

Precipitated nanocrystals were collected and re-dispersed in an appropriate solvent such as toluene, chloroform or hexane. In this way the starting colloidal solution can be divided into ~ 5 to 7 fractions of particles with different sizes and size distributions (5 – 10 %).

### 9.4. Scaling up the reaction

The first set of syntheses yielded approximately 30 mg of particles per synthesis. In some experiments and for some of the analyses it was necessary to use the same particles, e.g. from the same batch. For this reason the reaction was scaled up in order to produce larger amounts of the particles with the same quality. The concentrations of all chemicals, except Co<sub>2</sub>(CO)<sub>8</sub>, were increased two times. It was found that the amount of Co precursor has an influence on the shape and quality of the particles. The use of a larger syringe led to loss of a certain amount of the Co stock solution, smaller amounts of cobalt precursor were suitable for the reaction. This resulted in non-spherical particles and a broad size distribution. Different amounts of Co precursor were investigated and it was found that the best results were achieved with 0.092 g of Co<sub>2</sub>(CO)<sub>8</sub> (7 % higher amount than in the previous synthesis).

### 9.5. Synthesis of CoPt<sub>3</sub> nanoparticles stabilised only with ACA

The same amounts of precursors were used as described before in the scale-up reaction. Only ACA was used as ligand, and the solvent was DPE (12 ml was used) instead of HDA. A solution of Co<sub>2</sub>(CO)<sub>8</sub> was injected at 175 °C, and the reaction mixture was heated one hour at 175 °C and two hours at 230 °C. The particles were cleaned using the same post-preparative procedure as described before.

### 9.6. Ligand exchange with acids

#### **Chemicals**

Sorbic acid (SA, Aldrich), undecanoic acid (UDA, Merck), linoleic acid (LA, Aldrich), arachidic acid (ARA, Aldrich), adamantan carboxylic acid (ACA, 99%, Fluka), hexadecylamine (HDA, Merck), 2-propanol (Merck), chloroform (Merck) were used as a received without any further purification.

#### **Ligand exchange**

CoPt<sub>3</sub> nanoparticles were prepared and cleaned as described before. Before the ligand exchange, the rest of HDA and ACA were washed of as much as possible. In order to remove the ligands already present on the particle surface after synthesis the particles were precipitated by adding three times larger volume of 2-propanol to the stock solution and centrifuged for 10 min. After centrifugation the particles were re-dissolved in chloroform and the same procedure was repeated as many times as were necessary to remove the present ligands.

The cleaned particles were mixed with an excess of “new” ligands dissolved in chloroform. Different amounts of new ligands were used in order to find the necessary amount for the ligand exchange. The number of surface CoPt<sub>3</sub> molecules was calculated based on XRD measurements (related to the particle diameter and the crystal lattice) and thermo gravimetric measurements (concerning the particle to ligand ratio in solution). Experiments showed that the best results were obtained using 50 times higher amount of ARA and UDA and a 100 times larger amount of LA and SA in comparison to the amount of surface CoPt<sub>3</sub> molecules. After mixing the particles with a solution of “new” ligands for approximately 24 hours, unattached ligands were removed. The same amount of “new” ligands was added and the whole procedure

was repeated once more. The excess of LA and ARA after the ligand exchange apparently increases the solubility of the particles in the 2-propanol, making their removal less effective. To overcome this problem, a mixture of 2-propanol and methanol was used (instead of only 2-propanol). After the first washing step particle precipitation was carried out without problems. Similar problem appears in the case of the particles stabilized with SA. Excess of SA was removed with acetone that acts as a better solvent for SA compared to methanol / 2-propanol mixture.

After ligand exchange the particles were re-dissolved in chloroform, filtrated through a PTFE 0.2  $\mu\text{m}$  filter and stored in the refrigerator. Freshly prepared solutions were stable over months. In further discussions these solutions are referred to as non-washed solutions. In further text marks for one or more washing means one or more additional washing steps.

#### 9.7. Ligand exchange - thiols

Particles used in these experiments were first cleaned by the previously described post-preparative procedure. The excess of HDA and ACA present in the solutions was removed by two additional washing procedures, as in the case of ligand exchange with acids. The particles were re-dissolved in 1-2 ml of chloroform and transferred to a three-neck flask. Dodecanthiol (DDT) (5 ml) was added and the mixture was stirred under nitrogen or air at 90 °C. The reaction mixture changed the colour from black to dark red after a few minutes. The reaction mixture was kept at 90 °C and samples were taken (through the septum by a syringe) after 24, 48, 72 or 96 h. These samples were mixed with acetone / 2-propanol mixture (vol. ratio 3:1), in order to precipitate the particles and then centrifuged. The red coloured supernatant was removed and the particles were re-dissolved in chloroform. The same procedure was repeated as many times as it was necessary to remove the red supernatant from the nanoparticles. Cleaned nanoparticles were re-dissolved in chloroform. A ligand exchange with DDT was done at room temperature in small reagent bottles.

### 9.8. Ligand exchange – amines

Trihexylamine (Aldrich) and 1,4-diaminobutan (Aldrich) were used as received.

Poly(2-vinylpyridine) (P2VP) ( $M_w = 50\,000$  g/mol) (Polysciences, Inc.), poly(4-vinylpyridine) (P4VP) ( $\overline{M}_w = 50\,000$  g/mol) (Polysciences, Inc.) were used as received. Poly(ethylene oxide) terminated with one amino group (PEOA) was synthesized by anionic polymerisation ( $\overline{M}_p = 3200$  g/mol – PEOA-1 and  $\overline{M}_p = 1750$  g/mol – PEOA-2, determined by MALDI-TOFF)<sup>[6]</sup>.

### 9.9. Methods for particle characterization

**X-ray diffraction measurements (XRD)** were performed on a Philips X'Pert diffractometer (Cu  $K\alpha$ -radiation, variable entrance slit, Bragg-Brentano geometry, secondary monochromator). Colloidal solutions of CoPt<sub>3</sub> nanocrystals in toluene or chloroform were placed on standard single crystal Si support. After evaporation of the solvent the samples were ready for the measurements. XRD data reveal the internal structure of the average nanocrystals core and permit the calculation of the nanocrystal size. All samples were characterized by XRD measurements using following procedures:

	other ligands	thiols
Total time:	40 min	4 h
Start angle:	2°	30°
End angle:	100°	100°
Step size:	0.04°	0.04°
Time per step:	100 s	850 s

**Transmission Electron Microscopy (TEM) and high-resolution transmission electron microscopy (HRTEM)** was performed on a Philips CM-300 UT microscope operated at 300 kV. Samples for these measurements were prepared by deposition of a droplet of particle solution in toluene or chloroform onto carbon-coated copper grids. The excess of solvent was wicked away with a filter paper, and the grids were dried in air.

EDX (Energy Dispersive X-ray Spectroscopy) measurements were done using the DX4 system from EDAX. The detector was Si (Li), and accelerating voltage CM 300 UT. The images were made with a GATAN CCD camera, type 694.

**Scanning Electron Microscope (SEM)** images were obtained on a LEO 1550 scanning electron microscope (spatial resolution of ~1 nm, equipped with EDX (Si (Li) detector) and WDX INCA, OXFORD system). The samples were prepared on boron doped Si (100) wafers (resistance of 10  $\Omega$ cm).

WDX (Wavelength Dispersive X-ray Spectroscopy) measurements were performed using an accelerating voltage in the range of 100V – 30 KV. The samples were investigated by DSC before the WDX investigation. Aluminium crucibles from the DSC measurements were cut and used for the WDX measurements. In this way organics were removed from the particles by thermal decomposition during the DSC measurements.

**Attenuated Total Reflectance Fourier Transform Infrared (Golden Gate ATR/FT-IR) Spectroscopy.** IR spectra were recorded on a Bruker Equinox 55 spectrometer. A drop of the sample solution was placed on the crystal and after drying the spectra were recorded. The transmission IR spectra were collected in the range of 600-4000  $\text{cm}^{-1}$ . Each spectrum was obtained by averaging 64 interferograms with a resolution of 4  $\text{cm}^{-1}$ .

**Thermo Gravimetric Analysis (TGA)** studies were carried out using a Netzsch TG 209 C. All experiments were performed in nitrogen atmosphere. The samples were obtained by drying the sample solution directly in the crucibles at 100  $^{\circ}\text{C}$  for 5 min just prior to the measurements in order to remove solvent traces. After the drying step all TG measurements were performed in temperature range of 100  $^{\circ}\text{C}$  - 600  $^{\circ}\text{C}$  with a heating rate of 10 or 20  $^{\circ}\text{C}/\text{min}$ . Thermo gravimetric analyses, of all pure ligands, were performed without a previous drying step. Pure ligands were heated in the range from 25-600  $^{\circ}\text{C}$ , with a heating rate of 10 or 20  $^{\circ}\text{C}/\text{min}$ .

**Differential Scanning Calorimetry (DSC)** experiments were performed on a Netzsch differential scanning calorimeter 204 F1 under nitrogen (flow rate of 10 ml/min for purge gas and

5 ml/min for protective gas) using a sample mass of 2-6 mg. All data were recorded in a temperature range of 25-450 or 500 °C at a heating rate of 10 °C/min.

**Small Angle X-ray Scattering (SAXS)** investigations were performed with a rotating anode (Seifert, Ahrensburg; consisting a Cu-anode ( $\lambda = 0.1542$  nm)), crossed Göbel mirrors and an image plate detector (Fuji) mounted at a sample-detector distance of 1.05 m. The full path of X-rays was evacuated. The obtained data were analyzed using the “Scatter, version 1.0”<sup>[7]</sup> software.

### *General principle*

X-rays are used to investigate the structural properties of solids, liquids or gels. Photons interact with electrons, and provide information about the fluctuations of electronic densities in heterogeneous matter. The scattered intensity  $I(q)$  is the Fourier Transform of  $g(r)$ , the correlation function of the electronic density  $\rho(r)$ , which corresponds to the probability to find a scatter at position  $\rho$  in the sample if another scatter is located at position  $\Omega$ . Small angle scattering experiments are designed to measure  $I(q)$  at very small scattering vectors  $q \approx (4\pi/\lambda)\theta$ , with  $2\theta$  ranging from a few micro-radians to a tenth of a radian, in order to investigate systems with characteristic sizes ranging from crystallographic distances (few Å) to colloidal sizes (up to few microns).

The scattered intensity can be calculated as:

$$I(q) \propto \frac{d\sum(q)}{d\Omega} = \frac{N}{V} V_{particle}^2 (\rho_1 - \rho_2)^2 P(q)S(q)$$

$N$  – number of scatters in volume  $V$  of the sample;  $V_{particle}$  – volume of the individual scattering entity;  $\rho$ – density of the particle ( $\rho_1$ ) or the matrix ( $\rho_2$ );  $P(q)$  – form factor and  $S(q)$  – structure factor

For investigations of nanoparticles size, shape and ordering the form and the structure factor are important. The form factor gives information about particle size and shape, while the structure factor gives information about distances between the particles.

Experimentally, the **form factor  $P(q)$**  can be measured in a diluted regime where particles can be considered as independent scatters without any interactions. There are no correlations due to particle interactions, meaning that the structure factor component,  $S(q)$ , no longer affects the

scattering. The form factor yields shape and size information about the scatterers. It can be calculated and is found in many references for different simple shapes, such as spheres, cylinders etc [8]. Form factor for the spherically symmetric objects can be written as  $P(q) = F^2(q)$ , where  $F(q)$  is the amplitude of the form factor. The form factor amplitude of a homogeneous sphere was calculated already in 1911 by Lord Rayleigh<sup>[9]</sup>. For a sphere with radius  $R$ :

$$F_1(q, R) = \frac{3[\sin(qR) - qR \cos(qR)]}{(qR)^3}$$

The form factor of homogeneous spheres calculated using this equation has zeros for  $\tan qR = qR$  and it is displayed in Figure 9.2.

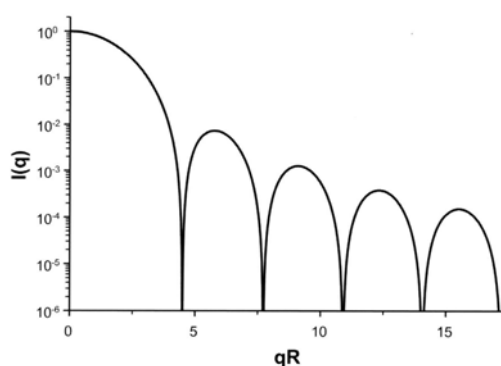


**Fig. 9.2.** Calculated form factor of homogeneous spheres

**Structure factor  $S(q)$**  - if the nanoparticles solution is concentrated and start to interact, correlation effects become important. The correlation behaviour appears as additional peaks in the scattering and can be used to determine the interparticle structure.

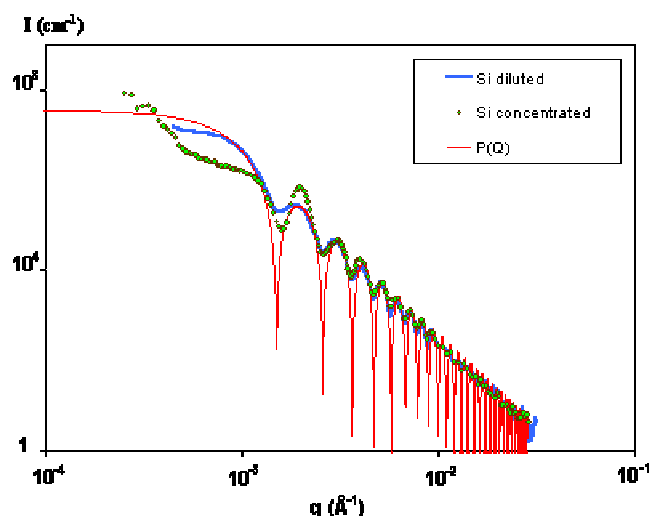


*Fig. 9.3. Experimental results obtained by SAXS measurements of silica spheres in diluted (influence of form factor) and concentrated solution (influence of form and structure factor). The theoretical values for perfect monodisperse spheres are also presented (calculated for form factor).*

The influence of both factors, as well as the calculated spectrum based on a theoretical model is shown in Figure 9.2. Measurements of diluted solutions of SiO<sub>2</sub> spheres demonstrate the influence of the form factor. In this case the measured data (red) can be directly related to the form factor for spheres (blue). There is no interaction and the structure factor is equal to 1 over the whole q-range.

If the solution of SiO<sub>2</sub> spheres is concentrated repulsive electrostatic interactions appear between these charged silica spheres. The experimental result is also shown in Figure 9.2. as green line. An interaction peak appears at small q, the position of which is related to the distance between neighbored particles. The signal results from the product of P(q) and S(q).

## **Film preparation**

---

### 9.10. Used chemicals

Solvents:

- Toluene, methanol, n-hexane, 2-propanol, ethanol (all p.a. Merck);

Chemicals used for wafer cleaning:

H<sub>2</sub>SO<sub>4</sub> (Merck, 97 %) and H<sub>2</sub>O<sub>2</sub> (Merck, 33 %)

Polymers as buffer layers:

- Poly(2-vinylpyridine) (P2VP) ( $M_w = 50\,000$  g/mol) (Polysciences, Inc.), poly(4-vinylpyridine) (P4VP) ( $\overline{M}_w = 50\,000$  g/mol) (Polysciences, Inc.), poly(ethylene glycol) bis(3-aminopropyl) terminated (PEODA) ( $\overline{M}_w = 1500$  g/mol) (Aldrich) and poly(ethylene glycol)-dimethylether ( $\overline{M}_w = 2000$  g/mol) (Merck) were used as received. Poly(ethylene oxide) terminated with one amino group (PEOA) was synthesized by anionic polymerization ( $\overline{M}_p = 3200$  g/mol, determined by MALDI-TOFF) [6]

Other chemicals:

- Ethyl-, diethylene- and triethylene-glycol (Merck) were used as received.

- Chlordimethylsilan (Fluka, p.a.)

### 9.11. Procedure for wafer cleaning

In order to clean the wafers two different procedures were used:

- *chemical procedure:*

Prior to the deposition of polymer films doped silicon substrates (P-type Boron doped, orientation  $\langle 100 \rangle$ , thickness 475-525  $\mu\text{m}$ , diameter  $100 \pm 0.5$  mm, resistance 5-15) were cleaned for 15 min in a freshly prepared 1:3 mixture of 30 %  $\text{H}_2\text{O}_2$  and  $\text{H}_2\text{SO}_4$  (*piranha solution*) followed by washing in water, 2-propanol and ethanol.

- *plasma cleaning:*

Silicon substrates were cleaned first with absolute ethanol, and then with oxygen plasma for 25-30 min in the plasma chamber SPI Plasma Prep II. Plasma cleaning removes just few atom layers at a samples surface. For that purpose the supplier recommended 10-watt plasma, but the used plasma chamber can only produce more energetic plasma. This probably changed our samples and caused different surface behaviors during the film preparation.

### 9.12. Silanization of silicon wafers

Chemically cleaned silicon wafers were covered with a drop of chlordinethylsilan and then immediately washed with THF and ethanol. Afterwards they were dried first with nitrogen and then for 1 h in the oven at 80 °C. Another way to modify the sample surface with the same compound was to keep the silicon wafers in the vapour of chlordinethylsilan for a few minutes.

### 9.13. Film preparation

**Spin coating** was performed with the spin coater MODEL P6700. All films were spin coated on cleaned or silanized Si wafers at rotation speeds of 1000, 2000 and 3000 rpm for 30 s. The amounts of used solutions were 50 – 75  $\mu\text{l}$ . In order to eliminate the effect of varying particle size on the film morphology, nanoparticles of almost identical sizes  $\sim d = 6.2$  nm were synthesised as determined by X-ray powder diffraction. Particles were washed with 2-propanol three times and then dissolved in hexane or toluene. Solutions were filtrated trough a 0.2  $\mu\text{m}$  filter. The prepared films were stored under room temperature.

Table 9.1. Program for spin coating:

	First phase	Second phase	Third phase	Fourth phase
Rotation speed, rpm	1000 (2000)	1000 (2000/3000)	1000 (2000/3000)	-
Acceleration time, s	1	1	1	1 (decreasing the speed to 0 rpm)
Spinning time, s	1	30	1	-

**Dip Coating** was performed with dip coater KSV DC. All films were deposited on previously cleaned or modified silicon oxide wafers. Wafers were 8 x 8 mm. Speeds were varied in the range from 1 to 40 mm/min. In all cases the deposition time was 30 s, and the sample was dipped into the solution with a speed of 70 mm/min.

**Langmuir Blodgett** films were made on Langmuir Blodgett trough NIMA 311D. The program NIMA 516 was used for programming the process and for collecting the data during production of LB films. For all experiments Millipore water, or glycols, were used and the films were made at room temperature ( $22 \pm 1$  °C). The trough was cleaned after each measurement, and fresh material was deposited.

If it is not specified differently, particles were prepared for Langmuir isotherm measurements in the following way:

After synthesis and size selective precipitation, the powder of the desired particles was weighted and then dissolved in a known amount of solution (toluene or chloroform). The solution was passed through a 0.45 µm pore size filter and stored in clean glassware. A 50 µl glass syringe was utilized to disperse a known amount of the particles uniformly across the water (glycol) surface. Depending on the nature of the particles and concentration of the solution, between 10 and 250 µl of material was used. The solution evaporated usually in 10-15 min after deposition. Pressure/area isotherm measurements were carried out using a compression rate of 30 mm/min

until the surface pressure started to increase and then 5 mm/min until the end of the measurement.

A so-called “Isotherm cycle” procedure was used for the formation of Langmuir films on glycols. Firstly, the isotherm was measured using the already described procedure and the desired pressure was chosen from the measured isotherm. The same amount of solution was dropped onto the glycol surface, and after the evaporation of the solution, the film was compressed using a compression rate of 30 mm/min until the surface pressure started to increase. At that point the barrier was stopped and certain parameters were set in the *Monolayer Menu*, for the further procedure:

Area increment, cm <sup>2</sup>	5
Wait interval, s	10
Target pressure, mN/m	chosen from isotherm
Barrier speed, cm <sup>2</sup> /min	5
Cycle required	100
Cycle Max Area, cm <sup>2</sup>	found from isotherm for Cycle Max Pressure
Cycle Min Area, cm <sup>2</sup>	found from isotherm for Cycle Min Pressure
Cycle Max Pressure, mN/m	target pressure
Cycle Min Pressure, mN/m	(target pressure – 1 mN/m)

This procedure led to a better compression of the particles since they have more time to relax. Repetition of the compression and looseness improved the particle packing. If the occupied surface is changing drastically during this procedure, it is an indication for a too small amount of particles, or for a pressure that is not near to the collapse pressure (the solid phase of the film was not reached). In this case a new isotherm should be measured and new parameters should be chosen.

All LB films, if it is not specified differently in the text, were taken out at the pressure just below the collapse pressure. Samples were made on previously cleaned or modified silicon wafers. The size of the wafer was 8 x 8 mm. Usually, films occupied a space of 5 x 8 mm. The usual creep speed was 1 mm/min. Samples that were prepared by film formation on glycols were dried in the oven under vacuum, at 80 °C for 24 h. All samples were kept under air afterwards.

## 9.14. Film characterisation

### 9.14.1. Scanning Electron Microscope (SEM)

Images were obtained on a LEO 1550 scanning electron microscope with a spatial resolution ~ 1nm. More details are given in the first part of this chapter.

### 9.14.2. Atomic force microscopy (AFM) <sup>[10]-[12]</sup>

#### **Experimental conditions**

The AFM images were obtained on a JPK Nanowizard ®Atomic Force Microscope and MultiMode™ SPM (Veeco Instruments Inc.) with a Nano Scope IV Controller and an AS-12V ("E" vertical) SPM Scanner. All investigations were made in intermittent contact mode using Si-tip ( $\nu = 280$  kHz,  $r = 10$  nm).

General principles of AFM:

The atomic force microscope (AFM) is special scanning probe microscope (SPM). In the AFM a sharp tip placed on cantilever moves over the surface of a sample in a raster scan. The movement of the tip or sample is performed by an extremely precise positioning device made from piezo-electric ceramics, most often in the form of a tube scanner. The scanner is capable of sub-angstrom resolution in x-, y- and z-direction. (Piezoelectric ceramics are a class of materials that expand or contract in the presence of a voltage gradient.)

The AFM operates by measuring attractive or repulsive forces between a tip and the sample. Therefore it is necessary to have a force sensor. A common type of force sensor utilizes the relationship between the motion of a cantilever and the applied force. By monitoring the motion of the probe, as it is scanned across the surface, a three dimensional image of the surface is constructed. Measuring the motion of the cantilever is possible with the "light lever" method. In the light lever method, the light is reflected from the backside of the cantilever into a photo-detector (Fig. 9.4.). The motion of the cantilever is then directly proportional to the output of the sectioned photo-detector. AFMs can achieve a lateral resolution of 0.2 to 3 nm, and unlike electron microscopes, can image samples in air and immersed liquids.

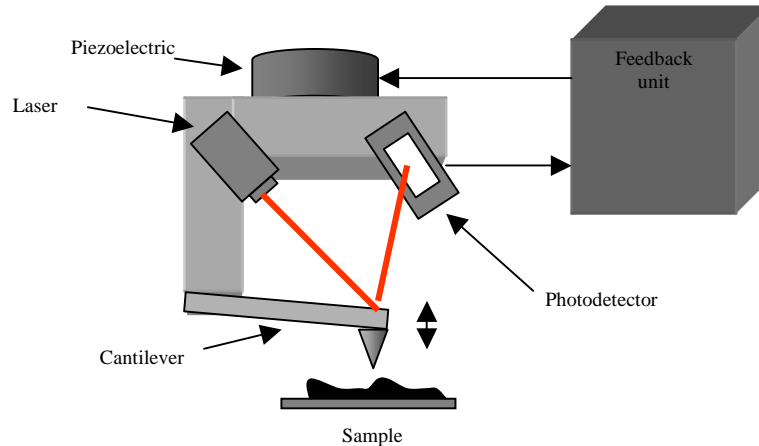


Fig. 9.4. The scheme of the primary components of the light lever atomic force microscope. The light lever sensor uses a laser beam to monitor the deflection of the cantilever. When the cantilever moves up and down, the light beam moves across the surface of the photo-detector.

The image contrast can be obtained in many ways. The three main classes of interaction are *contact mode*, *tapping mode* and *non-contact mode*<sup>[13]</sup>.

**Contact mode** is previously the most common method used in AFM. As the name suggests, the tip and sample remain in close contact as the scanning proceeds. In contact mode AFM, the probe directly follows the topography of the surface as it is scanned. The force of the probe is kept constant by feedback loop while an image is measured.

**Tapping mode**<sup>TM</sup> is nowadays the next most common mode used in AFM. When operated in air or other gases, the cantilever is oscillated near its resonant frequency (often hundreds of kilohertz) and positioned above the surface so that it only taps the surface for a very small fraction of its oscillation period. There is still contact with the sample in the sense defined earlier, but the very short time over which this contact occurs dramatically reduces lateral forces as the tip scans over the surface. For this reason this method is especially useful for investigation of poorly immobilised or soft samples.

### **Tip effects**<sup>[13]</sup>

One of the most important factors influencing the resolution that may be achieved with an AFM is the sharpness of the scanning tip. The best tips may have a radius of curvature of only around 5nm. The need for sharp tips is normally explained in terms of *tip convolution*. This term is often

used (slightly incorrectly) to group any influence the tip has on the image. The main influences are: broadening, compression, interaction forces and aspect ratio.

### 9.14.3. Grazing Incidence Small Angle X-Ray Scattering (GISAXS)

#### ***Experimental conditions***

The GISAXS measurements were done in two different facilities:

1) Grazing Incidence Small Angle X-Ray Scattering (GISAXS) experiments were performed at the SAXS beam-line 5.2 L located at the third generation synchrotron light source ELETTRA, Trieste, Italy. Samples were irradiated with monochromatic X-rays with an energy of 8 keV. A grazing angle of  $\alpha_i \approx 0.6^\circ$  (well above the critical angle of  $\alpha_c \approx 0.22^\circ$ ), and the 2-D scattering pattern was recorded using an X-ray charge-coupled device (CCD) camera mounted at a sample-detector distance of 1.08 m or 0.78 m, respectively<sup>[14]</sup>. In order to optimally match the measured intensity with the given dynamic range of the CCD detector, an aluminium absorber foil was introduced in front of the detector, suppressing the strong scattering intensity at  $q_y = 0$  due to the specularly reflected beam and the Yoneda peak [15] in favour of the GISAXS signal at finite values for  $q_y$ .

2) GISAXS measurements were done using the grazing incidence setup of the experimental station BW4 [16] at HASYLAB (Hamburg/Germany) equipped with a high resolution 2-dimensional CCD detector (MAR research, 2048 x 2048 pixel, pixel size 79  $\mu\text{m}$ ) at a distance of 2.5 m (sample-detector). The wiggler beam line was set to a wavelength of  $\lambda = 0.138$  nm. The flight path was fully evacuated and the beam size was focused by an additional beryllium lens system to a size of only 30  $\mu\text{m}$  (vertical) x 60  $\mu\text{m}$  (horizontal) at the sample position. Piezo driven slits were installed in front of the sample to reduce diffuse scattering from the collimation devices of the beam line. With this setup it was possible to determine structures within a scale of some nanometers up to around 400 nm.

#### ***General principle***

Grazing Incidence Small Angle X-ray Scattering (GISAXS) is a versatile tool for characterizing nanoscale density correlations and can be applicable to determine internal morphologies of thin films as well as top surface morphologies of thick films and substrates. GISAXS involves a combination of two techniques: GID (*Grazing Incidence Diffraction*), which

uses a reflection geometry to obtain surface and near surface sensitive X-ray scattering, and SAXS (*Small Angle X-ray Scattering*), which measures structures at a length scale of 1 - 100 nm in normal transmission mode<sup>[17],[18],[19]</sup>. In contrast to SAXS, the GISAXS technique is not limited on small sample volumes in the thin film geometry. Moreover GISAXS has also some advantages in comparison to AFM. With AFM only surface topographies are accessible, but with GISAXS probe the buried structure as well. Because a larger surface area is investigated, GISAXS also has a much larger statistical significance compared to AFM and SEM. Due to that GISAXS turned out to be a powerful advanced scattering technique for the investigation of nanostructured films specially block copolymer films<sup>[20],[21],[22]</sup> as well as combinations of polymer and nanoparticles films<sup>[23],[24]</sup>.

Some of the main advantages of GISAXS technique are<sup>[18],[22]</sup>:

- a non-destructive structural investigation;
- does not require a conducting surface or sample preparation (in-situ characterization possible);
- a sample preparation is easy;
- a highly intense scattering pattern is always obtained (even for films of nanoscale thickness) because the X-ray beam path length through the film plane is sufficiently long;
- yields an excellent sampling statistics (averages over macroscopic regions to provide information on nanometer scale);
- provides information on particle geometry, size distributions, spatial correlations.

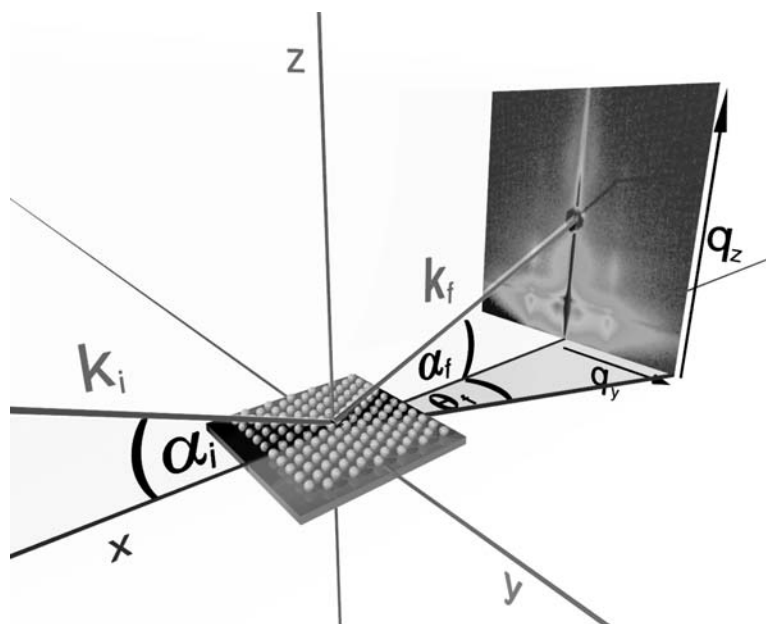


**Fig. 9.5.** Schematic of the basic principle of the GISAXS setup<sup>[25]</sup>

### ***GISAXS pattern***

Figure 9.5. shows a scheme of the GISAXS geometry created by the use of a two-dimensional detector. The sample surface is defined as the x, y plane. The incident beam is directed along the x-axis with an incident angle denoted as  $\alpha_i$ . The x, z plane denotes the plane of incidence and reflection. The area detector records the scattering intensity of scattered rays over a range of exit angle  $\alpha_f$  and scattering angles  $\theta_f$  in the surface plane. Two well-separated peaks are recognizable on the detector: the specular peak and the Yoneda peak. The specular peak is obtained for the specular condition  $\alpha_i = \alpha_f$ . The Yoneda peak is a maximum of the transmission functions that appears in the case either the incident or exit angle is equal to the critical angle of the material<sup>[15]</sup>.

In order to make X-ray scattering surface sensitive, a grazing incidence angle  $\alpha_i$  is usually chosen close to the critical angle  $\alpha_c$  of the total external reflection. The critical angle can be calculated using the equation<sup>[26]</sup>:

$$\alpha_c \approx \sqrt{2\delta} = \lambda \sqrt{\frac{r_e \rho_e}{\pi}}$$

where:  $\lambda$  is the wavelength of light,  $\mu$  is the absorption coefficient,  $r_e$  is classical electron radius, and  $\rho_e$  is the electronic density.

From the presented equations it is concluded that the critical angle depends on the system to be studied. When the condition of total external reflection holds, the penetration depth of the incident X-ray beam is only a few tens of angstroms, and the reflectivity is near unity. By increasing the incident angle above the critical angle, the reflectivity decreases rapidly, while the penetration depth increases. Therefore, for freestanding nanoparticles an incident angle below  $\alpha_c$  may be chosen to make the scattering exclusively surface-sensitive. In order to investigate the internal film structure the incident angle should be above  $\alpha_c$  of the film, to ensure a full penetration of the sample<sup>[18],[20],[21]</sup>.

### ***Different scans obtained from GISAXS pattern***

Transferred into reciprocal space the two-dimensional  $(\theta_f, \alpha_f)$ -map becomes a  $(q_y, q_z)$ -map. Instead of handling the complete two-dimensional intensity distribution, the analysis of the scattering data can be reduced to distinct cuts. Basically two different types of cuts are useful: horizontal slices at constant  $q_z$  and vertical slices at constant  $q_y$  (the naming of horizontal and vertical refers to the sample surface).

A horizontal slice depends on the wave vector component  $q_y$  only and as a consequence only structures parallel to the sample surface are investigated. The curve obtained from such a slice is analogue to the curve obtained by SAXS measurements and can be used for calculation of particle-particle distance in the case of nanoparticle films. Additionally, it gives information about the correlation length, and particle packing<sup>[20],[21]</sup>.

The information from vertical slices depends on the  $q_z$  component of the wave vector results. This scan basically investigates a structure perpendicular to the sample surface. As in the two-dimensional maps, the Yoneda and the specular peak are visible. The vertical scenes give information about Grazing Incidence Diffraction. In this way the film roughness and thickness can be investigated<sup>[20],[21]</sup>.

### ***Analysis Techniques***

Two different models can be used for the analyses of GISAXS data:

- *Born Approximation* - use standard SAXS analysis techniques;
- *Distorted Wave Born Approximation* - must be used when dealing with highly reflective surfaces or interfaces.

Influence of the substrate and the closeness of  $\alpha_i$  to the critical angle of total external reflection  $\alpha_c$ , lead to necessity to modify the Born approximation in order to take in account reflection-refraction effects. Therefore another theory is used, called the distorted-wave Born approximation, DWBA. A physical picture for the full calculation<sup>[27]-[29]</sup> for the scattering cross section in the DWBA for an island is depicted in Fig. 9.6., where  $k_i$  and  $k_f$  are the incident and the outgoing wave vectors, respectively. The four considered terms are connected with different scattering procedures that enclose or exclude a reflection of either the incident beam or the final beam collected on the detector. These waves interfere coherently, giving rise to the following effective form factor.

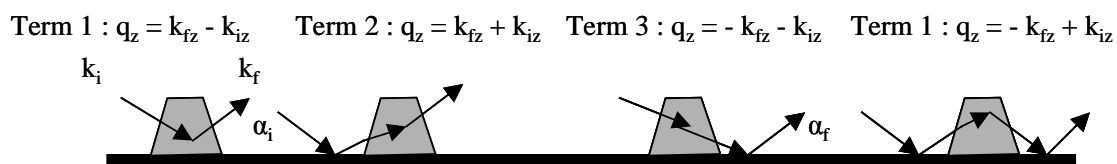


Fig. 9.6. The four terms in the scattering for a supported island are shown. The first term corresponds to the Born approximation<sup>[29]</sup>.

## 9.15. Literature

1. Shevchenko, E.V., et al., J. Am. Chem. Soc., 2002. **124**: p. 11480-11485.
2. Sang-Yup Lee, M.T.H., Journal of Colloid and Interface Science, 2006. **293**: p. 401-408.
3. Chemseddine, A. and H. Weller, Ber. Bunsenges. Chem., 1993. **97**: p. 636.
4. Murray, C.B., D.J. Norris, and M.G. Bawendi, J. Am. Chem. Soc., 1993. **115**: p. 8706.
5. Murray, C.B., C.R. Kagan, and M.G. Bawendi, *Synthesis and Characterisation of Monodisperse Nanocrystals and Closed Packed Nanocrystals Assemblies*. Annu. Rev. Mater. Sci., 2000. **30**: p. 545-610.
6. Stolzenburg, M., *Herstellung von endfunktionalisierten PDMS- und PEO- Polymeren mittels anionischer Polymerisation*, in *Institute for Physical Chemistry*. 2004, Hamburg: Hamburg.
7. S. Förster, A.T., M. Konrad, C. Schellbach, A. Meyer, S.S. Funari, P. Mulvaney, R. Knott, J. Phys. Chem. B, 2005. **109**: p. 1347.
8. Lindner, P. and T. Zemb, *Neutrons, X-Rays and Light - Scattering Methods Applied to soft Condensed Matter*. 2002, Amsterdam: Elsevier Science B.V.
9. Rayleigh, L., Proc. Roy. Soc. London, Ser. A, 1911. **84**: p. 25-46.
10. Baselt, D., *The tip-sample interaction in atomic force microscopy and its implications for biological applications*, in *California Institute of Technology*. 1993.
11. Mai, W., *Fundamental Theory of Atomic Force Microscopy*.
12. Nanotechnology, P., *General Tutorial: Atomic Force Microscopy*.
13. Round, A., *Atomic Force Microscopy*.
14. Huang, T.C., et al., J. Appl. Cryst, 1993. **26**: p. 180-184.
15. Yoneda, Y., Phys. Rev., 1963. **131**: p. 2010.
16. Gehrke, R., Rev. Sci. Instr., 1992. **63**: p. 455.
17. <http://physics.queensu.ca/~marsha/GISAXS.html>. GISAXS.
18. Smilgies, D.-M., GISAXS.
19. Smilgies, D.M., et al., *Characterization of Polymer Thin Films with Small-Angle X-ray Scattering under Grazing Incidence (GISAXS)*. Synchrotron Radiation News, 2002. **15**(5): p. 35-42.
20. Müller-Buschbaum, P., *Grazing incidence small-angle X-ray scattering: an advanced scattering technique for the investigation of nanostructured polymer films*. Anal. Bioanal. Chem., 2003. **376**: p. 3-10.
21. Müller-Buschbaum, P., et al., *Comparative analysis of nanostructured diblock copolymer films*. Spectrochimica Acta Part B, 2004. **59**: p. 1789-1797.
22. Lee, B., et al., *Structural Analysis of Block Copolymer Thin Films with Grazing Incidence Small-Angle X-ray Scattering*. Macromolecules, 2005. **38**: p. 4311-4323.
23. Lin, Y., et al., Nature, 2005. **434**: p. 55-59.
24. Flege, J.I., et al., *Grazing-incidence small-angle x-ray scattering investigation of spin-coated CoPt<sub>3</sub> nanoparticle films*. Nuclear Instruments & Methods in Physics Research, Section B: Beam Interactions with Materials and Atoms (2006), 246(1), 25-29
25. Frömsdorf, A., R. Capek, and S. Roth,  *$\mu$ -GISAXS experiment and simulation by using a simple model of a highly ordered monolayer of PMMA-beads*. submitted in J. Phys. Chem. B, 2006.

26. Meyer, A., *Untersuchung der molekularen Orientierung in dünnen Polymerfilmen mit Hilfe der Röntgenstreuung bei streifendem Einfall*, in *Fachbereiches Chemie*. 1998, University Hamburg: Hamburg. p. 130.
27. Sinha, S.K., et al.
28. Rauscher, M., et al., 1999. *J. Appl. Phys.* **86**: p. 6763–6769.
29. Lazzari, R., *IsGISAXS: a program for grazing-incidence small-angle X-ray scattering analysis of supported islands*. *J. Appl. Cryst*, 2002. **35**: p. 406–421.

## Chapter 10

### Summary

---

*Controlling the distance between the particles and producing ligand free particles is for instance, very important for the catalytic, magnetic or electric properties of the particle assemblies. This thesis focuses on the investigation of ligand exchange reactions applied to CoPt<sub>3</sub> nanoparticles after their synthesis in order to control particle-particle distance. In addition different techniques for film preparation were investigated in order to prepare high covered substrate with well-ordered packed CoPt<sub>3</sub> nanoparticles.*

#### ***Ligand exchange***

A new procedure was developed to exchange the ligands which were present on the CoPt<sub>3</sub> particle surface after syntheses with new ligands. As new ligands, different carboxylic acids, amines and thiols were used. The investigation shown that the applied ligand exchange procedure was successful in all cases.

Four different carboxylic acids with a different alkyl chain length were chosen as new ligands: sorbic (SA), undecanoic (UDA), linoleic (LA) and arachydic acid (ARA). Particles stabilised with the new ligands were stable for a long period of time. TG measurements proved that the ligand excess is completely removed after two washing steps. The number of ligand molecules connected to the particle surface decreased with increasing the length of the alkyl chain. Investigations of particles self-assembly revealed that particles stabilized with the new ligands were still able to self-assemble in well ordered 2-D and 3-D structures. Due to different alkyl chain lengths among the used acids, it was possible to vary the particle-particle distance from 13.6 nm (for ARA) to 9.9 nm (for SA). A good ordering in 3-D structures was obtained only in the presence of ligand excess.

In the case of thiols, the applied ligand exchange procedure led to more complex reactions than in the case of acids. It was observed that the exchange of ligands is accompanied by interactions of between particle atoms and dodecanthiol. The formation of Co complexes/clusters occurs at higher (90 °C) as well as at room temperature, and in air or

nitrogen. Particles of different sizes and different shapes express the same reactivity with dodecanthiol.

Strong interactions between amino groups and CoPt<sub>3</sub> nanoparticles were used for the attachment of longer polymer chains based on polyethylene oxide. Due to these interactions the same polymers were used as substrates during particle deposition by different techniques.

### *Film formation*

Three different techniques were used for the formation of CoPt<sub>3</sub> nanoparticles films: spin coating, dip coating and Langmuir-Blodgett technique.

All applied techniques are appropriate for CoPt<sub>3</sub> nanoparticle films preparation. Spin coating leads to the smooth and ultra-thin CoPt<sub>3</sub> nanoparticle films on the silicon wafer as well as on the different polymer substrates such as: poly(2-vinylpyridine) (P2VP), poly(4-vinylpyridine) (P4VP), poly(ethylene oxide) terminated with one (PEOA) and two amino groups (PEODA), respectively. In all cases the particles form a defective lattice with local hexagonal symmetry. The investigations show that amino groups strongly influence the particle deposition. GISAXS measurements indicate that the particle correlation in the film deposited on PEODA is superior to films that are identically prepared on PEOA, P2VP and P4VP buffer layers. Additionally, it is shown that the employment of P2VP and P4VP substrate layers on silicon results in large areas covered by particles. However, particles are in these cases packed in multi layers.

A better order of CoPt<sub>3</sub> nanoparticles on silicon wafers was obtained using the dip coating technique. By using statistical experimental design, the influence of a few parameters (particle concentration, dip speed, solvent and polarity of the wafer surface) and their mutual effects on the wafer coverage were investigated. The optimal conditions for obtaining highly covered areas on the hydrophobic substrates include application of particle solution is hexane with concentrations between 2.5 and 4 mmol/l, and using the dip speed of 1 and 10 mm/min.

The Langmuir-Blodgett technique applied at water/air interface gives dissatisfactory results in the case of CoPt<sub>3</sub> nanoparticles. Therefore, another approach was applied and instead of water, diethylenglycol was used. This procedure leads to a high coverage of the substrate and well-ordered packing. Investigations were performed with different particle size, under different substrate angles and with different amounts of ligands. In this procedure, the ligands have only a small effect on the film formation in comparison to the results achieved with water/air surfaces. The experiments show that the film compactness and particle order

are influenced by the substrate angle during the film deposition. Furthermore, this method is very efficient for the deposition as well on silicon as on different polymers (the same polymer substrates as in the case of spin coating). A GISAXS investigation confirms that the best particle order was achieved for the films prepared by Langmuir-Blodgett technique.

The prepared  $\text{CoPt}_3$  nanoparticles films on silicon are very stable in a broad temperature range. A heating procedure can be used until 400 °C without a significant loss of the particles order, despite simultaneous ligand removal. Higher temperatures lead to particles fusion. Such particle behavior gives the opportunity to use the heating procedure in order to produce high-order films of ligand free particles.

## Zusammenfassung

---

*Für die Untersuchung von katalytischen, magnetischen und elektrischen Eigenschaften an Partikelanordnung ist es bedeutend den Partikelabstand zu kontrollieren und die Liganden entfernen zu können. Diese Arbeit konzentriert sich sowohl auf die Untersuchung von Ligandenaustauschreaktionen an  $\text{CoPt}_3$  Nanopartikeln um den Partikelabstand variieren zu können als auch auf die Bildung von  $\text{CoPt}_3$  Nanopartikel-Filmen. Hierbei kamen verschiedene Techniken zum Einsatz.*

### Ligandenaustausch

Für den Ligandenaustausch wurde eine neue Methode entwickelt, um die durch die Synthese bedingten Liganden durch andere Liganden zu ersetzen. Als neue Liganden wurden Carbonsäuren, Amine und Thiole eingesetzt. Vier Carbonsäuren mit unterschiedlich langen Alkylresten wurden für den Austausch gewählt. Hierbei handelte es sich um Sorbinsäure (SA), n-Undecansäure (UDA), Linolsäure (LA) sowie Arachidinsäure (ARA). Nach dem Ligandenaustausch sind die Partikellösungen über einen Zeitraum hinweg stabil. TG Messungen bestätigten, dass ein Überschuss an Liganden nach zweimaliger Waschung vollständig entfernt werden konnte. Die Anzahl der Liganden auf der Partikeloberfläche verringerte sich mit steigender Alkylkettenlänge. Untersuchungen zur Selbstorganisation zeigten, dass die Partikel sich auch nach dem Ligandenaustausch regelmäßig in 2-D und 3-D Strukturen anordneten. Durch die unterschiedlich langen Alkylketten der verwendeten Carbonsäuren war es möglich, den Partikel zu Partikel Abstand zwischen 13.6 nm bis 9.9 nm zu variieren. Regelmäßig angeordnete 3-D Strukturen konnten nur bei Ligandenüberschuß erhalten werden.

Bei der Verwendung von Thiolen kam es zu komplexeren Reaktionen als bei den Carbonsäuren. Die Ergebnisse der Experimente zeigten nicht nur einen Ligandenaustausch, sondern zusätzlich Wechselwirkungen mit Atomen der Partikel. Co Komplexe/Cluster bilden sich bei Temperaturen über 90 °C genauso wie bei Raumtemperatur und in Sauerstoff oder Stickstoff Atmosphäre. Partikel mit verschiedenen Größen und verschiedenen Formen zeigten die gleiche Reaktivität mit 1-Dodecanthiol.

Die starken Wechselwirkungen zwischen Aminogruppen und CoPt<sub>3</sub> Nanopartikeln wurden ausgenutzt für die Bindung von auf Polyethylenoxid basierenden langen Polymerketten. Wegen dieser Wechselwirkungen wurden diese Polymere auch als Substrate verwendet, auf denen die Partikel mit unterschiedlichen Techniken abgeschieden wurden.

#### Filmpräparation

Zur Herstellung von Filmen bestehend aus CoPt<sub>3</sub> Nanopartikeln wurden drei verschiedene Techniken angewendet: Spin coating, Dip coating und das Langmuir Blodgett Verfahren. Alle verwendeten Techniken sind zur Formation von CoPt<sub>3</sub> Nanopartikel Filmen geeignet. Mittels Spin coating konnten ultra dünne CoPt<sub>3</sub> Nanopartikel Filme sowohl auf Silizium-Trägern als auch auf verschiedenen Polymersubstraten wie Poly(2-vinylpyridine) (P2VP), Poly(4-vinylpyridine) (P4VP), Poly(ethyleneoxid) terminiert mit (PEOA) und zwei Aminogruppen (PEODA) erzeugt werden. In allen Fällen bildeten sich Partikelanordnungen mit Fehlstellen aber lokaler hexagonaler Symmetrie. GISAXS Messungen deuten darauf hin, dass die Ordnung der Partikel in den auf PEODA abgeschiedenen Filmen stärker ausgeprägt ist als bei den auf PEOA, P2VP und P4VP Puffer-Schichten abgeschiedenen Filmen. Zusätzlich konnte gezeigt werden, dass dünne P2VP und P4VP Schichten auf Siliziumsubstraten gute Pufferschichten sind, um eine hohe Bedeckung zu erzielen was zu Mutschichten führt.

Eine bessere Anordnung der CoPt<sub>3</sub> Nanopartikel auf Siliziumsubstraten konnte mit der Dip coating Technik erzielt werden. Durch „Statistical Experimental Design“ konnten die Einflüsse verschiedener Parameter (Partikelkonzentration, Dipgeschwindigkeit, Lösungsmittel und Polarität der Substratoberfläche) auf die Substratbedeckung untersucht werden. Die Ergebnisse dieser Untersuchungsreihen zeigten, dass durch die Verwendung von n-Hexan Partikel-Lösungen mit Konzentrationen zwischen 2.5 und 4 mmol/L, und einer Dipgeschwindigkeit zwischen 1 und 10 mm/min ein hoher Bedeckungsgrade erzielt werden konnte.

Die Langmuir-Blodgett Technik mit einer Wasser/Luft Grenzfläche liefert unbefriedigende Ergebnisse für CoPt<sub>3</sub> Nanopartikel. Aus diesem Grund wurde ein neuer Ansatz gewählt, bei dem Anstelle von Wasser Diethylenglycol verwendet wurde, was zu einem höheren Bedeckungsgrad des Substrates mit regelmäßig angeordneten Partikeln führte. Gute Ergebnisse konnten mit unterschiedlichen Partikelgrößen, Substratwinkeln und Ligandenkonzentrationen erzeugt werden. In diesem Fall übt auch die Art der Liganden nur

einen geringen Einfluß auf die Ausbildung der Filme im Gegensatz zu den Ergebnissen mit einer Wasser/Luft Grenzfläche aus. Die Experimente zeigen, dass die Kompaktheit der Filme und die regelmäßige Anordnung der Partikel durch den Substrat Winkel während der Filmabscheidung beeinflusst werden. Weiterhin ist die Methode sehr effizient sowohl für die Abscheidung auf Siliziumträgern als auch auf verschiedenen Polymeren (die selben Polymere wie im Fall des Spin coatings). Eine GISAXS Untersuchung bestätigt, dass die (regelmäßigste) beste Partikelanordnung durch die Langmuir-Blodgett Technik erzielt wird.

Die hergestellten  $\text{CoPt}_3$  Nanopartikel Filme auf Siliziumträgern sind über ein breites Temperaturfenster hinweg stabil. Bis  $400\text{ }^\circ\text{C}$  bleibt die Anordnung der Partikel auf dem Substrat ohne nennenswerte Veränderung trotz der einhergehenden Abtrennung der Liganden erhalten. Daher können durch Erhitzen ligandenfreie  $\text{CoPt}_3$  Nanopartikel Filme hergestellt werden.

## Appendix

### Appendix 1. IR spectra of different ligands

IR spectra of ligands used during the synthesis of CoPt<sub>3</sub> nanoparticles

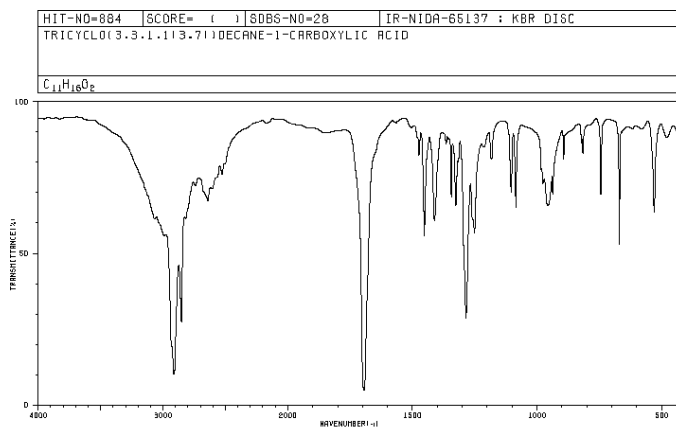


**Fig. 1.** IR spectra of adamantane carboxylic acid on KBr disc

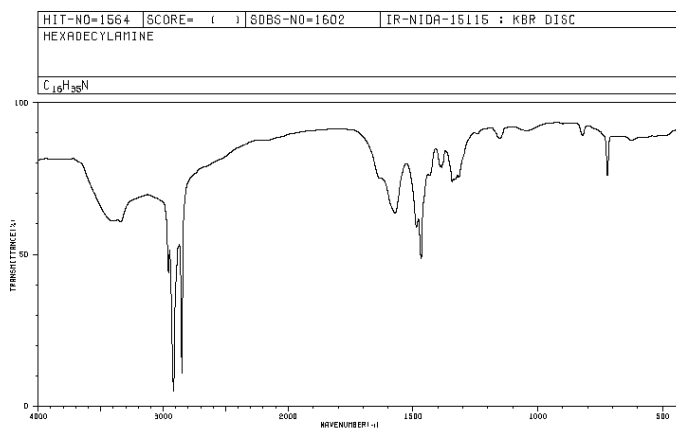


**Fig. 2.** IR spectra of hexadecylamine on KBr disc  
IR spectra of different ligands used during ligand exchange procedure

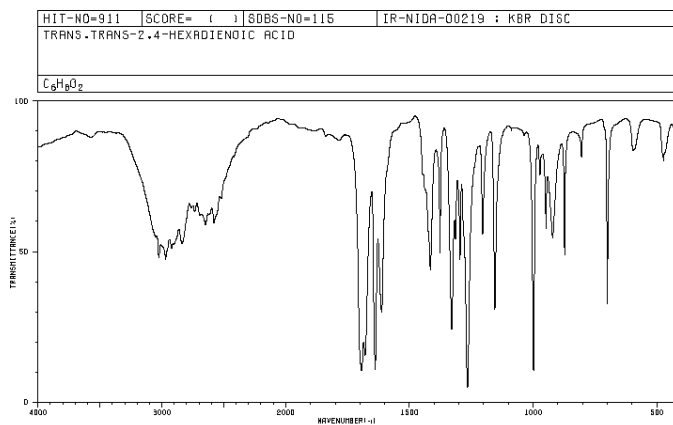


**Fig. 3.** IR spectra of sorbic acid on KBr disc (Chapter 2.)

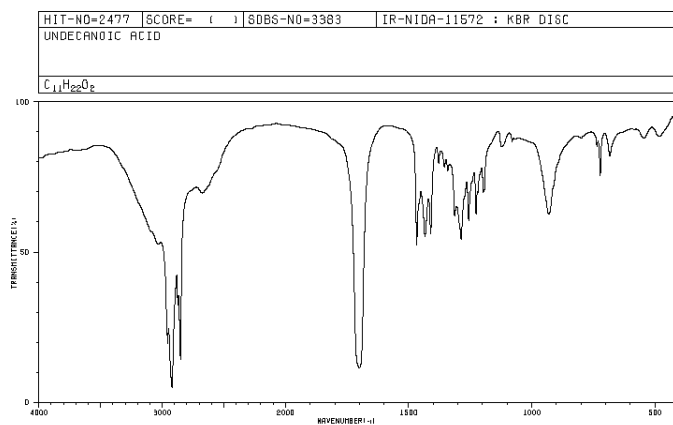


**Fig. 4.** IR spectra of undecanoic acid on KBr disc (Chapter 2.)

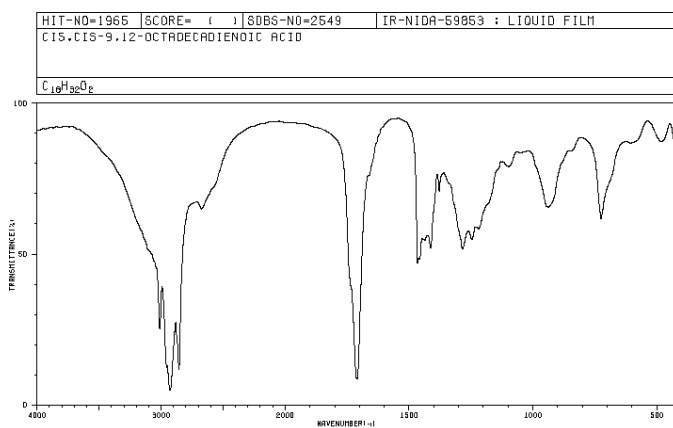


**Fig. 5.** IR spectra of linoleic acid – liquid film (Chapter 2.)

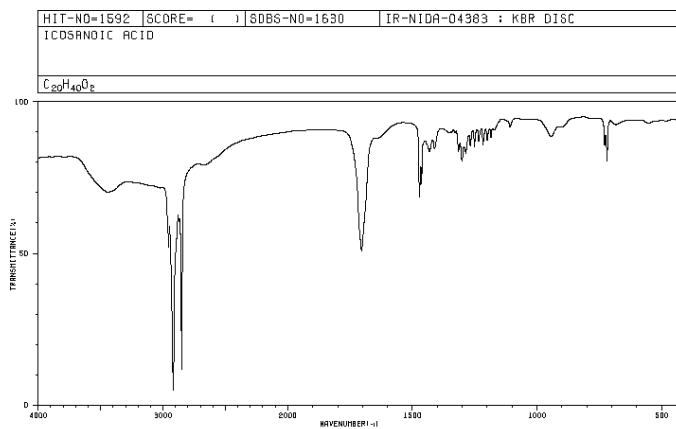


**Fig. 6.** IR spectra of arachidic acid on KBr disc (Chapter 2.)

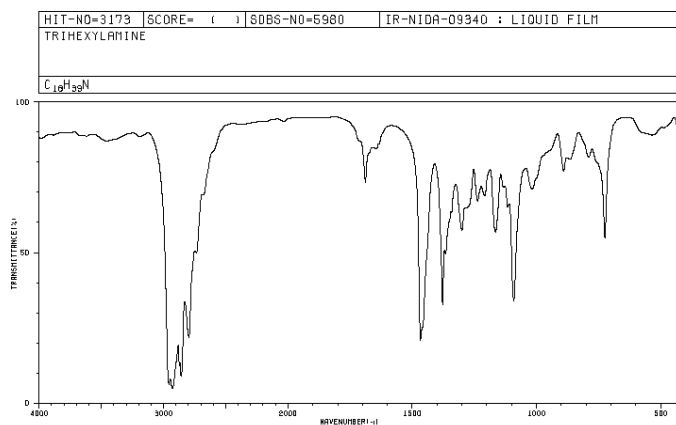


**Fig. 7.** IR spectra of trihexylamine – liquid film (Chapter 3.)

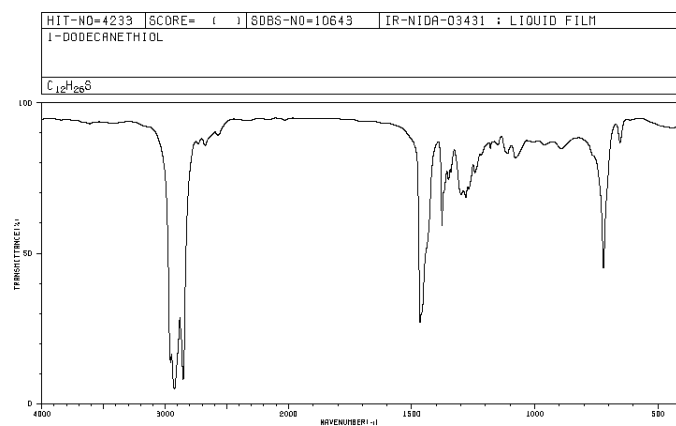


**Fig. 7.** IR spectra of 1-dodecanthiol – liquid film (Chapter 4.)

## Appendix 2. Safety precaution information on the used chemicals

Substance	R-phrases	S-phrases	Hazard signs
Acetone	11-36-66-67	9-16-26	[F][Xi]
Adamantanecarboxylic acid	1	26-24/25	
Arachaidic acid	-	-	-
Chloroform	22-38-40-48-/20/22	36/37	[Xn]
1,2-dichlorobenzene	22-36/37/38-50/53	23-60-61	[Xn][N]
Dicobalt octacarbonyl	11-22-26-40- 48/20-52/53-62- 65-67	16-28-36/37-45-62	[F][T]
Di-phenyl ether	51/53	60-61	[Xi]
Dioctylether	1	23-24/25	
Dodecylamine	22-35	26-28.1-36/37/39-45	[C]
Dodecanthiol	36/37/38	26-28.1	[Xi]
Dyethylene glycol	-	-	-
Ethanol	11	7-16	[F]
Ethylene glycol	22	-	-
1,2-Hexadecandiol	1	22-24/25	[Xn]
1-Hexadecanol	36/37/38	22-24/25	
Hexadecylamine	22-35	26-36/37/39-45	[C]
Hexane	11-48/20	9-16-24/25-29-51	[F][Xn][N]
Isopropanol	11-36-67	7-16-24/25-26	[F][Xi]
Lynoleic acid	-	-	-
Methanol	11-23/25	7-16-24-45	[F][T+]
Platinum(II)-acetylacetonate	20/21/22- 36/37/38-63	26-36/37/39	[Xn]
Sorbic acid	34	26-36/37/39-45 [C]	
Sulfuric acid, H <sub>2</sub> SO <sub>4</sub>	35	26-30-45	[C]
Toluene	11-20	16-25-29-33	[F][Xn]
Triethylene glycol	-	24/25	-
Undecanoic acid	36/37/38	26-36	[Xi]

---

**Risk (R-) and safety precaution (S-) phrases used in the classification, packaging, labeling and provision of information on dangerous substances**

**Risk phrases (R-Phrases)**

R1: Explosive when dry  
R2: Risk of explosion by shock, friction fire or other sources of ignition  
R3: Extreme risk of explosion by shock friction, fire or other sources of ignition  
R4: Forms very sensitive explosive metallic compounds  
R5: Heating may cause an explosion  
R6: Explosive with or without contact with air  
R7: May cause fire  
R8: Contact with combustible material may cause fire  
R9: Explosive when mixed with combustible material  
R10: Flammable  
R11: Highly flammable  
R12 : Extremely flammable  
R13: Extremely flammable liquefied gas  
R14: Reacts violently with water  
R15: Contact with water liberates highly flammable gases  
R16: Explosive when mixed with oxidising substances  
R17: Spontaneously flammable in air  
R18: In use, may form flammable/explosive vapor-air mixture  
R19: May form explosive peroxides  
R20: Harmful by inhalation  
R21: Harmful in contact with skin  
R22: Harmful if swallowed  
R23: Toxic by inhalation  
R24: Toxic in contact with skin  
R25: Toxic if swallowed  
R26: Very toxic by inhalation  
R27: Very toxic in contact with skin  
R28: Very toxic if swallowed  
R29: Contact with water liberates toxic gas  
R30: Can become highly flammable in use  
R31: Contact with acids liberates toxic gas  
R32: Contact with acids liberates very toxic gas  
R33: Danger of cumulative effects  
R34: Causes burns  
R35: Causes severe burns  
R36: Irritating to eyes  
R37: Irritating to respiratory system  
R38: Irritating to skin  
R39: Danger of very serious irreversible effects  
R40: Possible risk of irreversible effects  
R41: Risk of serious damage to eyes  
R42: May cause sensitisation by inhalation  
R43: May cause sensitisation by skin contact  
R44: Risk of explosion if heated under confinement  
R45: May cause cancer  
R46: May cause heritable genetic damage  
R47: May cause birth defects  
R48: Danger of serious damage to health by prolonged exposure  
R49: May cause cancer by inhalation  
R50: Very toxic to aquatic organisms  
R51: Toxic to aquatic organisms  
R52: Harmful to aquatic organisms  
R53: May cause long-term adverse effects in the aquatic environment  
R54: Toxic to flora  
R55: Toxic to fauna  
R56: Toxic to soil organisms  
R57: Toxic to bees  
R58: May cause long-term adverse effects in the environment  
R59: Dangerous to the ozone layer  
R60: May impair fertility  
R61: May cause harm to the unborn child  
R62: Possible risk of impaired fertility

R63: Possible risk of harm to the unborn child

R64: May cause harm to breastfed babies

#### Combination of risks

R14/15: Reacts violently with water, liberating highly flammable gases

R15/29: Contact with water liberates toxic, highly flammable gas

R20/21: Harmful by inhalation and in contact with skin

R20/21/22: Harmful by inhalation, in contact with skin and if swallowed

R20/22: Harmful by inhalation and if swallowed

R21/22: Harmful in contact with skin and if swallowed

R23/24: Toxic by inhalation and in contact with skin

R23/24/25: Toxic by inhalation, in contact with skin and if swallowed

R23/25: Toxic by inhalation and if swallowed

R24/25: Toxic in contact with skin and if swallowed

R26/27: Very toxic by inhalation and in contact with skin

R26/27/28: Very toxic by inhalation, in contact with skin and if swallowed

R26/28: Very toxic by inhalation and if swallowed

R27/28: Very toxic in contact with skin and if swallowed

R36/37: Irritating to eyes and respiratory system

R36/37/38: Irritating to eyes, respiratory system and skin

R36/38: Irritating to eyes and skin

R37/38: Irritating to respiratory system and skin

R42/43: May cause sensitisation by inhalation and skin contact.

R48/20: Harmful: danger of serious damage to health by prolonged exposure

R48/20/21: Harmful: danger of serious damage to health by prolonged exposure through inhalation and in contact with the skin

R48/20/21/22: Harmful: danger of serious damage to health by prolonged exposure through inhalation, in contact with skin and if swallowed

R48/20/22: Harmful: danger of serious damage to health by prolonged exposure through inhalation, and if swallowed

R48/21: Harmful: danger of serious damage to health by prolonged exposure in contact with skin

R48/21/22: Harmful: danger of serious damage to health by prolonged exposure in contact with skin and if swallowed

R48/22: Harmful: danger of serious damage to health by prolonged exposure if swallowed

R48/23: Toxic: danger of serious damage to health by prolonged exposure through inhalation

R48/23/24: Toxic: danger of serious damage to health by prolonged exposure through inhalation and in contact with skin

R48/23/24/25: Toxic: danger of serious damage to health by prolonged exposure through inhalation, in contact with skin and if swallowed

R48/23/25: Toxic: danger of serious damage to health by prolonged exposure through inhalation and if swallowed

R48/24: Toxic: danger of serious damage to health by prolonged exposure in contact with skin

R48/24/25: Toxic: danger of serious damage to health by prolonged exposure in contact with skin and if swallowed

R48/25: Toxic: danger of serious damage to health by prolonged exposure if swallowed

R50/53: Very toxic to aquatic organisms, may cause long term adverse effects in the aquatic environment

R51/53: Toxic to aquatic organisms, may cause long term adverse effects in the aquatic environment

R52/53: Harmful to aquatic organisms, may cause long-term adverse effects in the aquatic Environment

#### Safety precaution phrases (S-Phrases)

S1: Keep locked up

S2: Keep out of reach of children

S3: Keep in a cool place

S4: Keep away from living quarters

S5: Keep contents under . . . (appropriate liquid to be specified by the manufacturer)

S6: Keep under . . . (inert gas to be specified by the manufacturer)

S7: Keep container tightly closed

S8: Keep container dry

S9: Keep container in a well-ventilated place

S12: Do not keep the container sealed

S13: Keep away from food, drink and animal feeding stuffs

S14: Keep away from . . . (incompatible materials to be indicated by the manufacturer)

S15: Keep away from heat

S16: Keep away from sources of ignition-No Smoking

S17: Keep away from combustible material

S18: Handle and open container with care

S20: When using do not eat or drink

S21: When using do not smoke

S22: Do not breathe dust

S23: Do not breathe gas/fumes/vapor/spray (appropriate wording to be specified by manufacturer)

S24: Avoid contact with skin

S25: Avoid contact with eyes

- S26: In case of contact with eyes, rinse immediately with plenty of water and seek medical advice  
 S27: Take off immediately all contaminated clothing  
 S28: After contact with skin, wash immediately with plenty of . . (to be specified by the manufacturer)  
 S29: Do not empty into drains  
 S30: Never add water to this product  
 S33: Take precautionary measures against static discharges  
 S34: Avoid shock and friction  
 S35: This material and its container must be disposed of in a safe way  
 S36: Wear suitable protective clothing  
 S37: Wear suitable gloves  
 S38: In case of insufficient ventilation, wear suitable respiratory equipment  
 S39: Wear eye/face protection  
 S40: To clean the floor and all objects contaminated by this material use (to be specified by the manufacturer)  
 S41: In case of fire and/or explosion do not breath fumes  
 S42: During fumigation/spraying wear suitable respiratory equipment (appropriate wording to be specified by the manufacturer)  
 S43: In case of fire, use ... (indicate in the space the precise type of fire fighting equipment. If water increases the risk add "never use water".)  
 S44: If you feel unwell, seek medical advice (show the label where possible)  
 S45: In case of accident or if you feel unwell, seek medical advice immediately (show the label where possible)  
 S46: If swallowed, seek medical advice immediately and show the container or label  
 S47: Keep at temperature not exceeding ... °C (to be specified by the manufacturer)  
 S48: Keep wetted with ... (appropriate material to be specified by the manufacturer)  
 S49: Keep only in the original container  
 S50: Do not mix with ... (to be specified by the manufacturer)  
 S51: Use only in well ventilated areas  
 S52: Not recommended for interior use on large surface areas  
 S53: Avoid exposure - obtain special instructions before use  
 S54: Obtain the consent of pollution control authorities before discharging to waste-water treatment plants  
 S55: Treat using the best available techniques before discharge into drains or the aquatic environment  
 S56: Do not discharge into drains or the environment, dispose to an authorised waste collection point  
 S57: Use appropriate containment to avoid environmental contamination  
 S58: To be disposed of as hazardous waste  
 S59: Refer to manufacturer/supplier for information on recovery/recycling  
 S60: This material and/or its container must be disposed of as hazardous waste  
 S61: Avoid release to the environment. Refer to special instructions / safety data sheet  
 S62: If swallowed, do not induce vomiting: seek medical advice immediately and show the container or label

#### **Combined safety phrases**

- S1/2: Keep locked up and out of reach of children  
 S3/9: Keep in a cool, well-ventilated place  
 S3/7/9: Keep container tightly closed in a cool, well-ventilated place  
 S3/14: Keep in a cool place away from ... (incompatible materials to be indicated by the manufacturer)  
 S3/9/14: Keep in a cool, well-ventilated place away from ... (incompatible materials to be indicated by the manufacturer)  
 S3/9/49: Keep only in the original container in a cool, well-ventilated place  
 S3/9/14/49: Keep only in the original container in a cool, well-ventilated place away from (Incompatible materials to be indicated by the manufacturer)  
 S3/9/49: Keep only in the original container in a cool, well-ventilated place  
 S3/14: Keep in a cool place away from...(incompatible materials to be indicated by the manufacturer)  
 S7/8: Keep container tightly closed and dry  
 S7/9: Keep container tightly closed and in a well ventilated place  
 S7/47: Keep container tightly closed and at a temperature not exceeding ... °C (to be specified by manufacturer)  
 S20/21: When using do not eat, drink or smoke  
 S24/25: Avoid contact with skin and eyes  
 S29/56: Do not empty into drains, dispose of this material and its container to hazardous or special waste collection point  
 S36/37: Wear suitable protective clothing and gloves  
 S36/37/39: Wear suitable protective clothing, gloves and eye/face protection  
 S36/39: Wear suitable protective clothing, and eye/face protection  
 S37/39: Wear suitable gloves and eye/face protection  
 S47/49: Keep only in the original container at temperature not exceeding ... °C (to be specified by the manufacturer)

# Curriculum Vitae

## Personal information

Name: Vesna Aleksandrović  
Date of birth: October 14, 1973.  
Place of birth: Kruševac, Serbia  
Nationality: Serbian



## Working history

### **1997 - 2002 Faculty of Technology and Metallurgy, University of Belgrade:**

- 2002 Teaching assistant in Polymer synthesis for foreign students;
- 1999 - 2002 Teaching assistant in Macromolecular Chemistry;
- 1997 - 2002 Teaching assistant in Basic Chemistry;

## Education

### **2003-2005 PhD Thesis - University of Hamburg, Institute for Physical Chemistry**

Supervisor: Professor Horst Weller. Topic:

“CoPt<sub>3</sub> Nanoparticles: Ligand Exchange and Film Preparation”

### **1997-2001 M.Sc. Thesis - Faculty of Technology and Metallurgy, Belgrade**

Supervisor: Professor Jasna Djonlagić. Topic:

“Synthesis and characterization of thermoplastic poly(ester-ethers) modified with fumarates”,

### **1992-1997 Diploma studies - Faculty of Technology and Metallurgy, Belgrade**

Division: Organic Chemical Technology and Polymer Engineering;

Supervisor: Professor Jasna Djonlagić. Topic:

“Synthesis and characterization of thermoplastic copolyester elastomers”

## Publications:

### 2003-2006

1. *J. I. Flege, Th. Schmidt, G. Alexe, T. Clausen, S. Bernstorff, I. Randjelovic, V. Aleksandrovic, A. Kornowski, H. Weller, and J. Falta, **Grazing-incidence small-angle x-ray scattering investigation of spin-coated CoPt<sub>3</sub> nanoparticle films**, Nuclear Instruments & Methods in Physics Research, Section B: Beam Interactions with Materials and Atoms (2006), 246(1), 25-29.*
2. *M.S. Nikolic, M. Krack, V. Aleksandrovic, A. Kornowski, S. Förster, H. Weller, **Taylor-made ligands for biocompatible nanoparticles**, Angew. Chem. Int. Ed. (2006), 45, 1 – 6*
3. *B. Gehl, V. Aleksandrovic, U. Leist, H. Weller, K. Al-Shamery, M. Bäumer, submitted to Rev. Sci. Inst.*
4. *V. Aleksandrovic, J. I. Flege, Th. Schmidt, A. Kornowski, I. Randjelovic, G. Alexe, T. Clausen, J. Falta, S. Bernstorff, M. Stolzenburg, S. Förster, H. Weller **Polymers as surface modifiers for preparation of CoPt<sub>3</sub> nanoparticle monolayer films** Physics, Chemistry and Application of Nanostructures, Reviews and Short Notes to NANOMEETING-2005, Minsk, Belarus, May 24-27, 2005.*
5. *Flege, Jan I.; Schmidt, Thomas; Alexe, Gabriela; Clausen, Torben; Bernstorff, Sigrid; Randjelovic, Igor; Aleksandrovic, Vesna; Kornowski, Andreas; Weller, Horst; Falta, Jens **CoPt<sub>3</sub> nanoparticles adsorbed on SiO<sub>2</sub>: A GISAXS and SEM study**, Materials Research Society Symposium Proceedings (2005), Volume Date 2004, 840 Neutron and X-Ray Scattering as Probes of Multiscale Phenomena), 143-148.*

### *Papers in Conference Proceedings:*

1. *V. Aleksandrovic, J. I. Flege, Th. Schmidt, A. Kornowski, I. Randjelovic, G. Alexe, T. Clausen, J. Falta, S. Bernstorff, M. Stolzenburg, S. Förster, H. Weller **Polymers as surface modifiers for preparation of CoPt<sub>3</sub> nanoparticle monolayer films** Physics, Chemistry and Application of Nanostructures, Reviews and Short Notes to NANOMEETING-2005, Minsk, Belarus, May 24-27, 2005.*
2. *Flege, Jan I.; Schmidt, Thomas; Alexe, Gabriela; Clausen, Torben; Bernstorff, Sigrid; Randjelovic, Igor; Aleksandrovic, Vesna; Kornowski, Andreas; Weller, Horst; Falta, Jens **CoPt<sub>3</sub> nanoparticles adsorbed on SiO<sub>2</sub>: A GISAXS and SEM study** Materials Research Society Symposium Proceedings (2005), Volume Date 2004, 840 Neutron and X-Ray Scattering as Probes of Multiscale Phenomena), 143-148.*

### *Presentations*

1. *V. Aleksandrovic, A. Meyer, I. Randjelovic, M. Stolzenburg, S. Förster, A. Kornowski, H. Weller **Influence of polymer ligands on the self-assembly of magnetic nanoparticles**,*

EUROPOLYMER CONFERENCE 2005 (EUPOC 2005) Polymers in Nanoscience and Nanotechnology 29 May - 3 June, 2005, Gargnano, Italy (poster)

2. V. Aleksandrovic, I. Randjelovic, A. Kornowski, A. Mayer, H. Weller, J. I. Flege, Th. Schmidt, G. Alexe, T. Clausen, R. Kröger, J. Falta, S. Bernstorff **Ligand exchange on CoPt<sub>3</sub> nanoparticles and its influence on film formation**, 104th Bunsentagung, 104<sup>th</sup>, Bunsentagung, Frankfurt, 2005 (poster).

3. V. Aleksandrovic, I. Randjelovic, A. Kornowski, H. Weller, **Formation and quality of Langmuir-Blodgett films with different size and ligands of CoPt<sub>3</sub> nanoparticles**, European Research Conference on Interfaces and colloidal Systems, Giens, France, 10-15 September 2004 (poster)

## 1997-2002

### *Publications in main field:*

1. Aleksandrovic, Vesna; Poleti, Dejan; Djonlagic, Jasna **Poly(ether-ester)s modified with different amounts of fumaric moieties** Polymer (2002), 43(11), 3199-3208.

2. V. Aleksandrovic, J. Djonlagic, **Synthesis and characterization of thermoplastic copolyester elastomers modified with fumaric moieties** J. Serb. Chem. Soc. (2001), 66(3) 139-152.

### *Presentations on international conferences*

1. J. Djonlagic, V. Aleksandrovic, B. Dunjic, R. Jovanovic, **Synthesis and characterization of thermoplastic copolyester elastomers**, 3. Scientific-professional counseling with international participation, Belgrade 22-23 September, 1997 (printed paper)

2. V. Aleksandrovic, J. Djonlagic, **Investigation of the double bond influence on properties of thermoplastic copolyester elastomers**, Third Yugoslav Materials Research Society Conference, Held in Herceg-Novi, Yugoslavia, September 1999 (oral)

3. V. Aleksandrovic, D. Poleti, J. Djonlagic, **Characterization of poly(ester-ether)s based on terephthalic and fumaric acid**. 2<sup>nd</sup> International Conference of the Chemical Societies of the South - Eastern European Countries on «Chemical Sciences for Sustainable Development», Halkidiki-Greece, 6-9 June 2000. (poster)

4. E. Dzunuzovic, V. Aleksandrovic, J. Djonlagic, **Thermal stability of poly(ester-ether)s based on terephthalic and fumaric acid** Third Yugoslav Materials Research Society Conference, Held in Herceg-Novi, Yugoslavia, September 1999

5. J. Djonlagic, V. Aleksandrovic, D. Poleti, **Synthesis and characterization of poly(ether-ester) modified with different amount of fumaric moieties**, Polymer Chemistry: Past, Present and Future, A Symposium Honoring Robert W. Lenz, August 14/16 2002., Amherst.

# Lebenslauf

## Persönliche Daten:

Name: Vesna Aleksandrovic  
Geboren am: 14. Oktober 1973  
Geburtsort: Krusevac, Serbien  
Nationalität: Serbisch

## Berufserfahrung:

**2003-2006** Wissenschaftliche Mitarbeiterin an der Universität Hamburg  
**1997 - 2002** Fakultät der Technologie und Metallurgie, Universität Belgrad:  
2002 Wissenschaftliche Mitarbeiterin: Betreuung des Praktikums Polymersynthese  
1999 - 2002 Wissenschaftliche Mitarbeiterin: Betreuung des Fortgeschrittenenpraktikums  
in makromolekularer Chemie  
1997 - 2002 Wissenschaftliche Mitarbeiterin: Betreuung des Grundpraktikums in  
anorganischer Chemie

## Hochschulbildung:

**2003-2006** **Doktorarbeit** bei Prof. Horst Weller an der Universität Hamburg, Institut  
für Physikalische Chemie, zum Thema:  
„CoPt<sub>3</sub> Nanopartikel: Ligandenaustausch und Filmpräparation“  
**1997-2001** **Magisterarbeit** bei Prof. Jasna Djonlagic an der Fakultät für Technologie  
und Metallurgie, Universität Belgrad, zum Thema:  
„Synthese und Charakterisierung von thermoplastischen durch Fumarsäure  
modifizierten Poly(ester-ether) – Elastomeren“  
**1992-1997** **Diplomstudien** bei Prof. Jasna Djonlagic an der Fakultät der Technologie und  
der Metallurgie, Universität Belgrad, Abteilung: Organisch-chemische  
Technologie und Polymer Ingenieurwissenschaften:  
„Synthese und Charakterisierung von thermoplastischen Copolyester  
Elastomeren“

## **Declaration**

The materials contained in this thesis is the result of my own work and all sources of information as well as the results obtained in collaboration with other people are pointed out.

This dissertation has not been submitted in whole or in part for the award of a degree at this of any other university.

Hamburg, August 2006

MSc. Vesna Aleksandrovic